Nano-Optics and Nanophotonics

Motoichi Ohtsu *Editor*

Progress in Nanophotonics 1

Springer

NANO-OPTICS AND NANOPHOTONICS

NANO-OPTICS AND NANOPHOTONICS

The Springer Series in Nano-Optics and Nanophotonics provides an expanding selection of research monographs in the area of nano-optics and nanophotonics, science- and technology-based on optical interactions of matter in the nanoscale and related topics of contemporary interest. With this broad coverage of topics, the series is of use to all research scientists, engineers and graduate students who need up-to-date reference books. The editors encourage prospective authors to correspond with them in advance of submitting a manuscript. Submission of manuscripts should be made to the editor-in-chief, one of the editors or to Springer.

Please view available titles in *Nano-Optics and Nanophotonics*
on series homepage http://www.springer.com/series/8765

Motoichi Ohtsu
Editor

Progress in Nanophotonics 1

With 184 Figures

Springer

Editor
Motoichi Ohtsu
Graduate School of Engineering
The University of Tokyo
2-11-16 Yayoi, Bunkyo-ku, Tokyo 113-8656, Japan
ohtsu@ee.t.u-tokyo.ac.jp

Nano-Optics and Nanophotonics ISSN 2192-1970 e-ISSN 2192-1989
ISBN 978-3-642-17480-3 e-ISBN 978-3-642-17481-0
DOI 10.1007/978-3-642-17481-0
Springer Heidelberg Dordrecht London New York

Library of Congress Control Number: 2011934022

Cover design: eStudio Calamar Steinen

Printed on acid-free paper

Springer is part of Springer Science+Business Media (www.spinger.com)

Preface to *Progress in Nanophotonics*

As the first example, recent advances in photonic systems demand drastic increases in the degree of integration of photonic devices for large-capacity, ultrahigh-speed signal transmission and information processing. Device size has to be scaled down to nanometric dimensions to meet this requirement, which will become even more strict in the future. As the second example, photonic fabrication systems demand drastic decreases in the size of the fabricated patterns for assembling ultra-large-scale integrated circuits. These requirements cannot be met even if the sizes of the materials are decreased by advanced methods based on nanotechnology. It is essential to decrease the size of the electromagnetic field used as a carrier for signal transmission, processing, and fabrication. Such a decrease in the size of the electromagnetic field beyond the diffraction limit of the propagating field can be realized in optical near fields. Nanophotonics, a novel optical technology that utilizes the optical near field, was proposed by Ohtsu (the editor of this monograph series) in 1993 to meet these requirements. However, it should be noted that the true nature of nanophotonics involves not only its ability to meet the above requirements, but also its ability to realize qualitative innovations in photonic devices, fabrication techniques, energy conversion, and information processing systems by utilizing novel functions and phenomena made possible by optical near-field interactions, which are otherwise impossible as long as conventional propagating light is used. Based on interdisciplinary studies on condensed-matter physics, optical science, and quantum field theory, nano-materials and optical energy transfer in the nanometric regime have been extensively studied in the last two decades. Through these studies, novel theories on optical near fields have been developed, and a variety of novel phenomena have been found. The results of this basic research have been applied to develop nanometer-sized photonic devices, nanometer-resolution fabrication, highly efficient energy conversion, and novel information processing, resulting in qualitative innovations. Further advancement in these areas is expected to establish novel optical sciences in the nanometric space, which can be applied to further progress in nanophotonics to support the sustainable development of peoples' lives all over the world. This unique monograph series entitled *Progress in Nanophotonics* in the Springer Series in Nano-optics and Nanophotonics is being introduced to review the results of advanced studies in the field of nanophotonics and covers the most recent topics of theoretical and experimental interest in relevant fields, such as

classical and quantum optical sciences, nanometer-sized condensed matter physics, devices, fabrication techniques, energy conversion, information processing, architectures, and algorithms. Each chapter is written by leading scientists in the relevant field. Thus, this monograph series will provide high-quality scientific and technical information to scientists, engineers, and students who are and will be engaged in nanophotonics research. As compared with the previous monograph series entitled *Progress in Nano-Electro-Optics* (edited by Ohtsu, published in the Springer Series in Optical Science), this monograph series deals not only with optical science on the nanometer scale, but also its applications to technology. I am grateful to Dr Ascheron of Springer-Verlag for his guidance and suggestions throughout the preparation of this monograph series.

Tokyo
January 2011

Motoichi Ohtsu

Preface

This volume contains six review articles focusing on various but mutually related topics in nanophotonics written by the world's leading scientists. Chapter 1 describes the concept of the dressed photon and its applications to qualitatively innovative optical devices, fabrication techniques, energy conversion, and systems. Chapter 2 is devoted to describing basic concepts necessary for two-dimensional parallel processing of light–matter interactions on the nanometer scale to realize probe-free nanophotonic systems. Additionally, the concepts and some demonstrations of the hierarchy inherent in nanophotonics, based on the hierarchy between optical near- and far-fields, are described as practical applications of optical near-field interactions. Chapter 3 describes self-organized fabrication of composite semiconductor quantum dots, which can be exploited for size- and position-controlled quantum dots for novel nanophotonic devices. Chapter 4 is devoted to near-field spectroscopy of metallic nanostructures, particularly visualization of plasmon wave functions and optical fields using near-field methods. Chapter 5 concerns simple experimental approaches for constructing metallic nanoarrays on a solid surface for applications to miniaturized optical devices, sensors, and single-molecule detection. For these applications, the author describes a unique approach for fabricating one-dimensional metal nanoparticle arrays on surfaces by applying highly aligned DNA molecules or nanofibers on a surface as a template. The last chapter, Chap. 6, describes chemical preparation of metal nanoparticles and their assembly formation processes. Various metal and semiconductor nanoparticles are studied according to their unique properties controlled by their sizes. This volume is published with the support of Prof. Yatsui of the University of Tokyo, an Associate Editor. I hope that this volume will be a valuable resource for readers and future specialists in nanophotonics.

Tokyo
January 2011

Motoichi Ohtsu

Contents

1 Nanophotonics: Dressed Photon Technology for Qualitatively Innovative Optical Devices, Fabrication, and Systems 1
Motoichi Ohtsu

1.1 Introduction 1
1.2 Background and Principles 2
1.3 Fiber Probes, Sensing Systems, and 1 Tb in.$^{-2}$-Density Magnetic Storage Systems 6
1.4 Nanophotonic Devices 9
1.4.1 Basic Devices 9
1.4.2 Input and Output Terminals 17
1.4.3 Unique Features and Application to Information Processing Systems 20
1.5 Nanophotonic Fabrication 24
1.5.1 Photochemical Vapor Deposition 24
1.5.2 Photolithography 28
1.5.3 Self-Organized Smoothing 35
1.6 Nanophotonic Energy Conversion 44
1.6.1 Optical/Optical Energy Up-Conversion 44
1.6.2 Optical/Electrical Energy Up-Conversion 48
1.7 Nanophotonic Systems and Their Evolution to Related Sciences 53
1.8 Summary 54
References 55

2 Probe-Free Nanophotonic Systems: Macro-Scale Applications Based on Nanophotonics 59
Naoya Tate, Makoto Naruse, and Motoichi Ohtsu

2.1 Introduction 59
2.2 Probe-Free Nanophotonic Systems 61

2.3 Nanophotonic Matching as Macro-Scale Observation 63
2.3.1 Macro-Scale Observation 63
2.3.2 Quadrupole–Dipole Transform 63
2.3.3 Nanophotonic Matching 65
2.3.4 Experimental Demonstration 67
2.3.5 Outlook 70
2.4 Nanophotonics-Induced Phase Transition as Magnified-Transcription 72
2.4.1 Magnified-Transcription of Optical Near-Fields 72
2.4.2 Photoinduced Phase Transition 73
2.4.3 Experimental Demonstrations 74
2.4.4 Outlook 77
2.5 Nanophotonic Hierarchical Hologram 77
2.5.1 Background 77
2.5.2 Basic Concept 78
2.5.3 Nanophotonic Code 81
2.5.4 Numerical Evaluations 82
2.5.5 Experimental Demonstration 85
2.5.6 Outlook 89
2.6 Summary 90
References 91

3 Self-Formation of Semiconductor Quantum Dots 93
Koichi Yamaguchi

3.1 Introduction 93
3.2 Stranski–Krastaov Growth of Quantum Dots 94
3.3 Uniform Formation of Quantum Dots 96
3.3.1 Self Size-Limiting Growth of Uniform InAs/GaAs Quantum Dots 96
3.3.2 Capping Growth of Uniform InAs/GaAs Quantum Dots 100
3.3.3 Closely-Stacked Growth of Uniform InAs/GaAs Quantum Dots 103
3.4 Control of Quantum Energy Level 106
3.5 Density Control of Quantum Dots 109
3.5.1 Sb-Mediated Growth of High-Density InAs/GaAs Quantum Dots 109
3.5.2 Intermittent Growth of Low-Density InAs/GaAs Quantum Dots 113
3.6 Quantum Dot Array 116
3.6.1 Vertical Array of InAs/GaAs Quantum Dots 116
3.6.2 In-Plane Arrays of InAs/GaAs Quantum Dots 118
3.7 Conclusion 123
References 123

4 Near-Field Optical Imaging of Plasmon Wavefunctions and Optical Fields in Plasmonic Nanostructures 127
Kohei Imura and Hiromi Okamoto

4.1 Introduction 127
4.2 Optical Properties of Nanoparticles 128
4.2.1 Optical Properties of Ensemble of Nanoparticles 131
4.3 Plasmon Wavefunctions 133
4.4 Principle of Wavefunction Visualization 133
4.5 Near-Field Optical Microscope 135
4.5.1 Instrumentation of Near-Field Optical Microscope 135
4.5.2 Time-Resolved and Non-Linear Measurements 137
4.6 Photonic Local Density-of-States Calculation 138
4.7 Near-Field Transmission Measurements 139
4.7.1 Near-Field Transmission Measurement of Spherical Gold Nanoparticles 140
4.7.2 Near-Field Transmission Measurement of Gold Nanorods 141
4.8 Time-Resolved Measurement 145
4.9 Non-Linear Measurements 148
4.9.1 Gold Nanorods 149
4.9.2 Gold Nonoplates 151
4.9.3 Dimeric Nanoparticles 152
4.9.4 Larger Assemblies of Nanoparticles 154
4.10 Summary 156
References 157

5 Simple Approaches for Constructing Metallic Nanoarrays on a Solid Surface 161
Hidenobu Nakao

5.1 Introduction 161
5.2 Assembling MNPs in One Dimension 162
5.2.1 Chemical Self-Assembly 162
5.2.2 Physical Means 164
5.2.3 Template-Assisted Assembly 166
5.3 Highly Aligned DNA as Templates for 1D Assembly of MNPs 166
5.3.1 Stretching and Aligning DNA Molecules on Surfaces 167
5.3.2 Assembling AuNPs onto Aligned DNA Molecules 170
5.4 Fabrication and Patterning of Metallic Nanoarrays with Long-Range Order 176
5.4.1 Preparation of Longer Metallic Nanoarrays with DNA Nanofibers 177
5.4.2 Transfer Printing of Metallic Nanoarray 181
5.5 Conclusions 182
References 184

6 Assembly and Immobilization of Metal Nanoparticles 189
Nao Terasaki and Tetsu Yonezawa

6.1 Introduction 189
6.2 Preparation of Metal Nanoparticles 190
6.2.1 Preparation of Metal Nanoparticles by Chemical Reduction 190
6.3 Assembly Formation 194
6.3.1 Two Dimensional Assembly Formation of Nanoparticles by Simple Evaporation of Dispersions 195
6.3.2 Two Dimensional Arrays Formation on Liquid–Liquid Interfaces 197
6.3.3 Direct Preparation of Nanostructures on a Substrate 198
6.3.4 Control of Nanoparticle Assembly by Stabilizing Reagents 198
6.3.5 Nanoparticle Assembly with Templates 206
6.4 Conclusions 228
References 229

Index 233

Contributors

Kohei Imura Department of Chemistry and Biochemistry, School of Advanced Science and Engineering, Waseda University, 3-4-1 Okubo, Shinjuku, Tokyo 169-8555, Japan
and
PRESTO, Japan Science and Technology Agency, 4-1-8 Honcho, Kawaguchi, Saitama 332-0012, Japan, imura@waseda.jp

Hidenobu Nakao Ion Beam Group, National Institute for Materials Science, Namiki 1-1, Tsukuba, Ibaraki 305-0044, Japan, NAKAO.hidenobu@nims.go.jp

Makoto Naruse Photonic Network Research Institute, National Institute of Information and Communications Technology, 4-2-1 Nukui-kita, Koganei, Tokyo 184-8795, Japan, naruse@nict.go.jp

Motoichi Ohtsu Graduate School of Engineering, The University of Tokyo, 2-11-16 Yayoi, Bunkyo-ku, Tokyo 113-8656, Japan
and
Nanophotonics Research Center, The University of Tokyo, 2-11-16 Yayoi, Bunkyo-ku, Tokyo 113-8656, Japan, ohtsu@ee.t.u-tokyo.ac.jp

Hiromi Okamoto Institute for Molecular Science, 38 Nishigonaka, Myodaiji, Okazaki 444-8585, Japan
and
The Graduate University for Advanced Studies, 38 Nishigonaka, Myodaiji, Okazaki 444-8585, Japan, aho@ims.ac.jp

Naoya Tate Graduate School of Engineering, The University of Tokyo, 2-11-16 Yayoi, Bunkyo-ku, Tokyo 113-8656, Japan
and
Nanophotonics Research Center, The University of Tokyo, 2-11-16 Yayoi, Bunkyo-ku, Tokyo 113-8656, Japan, tate@nanophotonics.t.u-tokyo.ac.jp

Nao Terasaki Measurement Solution Research Center, National Institute of Advanced Industrial Science and Technology (AIST), 807-1, Shuku-machi, Tosu, Saga 841-0052, Japan, nao-terasaki@aist.go.jp

Koichi Yamaguchi Department of Engineering Science, The University of Electro-Communications, 1-5-1 Chofugaoka, Chofu, Tokyo 182-8585, Japan, kyama@ee.uec.ac.jp

T. Yonezawa Division Materials Science and Engineering Graduate School of Engineering Hokkaido University, Kita 13, Nishi 8, Kita-ku, Sapporo, Hokkaido 060-8628, Japan, tetsu@eng.hokudai.ac.jp

Chapter 1
Nanophotonics: Dressed Photon Technology for Qualitatively Innovative Optical Devices, Fabrication, and Systems

Motoichi Ohtsu

Abstract This chapter reviews the theoretical picture of the dressed photon by combining the concepts of quantum field theory, optical science, and condensed-matter physics. Based on the exchange of dressed photons, energy transfer to an electric dipole-forbidden energy level is described. Furthermore, the possibility of coupling a dressed photon with a coherent phonon is presented, revealing a novel phonon-assisted process in light–matter interactions in nanometric space. Applications to qualitatively innovative optical devices, fabrication techniques, energy conversion, and systems are exemplified.

1.1 Introduction

Nanophotonics, proposed by the author in 1993 [1–3], is a novel optical technology that utilizes the optical near-field. The optical near-field is the *dressed photons* that mediate the interaction between nanometric particles located in close proximity to each other. Nanophotonics allows the realization of *qualitative innovations* in photonic devices, fabrication techniques, and systems by utilizing novel functions and phenomena enabled by optical near-field interactions that would otherwise be impossible if only conventional propagating light were used. In this sense, the principles and concepts of nanophotonics are completely different from those of conventional wave-optical technology, encompassing photonic crystals, plasmonics, metamaterials, and silicon photonics. This review describes these differences and shows examples of such qualitative innovations.

M. Ohtsu
Graduate School of Engineering, The University of Tokyo, 2-11-16 Yayoi, Bunkyo-ku, Tokyo 113-8656, Japan
and
Nanophotonics Research Center, The University of Tokyo, 2-11-16 Yayoi, Bunkyo-ku, Tokyo 113-8656, Japan
e-mail: ohtsu@ee.t.u-tokyo.ac.jp

M. Ohtsu (ed.), *Progress in Nanophotonics 1*, Nano-Optics and Nanophotonics,
DOI 10.1007/978-3-642-17481-0_1,

1.2 Background and Principles

The author's primary motivation for proposing nanophotonics was to break the deadlock of optical technology that has existed due to the diffraction limit of the light. In the case of information transmission systems, communications technology roadmaps have claimed that the size of photonic devices should be decreased to several hundreds or tens of nanometers for future high-capacity optical transmission systems [4]; however, this is impossible due to the diffraction limit. In the case of photolithography, although the size of the fabricated patterns should be decreased to several tens of nanometers for mass-production of future semiconductor electronic devices, such as highly integrated DRAMs, this task is difficult due to the diffraction limit. Short-wavelength light sources (excimer lasers, extreme UV light sources, and synchrotron radiation sources) have undergone intense development for use in photolithography systems to decrease the sizes of the fabricated patterns down to the diffraction limit, in other words, to increase the resolution up to the diffraction limit. However, the resulting equipment is extremely large and expensive and consumes a great deal of power, which makes its practical use very difficult.

The focused spots of light are relatively large due to the diffraction limit. Therefore, photonic devices are large and the resolution of photolithography is low. Even if the physical dimensions of these devices could be decreased by nanotechnology, photonic devices cannot be reduced in size beyond the diffraction limit as long as conventional propagating light is used for driving them. To decrease the device size and increase the resolution of photolithography, the size (spatial extent) of the light itself must be decreased.

One promising candidate technology to decrease the size of light is nanophotonics, which was proposed by the author in 1993: If a nanometer-sized particle is illuminated by propagating light, it generates scattered light, which propagates to the far field and exhibits diffraction. However, also generated at the surface of the particle is an *optical near-field*, which is non-propagating light whose energy is localized at the particle surface. Furthermore, the extent of localization is equivalent to the particle size, which is independent of the incident light wavelength, and thus, in the case of a nanometric particle, it is much smaller than the wavelength. Therefore, if the optical near-field is utilized for devices and fabrication, novel technologies that can break through the bounds imposed by the diffraction-limit can be realized, thus enabling *quantitative innovations* in optical technology.

The optical near-field is a *virtual cloud of photons* that always exists around an illuminated nanometric particle. Its energy fluctuation, δE, and duration of the fluctuation, τ, are related by the Heisenberg uncertainty relation, $\tau \delta E \cong \hbar$, where $\hbar$ is Planck's constant divided by 2π. From this relation, the linear dimension of the virtual cloud of photons (the *virtual photons* for short) is given by $r \cong c\tau \cong \hbar c/\delta E$, where c is the speed of light. In the case of visible light illumination (photon energy $\sim$2 eV), r is estimated to be about 100 nm. This means that the effect of the virtual photons at the surface of the illuminated particle is important if the particle is smaller than 100 nm. In other words, the optical properties of sub-micron-sized matter are not free from the effects of virtual photons.

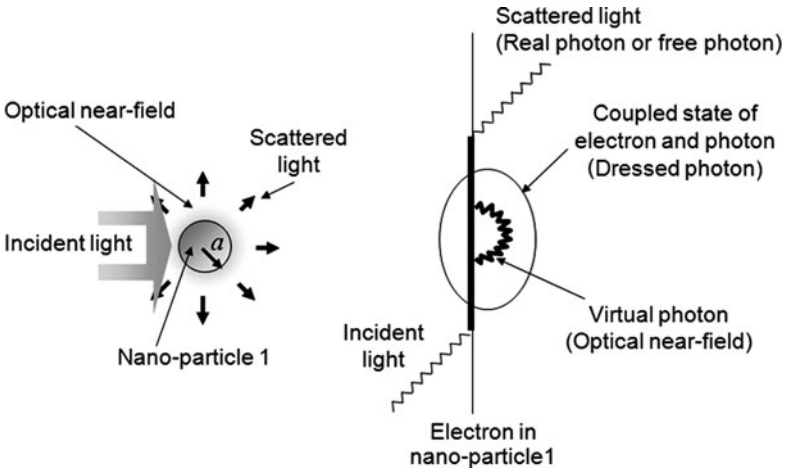

Fig. 1.1 Feynman diagram representing the generation of optical near-fields

This feature of the optical near-field, i.e., the virtual photons, can be most appropriately described by using a Feynman diagram (Fig. 1.1), popularly employed for elementary particle physics. In this figure, a photon is emitted from an electron in the illuminated nanometric particle and can be re-absorbed within a short duration. This photon is nothing more than a virtual photon, and its energy is localized at the surface of the nanometric particle. Independently of this virtual photon, a real photon (also called a free photon) can also be emitted from the electron. This photon is conventional propagating scattered light. Since the virtual photon remains in the proximity of the electron, it can couple with the electron in a unique manner. This coupled state, called a dressed photon, is a quasi-particle from the standpoint of photon energy transfer and has applications to novel nanophotonic devices and fabrication technologies. It is the dressed photon, not the free photon, that carries the material excitation energy. Therefore, the energy of the dressed photon, $h\nu_{\mathrm{dp}}$, is larger than that of the free photon, $h\nu$, due to contribution of the material excitation energy.

To detect the dressed photon, a second nanometric particle should be placed in close proximity to the first particle to disturb the dressed photon on the first particle. This disturbance generates a free photon, which is propagating scattered light that can be detected by a conventional photodetector installed in the far field. This detection scheme suggests that the dressed photon energy is exchanged between the two particles, which can also be represented by a Feynman diagram (Fig. 1.2). That is, after a dressed photon is generated in the first particle, it is transferred to the other particle. It can be transferred back to the first particle again, which means that the dressed photon can be exchanged between the two particles. The detectable free photon is generated in the process of this exchange.

The dressed photon is theoretically described by assuming a multipolar quantum electro-dynamic Hamiltonian in Coulomb gauge and single-particle states in a finite

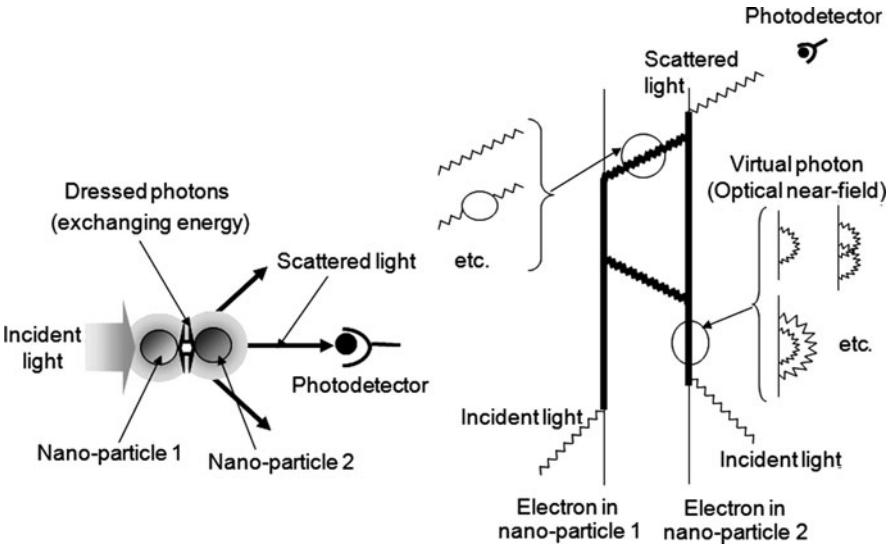

Fig. 1.2 Feynman diagram representing the detection of optical near-fields

nano-system [5]. After a unitary transformation and some simple calculations, its annihilation and creation operators are respectively expressed, in the lowest order, as

$$\tilde{a}_{\vec{k}\lambda} = a_{\vec{k}\lambda} - i N_{\vec{k}} \sum_{\substack{\alpha > F \\ \beta < F}} \left\{ \rho^*{}_{\beta\alpha\lambda} \left(\vec{k} \right) A^\dagger{}_{\alpha\beta} + \rho^*{}_{\alpha\beta\lambda} \left(\vec{k} \right) A_{\alpha\beta} \right\} \tag{1.1}$$

and

$$\tilde{a}^\dagger_{\vec{k}\lambda} = a^\dagger{}_{\vec{k}\lambda} + i N_{\vec{k}} \sum_{\substack{\alpha > F \\ \beta < F}} \left\{ \rho_{\alpha\beta\lambda} \left(\vec{k} \right) A^\dagger{}_{\alpha\beta} + \rho_{\beta\alpha\lambda} \left(\vec{k} \right) A_{\alpha\beta} \right\}, \tag{1.2}$$

where $\vec{k}$ is the wave-number of the free photon, λ is the polarization of a free photon, $N_{\vec{k}}$ is the normalization constant, α and β represent the electronic energy states above and below the Fermi energy level F, $\left(a_{\vec{k}\lambda}, a^\dagger{}_{\vec{k}\lambda}\right)$ and $\left(A_{\alpha\beta}, A^\dagger{}_{\alpha\beta}\right)$ are the annihilation and creation operators of the free photon and an electron–hole pair, respectively, and $\rho_{\alpha\beta\lambda}\left(\vec{k}\right)$ is the Fourier transform of the spatial distribution of the transition dipole, $\rho_{\alpha\beta\lambda}\left(\vec{r}\right)$, of the nanometric particle. Based on this dressed photon picture, interactions between the nanometric particles can be simply described by emission, absorption, and scattering of dressed photons, which provides a physically intuitive picture of the optical near-field interaction between the two particles.

The real system is more complicated because the nanometric subsystem (composed of the two nanometric particles and the dressed photons) is buried in a macroscopic subsystem composed of the macroscopic substrate material and the

macroscopic incident and scattered light fields. A novel theory was developed to avoid describing all of the complicated behaviors of these subsystems rigorously, since we are interested only in the behavior of the nanometric subsystem. In this theory, the macroscopic subsystem is expressed as an exciton–polariton, which is a mixed state of material excitation and electromagnetic fields. Since the nanometric subsystem is excited by an electromagnetic interaction with the macroscopic subsystem, the projection operator method is effective for describing the quantum mechanical states of these systems [6]. As a result of this projection, the nanometric subsystem can be treated as being isolated from the macroscopic subsystem, where the magnitudes of effective interaction energy between the elements of the nanometric subsystem are influenced by the macroscopic subsystem. This local electromagnetic interaction can take place within a sufficiently short duration in which the uncertainty relation allows the exchange of dressed photons non-resonantly, as well as the exchange of a free photon resonantly. The interaction due to the non-resonant process is expressed by a screened potential using a Yukawa function $\exp(-r/a)/r$, which represents the localization of the optical near-field around the nanometric particles. Its decay length a is equivalent to the particle size [6], which means that the extent of localization of the optical near-field is equivalent to the particle size, as was described above. On the other hand, the interaction due to the resonant process is expressed by a conventional spherical wave function, which is mediated by a free photon (a conventional propagating field).

Because the extent of localization of the dressed photon is equivalent to the nanometric particle size, the long-wavelength approximation, which has always been employed for conventional light–matter interaction theory, is not valid. This means that an electric dipole-forbidden state in the nanometric particle can be excited as a result of the dressed photon exchange between closely placed nanometric particles, which enables the operation of novel nanophotonic devices. Details of such devices will be reviewed in Sect. 1.4.

A real nanometric material is composed not only of electrons but also of a crystal lattice. In this case, after a dressed photon is generated on an illuminated nanometric particle, its energy can be exchanged with the crystal lattice, as shown by the Feynman diagram of Fig. 1.3a. By this exchange, the crystal lattice can excite the vibration mode coherently, creating a coherent phonon state. As a result, the dressed photon and the coherent phonon can form a coupled state, as is schematically explained by Fig. 1.3b. The creation operator $\hat{a}_i^\dagger$ of this novel form of elementary excitation is expressed as

$$\hat{a}_i^\dagger = \tilde{a}_i^\dagger \exp\left\{-\sum_{p=1}^{N} \frac{\chi_{ip}}{\Omega_p}\left(b_p{}^\dagger - b_p\right)\right\}, \tag{1.3}$$

where $\tilde{a}_i^\dagger$ is the creation operator of the dressed photon (refer to (1.2)) localized on the ith site of the crystal lattice, N is the number of sites, χ_{ip} is the phonon–photon coupling in mode p at site i, and Ω_p is the eigen-frequency of the phonon mode p. The exponential function in this equation is called a displacement operator,

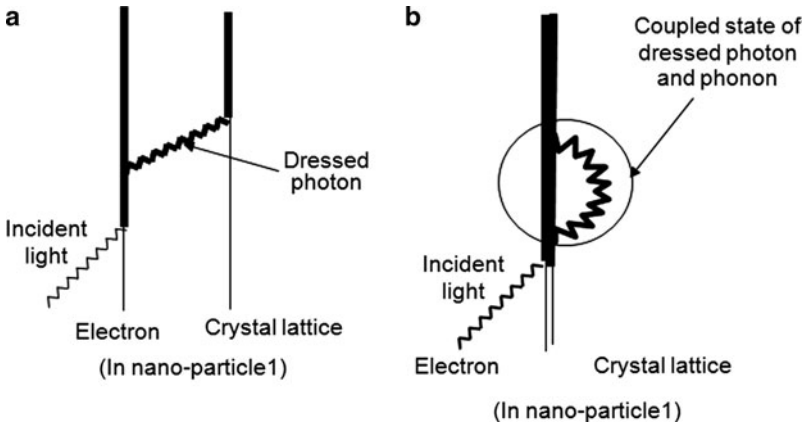

Fig. 1.3 Feynman diagrams representing the coupling of a dressed photon with phonons. (**a**) Generation of a dressed photon and exchange with the crystal lattice. (**b**) A coupled state of a dressed photon and a coherent phonon

composed of the phonon creation and annihilation operators $\left({b_p}^{\dagger} - b_p\right)$. This is an operator representing the creation of the coherent phonon state [7, 8]. This coupled state (*the dressed photon carrying the coherent phonon energy* (DP–CP)) is a quasi-particle and is generated only when the particle size is small enough to excite the crystal lattice vibration coherently. If not, the vibration is incoherent, and thus, its energy is dissipated, heating the particle.

It is easily understood that the energy of the DP–CP, $h\nu_{\mathrm{DP-CP}}$, is higher than that of the dressed photon. It is also higher than the free photon energy, $h\nu_{\mathrm{FP}}$, incident on the nanometric particle. The relation between these energies is represented by

$$h\nu_{\mathrm{FP}} < h\nu_{\mathrm{DP}} < h\nu_{\mathrm{DP-CP}}. \tag{1.4}$$

The first and second inequalities originate from the contribution of the electron and coherent phonon energies, respectively. Novel fabrication techniques allowing qualitative innovations can be developed by utilizing the DP–CP. Several examples of such innovations will be reviewed in Sect. 1.5.

1.3 Fiber Probes, Sensing Systems, and 1 Tb in.$^{-2}$-Density Magnetic Storage Systems

To generate optical near-fields efficiently and reproducibly, selective chemical etching technology has been established for fabricating high-quality fiber probes [9, 10]. This led to the realization of a high-resolution probe with a 1 nm-radius apex, a high-efficiency probe with 10% optical near-field generation efficiency, and other

related devices. Elsewhere in the world, methods involving heating and pulling fiber were most popular at that time [11], although the performance of chemically etched fiber probes was superior. The method used to fabricate these probes was transferred to industry, resulting in high-quality commercial fiber probes. A near-field optical microscope has been developed using these fiber probes, and a variety of ultrahigh-resolution images have been achieved, such as the image of a single-stranded DNA molecule with a resolution greater than 4 nm [12], which is a world record.

A near-field spectrometer has also been developed for diagnosing single semiconductor quantum dots [13], semiconductor devices [14], single organic molecules [15], and biological specimens [16]. Many experimental results on spatially resolved photoluminescence and Raman spectra with 10 nm resolution have been accumulated [17]. Patents have been transferred to industry to produce commercial near-field photoluminescence spectrometers that operate in the ultraviolet-infrared region, at liquid helium-room temperature ranges, and in high magnetic fields [18]. Since their introduction in the market, they have been popularly used in a variety of nanoscience and nanotechnology fields. Instead of using fiber probes, apertureless probes are sometimes used because of their simplicity of fabrication and the possibility of field enhancement. However, it has been demonstrated that apertureless probes cannot realize high resolution due to the scattering of residual propagating light [19].

Technology for fabricating a triple-tapered fiber probe has been developed to increase the optical near-field generation efficiency by up to 1,000 times through efficient excitation of the EH_{11} mode in a fiber [20,21]. This was applied to develop a pyramidal silicon probe on a contact slider for writing and reading in a phase-change optical storage disk system [21,22]. The shortest mark length and the carrier-to-noise ratio were 110 nm and 10 dB, respectively, with a data transmission rate of 2.0 MHz. Using the two-dimensional probe array, the rate was expected to increase to 200 MHz. This and related work triggered the development of an optical near-field assisted magnetic storage system.

The upper limit of the storage density of conventional magnetic storage systems is about 0.3 Tb in.$^{-2}$, which is limited by the thermal instability of the magnetic domains on the disk. To break this limit, an optical near-field was used to locally heat a magnetic domain to decrease the coercivity, followed by immediately applying a magnetic field to the domain to write a pit. With this technique, a storage density as high as 1 Tb in.$^{-2}$ is expected, which meets the requirements of the technology roadmaps of future magnetic storage systems.

To realize such a high-density magnetic storage system, a Japanese national project was organized with academia-industry collaboration, supervised by the author and involving eight Japanese companies [23]. This project developed three main technologies:

(1) *Near-field storage media technology* [24]. Two or three rows of magnetic dots were aligned circumferentially in guide grooves that were drawn using an electron beam mastering method. A process for flattening surfaces was also developed. Nano-patterned media (20 nm in diameter) were fabricated at 30-nm intervals, and individual magnetic dots were grown on them. A self-assembly

method was developed for circumferential alignment using an Si master disk. In addition, regularly aligned dot patterns were obtained with block copolymers. Co/Pd multilayers that had a perpendicular anisotropy of 9.2×10^6 erg/cc were developed, and a magnetization reversal size of 20 nm was obtained by patterning the film into dots.

(2) *Recording technology* [25, 26]. A device made of a baked metallic plate, named a "nano-beak" was developed for generating an optical near-field with a spot diameter of 20 nm with efficiency of several percent. A near-field optical slider head was then fabricated to mount the nano-beak and a solid immersion lens. The slider head ran with a linear velocity higher than 7 nm s^{-1} in a stable manner, maintaining a flying height of 20 nm. An isolated dot of 20 nm in diameter was recorded on a Co/Pd multilayer magnetic nano-patterned medium.

(3) *Nano-mastering technology.* A novel electron beam (EB) technique was developed to converge the EB spot to a diameter of 20 nm with a current density of 8 kA cm^{-2}. Using this technique, master disks were fabricated for 1 Tb $in.^{-2}$-class storage with a groove width of 15 nm and track pitch of 30 nm. The standard deviation of the track pitch was less than 1.5 nm. A formatter was also improved to increase the drawing speed and accuracy.

By assembling these technologies, isolated pits of 20 nm-diameter at 30 nm-pitch were successfully written on a storage disk, corresponding to a storage density of 1.5 Tb $in.^{-2}$ (Fig. 1.4). These technical developments realized a storage density

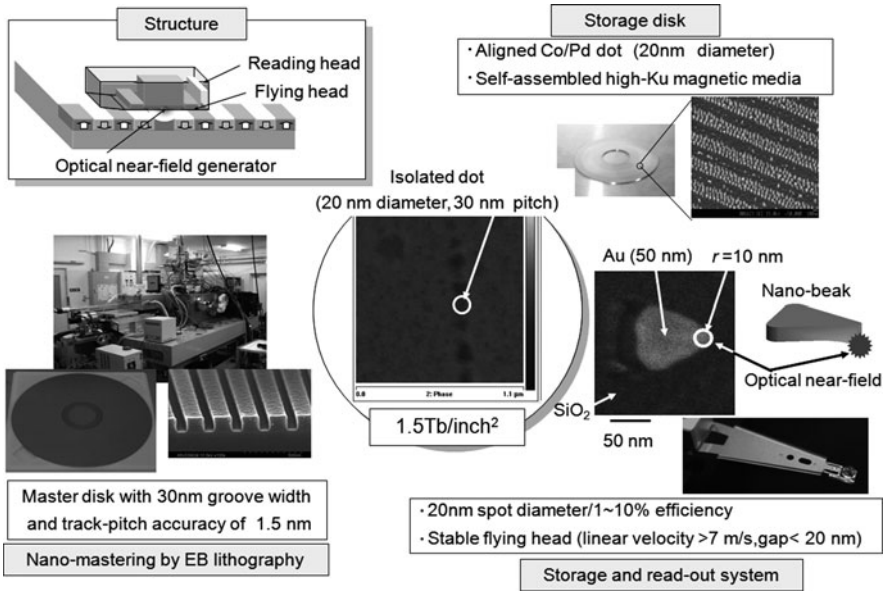

Fig. 1.4 Technologies for optical near-field assisted magnetic storage system with 1.5 Tb $in.^{-2}$ storage density

higher than that dictated by the fundamental limits due to thermal fluctuations. Furthermore, with the recent progress of EB lithography, a track pitch as small as 3.5 nm was achieved in 2010 [27], from which a storage density reaching 10 Tb in.$^{-2}$ can be expected in the near future. A technology roadmap predicting a future storage density as high as 1 Pb in.$^{-2}$ by the year 2025 has also been published [28]. To achieve such quantitative innovations in storage density, this roadmap predicts that conventional memory systems using moving devices (such as flying heads and rotating disks) will be completely replaced by novel solid-state elements using various kinds of nanophotonic devices and their associated integrated circuits. These will be reviewed in the next section.

1.4 Nanophotonic Devices

The size and energy consumption of electronic and optical devices must be reduced to improve the performance of information processing systems and energy conversion systems. It should be noted that conventional electronic devices can hardly meet these requirements because they need electrical wires for connection with external devices to fix the direction of the energy flow and the transmitted signal intensity. This means that they dissipate a large amount of energy in the external macroscopic wires. Furthermore, these electronic wires are susceptible to non-invasive attacks [29]. Conventional optical devices also need connecting lines, such as optical fibers and dielectric optical waveguides, as long as propagating light is used as a signal carrier. Even macroscopic free space in vacuum may play the role of the connecting line here.

Nanophotonics is a promising candidate for meeting the above requirements for two reasons: (1) a signal can be transferred by the dressed photon exchange between nanometric particles without using any wires and (2) a non-invasive attack is impossible because the signal intensity is fixed by the energy dissipation inside the nanometric particles [30]. This section reviews the principles, operations, and applications of these nanophotonic devices.

1.4.1 Basic Devices

Because the long-wavelength approximation is not valid due to the localized nature of the dressed photon (refer to Sect. 1.2), an electron in the nanometric particle can be excited even to an electric dipole-forbidden energy level as a result of the dressed photon exchange between closely spaced nanometric particles, which enables novel nanometer-scale wireless optical devices with dimensions beyond the diffraction-limit, low energy consumption, and resistance to non-invasive attacks.

Figure 1.5 explains the principle of operation. Two semiconductor cubic quantum dots (QD) of different sizes are placed in close proximity to each other. The

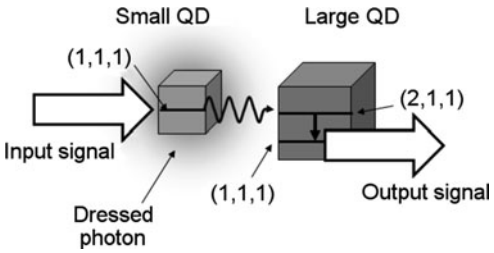

Fig. 1.5 Operating principle of nanophotonic device

small and large QDs are used as input and output ports of the device, respectively. Quantized energy levels of excitons that are relevant to the device operation are also illustrated in this figure. The (1,1,1) exciton energy level in the small QD and the (2,1,1) energy level in the large QD are resonant with each other when the ratio of their sizes is $1 : \sqrt{2}$. However, it should be noted that these levels are electric dipole-allowed and -forbidden, respectively. If the input optical signal is applied to the small QD, an exciton can be excited to the (1,1,1) energy level resulting in the generation of a dressed photon. Then, this dressed photon can excite the exciton to the electric dipole-forbidden (2,1,1) energy level in the large QD because the long-wavelength approximation is not valid. After this excitation, the subsequent fast relaxation from the (2,1,1) to the (1,1,1) energy level in the large QD can block energy back-transfer to the small QD, guaranteeing unidirectional signal transfer from the input to the output port. It should be noted that such energy transfer to the electric dipole-forbidden level has never been realized in conventional optical devices, and thus, Fig. 1.5 represents a qualitative innovation in device operation.

Based on this operating principle, novel nanophotonic devices and their associated integrated circuits have been proposed (Fig. 1.6) [31]. They are connected with conventional macroscopic fiber transmission lines. The integrated circuit includes light emitting devices, functional devices such as optical switches (AND gates), and photodetectors, which are all composed of nanometric particles. By applying the input optical signal through the input terminal, a dressed photon is generated on one particle and is transferred to the adjacent one, and finally, the output signal exits through the output terminal.

An optical switch (an AND gate) (Fig. 1.7) is the first example of the basic devices to be reviewed in this section [32]. Three different-sized QDs are used as input, output, and control ports. By fixing their size ratio to $1 : \sqrt{2} : 2$, they satisfy the resonant condition of Fig. 1.5. When the input signal is applied to the input QD to excite the exciton to the (1,1,1) energy level, the dressed photon exchange allows resonant energy transfer to the electric dipole-forbidden (2,1,1) energy level of the output QD. After subsequent relaxation from the (2,1,1) to (1,1,1) energy level in the output QD, the energy is then resonantly transferred to the (2,1,1) energy level of the control QD. Similar transfer is possible also from the (1,1,1) energy level of the input QD to the (2,2,2) energy level of the control QD. Finally, all the energies are transferred to the control QD, and the exciton relaxes to the (1,1,1) energy level to be dissipated to the external heat bath. This means that the output QD does

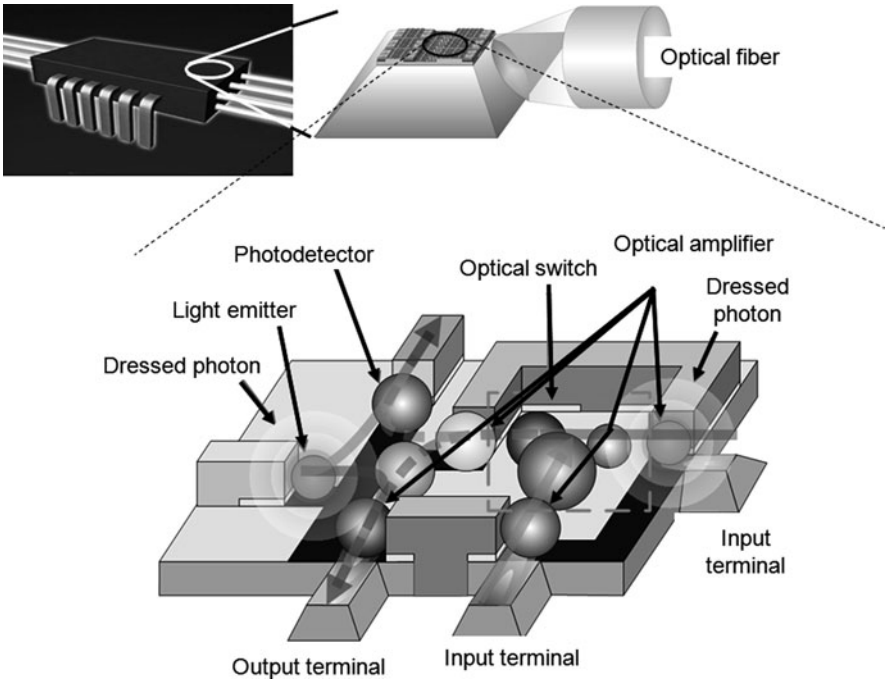

Fig. 1.6 Integrated circuit of nanophotonic devices

not generate any output signals, which corresponds to the off-state of the switch (Fig. 1.7a). To turn the switch on, the control signal is applied to the control QD to excite an exciton to its (1,1,1) energy level (Fig. 1.7b). This excitation prohibits any energy transfers from the other QDs to the control QD due to the shifts of the energy levels of the control QD originating from the many-body effect of the exciton. As a result, an output signal is generated from the (1,1,1) energy level of the output QD.

A switching operation has been experimentally confirmed by using cubic CuCl QDs with sizes 4, 6, and 8 nm separated from each other by 3 nm. They were grown in a self-assembled manner in an NaCl crystal. Figure 1.8 shows the experimental result obtained at a temperature of 5 K. By applying the control signal pulse, the input signal was transferred to the output QD to generate the output signal, which was detected by a near-field spectrometer (Fig. 1.8a). The magnified output pulse shape in Fig. 1.8b represents a 25 ps rise time, determined by the time constant T of the dressed photon exchange, which is inversely proportional to the optical near-field interaction energy represented by the Yukawa function. The fall time is 4 ns, which is determined by the carrier lifetime τ_c, i.e., the time constant of the energy dissipation from the (1,1,1) energy level of the control QD to the heat bath. The fall time can be decreased by extracting the energy of the (1,1,1) energy level of the control QD into the other energy levels in additional QDs to be placed adjacent to it. The solid curve of the magnified output pulse profile in Fig. 1.8b represents the

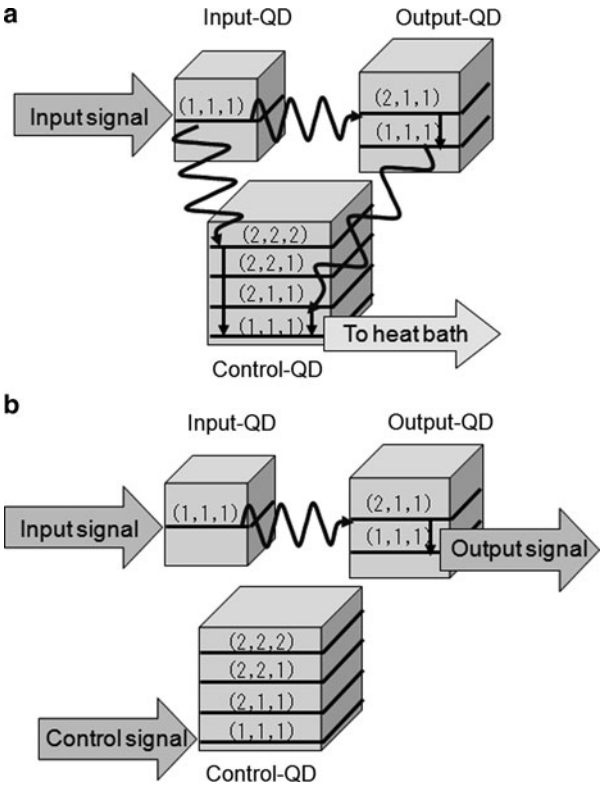

Fig. 1.7 An optical switch. (**a**) Off state. (**b**) On state

value calculated by the dressed photon theory, which agrees well with the experimental values. The oscillatory behavior in the solid curve is due to the residual bi-directional energy transfer by the dressed photon exchange between the input and output QDs.

To demonstrate room-temperature operation necessary for practical industrial applications, three layers of InAs QDs were grown in a size- and position-controlled manner by a molecular beam epitaxy method. After the growth, the sides of the layered structure were removed by phonon-assisted photolithography to form a switching device module (Fig. 1.9a-refer to Sect. 1.5.2 and also to Fig. 1.11a). Device operation at a wavelength of 880 nm has been confirmed at a temperature as high as 210 K (Fig. 1.9b). Recently fabricated InAs QDs exhibit a very strong photoluminescence signal at 273 K, showing the potential for room-temperature operation for practical switching devices. By slight modification of the device structure, switching operation was confirmed also by using two closely spaced ZnO quantum wells in a ZnO nanorod [33].

The second example is a NOT gate, illustrated in Fig. 1.10 [34]. Small and large QDs are used as output and input ports, respectively. Since their size ratio slightly

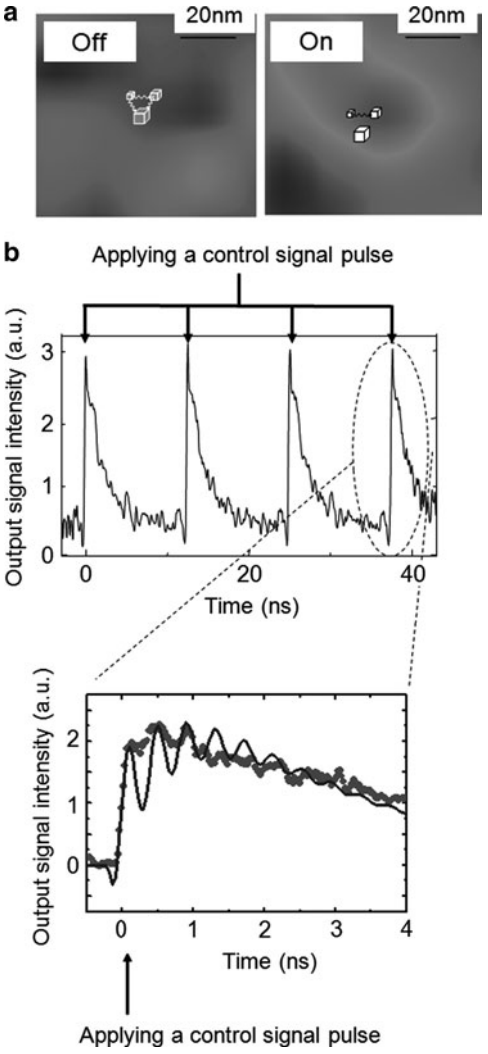

Fig. 1.8 Experimental results of switching operation using cubic CuCl QDs at a temperature of 5 K. (**a**) Near-field optical images of the output signal intensity. (**b**) Temporal behavior of the output signal intensity and its magnified profile. The *solid curve* and *closed circles* represent theoretical and experimental values, respectively

deviates from $1 : \sqrt{2}$, the energy levels of the two QDs are off-resonant. CW optical energy, serving as a power supply for the device, is applied to the (1,1,1) energy level of the output QD to generate the dressed photon. However, due to the off-resonant condition, the generated dressed photon is not transferred to the (2,1,1) energy level of the input QD. As a result, the dressed photon is directly extracted as an output signal from the output QD (Fig. 1.10a). This represents output signal generation in the absence of the input signal.

By applying an input signal to excite an exciton to the (1,1,1) energy level of the input-QD, the linewidth of the (2,1,1) energy level of the input QD is broadened due to the decrease in the phase-relaxation time of the exciton induced by carrier–carrier

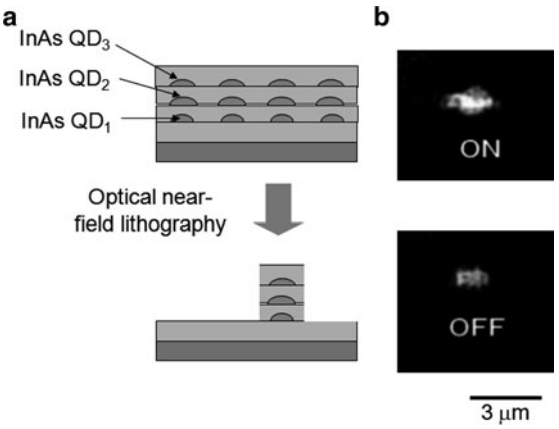

Fig. 1.9 An optical switch using InAs QDs for room-temperature operation. (**a**) Schematic cross-sectional profile of the three-layered QDs. (**b**) Near-field optical image of the output signal intensities for on and off states

scattering. This broadening allows this energy level to be made resonant with the (1,1,1) energy level of the output QD, by which the dressed photon, generated by the CW light, is transferred from the (1,1,1) energy level of the output QD to the (2,1,1) energy level of the input QD. After this transfer and subsequent relaxation to the (1,1,1) energy level in the input QD, the energy is dissipated to the heat bath, resulting in no dressed photon generation from the output QD. This means that no output signal is extracted even though the input signal is applied to the input QD (Fig. 1.10b). Such mutually anti-correlated relation features between the input and output signals, as shown by Fig. 1.10a, b, represent a NOT gate operation.

The NOT gate operation was experimentally confirmed by using CuCl QDs, as in the case of the nanophotonic switch. Figure 1.10c shows the temporal behavior of the output signal intensity, which decreases when applying the input signal pulse. For room-temperature operation, two layers of InAs QDs were grown in a size- and position-controlled manner, as in the case of the nanophotonic switch. After the growth, the sides of the layers were removed by phonon-assisted photolithography (refer to Sect. 1.5.2) to form a two-dimensional array of NOT gate modules [34]. Figure 1.11a shows an AFM image representing a two-dimensional array of more than 100 NOT gate devices which were fabricated within a substrate area of $5\,\mu m \times 5\,\mu m$. Figure 1.11b shows the temporal behavior of the signal intensity generated at a temperature of 298 K.

By combining AND and NOT gate operations, NOR, OR, and NAND gates can be assembled (Fig. 1.12), allowing a complete set of logic gates to be realized for application to future information processing systems. Fan-out F is an important parameter that represents the ability to series-connect multiple nanophotonic devices. It is given by $F = \tau_c/2T$, where τ_c and T are the carrier lifetime and the time constant of dressed photon exchange, respectively. In the case of the above-mentioned nanophotonic switch and NOT gate composed of CuCl QDs, the value of F is 10 because τ_c and T are 2 ns and 100 ps, respectively. In the case of InAs QDs, it is 5 because τ_c and T are 1 ns and 100 ps, respectively. These values of F are sufficiently large for practical applications.

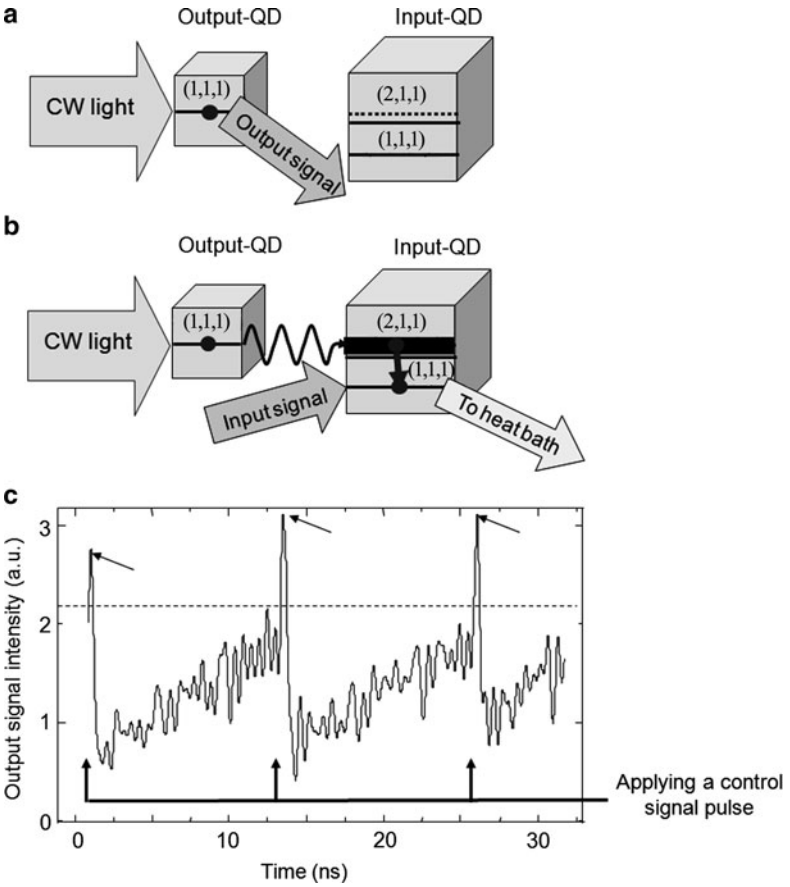

Fig. 1.10 A NOT gate. (**a**), (**b**) Principles of operation. (**c**) Experimental results obtained using cubic CuCl QDs. Three peaks indicated by *arrows* represent artifact signals induced by the pulsed laser used as an input signal source

As was illustrated in Fig. 1.5, the photon energy $h\nu_2$ of the output signal is lower than that of the input signal $h\nu_1$. For up-conversion of the output signal frequency ν_2 to ν_1, the nanophotonic switch of Fig. 1.7 can be used, as illustrated in Fig. 1.13. For designing a frequency up-converter, it should be noted that the size of the QDs can be easily adjusted, so that the output signal frequency is tuned to the input signal frequency ν_1 of the nanophotonic device 1 in this figure. With this adjustment, the output signal of the nanophotonic device 2 is applied to the control QD of the up-converter, whereas a CW optical signal is applied to the input QD. Via the dressed photon exchange between the three QDs in the up-converter and subsequent fast relaxation, it is easy to grasp from Fig. 1.13 that an output signal with frequency ν_1 is generated from the output QD.

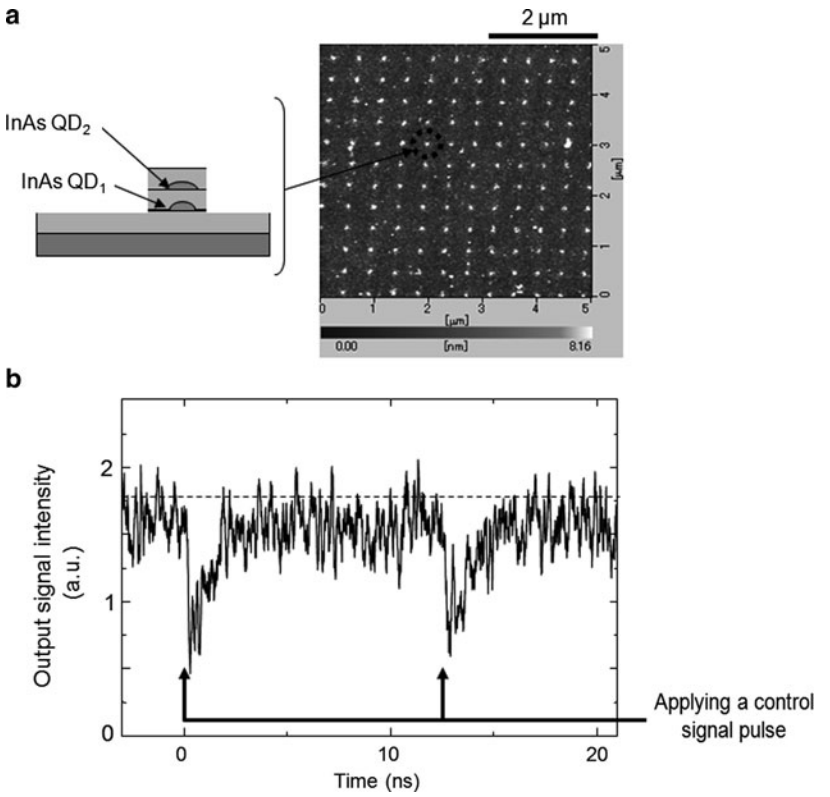

Fig. 1.11 A NOT gate using InAs QDs for room-temperature operation. (**a**) AFM image of a two-dimensional array of the NOT gates. (**b**) Temporal behavior of the output signal intensity

In addition to the basic logic gate devices reviewed above, a variety of novel devices are made possible by nanophotonics. A light emitting device, namely, an optical pulse generator, has been invented by using a chain of closely spaced QDs. Cooperative behavior of the induced electric dipoles in these QDs has been used to realize Dicke's super-radiant photon emission [35]. An optical buffering device has also been invented by utilizing bi-directional energy transfer due to the dressed photon exchange. Its operation has been experimentally confirmed by using a multi-quantum well in the ZnO nanorod [33]. Furthermore, optical buffering operation has also been confirmed by utilizing a time-delayed energy concentration feature of a so-called optical nano-fountain (refer to Fig. 1.15b) [36]. For connecting nanophotonic devices in the integrated circuit of Fig. 1.6, a nano-dot coupler has been invented based on the dressed photon exchange, and its successful operation has been confirmed by using a chain of CdSe QDs [37]. A novel method of fabricating a chain of ZnO QDs has been developed by utilizing DNA as a template [38].

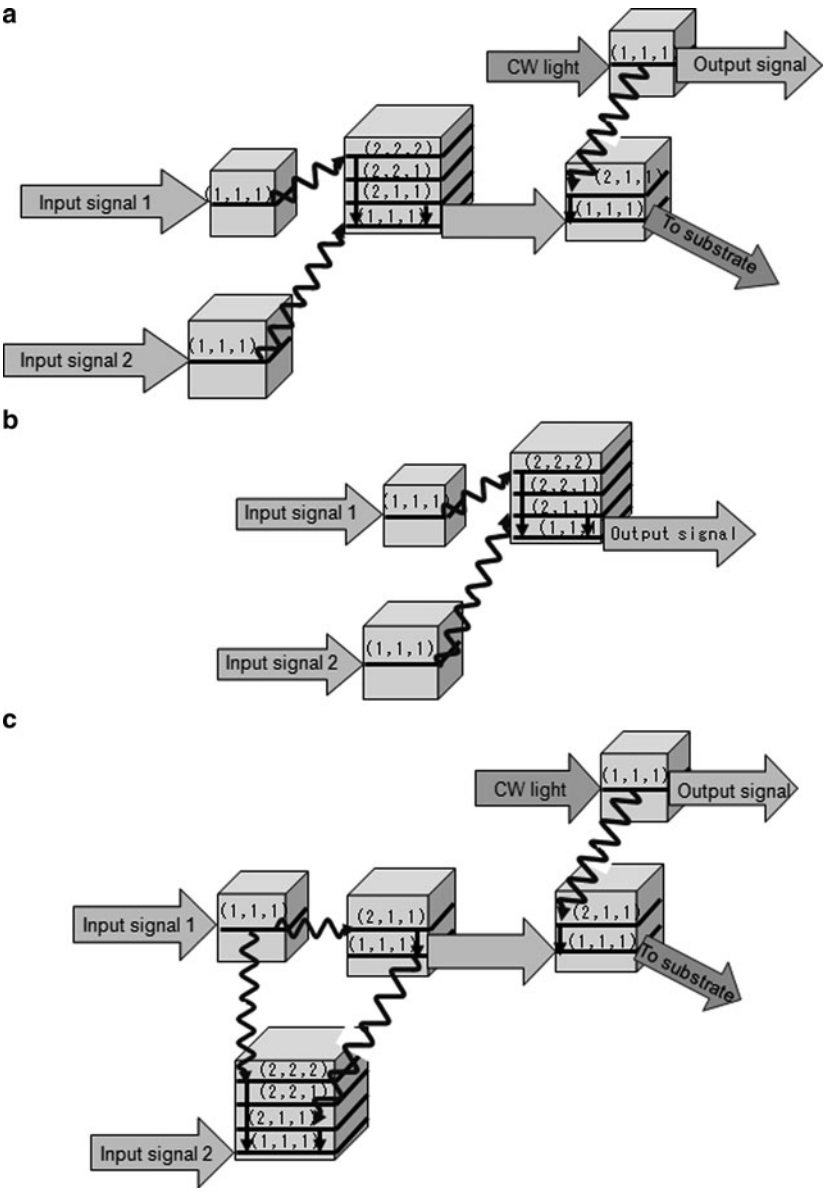

Fig. 1.12 (**a**) NOR, (**b**) OR, and (**c**) NAND gates

1.4.2 Input and Output Terminals

Input and output terminals are used to connect the nanophotonic device in the integrated circuit with external macroscopic photonic devices. The input terminal is used to convert the incident propagating light (free photons) to the optical near-field

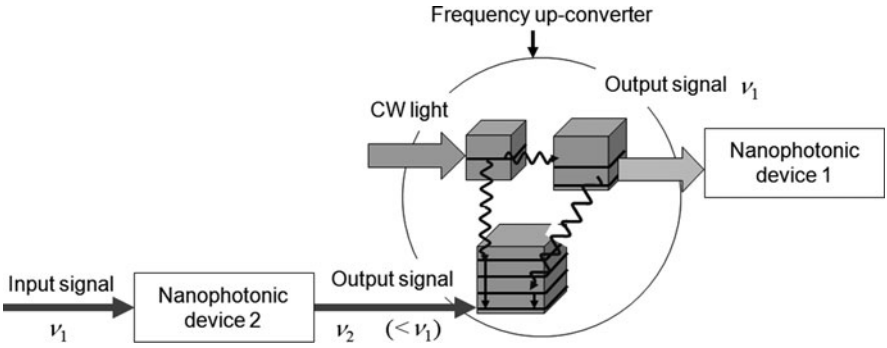

Fig. 1.13 A frequency up-converter

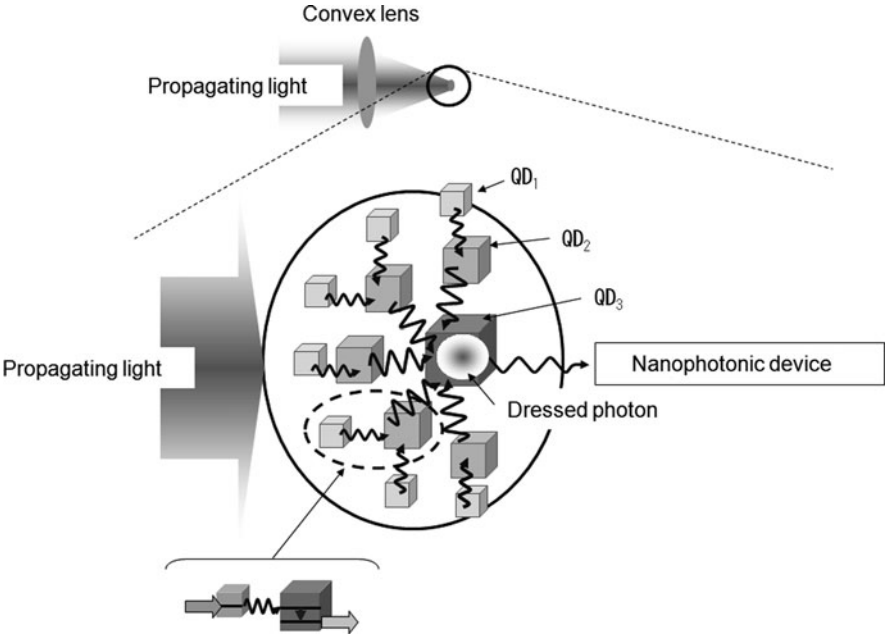

Fig. 1.14 An optical nano-fountain

(dressed photons). A novel device called an *optical nano-fountain* has been invented for such conversion; its operation is similar to that of the light-trapping antennae in light-harvesting bacteria [39]. As illustrated in Fig. 1.14, it utilizes the dressed photon exchange between QDs of different sizes and subsequent fast relaxation. Finally, all of the energy of the incident propagating light is concentrated to the largest QD located at the center, resulting in the generation of dressed photons. The conversion efficiency from the free to the dressed photon energies is high because the energy is dissipated only through relaxation from upper to lower quantized energy levels in each QD.

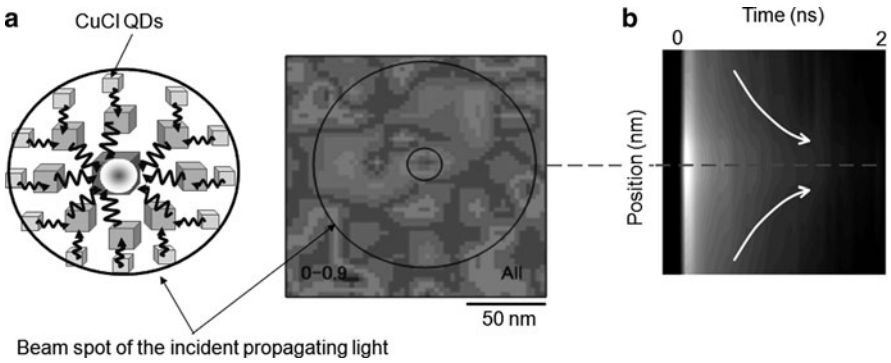

Fig. 1.15 Experimental results of the optical nano-fountain realized using CuCl QDs. (**a**) Near field-optical image of the output optical spot. (**b**) Temporal behavior of the optical energy concentration

Proper device operation has been experimentally confirmed by using CuCl QDs at low temperature, as with the nanophotonic switch and the NOT gate. Figure 1.15a shows an output optical spot with a diameter of less than 10 nm measured by a near-field spectrometer; in contrast, the spot size of the incident light (wavelength: 325 nm) was as large as 150 nm. This means that the equivalent numerical aperture of focusing is much larger than unity. Figure 1.15b shows the temporal behavior of the optical energy transfer to the central largest QD, whose time constant is governed by the time constant T for dressed photon exchange.

For room-temperature operation, multi-layered InAs QDs were grown by molecular beam epitaxy in a size- and position-controlled manner (Fig. 1.16) [40], as with the basic devices reviewed in Sect. 1.4.1. A layer of large QDs was sandwiched by 30 layers of small QDs. The dressed photons generated by applying the input propagating light to the small QDs were transferred to the large QDs. The resultant photoluminescence intensity emitted from the large QDs (wavelength: 1,581 nm) was confirmed to be 40 times larger than that from a solitary layer of large QDs.

An output terminal can be easily realized by fixing a metallic nanometric particle in close proximity to the output QD of a nanophotonic device. The dressed photon is transferred from the output QD to the metallic nanometric particle to generate a scattered free photon, as a result of the large electric dipole and the fast relaxations of phase and energy in the metallic nanometric particle. This device operation was confirmed by fixing a gold nanometric particle on the top of a cap layer of InAs QDs. Figure 1.17 shows the two-dimensional array of scattered light spots originating from the gold particles on the two-dimensionally arrayed InAs QDs. An increase in the photoluminescence intensity from the InAs QDs is due to the gold nanometric particles. This is because the impedance due to the fast relaxations of phase and energy are matched to that of free space, resulting in efficient energy conversion from the dressed photon to the free photon.

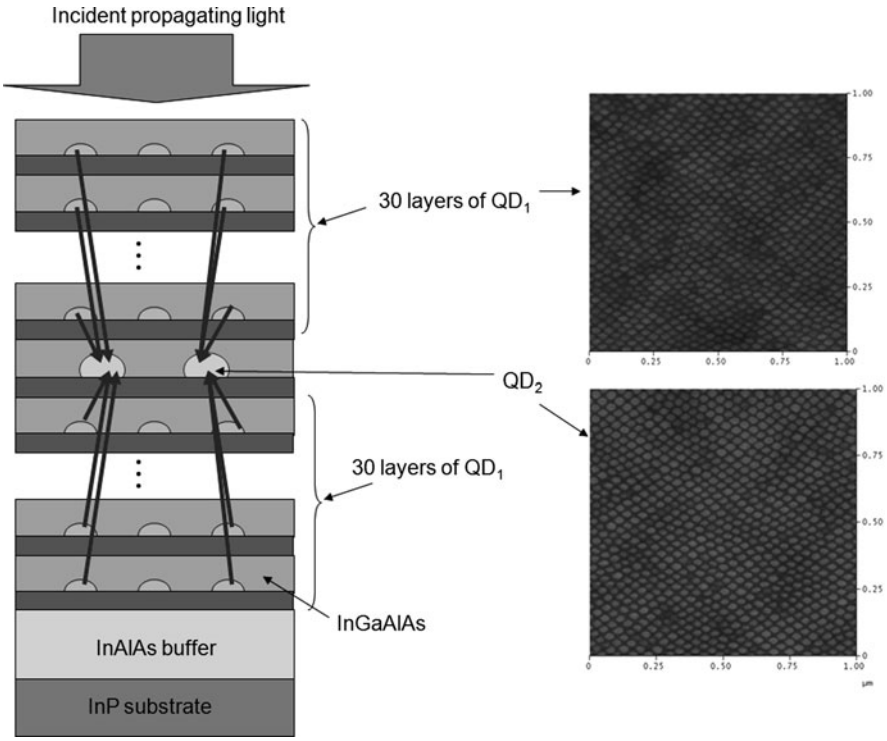

Fig. 1.16 Cross-sectional profile and AFM images of the optical nano-fountain using InAs QDs for room-temperature operation

1.4.3 Unique Features and Application to Information Processing Systems

Nanophotonic devices have several unique features, by which their predominance over conventional photonic devices has been established for application to next-generation information processing systems. One feature is undoubtedly their nanometer-scale dimensions beyond the diffraction limit, which is an example of a quantitative innovation of optical technology. However, it should be noted again that the true nature of nanophotonic devices involves their ability to realize qualitative innovations, originating from their unique features. These features are:

(1) *Low heat generation and low energy dissipation*. A nanophotonic device dissipates energy only through the relaxation from an upper electric dipole-forbidden energy level to a lower electric dipole-allowed energy level. The rate of relaxation is expressed as

$$\Gamma = 2\pi |g(\omega)|^2 D(\omega), \tag{1.5}$$

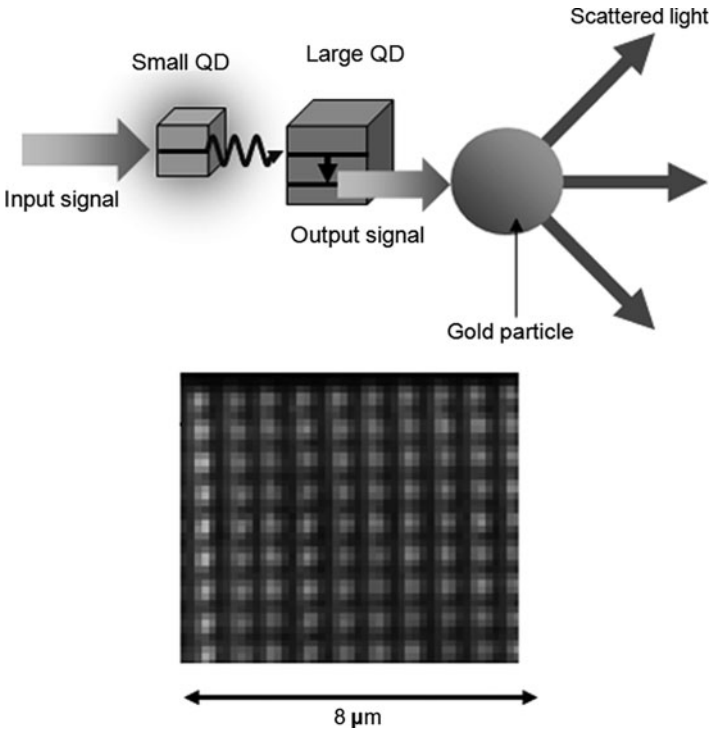

Fig. 1.17 Two-dimensional array of scattered light spots originating from the gold particles on two-dimensionally arranged InAs QDs

where $g(\omega)$ and $D(\omega)$ represent the exciton–phonon coupling energy divided by $\hbar$ and the phonon density of states, respectively. The value of Γ depends on the size and structure of the QD. Typical values are, for example, 10 meV and 50 meV for CuCl and InAs QDs, respectively, from which the magnitude of the heat generated from a nanophotonic switch is estimated to be about 10 pW for an operating frequency of 1 GHz. On the other hand, it is estimated to be as high as 100 nW in the case of a conventional electronic transistor device with an operating frequency of 1 GHz. This comparison shows that the heat generation is only 10^{-5} times that of conventional electronic devices, which is advantageous in building a highly integrated circuit of nanophotonic devices.

For more detailed estimation of the energy dissipation, the relation with the error ratio (the bit error rate) should be discussed. By referring to Fig. 1.5, the output signal is correctly generated only when the input signal is transferred from the (1,1,1) energy level of the small QD to the (2,1,1) energy level of the large QD, with subsequent relaxation to the (1,1,1) energy level of the large QD. An invalid output is generated if the input signal is transferred directly to the (1,1,1) energy level in the large QD without going through the (2,1,1) energy level. The possibility of this direct transfer depends on the value of the relaxation rate Γ. Based

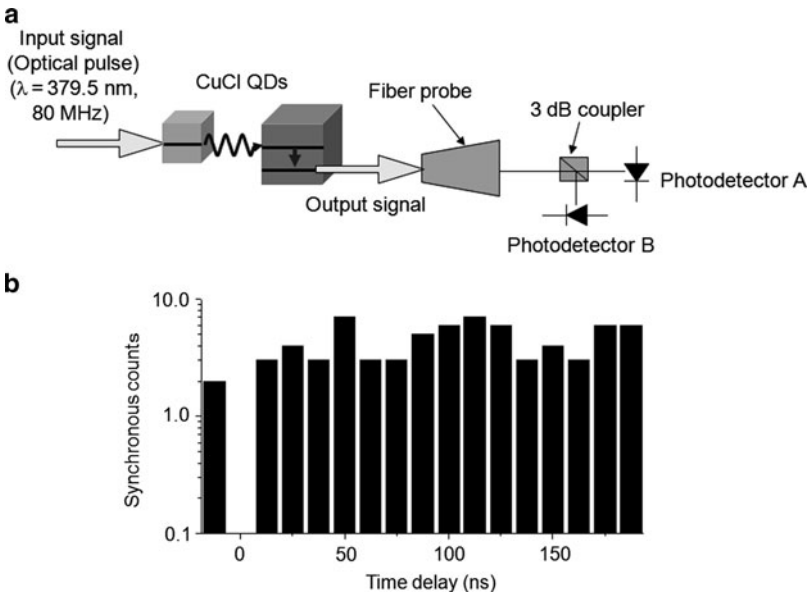

Fig. 1.18 Single-photon operation of a nanophotonic device using CuCl QDs. (**a**) Experimental setup. (**b**) Measured relation between the time delay and the number of synchronous counts

on a master-equation analysis, it was found that the error ratio due to this invalid output remained lower than 10^{-6} if the magnitude of the energy dissipation due to Γ in the large QD was larger than 25 μeV [41]. This small value of energy dissipation suggests that the heat generation of nanophotonic devices could be substantially lower than that of conventional electronic logic devices [42]. In fact, this low energy dissipation could be as low as that of the computational operations in biological systems [43].

(2) *Single photon operation*. The single photon operation capability of nanophotonic devices has been confirmed by the Hanbury Brown and Twiss method (Fig. 1.18a) [44], where two closely spaced CuCl QDs were used at 15 K [45]. The thick black bars in Fig. 1.18b show the measured results of the synchronous counts with different electric time-delays, which were acquired by using two synchronous photodetectors. In this figure, the value of the synchronous count is very small at the time origin ($t = 0$). This clear anti-bunching feature indicates that the two QDs were acting as a single photon emitter. A 99.3% plausibility of single-photon emission was confirmed with 99.98% accuracy. Such clear single-photon operation was attributed to three blockade mechanisms: (1) If one tries to generate two excitons in the small QD, its (1,1,1) energy level is shifted by -30 meV, which corresponds to the binding energy of the exciton molecule. This implies that the energy level becomes detuned from the input signal, and thus, exciton generation is prohibited. (2) Only a single exciton is transferred from the smaller QD to the larger QD by dressed photon exchange because the

(1,1,1) energy level of the small QD becomes off-resonant with respect to the (2,1,1) energy level of the large QD if multiple excitons are generated in the small QD. (3) After the energy transfer, a single exciton can remain stable in the large QD due to the large binding energy of the exciton molecule. Hence, a single photon is emitted from the (1,1,1) energy level of the large QD after fast relaxation from the (2,1,1) energy level.

(3) *Resistance to non-invasive attacks*. As was pointed out at the beginning of this section, conventional electronic and optical devices need electrical or optical wires to dissipate their energies toward the external macroscopic wires to fix the output signal intensity. Since it is straightforward to monitor the signals transmitted through these wires by using conventional electrical or optical sensing probes, non-invasive attacks are possible [29]. In contrast, a nanophotonic device dissipates the energy only through the relaxation from the higher to the lower energy levels in the QD. Because the energy is dissipated by non-radiative relaxation to the crystal lattice vibration (phonon) in the QD (refer to (1.5)) and also because its magnitude is very low, non-invasive attacks are extremely difficult, and thus, the tamper resistance is high [30, 46]. This is advantageous for maintaining security in information processing systems.

In addition to the unique features outlined above, further advantages of nanophotonic devices over conventional optical devices include the possibility of novel logic operations and correlation functions. Additionally, for application to information transmission systems, their operating wavelengths are compatible with WDM systems. Although the operating speed of current WDM systems is about 10 Gbps, higher speeds are expected in the near future by decreasing the fall time (refer to Fig. 1.8b).

Based on these advantages, nanophotonic devices have already been employed for demonstrating prototype novel information processing systems. An example is a highly integrated content addressable memory (CAM) of an optical router system, whose main component is a routing table [47]. The global sum system (the input port of the routing table) was assembled by using an optical nano-fountain (refer to Sect. 1.4.2). As shown in Fig. 1.19a, three small CuCl QDs of different sizes were used as input ports, and a large QD was used as an output port. This figure shows the photoluminescence spectral profiles of the three inputs and the output signals, showing that the output spectral intensity is proportional to the number of bits of the input signals. It demonstrates that this device worked as a three-bit digital-to-analog converter, and thus, the global sum operation was confirmed. For the broadcast system (the output port of the routing table), three nanophotonic switches were used, as shown in Fig. 1.19b. The input signals applied to the input ports of three switches were transferred to their output ports at the moment the control signal pulse was applied. This represents the operation of a three-channel broadcast system. These experimental results demonstrated successful operation of a highly integrated CAM that is much more effective than the huge, high-power-consumption conventional optical router systems.

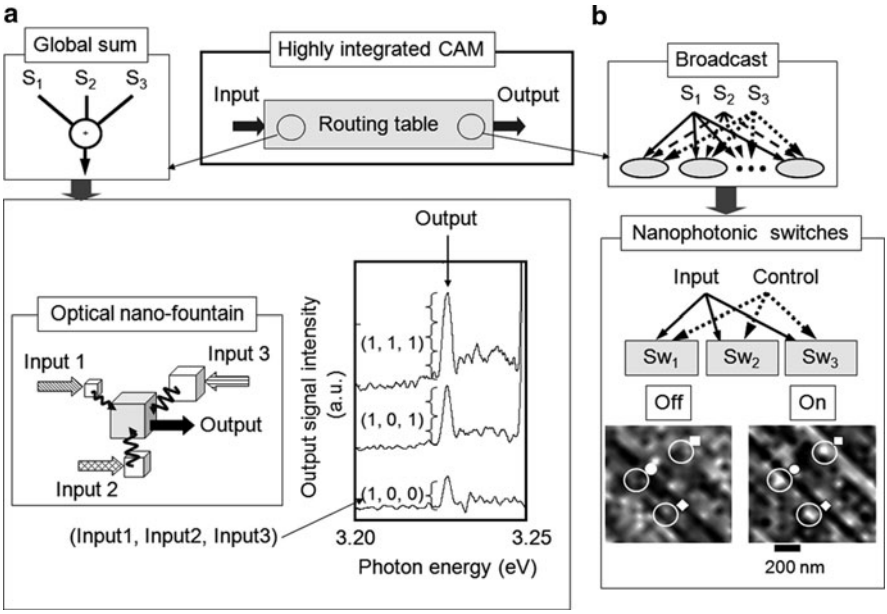

Fig. 1.19 Demonstration of content addressable memory (CAM). (**a**) Global sum system realized by using an optical nano-fountain with three input-ports. (**b**) Broadcast system realized by using three nanophotonic switches

1.5 Nanophotonic Fabrication

The unique phenomena originating from dressed photon exchange have been applied also to the development of novel high-resolution fabrication techniques. As has been described in Sect. 1.2 (refer to (1.3) and (1.4) and Fig. 1.3), the principle of fabrication utilizes the dressed photon, which carries the coherent phonon energy (DP–CP). Several examples are reviewed in this section.

1.5.1 Photochemical Vapor Deposition

Photochemical vapor deposition (PCVD) involves depositing particles or films on a substrate by photo-dissociating organic molecules. Before reviewing a novel PCVD method using the DP–CP, the principle of conventional PCVD is described first, taking metallic Zn deposition as an example. For this deposition, a popularly employed metal-organic molecule is gaseous diethylzinc (DEZ), whose photo-absorption energy E_{abs} and dissociation energy E_{dis} are 4.59 eV and 2.26 eV, respectively. The molecule stably remains in the lowest energy state $\left|E_g; el\right\rangle \otimes |E_l; vib\rangle$, where $\left|E_g; el\right\rangle$ and $|E_l; vib\rangle$ represent the ground electronic state and the lowest

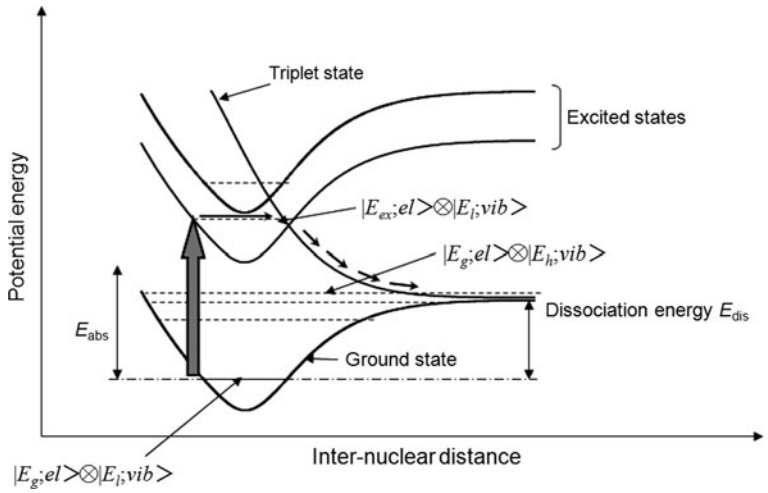

Fig. 1.20 Energy levels of electrons and molecular vibrations

molecular vibrational energy state, respectively (Fig. 1.20). To dissociate the molecule, the simplest way is to excite it to the state $|E_g;el\rangle \otimes |E_h;vib\rangle$ (where $|E_h;vib\rangle$ is a higher molecular vibrational energy state), whose energy is higher than E_{dis}. However, optical excitation is not possible because the transition from $|E_g;el\rangle \otimes |E_l;vib\rangle$ to $|E_g;el\rangle \otimes |E_h;vib\rangle$ is electric dipole-forbidden. Thermal excitation is also very difficult because the molecule must be heated up to an extremely high temperature. To make the dissociation possible, the conventional method is to optically excite the molecule to the excited electronic state $|E_{\text{ex}};el\rangle \otimes |E_l;vib\rangle$, whose energy is much higher than E_{dis}. This is possible because the transition from $|E_g;el\rangle \otimes |E_l;vib\rangle$ to $|E_{\text{ex}};el\rangle \otimes |E_l;vib\rangle$ is electric dipole-allowed. This excitation process is called *adiabatic* because vibrational motions of heavy nuclei are not excited, and these nuclei stay in the lowest vibrational state. Because of this, the Born–Oppenheimer approximation is effective.

This adiabatic PCVD requires short-wavelength light with a photon energy higher than E_{abs} (270 nm wavelength in the case of DEZ), which corresponds to the energy difference between the $|E_{\text{ex}};el\rangle \otimes |E_l;vib\rangle$ and $|E_g;el\rangle \otimes |E_l;vib\rangle$ states. After the molecule is excited to the $|E_{\text{ex}};el\rangle \otimes |E_l;vib\rangle$ state by absorbing this photon, it transits to the triplet state. By this transition, the inter-nuclear distance increases to infinity, resulting in dissociation of the molecule and deposition of dissociated Zn atoms on the substrate.

Instead of the conventional adiabatic PCVD described above, the DP–CP generated at a fiber probe tip enables a novel PCVD because the molecule can transit from $|E_g;el\rangle \otimes |E_l;vib\rangle$ to $|E_g;el\rangle \otimes |E_h;vib\rangle$ by absorbing the DP–CP energy even though the transition is electric dipole-forbidden. If the DP–CP energy $h\nu_{\text{DP–CP}}$ is higher than E_{dis}, transfer of a single DP–CP from the fiber probe tip to the molecule

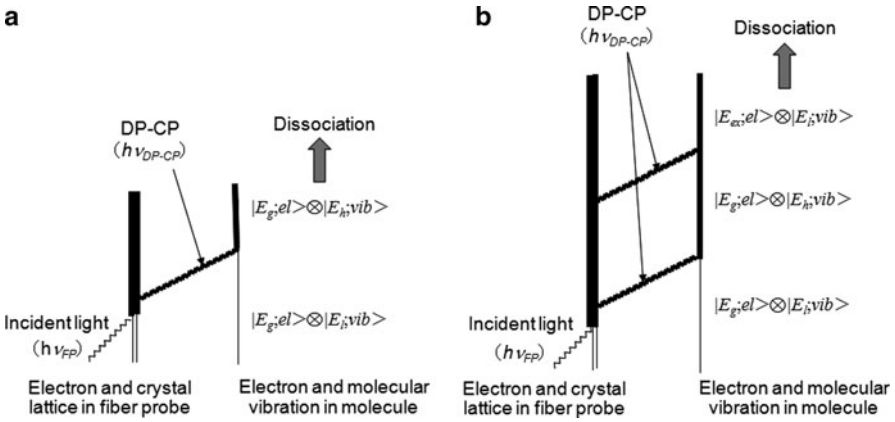

Fig. 1.21 Feynman diagram of DP–CP energy transfer from a fiber probe tip to a molecule. (**a**) and (**b**) show single-step and two-step dissociations, respectively

is sufficient for dissociation, as is schematically explained by the Feynman diagram of Fig. 1.21a. When, $h\nu_{\mathrm{DP-CP}} < E_{\mathrm{dis}}$ multiple DP–CP transfer is required for dissociation, by which the molecule can be excited to the excited electronic state $|E_{\mathrm{ex}}, el\rangle \otimes |E_l, vib\rangle$. Figure 1.21b shows the case where two DP–CPs are transferred, i.e., two-step excitation of the molecule for dissociation. These excitation processes are not adiabatic because vibration modes of the nuclei are excited by the coherent phonon which couples with the dressed photon. Thus, these processes are named *nonadiabatic* or *phonon-assisted*. For these processes, an explanation based on Fig. 1.20 is not valid because the inter-nuclear distance is no longer an independent variable. One technical advantage of these processes is that a high-power-consumption short-wavelength light source is not required. In principle, one can use a longer-wavelength light source even if its photon energy is lower than E_{dis}, which represents a qualitative innovation of this novel PCVD.

Figure 1.22a–c show AFM images of the nanometric Zn particles deposited on a sapphire substrate as a result of dissociating DEZ molecules by the phonon-assisted PCVD using ultraviolet ($h\nu_{\mathrm{FP}} = 3.81\,\mathrm{eV}$; wavelength = 325 nm), blue ($h\nu_{\mathrm{FP}} = 2.54\,\mathrm{eV}$; wavelength = 488 nm), and red ($h\nu_{\mathrm{FP}} = 1.81\,\mathrm{eV}$; wavelength = 684 nm) light sources, respectively, for generating the DP–CP at the fiber probe tip [48]. On the other hand, Fig. 1.22d is an image of a nanometric Zn particle deposited by dissociating Zn(acac)2 molecules [49]. It should be noted that this molecule is optically inactive, i.e., adiabatic dissociation is not possible; however, it was successfully dissociated by the phonon-assisted process.

Figure 1.23 shows the relation between the photon flux I of the light incident on the fiber probe tip for generating the DP–CP and the deposition rate R of the Zn nanometric particles on the substrate. It can be expressed as

$$R = aI + bI^2 + cI^3 + \cdots, \tag{1.6}$$

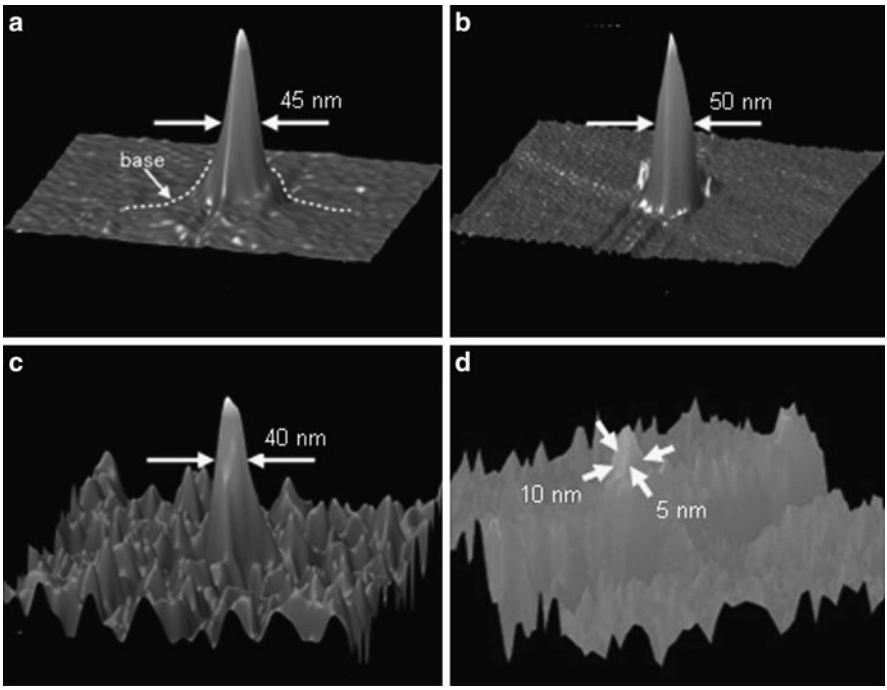

Fig. 1.22 AFM images of nanometric Zn particles deposited on a sapphire substrate by phonon-assisted PCVD using (**a**) ultraviolet, (**b**) blue, and (**c**) red light sources. (**d**) is an image of a nanometric Zn particle deposited by dissociating optically inactive Zn(acac)2 molecules

where the first, second, and third terms represent single-, two-, and three-step excitation by the DP–CP, respectively. Closed triangles in this figure represent the experimental results obtained by using the ultraviolet light source of Fig. 1.22a. Since its photon energy $h\nu_{\mathrm{FP}}$ is higher than E_{dis}, single-step excitation is sufficient to dissociate the DEZ molecules. The experimental results are fitted by the solid line $R = aI$. Since the photon energy $h\nu_{\mathrm{FP}}$ of the blue light (Fig. 1.22b) is still higher than E_{dis}, single-step excitation is sufficient here, too. However, by increasing the incident light intensity I, two-step excitation becomes possible. The experimental results (closed squares) are fitted by the solid curve $R = aI + bI^2$. In the case of the red light (Fig. 1.22c), the photon energy $h\nu_{\mathrm{FP}}$ is lower than E_{dis}; thus, two-step excitation is essential for dissociation. By increasing I, even three-step excitation becomes possible. The experimental results (closed circles) are fitted by the solid curve $R = bI^2 + cI^3$. Theoretical studies have proved that the ratios between the coefficients of (1.6) satisfy the relation

$$\frac{b}{a} = \frac{c}{b} = \cdots. \tag{1.7}$$

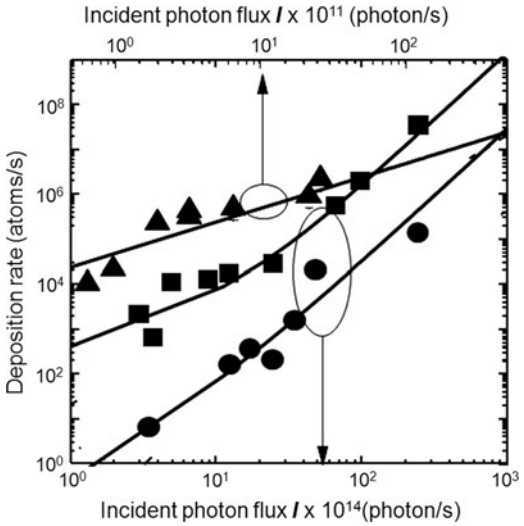

Fig. 1.23 The relation between the photon flux I of the light incident on the fiber probe tip and the deposition rate R of the Zn nanometric particles. *Closed triangles*, *squares*, and *circles* represent the results obtained by using the ultraviolet, blue, and red light sources, as in the cases of Fig. 1.22a, b, and c, respectively

This relation was confirmed experimentally by measuring the values of b/a and c/b, which were found to be on the order of 10^{-15}, thus supporting the validity of the theory based on the DP–CP picture [50].

On the basis of the dressed photon theory and the important role of electric dipole-forbidden molecular vibrational excitations, recent theoretical studies have proposed a simple model to describe atom or atom-cluster desorption due to the dressed photons from a nanometric particle deposited on a substrate [49]. Assuming an anharmonic potential for each atomic binding, an effective atom-nanodot potential was evaluated to determine the desorption energy and the stabilized dot size. The model shows that electric dipole-forbidden molecular vibrational excitations play an important role in the phonon-assisted process, which could potentially lead to a novel fabrication method, in addition to controlling the size and position of nanostructures [51].

1.5.2 Photolithography

The phonon-assisted process can be applied also to photolithography to pattern widely available commercial photoresists by using a visible light source even though such photoresists are sensitive only to UV light. To confirm this patterning ability, a film of commercial photoresist (OFPR) was coated on a substrate, and a photomask having a sub-wavelength sized aperture was mounted on it, as illustrated in Fig. 1.24a. Applying visible light to the photomask, low-intensity propagating light passes through aperture. However, the photoresist was not patterned by this propagating light because it is sensitive only to the UV propagating light. In contrast, a DP–CP is generated at the edge of the photoresist, and its energy is transferred to

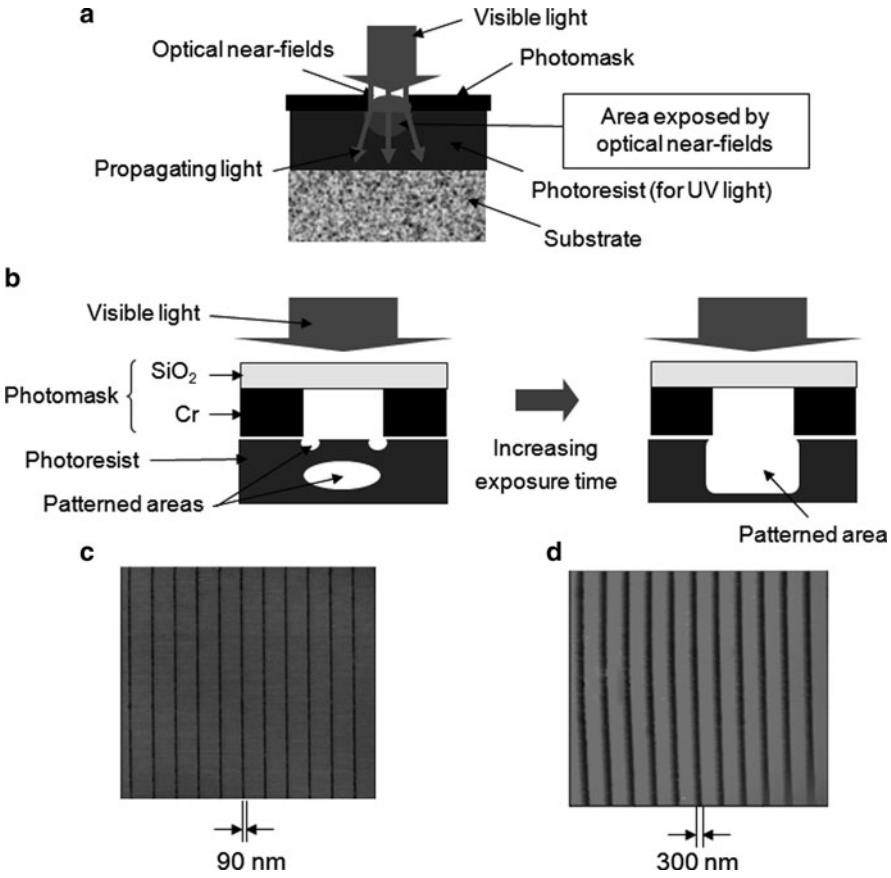

Fig. 1.24 Photolithography by phonon-assisted process. (**a**) Experimental set up. (**b**) Dependence of the cross-sectional profiles of the patterned photoresist areas on the exposure time. (**c**) and (**d**) are AFM images of the OFPR photoresist patterned by visible and UV light, respectively

the photoresist, by which the photoresist is activated and patterned by the phonon-assisted process [52]. From a theoretical analysis, it was found that the DP–CP was transferred not only to the surface of the photoresist but also to its inner part, by which these two parts of the photoresist could be effectively patterned with a short exposure time (Fig. 1.24b). By increasing the exposure time, the volumes of these patterns increased, and finally with an exposure time longer than a threshold value, they were connected with each other to form a pattern with a stable spatial profile that depended on the aperture size in the photomask. Figure 1.24c shows an AFM image of the linear pattern formed on the OFPR photoresist with an exposure time longer than the threshold. The linewidth of the fabricated pattern was as narrow as 90 nm, which is equivalent to the width of the aperture and is much narrower than the wavelength (550 nm) of the incident visible light. For comparison with the conventional photolithography based on the adiabatic process, the same OFPR

photoresist and the same photomask were used. However, they were illuminated by UV light to which the OFPR photoresist was sensitive. As shown in Fig. 1.24d, the resultant linewidth of the pattern was as wide as 300 nm, which is much broader than that of Fig. 1.24c. Such a broader linewidth was due to the diffraction of the propagating UV light passing through the aperture, to which the photoresist is sensitive. By comparing Fig. 1.24c, d, it is concluded that higher resolution was obtained by using a longer-wavelength light source, which is longer than the absorption band edge wavelength of the photoresist. This means that large, expensive, high-power-consumption, short-wavelength X-ray, EUV, and UV light sources are not required for phonon-assisted photolithography.

In addition to the high resolution obtained with a visible light source, this method based on the phonon-assisted process has several advantages, including:

(1) *Multiple exposure*. Figure 1.25a illustrates a UV-sensitive photoresist coated on a transparent substrate. A photomask was mounted on the photoresist, and visible light was applied from the back surface of the transparent substrate. After the visible light passed through the transparent substrate, it reached the surface of the photomask, resulting in generation of a DP–CP without activating the photoresist. The photomask was then patterned by this DP–CP due to the phonon-assisted process. An AFM image of the fabricated linear pattern is shown in Fig. 1.25b. Next, the photomask was mounted again on the same photoresist after rotating the direction of its linear axis by 90° (Fig. 1.25c). By applying the visible light again to generate the DP–CP on the photomask, the photoresist was patterned by the DP–CP without suffering any effects from the propagating visible light. The result is shown Fig. 1.25d, which shows a two-dimensional lattice structure formed by double-exposure through the linear-patterned photomask. By repeating these exposures, more complicated patterns can be realized. It should be pointed out that the contrast of this pattern (Fig. 1.25e) remained high even after multiple exposures because the photoresist was insensitive to the incident visible light.

(2) *Patterning of optically inactive films* [52]. As in the case of dissociating optically inactive $Zn(acac)_2$ molecules by the phonon-assisted PCVD (Fig. 1.22d), this method can pattern even optically inactive films. To confirm this, ZEP-520A, which has been popularly used as a resist film for electron beam (EB) lithography, was used as a test material. The surface of the film was spatially homogeneous and, thus, advantageous for realizing high resolution in EB lithography. However, it was optically inactive. For patterning by the present method, a ZEP-520A film was coated on a substrate, and a photomask was mounted on the film and illuminated by visible light (wavelength: 355 nm). The result is shown in Fig. 1.26, which shows that the pattern of the two-dimensional array of disks was transferred to the surface of the ZEP-520A film. This result confirms that the phonon-assisted lithography can pattern even an optically inactive film.

Based on the results outlined above, a prototype machine for producing commercial products has been constructed in collaboration with industry [53]. As shown in Fig. 1.27, it occupies an area as small as 1 m^2. It uses a conventional Xe lamp

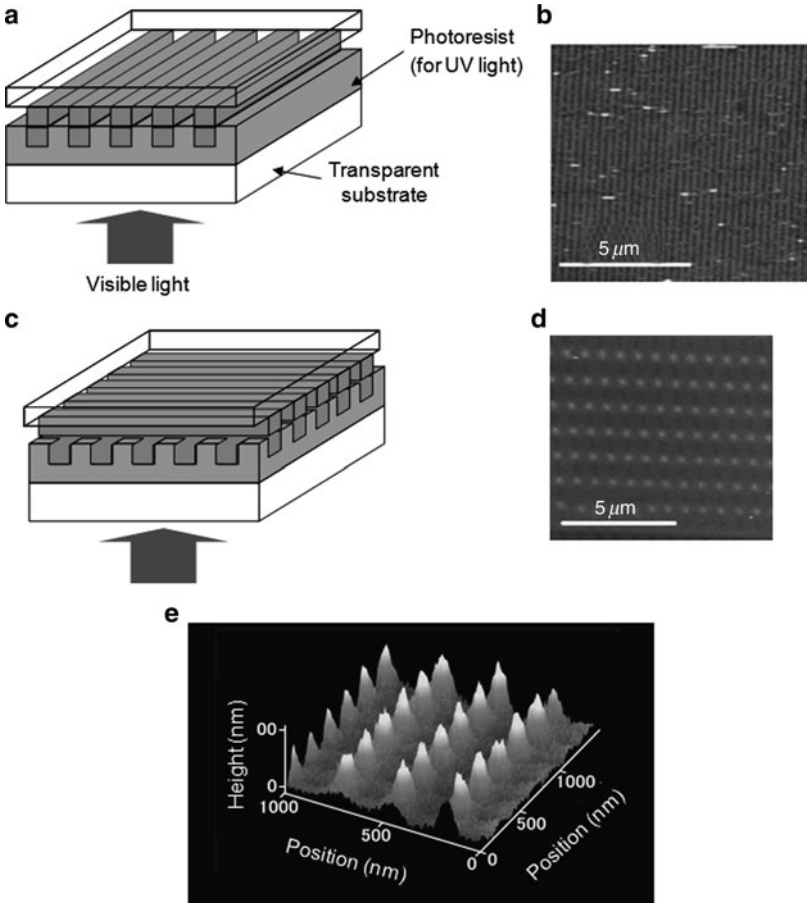

Fig. 1.25 Illustration of multiple exposure. (**a**) and (**b**) are the first-step exposure and AFM image of the patterned photoresist, respectively. (**c**), (**d**), and (**e**) are the second-step exposure, AFM images of the patterned photoresist, and a bird's eye view of (**d**), respectively

as a light source and is operated by computer-controlled robotics. A resolution of 20–50 nm is guaranteed for a substrate area of 50 mm × 60 mm. A wider patterned area is expected by employing a mechanical stepper system. A two-layer resist film is employed to fabricate a high-aspect-ratio pattern, a lubricant is coated to remove the photomask from the photoresist without damaging the photomask surface, and a novel photoresist material is composed to realize a sufficiently homogeneous film for high resolution. Although photomasks have been fabricated by electron beam lithography in the early stage of the present study, it has become possible to fabricate them by phonon-assisted photolithography.

It should be pointed out that a metallic photomask may sacrifice the resolution due to diffraction of the plasmonic wave. To solve this problem, the plasmonic wave

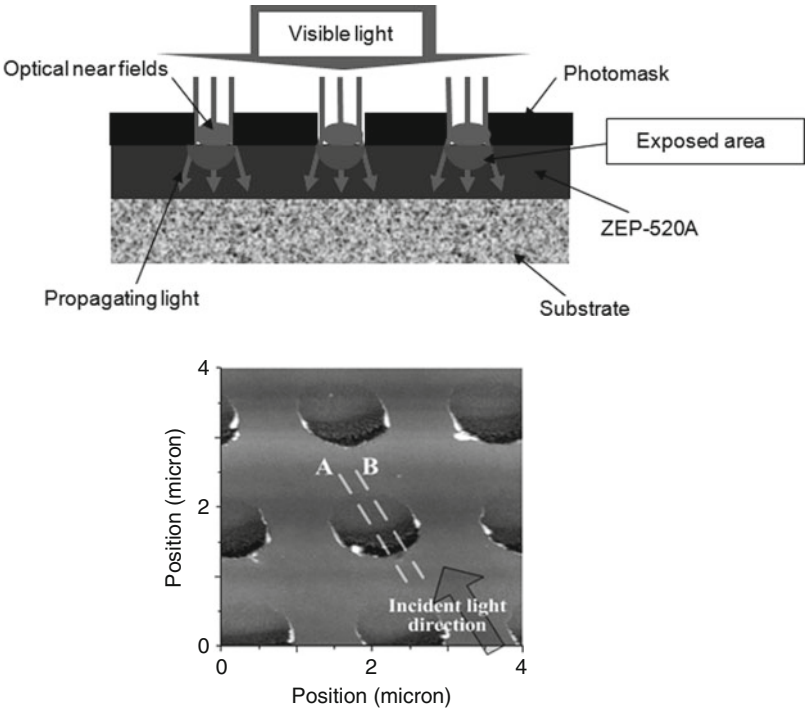

Fig. 1.26 Image of a two-dimensional array of disks patterned on an optically inactive ZP-520A film

on the photomask surface must be suppressed, for which it is advantageous to use Si as a photomask material.

Examples of the patterns fabricated by this machine are: a 40 nm-linewidth linear pattern (Fig. 1.28a), a high-aspect-ratio pattern (Fig. 1.28b), a pattern with a minimum linewidth of 22 nm realized by making high-resolution photoresist (Fig. 1.28c), two-dimensional arrays of rings and disks (Fig. 1.28d, e), and so on [53]. This machine has been made available for public use since April 2006. Examples of its use include the fabrication of a two-dimensional array of room-temperature operated nanophotonic NOT gates composed of InAs QDs (refer to Fig. 1.11), linear and curved Si optical waveguides, and so on.

Other examples of fabricated structures include diffraction gratings and Fresnel zone plates for soft X-rays with a wavelength of 0.5–1.0 nm. It should be pointed out that these devices were fabricated by using green light, whose wavelength is more than 500 times longer than that of soft X-rays. For the diffraction gratings, corrugations of 7,600 lines/mm were patterned on an Si substrate, as shown in Fig. 1.29a, which were coated with Mo/SiO_2 multilayer films. Figure 1.29b shows the evaluated diffraction efficiency, which is as high as 3% in the wavelength range of 0.5–1.0 nm. This is higher than that of a commercially available diffraction grating using the crystal lattice of KAP[54]. This high efficiency confirms the high resolution and

Fig. 1.27 Photograph of a prototype machine for a commercial product

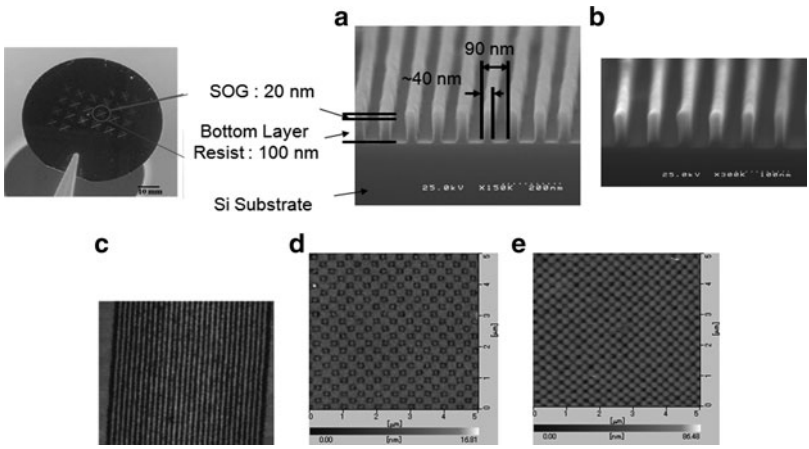

Fig. 1.28 Examples of patterns fabricated by the machine in Fig. 1.28. (**a**) A linear pattern of 40-nm width lines at 90-nm intervals. (**b**) High-aspect-ratio patterns with a half pitch of 32 nm. (**c**) The minimum linewidth (22 nm) of the linear patterns. (**d**) Two-dimensional array of 100-nm diameter rings. (**e**) Two-dimensional array of disks with 125-nm pitch

high reproducibility of the prototype lithography machine. For Fresnel zone plates, concentric circular patterns were fabricated on a Ta film [55]. Figure 1.30a shows a high-contrast SEM image of a fabricated Fresnel zone plate. The outer diameter, linewidth on the rim, and number of rings were 400 μm, 420 nm, and 230, respectively. The thickness of the Ta was 65 nm. The contrast of the pattern is plotted as a function of the order of the rings in Fig. 1.30b. This figure shows that the present phonon-assisted photolithography realized higher contrast than the conventional adiabatic photolithography, especially for rings of higher order.

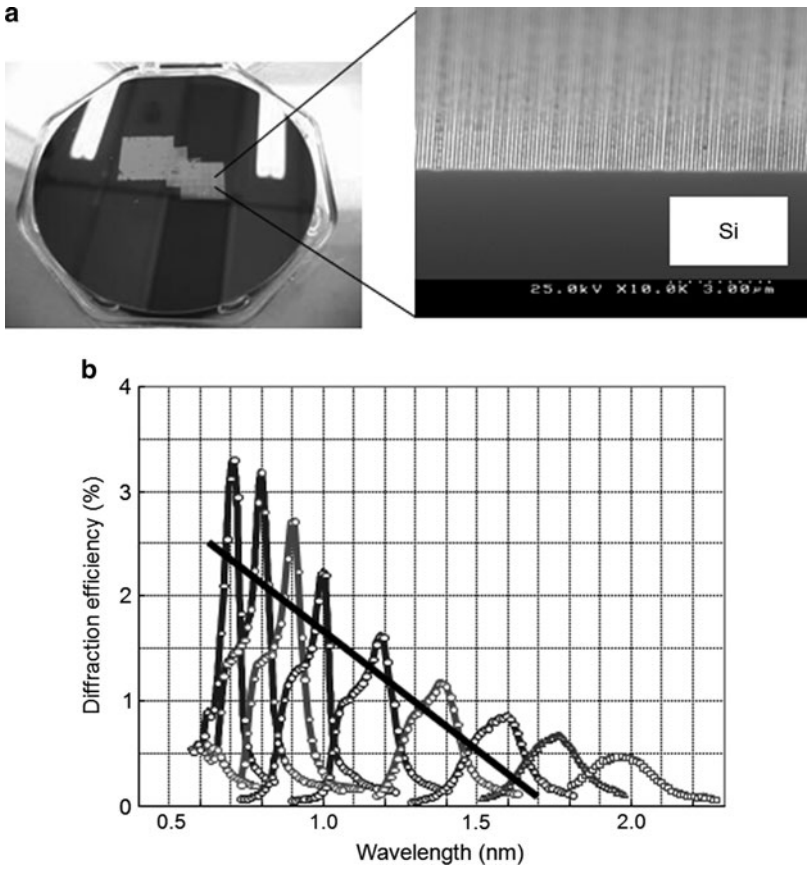

Fig. 1.29 Fabricated diffraction grating for soft X-rays. (**a**) SEM image. (**b**) Diffraction efficiency. The *black line* represents the efficiency of a commercially available one using the crystal lattice of KTP

A notable advantage of this method of fabricating soft X-ray optical devices is its mass-production capability. For example, Figure 1.31 shows a two-dimensional array of Fresnel zone plates prepared on the photomask. With an exposure of several minutes, these patterns were transferred to the photoresist, and thus, 49 Fresnel zone plates were simultaneously fabricated. This process demonstrates that the fabrication throughput is much higher than that of raster-scanned electron beam lithography, which has been conventionally used for fabricating Fresnel zone plates. This demonstrates that the dressed photon technology shows the possibility of mass-producing even devices for soft X-rays, from which novel applications are expected, such as portable soft X-ray fluorescence spectrometers for analyzing items of cultural heritage and security inspection systems.

Although the prototype machine of Fig. 1.27 is fully automatic and can be used to fabricate a variety of devices, a more compact and simple machine is sufficient

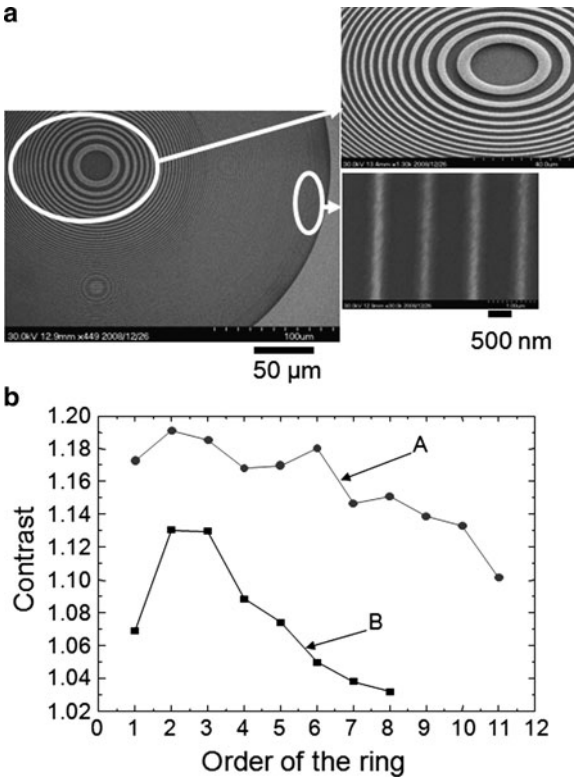

Fig. 1.30 Fabricated Fresnel zone plate. (**a**) SEM image. (**b**) Relation between the order of rings and the contrast. Zigzag lines A and B represent the contrasts of the Fresnel zone plates made by phonon-assisted and conventional adiabatic lithography, respectively

for the purpose of fabricating a limited species of devices. Figure 1.32 shows such a compact, desk-top machine with a footprint of only 0.03 m^2. A single light emitting diode (LED) emitting green light with a power of 30 mW and driven with input electrical power of 4.5 W was used as a light source. Even such a simple machine can fabricate a two-dimensional array of room-temperature operated nanophotonic NOT gates, linear and curved Si optical waveguides, diffraction gratings, and Fresnel zone plates for soft X-rays. Such machines have many benefits compared with conventional photolithography stepper systems, which are large and expensive and have high power consumption because they need short-wavelength light sources.

1.5.3 Self-Organized Smoothing

To demonstrate the phonon-assisted PCVD described in Sect. 1.5.1, a fiber probe was used for generating a DP–CP. Although arbitrary patterns can be drawn by raster-scanning the fiber probe, the throughput of the pattering is limited by its low scanning speed. Replacing the fiber probe with a photomask has drastically increased the throughput of phonon-assisted photolithography, which has enabled

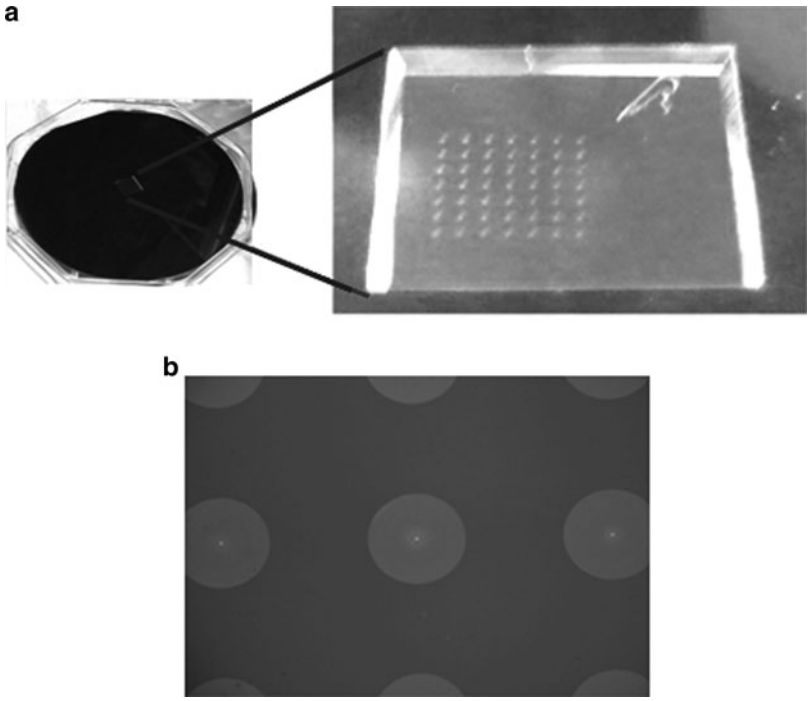

Fig. 1.31 Two-dimensional array of 7 × 7 Fresnel zone plates. (**a**) Patterns on the photomask. (**b**) Patterns transferred to the photoresist

the mass-production of devices for soft X-rays. Further increases in throughput are expected if the photomask can be removed entirely. Such maskless methods are reviewed in this section.

The key to these methods is to exploit the fact that optical near-fields, and thus DP–CPs, can always be generated on a nanometrically rough material surface when it is illuminated with light. Even if the surface is flat, DP-CSs are also generated at the parts at which the structure or component is nanometrically singular. The generated DP–CPs cause smoothing of locally rough parts or make the sizes of individual parts uniform. After they become flat or homogeneous, the smoothing or homogenizing stops automatically because the DP–CPs are no longer generated. Thus, they are called self-organized processes.

It should be noted that the methods reviewed below can be applied not only to a planar substrate but also to convex and concave substrates. They can also be applied to an inner wall surface of a cylinder if it can be illuminated by propagating light. Furthermore, they can be used for a variety of materials, such as glasses, crystals, ceramics, metals, plastics, and so on. Since a high optical power is not required, visible LEDs can be employed as low-power-consumption light sources.

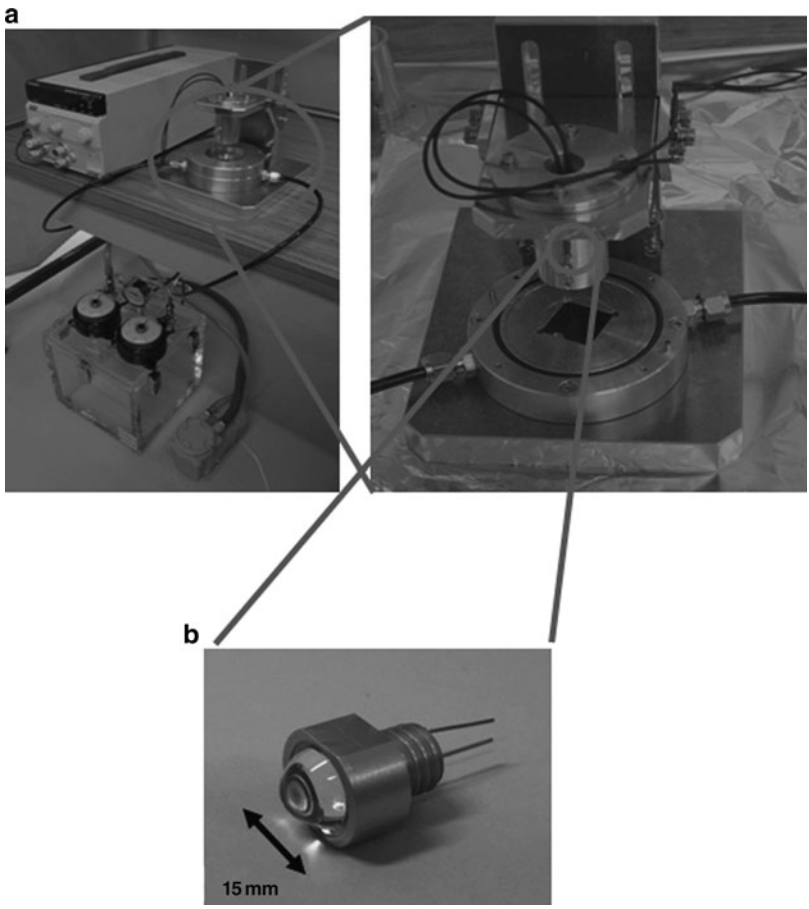

Fig. 1.32 A compact desk-top machine. (**a**) Photograph of the machine. (**b**) LED used as a light source

1.5.3.1 Repairing Surface Roughness

Surface roughness can be repaired by two methods, which are reviewed in this section

1. *Etching* [56]. Phonon-assisted photochemical etching was developed for smoothing the surface of glass, with the goal of fabricating high-quality mirrors for high-power, short-pulse laser systems. The experimental setup is shown in Fig. 1.33. A glass substrate with nanometric surface roughness is installed in a vacuum chamber filled with gaseous Cl_2 molecules. Although the absorption band edge wavelength of these molecules is 400 nm, green propagating light with a wavelength as long as 532 nm is used for photochemical etching. The Cl_2 molecules remain stable above the flat glass surface because of the absence

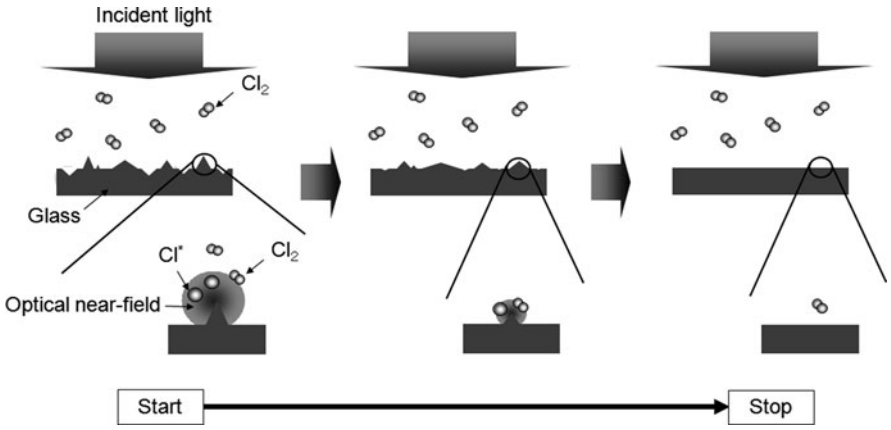

Fig. 1.33 Schematic explanation of phonon-assisted photochemical etching of a glass substrate surface

of DP–CPs. However, DP–CPs are generated at the tips of bumps on the illuminated rough surface, and by exchange of DP–CPs between the bumps and the Cl_2 molecules, the Cl_2 molecules are dissociated to produce radical Cl atoms, which etch the tips of the bumps. By this phonon-assisted process, the photochemical etching starts spontaneously to remove the bumps when the glass surface is illuminated with incident propagating light, and it stops spontaneously when the glass surface becomes so flat that DP–CPs are no longer generated. Thus, it is a self-organized method of smoothing the surface.

As shown in Fig. 1.34a, the magnitude of the roughness is represented by the quantity Ra, which decreased from 0.23 to 0.13 nm after 60 min of photochemical etching. This figure shows that the scratches, bumps, and digs formed in the process of preliminary mechano-chemical polishing were successfully removed by the phonon-assisted photochemical etching. Statistical analysis of the roughness quantitatively confirmed that the roughness was drastically removed after the photochemical etching (Fig. 1.34b)[57].

2. *Desorption* [58]. Phonon-assisted desorption was developed for smoothing the surface of transparent alumina (Al_2O_3), which is a hard polycrystalline ceramic, with the aim of fabricating low-loss gain media for ceramic lasers to be used in laser-driven spark plugs for the ignition systems in automobile engines [59]. It was expected that surface roughness, including the scratches formed in the preliminary grinding by diamond abrasive grains, would be repaired by sputtering Al_2O_3 particles and phonon-assisted desorption. An alumina substrate is placed in a vacuum chamber, and Al_2O_3 particles are deposited on the substrate by RF sputtering. In the case of conventional RF sputtering, the migration length of Al_2O_3 particles on the substrate surface depends on the Schwöbel barrier in the free energy and is very short at the ridges of scratches. This means that the deposition rate of the Al_2O_3 particles is higher at the ridges than at flat areas.

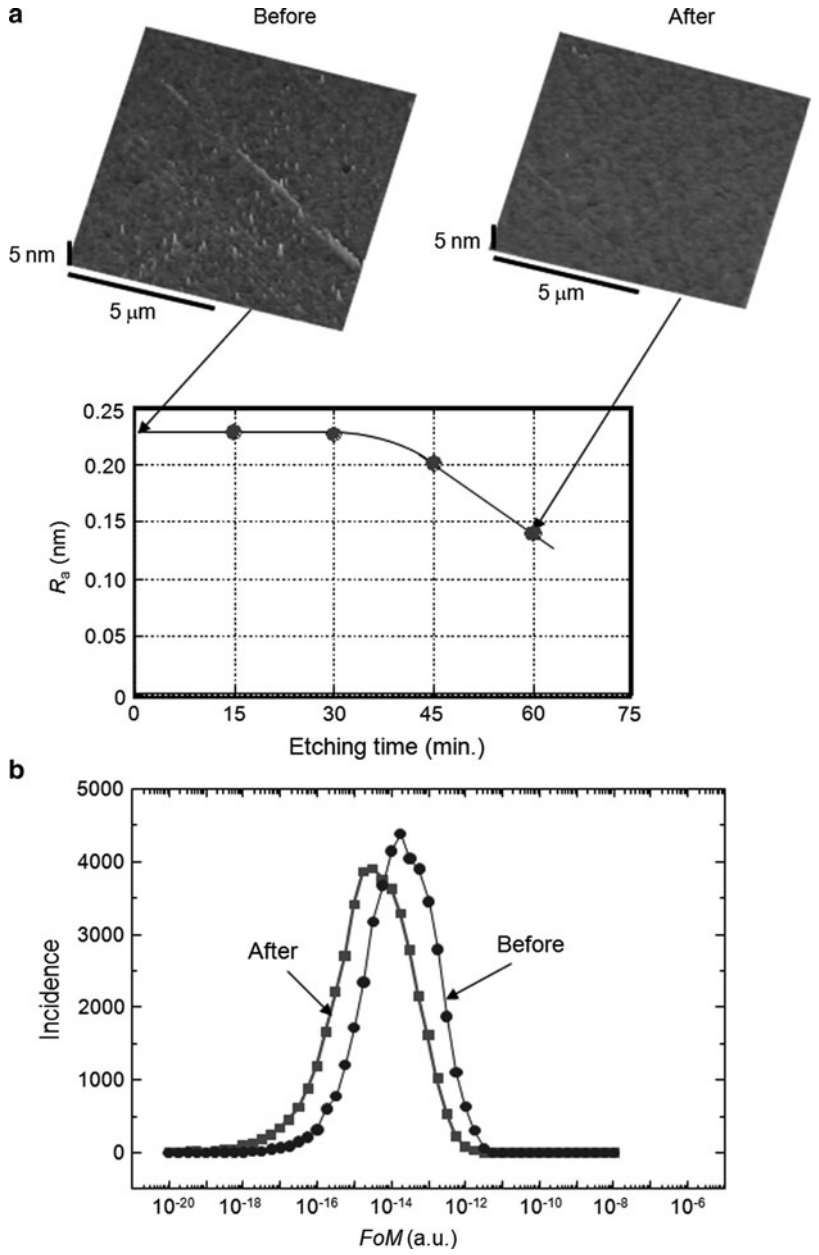

Fig. 1.34 Results of phonon-assisted photochemical etching of a glass substrate surface. (**a**) AFM images of the glass surfaces before and after the etching. Relation between the etching time and the surface roughness Ra is also shown. (**b**) Incidence pattern of the figure of merit, FoM, before and after the etching

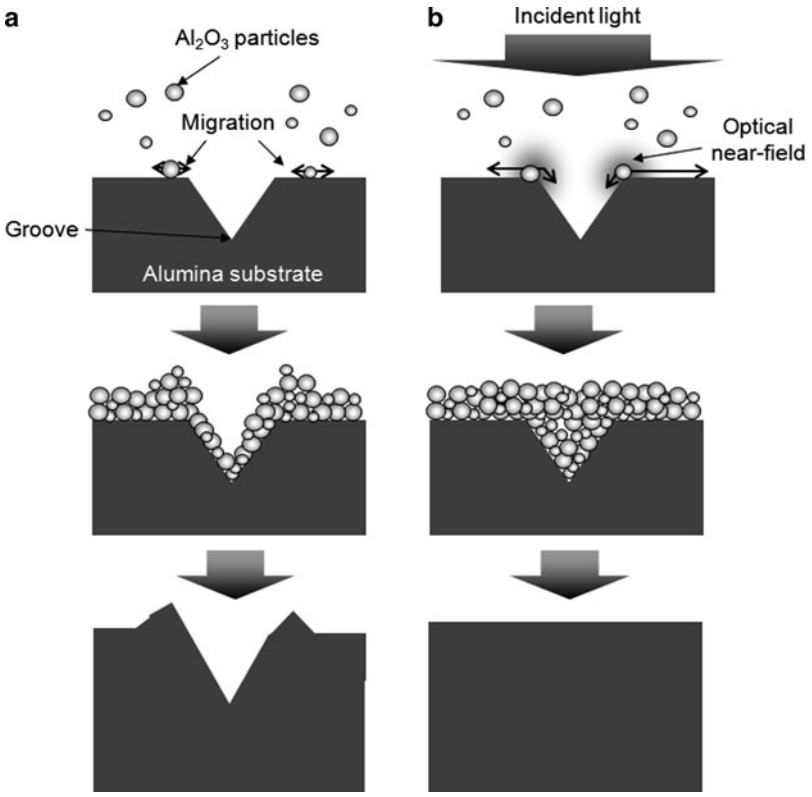

Fig. 1.35 Illustration of sputtering of Al_2O_3 particles on an alumina substrate surface (**a**) by conventional RF sputtering, and (**b**) by RF sputtering under visible light illumination

As a result of the difference in the deposition rate, Al_2O_3 particles are preferentially deposited on the ridges of scratches, as illustrated in Fig. 1.35a, making it impossible to repair the scratches. To repair them, the substrate is illuminated with visible light (400 mW cm^{-2} power density) whose wavelength (473 nm) is longer than that of the absorption band edge wavelength (260 nm) of the Al_2O_3 particles, as shown in Fig. 1.35b. By this illumination, DP–CPs are generated on the ridges of the scratches, which causes the Al_2O_3 particles to be activated, increasing the migration length, or which causes them to be desorbed from the ridge. On the other hand, on the flat areas and the slopes of the scratches, the Al_2O_3 particles are deposited with the same deposition rate as that of Fig. 1.35a because of the absence of DP–CPs. It should be pointed out that the DP–CPs are not generated at the bottom of the scratches because the substrate material around the bottom does not have nanometer-scale dimensions but is bulky, making it impossible to excite coherent phonons. By this phonon-assisted process, the deposition at the ridges is suppressed, whereas the bottoms of the scratches are filled by the Al_2O_3 particles, and finally, the scratches are repaired. It is a

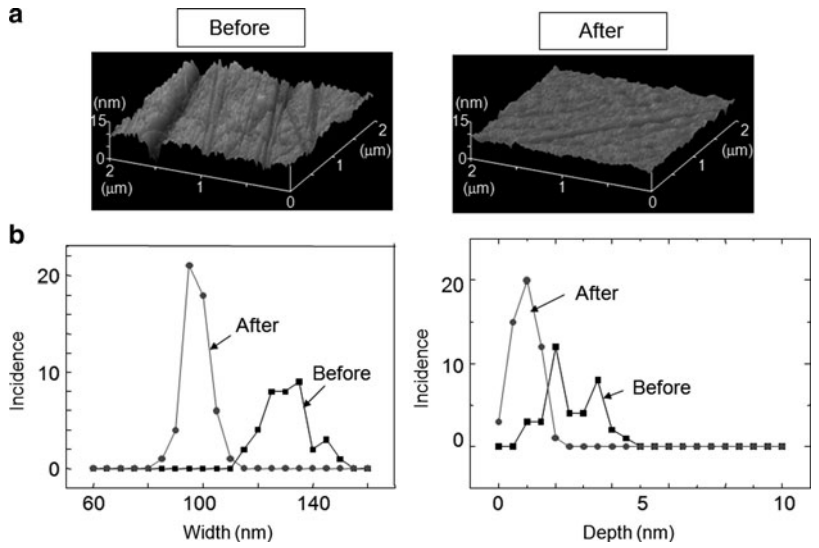

Fig. 1.36 Experimental results of the RF sputtering. (**a**) AFM images of the alumina substrate surface before and after the RF sputtering under visible light illumination. (**b**) The results of performing Hough transforms of the AFM images

self-organized method of smoothing the surface, as in case (1). Experimental results are shown in Fig. 1.36a, which shows a drastic change in the surface profile. Statistical analysis using a Hough transform revealed that the average width of the scratches decreased from 128 to 92 nm using this method. The average depth decreased from 3 to 1 nm, as shown in Fig. 1.36b.

1.5.3.2 Homogenizing Mole-Fraction Ratio

It should be pointed out that the DP–CPs are always generated at parts at which the structure or component of a substrate is locally singular even though its surface is morphologically flat. By exploiting this, the spatial distribution of the mole-fraction ratio, x, of indium (In) in an $In_xGa_{1-x}N$ film was homogenized by phonon-assisted desorption in a self-organized manner [60]. The motivation for this homogenization is to increase the color-rendering index of an $In_xGa_{1-x}N$ LED by controlling the spectral profile of the emitted light for applications to high-quality lighting, displays, and so on. It is possible to control this index because the emission wavelength, λ_e, increases from 400 nm to 1.50 μm by increasing x from 0 to 1, as a result of the decrease in the bandgap energy, E_g, from 3.10 to 0.83 eV. The principle of this homogenization is illustrated in Fig. 1.37. While the TEI, TMG, and NH_3 source gases are supplied for doping In, Ga, and N, respectively, in the $In_xGa_{1-x}N$ on the substrate, the film surface is illuminated with visible light. Due to this illumination, DP–CPs are generated on the film surface with a spatial profile that depends

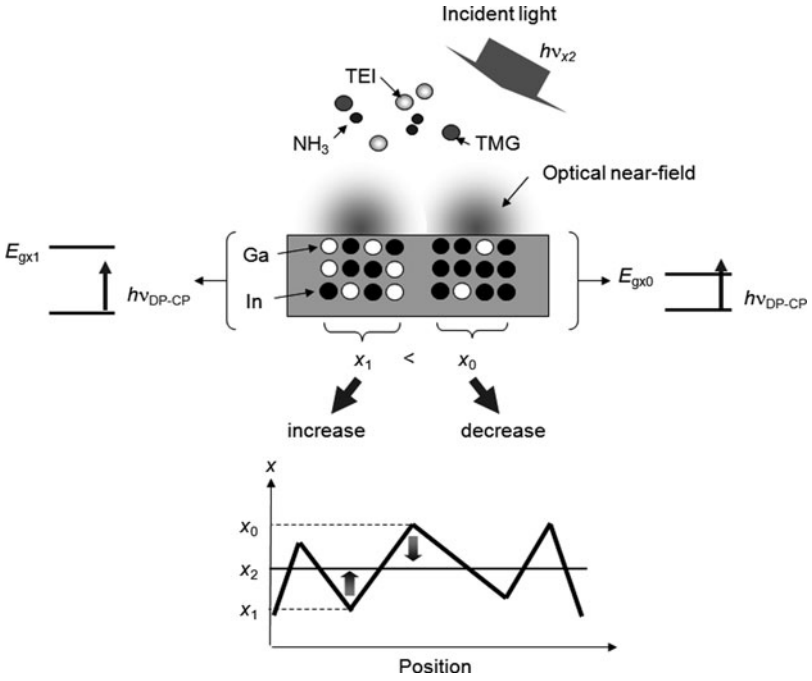

Fig. 1.37 Schematic explanation of homogenizing mole-fraction ratio x of $In_xGa_{1-x}N$ by phonon-assisted desorption

on the local singularities, i.e., on the mole-fraction ratio, x. In an area of larger mole-fraction ratio x_0 and bandgap energy E_{g0} lower than the energy $h\nu_{DP-CP}$ of the DP–CPs, the $In_xGa_{1-x}N$ film absorbs the DP–CP energy and transfers it to the doped In for desorption. As a result, the mole-fraction ratio x_0 decreases. On the other hand, in an area of lower mole-fraction ratio x_1 and bandgap energy E_{g1} higher than the energy $h\nu_{DP-CP}$, the $In_xGa_{1-x}N$ film does not absorb the DP–CP energy, and thus, the In can be steadily doped into the substrate without desorption. As a result, the mole-fraction ratio x_1 increases. The decrease and increase continue until the bandgap energies E_{g0} and E_{g1} reach $h\nu_{DP-CP}$. Finally, both the mole-fraction ratios x_0 and x_1 reach a value x_{DP-CP}, which is determined by $h\nu_{DP-CP}$. This means that the mole-fraction ratio can be spatially homogenized in a self-organized manner. Further, the photon energy of the incident light can determine the value x_{DP-CP} of the homogenized mole-fraction ratio and the wavelength of the light emitted from the $In_xGa_{1-x}N$ film.

For experimental confirmation of this effect, room-temperature PCVD was employed to grow an $In_xGa_{1-x}N$ film on a sapphire substrate [61] while visible light was made incident on the film surface for desorbing In. Figure 1.38 shows the spectral profiles of the photoluminescence emitted from the $In_xGa_{1-x}N$ film grown in this way. In Fig. 1.38a, spectral narrowing is seen in the area of the photon energy lower than that of the incident light ($h\nu_{FP} = 2.71$ eV; wavelength = 457 nm;

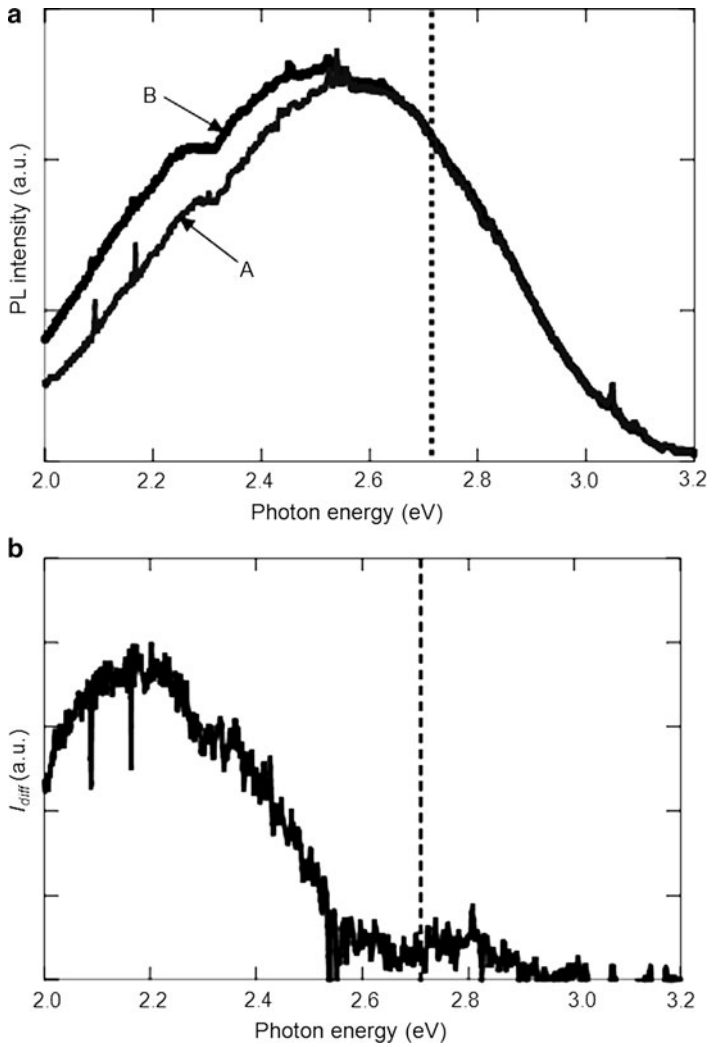

Fig. 1.38 Spectral profiles of the photoluminescence emitted from the $In_xGa_{1-x}N$ film. (**a**) Curves A and B represent the spectra from the film grown by the present method and by the conventional method, respectively. (**b**) Difference of spectral intensities of the curves A and B in (**a**). The *broken vertical lines* in these figures represent the photon energy of the incident light (= 2.71 eV)

power = 200 mW). Furthermore, the differential spectral intensity monotonically decreases with the increase of the photon energy (Fig. 1.38b). These features represent the results of homogenization of the mole-fraction ratio by phonon-assisted desorption.

1.6 Nanophotonic Energy Conversion

Noting that (1.4) represents energy up-conversion from the free photon to the DP–CP, this section reviews novel methods of optical/optical energy conversion and optical/electrical energy conversion.

1.6.1 Optical/Optical Energy Up-Conversion

To confirm the optical energy up-conversion, powdery grains of DCM organic dye molecules were placed in a quartz container and used as a test material [62]. Although the absorption band-edge wavelength of the DCM is as short as 670 nm, the grains were illuminated by near infrared light of 805-nm wavelength, as illustrated in Fig. 1.39a. This illumination generated the DP–CPs at the edges of grains, which were then exchanged between the adjacent grains. As a result of this exchange, an electron in the adjacent grain was excited by a phonon-assisted process, and then, it emitted light whose photon energy was higher than that of the incident light due to the contribution of the phonon energy. Figure 1.39b shows the spot of red light emitted from the grains as a result of the frequency up-conversion. Figure 1.39c shows an optical microscopic image of the 650-nm wavelength spectral component of the emitted light. The spatial distribution of the emitted light intensity in this figure is inhomogeneous because the light was emitted selectively from the edges of the grains, which demonstrates the phonon-assisted process due to the DP–CPs generated at the edges of the grains. For comparison, Fig. 1.39d shows an optical microscopic image of conventional 650-nm fluorescence, which is emitted as a result of the frequency down-conversion under illumination with 402-nm wavelength light. The spatial distribution of the fluorescence intensity is homogeneous, in contrast to that of Fig. 1.39c.

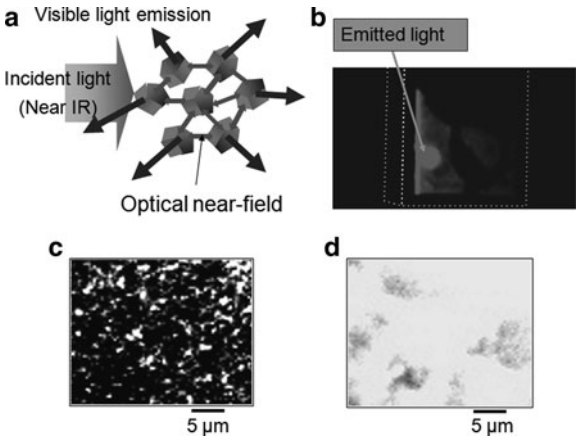

Fig. 1.39 Frequency up-converted light emission from powdery grains of DCM organic dye molecules. (**a**) Illustration of the emission mechanism. (**b**) Light spots emitted from the grains placed in a quartz container. (**c**) Optical microscopic image of the frequency up-converted light (wavelength, 650 nm). (**d**) Optical microscopic image of conventional fluorescence

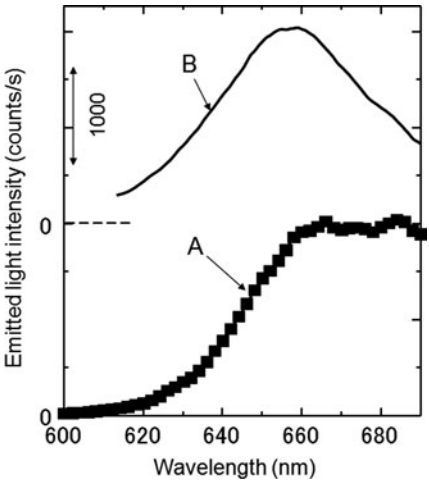

Fig. 1.40 Spectral profiles of the frequency up-converted light. Curve A is the spectrum obtained by applying near-infrared light with a wavelength of 805 nm. Curve B is the conventional fluorescence spectrum

The curve A in Fig. 1.40 shows the spectral profile of the frequency up-converted light measured by applying near infrared light with a wavelength of 805 nm. The curve B shows the conventional fluorescence spectral profile excited by the 402-nm wavelength light. Spectral profiles in the wavelength range shorter than 660 nm show similar curves, which means that the up-converted light is emitted from the electrons in the same excited state as that involved in emitting the fluorescent light. Experimental results of the temporal behaviors of the frequency up-converted light intensity were least squares-fitted to an exponentially decaying function with two decay constants, 0.45 and 1.37 ns. This fitting confirmed again that the up-converted photon was emitted from the electron of the same excited state as that for the fluorescence. However, the spectral intensity of curve A in the longer wavelength range is as high as that of its spectral peak, which means that the longer wavelength light is emitted from a long-lived electronic excited state to which the electron relaxes after the phonon-assisted excitation.

Figure 1.41a shows the relation between the incident light intensity I used for excitation and the frequency up-converted light intensity I_{uc} emitted from the powdery grains of the DCM organic dye molecules. Experimental results are presented for the wavelength components of 650 and 690 nm, to which the curve

$$I_{\mathrm{uc}} = aI + bI^2 \tag{1.8}$$

was least-squares fitted. The fitted results are represented by solid curves. The fitted curves show that the frequency up-conversion is due to the two-step excitation by the DP–CP, as described in the following (Fig. 1.41b); here, $|E_\alpha; el\rangle$ and $\left|E_\beta; vib\right\rangle$ represent molecular electronic and vibration (phonon) states, respectively, and E_α ($\alpha = g, ex$) and E_β ($\beta = i, a, b, thermal, em$) represent the molecular electronic and vibrational energies, respectively:

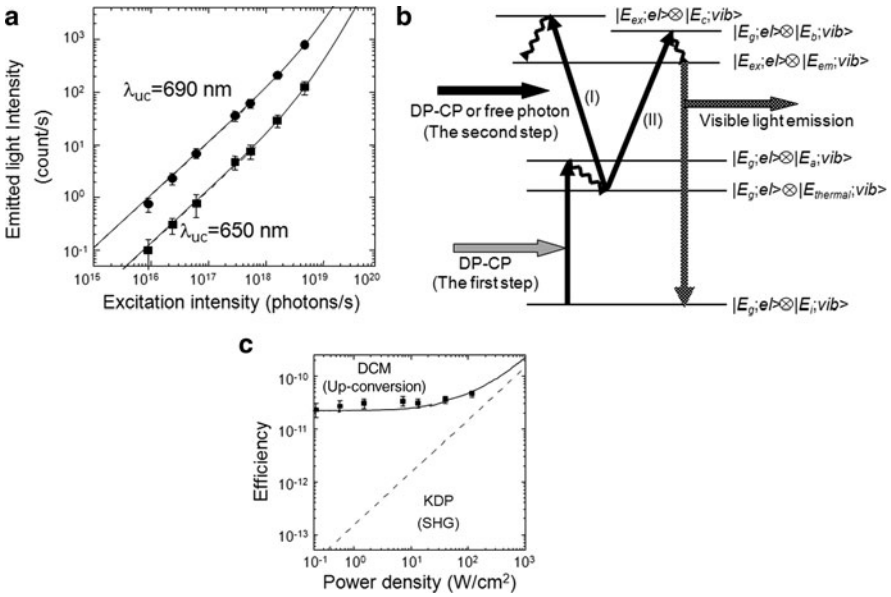

Fig. 1.41 (**a**) Relation between the incident light intensity and the frequency up-converted light intensity. (**b**) Illustration of the two-step excitation and subsequent light emission. (**c**) Efficiency of the frequency up-conversion as a function of the incident light power density. For comparison, the efficiency of the second harmonic generation from a KDP crystal is also shown

1. *First-step excitation.* After the excitation light generates a DP–CP at the edge of the DCM grain, the DP–CP induces the transition from $\left|E_g;el\right\rangle \otimes |E_i;vib\rangle$ to $\left|E_g;el\right\rangle \otimes |E_a;vib\rangle$ due to the phonon-assisted excitation.
2. *Second-step excitation.* After the first-step excitation, the excited coherent phonon relaxes to the thermal equilibrium state $\left|E_g;el\right\rangle \otimes |E_{\text{thermal}};vib\rangle$ with a relaxation rate of about 100 meV ps^{-1}. If the energy of the re-distributed phonon in the $\left|E_g;el\right\rangle \otimes |E_{\text{thermal}};vib\rangle$ state exceeds the energy difference of 0.34 eV between the electronic excited state in a molecule and the photon energy of the incident light, the excitation occurs via two possible routes. One route (I) is from $\left|E_g;el\right\rangle \otimes |E_{\text{thermal}};vib\rangle$ to $|E_{\text{ex}};el\rangle \otimes |E_c;vib\rangle$ due to the conventional adiabatic photo-excited process. The other (II) is from $\left|E_g;el\right\rangle \otimes |E_{\text{thermal}};vib\rangle$ to $\left|E_g;el\right\rangle \otimes |E_b;vib\rangle$. After the excitation (I) or (II), both $|E_{\text{ex}};el\rangle \otimes |E_c;vib\rangle$ and $\left|E_g;el\right\rangle \otimes |E_b;vib\rangle$ relax to $|E_{\text{ex}};el\rangle \otimes |E_{\text{em}};vib\rangle$ due to cooling or the coupling of the phonon and electronic states, respectively.

After the two-step transition described above, visible light is emitted by the transition from $|E_{\text{ex}};el\rangle \otimes |E_{\text{em}};vib\rangle$ to $\left|E_g;el\right\rangle \otimes |E_i;vib\rangle$. Since the excitation (I) is a conventional adiabatic process, its probability of occurrence is more than 10^6 times that of the first-step excitation. Furthermore, the probability of visible light emission by the infrared excitation is governed only by the phonon-assisted excitation of the first step because the second-step transition easily saturates. This is the origin

of the linear intensity dependence (the first term of (1.8)). Because the excitation (II) is phonon-assisted, its probability of occurrence is equal to that of the first-step transition. This is the origin of the squared dependence (the second term of (1.8)). As a whole, the relation between I and I_{uc} is represented by (1.8) [63].

The efficiency of the frequency up-conversion is plotted in Fig. 1.41c as a function of the incident light power density. For comparison, this figure also shows the efficiency of conventional second harmonic generation from a popular KDP crystal, which has the same optical thickness as that of the powdery grains of DCM organic dye molecules placed in the quartz container. It is easily found that the efficiency of the frequency up-conversion is more than 100 times higher than that of the second harmonic generation for an incident light power density lower than 1 W cm^{-2}. By increasing the incident light power density, the second-step excitation of the phonon-assisted process becomes dominant, and thus, the conversion efficiency increases in proportion to the incident light power density due to the second term of (1.8). This term maintains the conversion efficiency higher than that of the second harmonic generation even at higher incident power density, by which it is confirmed that the efficiency of this frequency up-conversion is sufficiently high.

In addition to the two-step excitation due to the two degenerate DP–CPs generated by a single type of incident light as was reviewed above, it has been found that non-degenerate two-step excitation can also emit higher-frequency light by using two mutually independent light beams with different wavelengths [64]. Using this non-degenerate two-step excitation with high conversion efficiency, a novel system for optical pulse shape measurement has been developed: An optical pulse to be measured is incident on the powdery grains of the organic dye molecules. Simultaneously, a reference optical pulse with sufficiently short pulse duration is also incident on the grains with a variable time delay. Due to these two non-degenerate optical pulses, the grains are excited by the two-step phonon-assisted process. By measuring the emitted light intensity with a conventional visible photo-detector as a function of the time delay of the reference optical pulse incidence, the optical pulse shape to be measured can be acquired. Several experiments using DCM dye molecules have confirmed that the optical pulse shape of the 800-nm wavelength was measured with a temporal resolution of 0.8 ps, which was limited by the lifetime of the intermediate state involved in the two-step excitation. It should be noted that the measured optical pulse shape has low jitter because the present measurement system employs only an optical process, unlike the conventional streak-camera system employing an electro-optical process. By using other commercially available dye molecules, the measurable wavelength range can be extended to 1.3–1.55 μm with a temporal resolution of 0.8 ps, which enables optical pulse shape measurement for optical fiber transmission systems.

Instead of the powdery grains of organic dye molecules, a variety of materials can be used for optical frequency up-conversion so long as the DP–CPs are efficiently generated on their surfaces.

1.6.2 Optical/Electrical Energy Up-Conversion

The DP–CP can be used to convert optical energy to electrical energy with frequency up-conversion. This section reviews two examples.

1. *Selective photocurrent generation in the transparent wavelength range of an organic thin film photovoltaic device* [65]. Frequency up-conversion can extend the photodetection bandwidth of a photovoltaic device. For confirming this, a poly(3-hexylthiophene) (P3HT) organic thin film was used as a p-type semiconductor, whereas a ZnO film was used as an n-type semiconductor. They were sandwiched by a transparent ITO film and an Ag film to be used as electrodes. It should be noted that no photocurrent is generated from this device if it is illuminated by light whose wavelength is longer than the absorption band-edge wavelength λ_c (=570 nm), which is governed by the bandgap energy E_g of the P3HT.

For generating a DP–CP effectively, a novel method is employed to fabricate a nanometric structure on an Ag film. That is, while the Ag is deposited by RF-sputtering, the surface of the Ag film is illuminated with light whose wavelength is longer than the absorption band-edge wavelength of the P3HT. As a result of this illumination, an intrinsic nanometric structure is spontaneously formed on the surface of the Ag film due to the phonon-assisted process, as has been experimentally demonstrated previously [51]. The present device is operated by using this Ag thin film as an electrode. Utilizing the phonon-assisted process induced by the DP–CP, the present method expands the working wavelength range of this device beyond the one limited by E_g even though the semiconductor materials remain untreated. Furthermore, a wavelength-selective feature of photocurrent generation is realized by controlling the morphology of the metallic electrode surface.

It is possible to excite electrons by a two-step phonon-assisted process for creating electron–hole pair (Fig. 1.42): The first step is the transition from the initial state in the HOMO ($|E_g; el\rangle \otimes |E_{\mathrm{ex,thermal}}; phonon\rangle$) to the intermediate state ($|E_g; el\rangle \otimes |E_{\mathrm{ex}}; phonon\rangle$) by the DP–CP. Here, $|E_g; el\rangle$ represents the ground state of the electron, $|E_{\mathrm{ex,thermal}}; phonon\rangle$ represents the thermal equilibrium state of a phonon whose energy is determined by the lattice temperature, and $|E_{\mathrm{ex}}; phonon\rangle$ represents the excited state of a phonon whose energy depends on the energy of the DP–CP. The DP–CP is indispensable for this transition because it is electric dipole-forbidden.

The second step is the transition from the intermediate state to the final excited state in the LUMO ($|E_{\mathrm{ex}}; el\rangle \otimes |E_{\mathrm{ex}'}; phonon\rangle$) by the DP–CP or the free photon (conventional propagating light). Here, $|E_{\mathrm{ex}}; el\rangle$) represents the excited state of the electron, and $|E_{\mathrm{ex}'}; phonon\rangle$ represents the excited state of a phonon whose energy depends on the photon energy used for the transition. Since this transition is electric dipole-allowed, it can be brought about not only by the DP–CP but also by the free photon. After this transition, the excited phonon relaxes to the thermal equilibrium state. $|E_{\mathrm{ex}',\mathrm{thermal}}; phonon\rangle$

The phonon-assisted process is used twice: once for efficient photocurrent generation in the wavelength range beyond the one limited by E_g, and once for fabricating a metallic electrode for the device, in which the morphology of the electrode surface

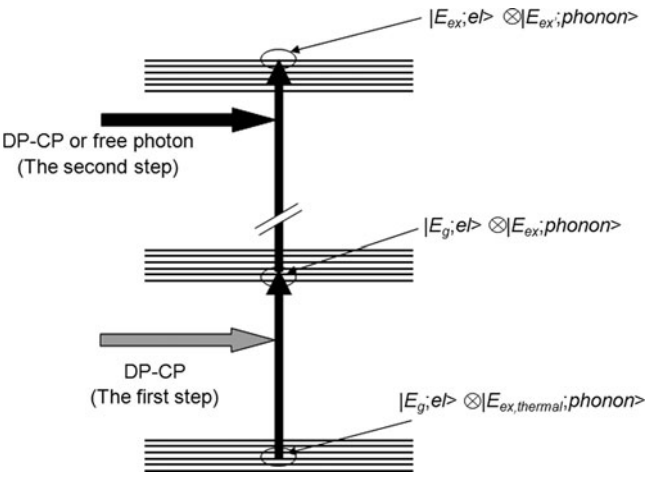

Fig. 1.42 Illustration of the two-step phonon-assisted process

can be controlled in a self-organized manner so that the phonon-assisted process is efficiently induced for photocurrent generation. For this self-organized control, Ag is deposited by RF-sputtering under light illumination on the previously deposited Ag thin film while the P3HT/ZnO pn-junction is reversely biased with a DC voltage V_b. Here, V_b was fixed to -1.5 V, and the wavelength λ_0 of the incident light was 660 nm, which is longer than λ_c of the P3HT. It is expected that this deposition with light illumination controls the morphology of the Ag film as a result of the phonon-assisted process induced by the DP–CP. When the Ag film with this controlled morphology is used as an electrode of the device, it is also expected that a conspicuous phonon-assisted process will be induced for photocurrent generation.

The mechanism of controlling the morphology is:

Step 1: Under light illumination, an optical near-field is generated on the Ag surface. This optical near-field excites a coherent phonon at the pn-junction, resulting in generation of a DP–CP. By the two-step phonon-assisted process, electrons can be excited to create electron–hole pairs at the pn-junction even though the photon energy of the incident light is lower than E_g.

Step 2: The created electron–hole pairs disappear because the electrons and positive holes are separated from each other due to the electric field of the reverse bias voltage. As a result, the positive holes are injected into the deposited Ag.

Step 3: Since the sputtered Ag is positively ionized due to the transmission of the Ag through the argon plasma or due to the collision of the argon plasma with the Ag-target used for RF-sputtering, these positively ionized Ag particles are repulsed from the area of the positively charged Ag film in which the positive holes have been injected in the manner described in Step 2. This

means that subsequent deposition of Ag is suppressed in the area in which the DP–CP is generated efficiently. As a result, a unique granular Ag film is formed, which depends on the spatial distribution of the DP–CP energy. This granular Ag film grows in a self-assembled manner with increasing RF-sputtering time, resulting in the formation of a unique morphology.

By using this morphology-controlled Ag film as an electrode of the device and by applying the incident light from the rear surface of the sapphire substrate, it is expected that the DP–CP can be efficiently generated on the electrode. Thus, electron–hole pairs can be created efficiently by the phonon-assisted process if the photovoltaic device is illuminated by light with the same wavelength λ_0 as the one used for controlling the morphology of the Ag film. On the other hand, if it is illuminated by light of a different wavelength λ_1, the efficiency of the electron–hole pair creation should be lower because the spatial profile and the photon energy of the generated DP–CP are different from those in the case of using λ_0 for controlling the morphology. Thus, this device should exhibit wavelength-selectivity in the photocurrent generation, which should take a maximum at the wavelength λ_0. Furthermore, since this wavelength is longer than λ_c, the working wavelength becomes longer than that limited by E_g.

Ag was deposited on the previously fabricated Ag film by RF sputtering. Device 1 was fabricated without applying V_b and the incident light power P, which was used as a reference to evaluate the performance of Device 2. For Device 2, V_b and P were -1.5 V and 70 mW, respectively. Figure 1.43a, b show SEM images of the Ag film surfaces of Devices 1 and 2. By comparing them, it is clear that the Ag surface of Device 2 (Fig. 1.43b) was very rough, with larger grains than those of Device 1 (Fig. 1.43a). The average and standard deviation of the diameters of the grains of Fig. 1.43b were 86 and 32 nm, respectively. The sum of the thicknesses of the Ag and P3HT was estimated to be less than 70 nm. Therefore, it is expected that the DP–CP generated on the Ag grains of Fig. 1.43b can extend to the pn-junction because the average diameters of these grains were 90 and 86 nm, respectively. As a result, it is expected that this DP–CP efficiently creates electron–hole pair at the pn-junction by the phonon-assisted process.

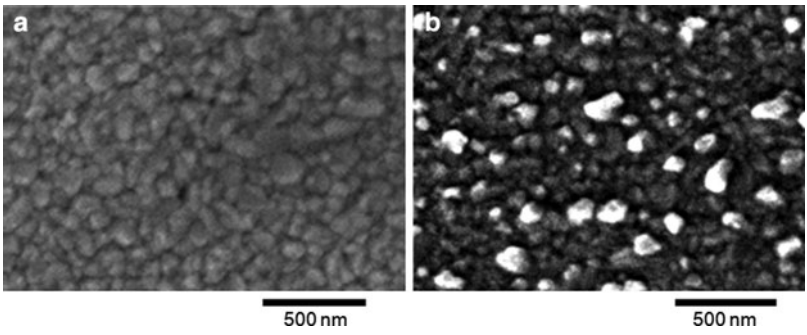

Fig. 1.43 SEM images of Ag film surfaces. (**a**) and (**b**) are for Devices 1 and 2, respectively

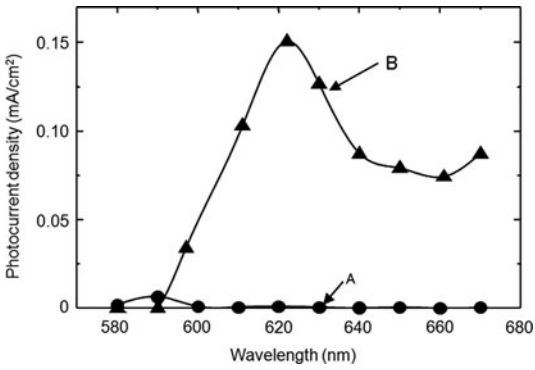

Fig. 1.44 Dependence of the generated photocurrent densities on the wavelength of the incident light. Curves A and B are for Devices 1 and 2, respectively

The detailed wavelength dependences of the photocurrent generation in the longer wavelength range beyond E_g of P3HT were evaluated, and the experimental results are shown in Fig. 1.44 for the wavelength range 580 nm $\leq \lambda_i \leq$ 670 nm. A linear relation between the incident light power and the generated photocurrent density was confirmed by preliminary experiments by applying low-power incident light (0.02–20 mW, corresponding to a power density of 2.5 mW cm^{-2} to 2.5 W cm^{-2}). This linear relation was attributed to the fact that the rate of creating electron–hole pairs was governed only by the electric dipole-forbidden transition of the first-step excitation under low-power-density excitation. The creation rate by the second-step excitation was sufficiently high because of the electric dipole-allowed transition. Based on this linear relation, the incident light power density was fixed to 125 mW cm^{-2} (1 mW optical power) for photocurrent density measurements. The photocurrent density from Device 1 was also very low, but it is shown by curve A as a reference.

Curve B represents the measured photocurrent densities from Device 2, generated by incident light with wavelengths up to $\lambda_i = 670$ nm, which clearly demonstrates the extension of the working wavelength range beyond that limited by E_g of P3HT. This curve also indicates the possibility of photocurrent generation even in the wavelength range longer than 670 nm. The photocurrent of curve B was the highest at $\lambda_{ip} = 620$ nm. Thus, Device 2 is effectively a wavelength-selective photovoltaic device for incident light with a wavelength beyond that limited by E_g. This wavelength λ_{ip} (= 620 nm) is 40 nm shorter than λ_0 (= 660 nm) used for controlling the morphology of the Ag film. This difference is attributed to the DC Stark effect induced by the reverse bias voltage V_b (= −1.5 V) applied in the process of controlling the morphology of the Ag film. The photocurrent density was 0.15 mW cm^{-2} at the peak of curve B ($\lambda_{ip} = 620$ nm), which corresponds to a quantum efficiency of 0.24% because the incident light power density was 125 mW cm^{-2}. This efficiency is as high as that of a conventional hetero-junction photovoltaic device using P3HT [66]. However, it should be pointed out that Device 2 realized such high quantum efficiency even for wavelengths longer than the one limited by E_g of P3HT.

It is expected that this method can be applied not only to P3HT but also to other organic and inorganic semiconductors because the phonon-assisted process was induced merely by controlling the morphology of the electrode while the semiconductor materials remained untreated. Higher efficiency can be expected by fine adjustment of the reverse bias voltage, light power, and wavelength used for controlling the morphology.

(2) *Extending the detection bandwidth of a GaN-MSM photodetector* [67]. A conventional metal–semiconductor–metal (MSM) photodetector, composed of two metallic electrodes and GaN, does not have any detection sensitivity for incident light with a wavelength longer than the absorption band-edge wavelength λ_c(=360 nm) of GaN. However, by sharpening the edges of the metallic electrodes, the incident light can generate a DP–CP at the boundary between the edge of the metal and the semiconductor. Since the exchange of the DP–CP between the metal and semiconductor can excite free electrons in a phonon-assisted manner, the photocurrent can flow out to the external circuit if a bias voltage is applied, by which the optical energy can be converted to electrical energy. It should be noted that the energy is converted in a frequency up-converted manner because the free electrons are generated even by applying incident light whose wavelength is longer than λ_c. Figure 1.45a shows the SEM image of a metallic Au electrode whose edge has been sharpened. Figure 1.45b shows the dependences of the photocurrent on the bias voltage and the wavelength of the incident light. From these experimental results, it was confirmed that the long-wavelength cut-off was extended up to at least 532 nm.

There are at least two methods of increasing the conversion efficiency of photodetecting devices, including photovoltaic devices and solar cell batteries. For solar cell batteries, the first method is to increase the efficiency within the visible range, i.e., the wavelength range shorter than that of the absorption band edge of the material to be used as an active medium. This method has been conventionally employed; however, it is reaching fundamental and technical limits. The second method is to utilize the infrared component of the solar energy whose wavelength is longer than the absorption band edge. This method is effective to increase the conversion efficiency because sunlight contains large numbers of photons in the infrared region. Since most of the materials to be used as the active media (Si, P3HT, and so on) for solar cell batteries are active only in the visible region, they must be replaced by other exotic materials, e.g., compound semiconductors, to utilize the infrared photons. However, they are often toxic or rarely excavated. Instead, the examples (1) and (2) reviewed above demonstrated that the infrared photons can be utilized, even by using nontoxic and commonly produced conventional materials, if a nanometric structure is formed on the electrode, while the semiconductor materials remained untreated. Due to this technological advantage, nanophotonics can enable novel device functions by using conventional materials, which can realize qualitative innovations in optical technology. In the other words, nanophotonics is not a conventional material technology but a novel *size- and conformation-controlling technology* to enable novel device functions even by using conventional materials.

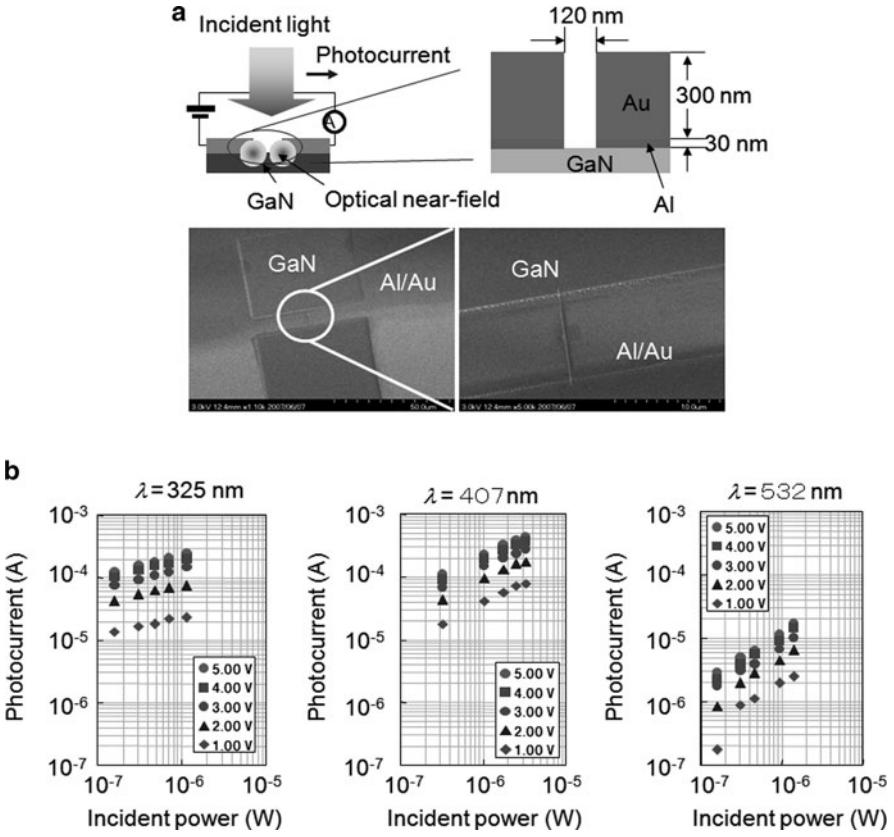

Fig. 1.45 (**a**) Cross-sectional structure of an MSM photodetector and SEM image of metallic Au electrodes 9 μm in length with a gap of 120 nm. (**b**) Relation between the incident light power and the photocurrent for incident light wavelengths of 325, 407, and 532 nm. The values of the bias voltage are also shown in the inset

1.7 Nanophotonic Systems and Their Evolution to Related Sciences

Nanophotonics has realized both quantitative and qualitative innovations. For example, novel architectures have been proposed for optical signal transmission systems, and their performance has been confirmed experimentally. They include computing using nanophotonic switches and an optical nano-fountain [68], as well as data broadcasting using multiple nanophotonic switches [69]. Quantitative innovations have been realized by decreasing the device size and power consumption beyond the diffraction-limit. More importantly, qualitative innovations have been realized by exploiting the novel functions of nanophotonic devices, which are otherwise impossible using conventional photonic devices. Quantitative innovations have already

been realized by breaking the diffraction-limit of optical/magnetic hybrid disk storage density (refer to Sect. 1.3). Qualitative innovations have also been proposed by applying the hierarchy inherent in optical near-fields to memory retrieval [70].

An example of evolution to a related science is atom photonics, in which the thermal motions of neutral atoms in a vacuum are controlled using optical near-fields [71]. Theoretical studies have examined single-atom manipulation based on the dressed photon model [72], and experimental studies have involved the first successful guidance of an atom through a hollow optical fiber [73]. Recent studies have examined atom-detecting devices [74], atom deflectors [75], and an atomic funnel [76]. Atom photonics will open up a new field of science that examines the interactions between dressed photons and single atoms.

Basic research in nanophotonics is being actively carried out. An optical near-field problem has been formulated in terms of the Carniglia–Mandel model as a complete and orthogonal set that satisfies the infinite planar boundary conditions between a dielectric and a vacuum. This approach has revealed interesting atomic phenomena occurring near the surface, which have been analyzed based on an angular spectrum representation [77, 78]. For example, optical radiation from an excited molecule on a substrate surface has been analyzed, and the results agreed quantitatively with experimental results [79]. A self-consistent, nonlocal, semiclassical theory of light–matter interactions has been developed to discuss the optical response of a variety of nanostructures [80]. In particular, the size dependence and allowance of a dipole-forbidden transition in a nanometric quantum dot system were noted [81, 82]. The optical manipulation of nanometric objects in superfluid helium has been investigated based on nonlocal semiclassical theory [83]. Electron transport through molecular bridges connecting nanoscale electrodes has been formulated [84], and a unified method has been proposed to treat extended and polaron-like localized states coupled with molecular vibrations. A one-dimensional molecular bridge made of thiophene molecules has been analyzed numerically. The study of optical near-fields associated with molecular bridges is now underway. In addition, as basic experimental work, desorption and ionization assisted by optical near-fields have been carried out, and their application to mass spectroscopy has been proposed [85, 86]. From both fundamental and applied perspectives, the role of spin degrees of freedom in excitation energy transfer driven by optical near-fields is an intriguing and important issue. A new approach has been proposed to discuss spin information achieved by energy transfer in a quantum dot pair and the effects of spin relaxation due to interactions with the environment [87, 88].

1.8 Summary

By combining the concepts of quantum field theory, optical science, and condensed-matter physics, the author has studied nanometric materials and optical energy transfer in nanometric space. Through these studies, a theoretical picture of dressed photons was obtained. Based on this picture, the exchange of dressed photons was

studied, revealing energy transfer to electric dipole-forbidden energy levels. Furthermore, the possibility of coupling a dressed photon with a coherent phonon was found, revealing a novel phonon-assisted process in light–matter interactions in nanometric space. These discoveries were applied to develop novel technologies, such as devices, fabrication techniques, energy conversion, information systems, architectures and algorithms.

Fundamental concepts such as the behavior of photons in nanometric space, excitation transfer and relaxation in a nanometric space, and the primary mechanisms of the phonon-assisted process should be delved into more deeply. Such fundamental studies are expected to bring about further discoveries involving the coupling of dressed photons with various elementary excitations besides coherent phonons, leading to the discovery of novel applications. This marriage of basic studies and technological applications is expected to establish a new field of dressed photon science and technology in the near future.

Dressed photons can be utilized to establish fundamental new technologies that can replace a wide range of conventional optical technologies. Even though users will not notice their existence, it is expected that technologies exploiting dressed photons will be widely used in everyday life in the near future. This is because dressed photons can be generated universally on the surface of illuminated nanometric materials.

The name "nanophotonics" is occasionally used for photonic crystals, plasmonics, metamaterials, silicon photonics, and quantum dot lasers using conventional propagating light. Here, one should consider the stern warning by Shannon on the casual use of the term "information theory," which was a trend in the study of information theory during the 1950s [89]. The term "nanophotonics" has been used in a similar way, although some work in "nanophotonics" is not based on optical near-field interactions. For the true development of nanophotonics, one needs deep physical insight into the behavior of virtual photons and the nanometric subsystem composed of electrons and photons.

Acknowledgements The author sincerely thanks Prof. K. Kitahara (International Christian University) and Prof. M. Tsukada (Tohoku Univ.) for their encouragement throughout his study of nanophotonics and dressed photon science and technology. He also thanks Profs. H. Hori, K. Kobayashi, I. Banno (University of Yamanashi), Profs. T. Yatsui, T. Kawazoe (University of Tokyo), Prof. M. Naruse (National Institute for Communication Technology and University of Tokyo), and Drs. W. Nomura, N. Tate, and K. Kitamura (University of Tokyo) for their collaboration.

References

1. M. Ohtsu, T. Kawazoe, T. Yatsui, M. Naruse, IEEE J. Sel. Top. Quant. Electron. **14**, 1404 (2008)
2. M. Ohtsu, K. Kobayashi, T. Kawazoe, T. Yatsui, M. Naruse, in *Preface*. Principles of Nanophotonics (Tailor & Francis, FL, 2008), pp. ix–x

3. M. Ohtsu, in *Preface to Volume V*, ed. by M. Ohtsu. Progress in Nano-Electro-Optics V (Springer, Berlin, 2006), pp. VII–VIII
4. MIT Microphotonics Center, Communication Technology Roadmap (2005), http://mph-roadmap.mit.edu/
5. K. Kobayashi, S. Sangu, H. Ito, M. Ohtsu, Phys. Rev. A **63**, 013806 (2001)
6. M. Ohtsu, K. Kobayashi, *Optical Near Fields* (Springer, Berlin, 2004), pp. 109–120
7. Y. Tanaka, K. Kobayashi, J. Microsc. **229**, 228 (2008)
8. A. Sato, Y. Tanaka, F. Minami, K. Kobayashi, J. Luminescence **129**, 1718 (2009)
9. S. Mononobe, in *Near-Field Optical Fiber Probes and the Imaging Application*, ed. by M. Ohtsu. Progress in Nano-Electro-Optics III (Springer, Berlin, 2005), pp. 1–56
10. M. Ohtsu, *Near-Field Nano/Atom Optics and Technology* (Springer, Berlin, 1998), pp. 33–69
11. E. Betzig, J.K. Trautman, Science **257**, 189 (1992)
12. U. Maheswari Rajagopalan, S. Mononobe, K. Yoshida, M. Yoshimoto, M. Ohtsu, Jpn. J. Appl. Phys. **38**, 6713 (1999)
13. K. Matsuda, T. Saiki, H. Saito, K. Nishi, Appl. Phys. Lett. **76**, 73 (2000)
14. H. Fukuda, T. Saiki, M. Ohtsu, Sensors Mater. **13**, 445 (2001)
15. N. Hosaka, T. Saiki, J. Microsc. **202**, 362 (2001)
16. T. Ushiki, Scanning near-field optical/atomic force microscopy in biology, Presented at the 5th Asia-Pacific Conference on Near-Field Optics. Optical Society of Japan, Niigata, Japan, Paper 2-1, 15–17 November 2005
17. Y. Narita, T. Tadokoro, T. Ikeda, T. Saiki, S. Mononobe, M. Ohtsu, Appl. Spectros. **52**, 1141 (1998)
18. F. Sato, Jasco Report, **46**, 34 (2004)
19. C. Hubert, G. Lerondel, R. Bachelot, S. Kostcheev, J. Grand, A. Vial, D. Barciesi, P. Royer, S.H. Chang, S.K. Gray, G.P. Wiederrecht, G.C. Shatz, Near-field photochemical imaging of noble metal nano-object using an azodyne polymer: From single to near field coupled objects, presented at the 5th Asia-Pacific Conference on Near-Field Optics. Optical Society of Japan, Niigata, Japan, Paper 3-4, 15–17 November 2005
20. T. Yatsui, M. Kourogi, M. Ohtsu, Appl. Phys. **73**, 2090 (1998)
21. T. Yatsui, M. Ohtsu, in *High-Throughput Probes for Near-Field Optics and Their Applications*, ed. by M. Ohtsu. Progress in Nano-Electro-Optics I (Springer, Berlin, 2003), pp. 1–28
22. T. Yatsui, M. Kourogi, K. Tsutsui, M. Ohtsu, J. Takahashi, Opt. Lett. **25**, 1279 (2000)
23. M. Ohtsu, Nanophotonics and application to future storage technology, Technical Digest, The Joint International Symposium on Optical Memory and Optical Data Storage 2008, (ISOM/ODS'08), HI, USA, pp. 24–26 (paper number MA01 TD0501), 13–17 July 2008
24. H. Hieda, in *Nanopatterned Media for High-Density Storage*, ed. by M. Ohtsu. Nanophotonics and Nanofabrication (Wiley-VCH, Weinheim, 2009), pp. 147–165
25. T. Nishida, T. Matsumoto, F. Akagi, H. Hieda, A. Kikitsu, K. Naito, T. Koda, N. Nishida, H. Hatano, M. Hirata, J. Nanophoton. **1**, 011597 (2007)
26. T. Nishida, T. Matsumoto, F. Akagi, in *Nanoophotonics Recording Device for High-Density Storage*, ed. by M. Ohtsu. Nanophotonics and Nanofabrication (Wiley-VCH, Weinheim, 2009), pp. 167–178
27. H. Kitahara, Y. Ueno, H. Suzuki, T. Kobayashi, H. Tanaka, Y. Kojima, M. Kobayashi, M. Katsumura, Y. Wada, T. Iida, Jpn. J. Appl. Phys. **49**, 06GE02 (2010)
28. M. Ohtsu, *Technology Roadmap for Information Storage* (Optical Industry Technology Development Association, Tokyo, 2006), pp. 35–78
29. P. Kocher, J. Jaffe, B. Jun, Introduction to differential power analysis and related attacks, http://www.cryptography.com/resources/whitepapers/DPATechInfo.pdf
30. M. Naruse, H. Hori, K. Kobayashi, M. Ohtsu, Opt. Lett. **32**, 1761 (2007)
31. M. Ohtsu, K. Kobayashi, T. Kawazoe, S. Sangu, T. Yatsui, IEEE J. Sel. Top. Quant. Electron. **8**, 839 (2002)
32. T. Kawazoe, K. Kobayashi, S. Sangu, M. Ohtsu, Appl. Phys. Lett. **82**, 2957 (2003)
33. T. Yatsui, S. Sangu, T. Kawazoe, M. Ohtsu, S.J. An, J. Yoo, G.-C. Yi, Appl. Phys. Lett. **90**, 223110 (2007)

34. T. Kawazoe, K. Kobayashi, K. Akahane, M. Naruse, N. Yamamoto, M. Ohtsu, Appl. Phys. B **84**, 243 (2006)
35. A. Shojiguti, K. Kobayashi, S. Sangu, K. Kitahara, M. Ohtsu, J. Phys. Soc. Jpn. **72**, 2984 (2003)
36. T. Kawazoe, M. Naruse, M. Ohtsu, CCLEO/QELS06, paper CFE3, Baltimore, May 2006
37. W. Nomura, T. Yatsui, T. Kawazoe, M. Ohtsu, J. Nanophoton. **1**, 011591 (2007)
38. T. Yatsui, Y. Ryu, T.Morishima, W. Nomura, T. Kawazoe, T. Yonezawa, M. Washizu, H. Fujita, M. Ohtsu, Appl. Phys. Lett. **96**, 133106 (2010)
39. T. Kawazoe, K. Kobayashi, M. Ohtsu, Appl. Phys. Lett. **86**, 103102 (2005)
40. K. Akahane, N. Yamamoto, M. Naruse, T. Kawazoe, T. Yatsui, M. Ohtsu, Extended Abstracts (The 57th Spring Meeting, 2009); The Japan Society of Applied Physics and Related Societies, paper 18a-P4-19, March 2010, Kanagawa, Japan or K. Akahane, N. Yamamoto, M. Naruse, T. Kawazoe, T. Yatsui, M. Ohtsu, Abstract, SSDM 2010
41. M. Naruse, N. Tate, O plus E **32**, 145 (2010)
42. L.B. Kish, IEE Proc. Circ. Dev. Syst. **151**, 190 (2004)
43. V.P. Carey, A.J. Shah, J. Electron. Packag. **128**, 346 (2006)
44. R.H. Brown, R.Q. Twiss, Nature **178**, 1447 (1956)
45. T. Kawazoe et al., J. Nanophoton. **2**, 029502 (2008)
46. H. Hori, in *Optical and Electronic Process of Nano-Matters*, ed. by M. Ohtsu (Kluwer, Dordrecht, 2001), pp. 1–55
47. M. Naruse, T. Miyazaki, F. Kubota, T. Kawazoe, K. Kobayashi, S. Sangu, M. Ohtsu, Opt. Lett. **30**, 201 (2005)
48. T. Kawazoe, K. Kobayashi, S. Takubo, M. Ohtsu, J. Chem. Phys. **122**, 024715 (2005)
49. K. Kobayashi, A. Sato, T. Yatsui, T. Kawazoe, M. Ohtsu, Appl. Phys. Express **2**, 075504 (2009)
50. T. Kawazoe, K. Kobayashi, M. Ohtsu, Appl. Phys. B **84**, 247 (2006)
51. T. Yatsui, W. Nomura, M. Ohtsu, Nano Lett. **5**, 2548 (2005)
52. H. Yonemitsu, T. Kawazoe, K. Kobayashi, M. Ohtsu, J. Photoluminescence **122**, 230 (2007)
53. Y. Ito, S. Nakasato, R. Kuroda, M. Ohtsu, Microelectronic Eng. **84**, 705 (2007)
54. M. Koike, S. MIyauchi, K. Sano, T. Imazono, in *X-ray Devices and the Possibility of Applying Nanophotonics*, ed. by M. Ohtsu. Nanophotonics and Nanofabrication (Wiley-VCH, Weinheim, 2009), pp. 179–191
55. T. Kawazoe, H. Fujiwara, K. Kobayashi, M. Ohtsu, Appl. Phys. B **98**, 5 (2010)
56. T. Yatsui, K. Hirata, W. Nomura, Y. Tabata, M. Ohtsu, Appl. Phys. B **93**, 55 (2008)
57. M. Naruse, T. Yatsui, W. Nomura, K. Hirata, Y. Tabata, M. Ohtsu, J. Appl. Phys. **105**, 63156 (2009)
58. W. Nomura, T. Yatsui, Y. Yanase, K. Suzuki, M. Fujita, A. Kamata, M. Naruse, M. Ohtsu, Appl. Phys. B **99** 75 (2010)
59. D. Graham-Rowe, Nat. Photon. **2**, 515 (2008)
60. T. Yatsui, S. Yamazaki, K. Ito, H. Kawamura, M. Mizumura, T. Kawazoe, M. Ohtsu, Appl. Phys. B **97**, 375 (2009)
61. S. Yamazaki, T. Yatsui, M. Ohtsu, Appl. Phys. Express **1**, 061102 (2008)
62. T. Kawazoe, H. Fujiwara, K. Kobayashi, M. Ohtsu, IEEE J. Sel. Top. Quant. Electron. **15**, 1380 (2009)
63. H. Fujiwara, T. Kawazoe, M. Ohtsu, Appl. Phys. B **98**, 283 (2010)
64. H. Fujiwara, T. Kawazoe, M. Ohtsu, Appl. Phys. B **100**, 85 (2010)
65. S. Yukutake, T. Kawazoe, T. Yatsui, W. Nomura, K. Kitamura, M. Ohtsu, Appl. Phys. B **99** 415(2010)
66. S. Guenes, H. Neugebauer, S. Sariciftci, Chem. Rev. **107**, 1324 (2007)
67. S. Yamazaki, W. Nomura, T. Kawazoe, M. Ohtsu, Extended Abstracts (The 68th Autumun Meeting, 2007); The Japan Society of Applied Physics, paper number 7p-Q-10, Sapporo, Japan, September 2007
68. M. Naruse, T. Miyazaki, T. Kawazoe, K. Kobayashi, S. Sangu, F. Kubota, M. Ohtsu, IEICE Trans. Electron. **E88-C**, 18171823 (2005)
69. M. Naruse, T. Kawazoe, S. Sangu, K. Kobayashi, M. Ohtsu, Opt. Express **14**, 306 (2006)
70. M. Naruse, T. Yatsui, W. Nomura, N. Hirose, M. Ohtsu, Opt. Express **13**, 9265 (2005)

71. M. Ohtsu (ed.), *Near-Field Nano/Atom Optics and Technology* (Spinger, Berlin, 1998), pp. 218–293
72. K. Kobayashi, S. Sangu, H. Ito, M. Ohtsu, Phys. Rev. A **63**, 013806 (2001)
73. H. Ito, T. Nakata, K. Sakaki, M. Ohtsu, K. I. Lee, W. Jhe, Phys. Rev. Lett. **76**, 4500 (1996)
74. K. Totsuka, H. Ito, T. Kawamura, M. Ohtsu, J. Appl. Phys. **41**, 1566 (2002)
75. K. Totsuka, H. Ito, K. Suzuki, K. Yamamoto, M. Ohtsu, T. Yatsui, Appl. Phys. Lett. **82**, 1616 (2003)
76. A. Takamizawa, H. Ito, S. Yamada, M. Ohtsu, Appl. Phys. Lett. **85**, 1790 (2004)
77. T. Inoue, H. Hori, Phys. Rev. A **63**, 063805 (2001)
78. T. Inoue, H. Hori, in *Quantum Theory of Radiation in Optical Near Field Based on Quantization of Evanescent Electromagnetic Waves Using Detector Mode*, ed. by M. Ohtsu. Progress in Nano- Electro-Optics IV (Springer, Berlin 2005), pp. 127–199
79. T. Inoue, H. Hori, IEICE Trans. Electron. **E88-C**, 1836 (2005)
80. K. Cho, Progr. Theor. Phys. Suppl. **106**, 225 (1991)
81. H. Ishihara, K. Cho, Phys. Rev. B **48**, 7960 (1993)
82. K. Cho, Y. Ohfuti, K. Arima, Surf. Sci. **363**, 378 (1996)
83. T. Iida, H. Ishihara, IEICE Trans. Electron. **E88-C**, 1809 (2005)
84. K. Mitsutake, M. Tsukada, e-J. Surf. Sci. Nanotechnol. **4**, 311 (2006)
85. L.C. Chen, J. Yonehama, T. Ueda, H. Hori, K. Hiraoka, J. Mass Spectrom. **42**, 346 (2007)
86. L.C. Chen, T. Ueda, M. Sagisaka, H. Hori, K. Hiraoka, J. Phys. Chem. **111**, 2409 (2007)
87. A. Sato, F. Minami, K. Kobayashi, Physica E, **40**, 313 (2007)
88. A. Sato, F. Minami, H. Hori, K. Kobayashi, J. Comput. Theor. Nanoscience **7**, 1–10 (2010)
89. C.E. Shannon, IEEE Trans. Inform. Theor. **IT-2**, 3 (1956)

Chapter 2
Probe-Free Nanophotonic Systems: Macro-Scale Applications Based on Nanophotonics

Naoya Tate, Makoto Naruse, and Motoichi Ohtsu

Abstract To implement innovative nanometric optical processing systems as probe-free nanophotonic systems, it is necessary to exploit the unique attributes of nanometer-scale optical near-field interactions in a completely parallel fashion. This chapter is devoted to describing basic concepts necessary for two-dimensional parallel processing of light–matter interactions on the nanometer scale to realize probe-free nanophotonic systems. Additionally, the concepts and some demonstrations of the hierarchy inherent in nanophotonics, based on the hierarchy between optical near- and far-fields, are described as practical applications of optical near-field interactions.

2.1 Introduction

Nanophotonics is a novel technology that utilizes the optical near-field, the electromagnetic field that mediates the interactions between closely spaced nanometric matter [1, 2]. By exploiting optical near-field interactions, nanophotonics has broken the integration density restrictions imposed on conventional optical devices by the diffraction limit of light. This higher integration density has enabled realization of *quantitative* innovations in photonic devices and optical fabrication technologies [3, 4]. Moreover, *qualitative* innovations have been accomplished by utilizing novel functions and phenomena made possible by optical near-field interactions that are otherwise unachievable with conventional propagating light [5, 6].

N. Tate (✉)
Graduate School of Engineering, The University of Tokyo, 2-11-16 Yayoi, Bunkyo-ku, Tokyo 113-8656, Japan
and
Nanophotonics Research Center, The University of Tokyo, 2-11-16 Yayoi, Bunkyo-ku, Tokyo 113-8656, Japan
e-mail: tate@nanophotonics.t.u-tokyo.ac.jp

M. Ohtsu (ed.), *Progress in Nanophotonics 1*, Nano-Optics and Nanophotonics,
DOI 10.1007/978-3-642-17481-0_2,

One of the most important technological vehicles that has contributed to the study of nanophotonics so far is high-quality optical near-field probing tips, such as those based on optical fiber probes [7]. They have achieved high spatial resolution and high energy efficiency – up to 10% optical near-field generation efficiency in some cases. For instance, near-field optical microscopes (NOMs) have been widely used to obtain ultrahigh-resolution images [8]. However, methods of characterizing optical near-fields using probing tips normally require one-dimensional (1D) scanning processes, which severely limits the throughput in obtaining two-dimensional (2D) information on the nanometer scale. Additionally, precision technologies are indispensable in fabricating probe tips and also in controlling their position during processing. In particular, such technologies become large obstacles to implementing nanometric information processing and realizing further applications. Therefore, eliminating 1D scanning processes, or in other words, achieving *probe-free nanophotonics*, is an important step toward further exploiting the possibilities of light–matter interactions on the nanometer scale.

In fact, utilization of optical near-field interactions without any scanning processes has been successfully demonstrated in nano-optical fabrication: For instance, optical near-field lithography, utilizing the near-field interactions between photomasks and photoresists, has already been developed [9]. Furthermore, non-adiabatic processes, meaning that optical near-field interactions activate conventionally light-insensitive materials, are additional novelties that are available in fabricating nano-structures by nanophotonics [10]. Optical near-field etching is another example of probe-free nanophotonics; here, photochemical reactions are selectively excited in regions where optical near-fields are generated. This approach has been successfully demonstrated in flattening the rough surfaces of optical elements [11].

To implement innovative nanometric optical processing systems as probe-free nanophotonic systems, it is necessary to exploit the unique attributes of nanometer-scale optical near-field interactions in a completely parallel fashion. In this review, we highlight the basic concepts necessary for 2D parallel processing of light–matter interactions on the nanometer-scale instead of the conventional 1D scanning method, based on our recent achievements. Those techniques allow us to observe optical far-field signals that originate from the effects occurring at the nanometer scale. The concepts and principles are numerically and experimentally verified within several frameworks of particular applications realized by precisely designing and fabricating nanostructures. Additionally, the concepts and some demonstrations of hierarchic applications of nanophotonics, based on the hierarchy between optical near- and far-fields, are described as one of the practical applications of the optical near-field interactions induced by such designed nanostructures.

2.2 Probe-Free Nanophotonic Systems

Nanometric optical processing systems, whose features include high integration density, low-energy operation, and innovative functions, are practical embodiments of the qualitative innovations offered by nanophotonics. Several fundamental proposals have been developed for their implementation; for instance, nanophotonic devices that consist of nanometric logic gates, switches, and wiring based on optical near-field interactions, as well as several related technologies, have been developed [12–15]. However, integration technologies are still required to implement actual processing systems based on existing nanophotonic devices. Moreover, regarding the interfaces between those nanometric systems and their associated surrounding systems, existing concepts that apply to conventional optical systems are not entirely applicable since the physical basis is completely different between conventional propagating light and optical near-fields. Hence, appropriate interfacing concepts and techniques that are well-matched with the features of nanophotonics are strongly demanded. From such a viewpoint, optical near-field interactions and their characteristic behaviors *autonomy* and *robustness*, which are revealed only at the nanometric scale, ought to be focused on as key features for implementing nanometric information processing. For example, energy transfer in an optical near-field channel based on nanometric quantum dots that autonomously select an appropriate channel has been demonstrated to work with few problems, although the functions of some quantum dots have been lost [16]. In other types of applications, in the fabrication phase of a nanometric device, the most appropriate structure serving as the optical near-field source has been autonomously formed via induced optical near-field interactions with the assistance of suitable laser irradiation parameters, such as intensity, polarization, etc. [17].

On the other hand, to realize more advanced computing systems, in terms of processing performance, development of parallel processing from both system architecture and algorithm aspects has been the general idea since the first prototype computing systems were invented. Parallel computing is defined as a processing system that utilizes multiple processors at the same time to rapidly execute a single program [18]. In general, to ideally implement such processing, it is necessary to realize spatially parallel operations in a two-dimensionally expanded information space, and this is one of the motivations that has been actively researched in *classical* optical computing, utilizing the parallelism and higher velocity of light [19]. Although the original meaning of optical computing has been lost in a certain sense, the basic concept can be usefully applied to the implementation of nanometric optical processing systems. In this case, the autonomy and the robustness of optical near-field interactions are quite appealing. Once the concepts and techniques of nanometric parallel processing have been successfully established, they can be directly expanded to macro-scale applications, which is expected to dramatically expand the scope of application of nanophotonics.

Figure 2.1a, b show schematic diagrams that conceptually illustrate two kinds of representative *nanometric* parallel processing systems. The system shown in

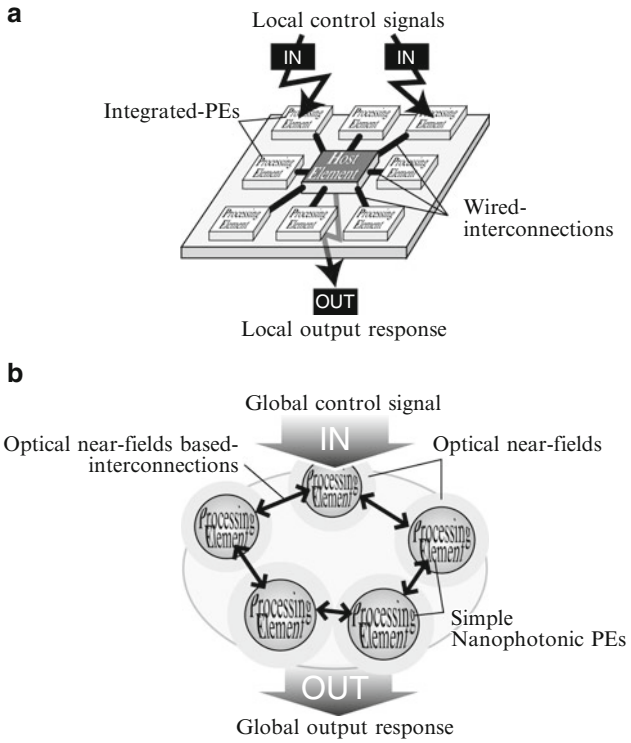

Fig. 2.1 Basic concept of nanometric parallel processing systems (**a**) based on existing processing protocol and (**b**) utilizing nanophotonics as a probe-free nanophotonic system

Fig. 2.1a is operated by the host element located at the center. All of the processing elements around the center are precisely controlled by the host element. In the case of such nanometric processing with existing techniques, however, this kind of centralized architecture is difficult to apply since it is technically difficult to precisely align a number of nanometric components and to precisely and flexibly interconnect each component. On the other hand, the system schematically shown in Fig. 2.1b is proposed for the implementation of nanometric optical processing systems. The processing elements are connected in an autonomous manner via optical near-field interactions, and the global control signals do not specify the detailed operations of each component. The local interactions between components in the system, involving optical near-field interactions, bring about certain behavior in the system as a whole.

To realize the parallel processing system shown in Fig. 2.1b, it is necessary to retrieve the information located at the nanometer scale and expose it at the submicrometer scale so that the outputs of the system are obtainable in the optical far-field. For this purpose, here we propose two fundamental techniques: one is

the *macro-scale observation* of optical near-field interactions, and the other is the *magnified-transcription* of the optical near-field [20]. These techniques eliminate 1D scanning processes; in other words, probe-free nanophotonics is accomplished.

2.3 Nanophotonic Matching as Macro-Scale Observation

2.3.1 Macro-Scale Observation

As we described in Sect. 2.2, to control and observe a spatially expanded nanometric field using existing optical techniques, it must be one-dimensionally scanned. Although it does not matter for measurement or fabrication, the loss of synchronism is a crucial disadvantage for use as an actual information processing system. To find a solution to this problem, in our idea, multiple nanometric processing components are aligned in a micrometer-scale unit, and the I/Os at each unit consist of parallel control with *broadcast* of the input signal and bundled retrieval with *narrowcast* of the output signals. The components are assigned individual functions and execute their functions based on holistic instructions from an external environment and interactions between neighboring components. An analogy of this concept can be seen in common biological systems, such as the human body, which is one of the most ideal and effectively constructed information processing systems.

This idea is one of the most effective solutions to utilize multiple nanometric components without impairing the spatial parallelism or the superior speed of optical signals. The key to this idea is how to determine the arrangement of nanometric components that generates the intended optical near-field interactions. This can be achieved by precisely designing and fabricating nanostructures, such as shapes, layouts, compositions, and so on, that can induce arbitrary optical near-field interactions [21, 22]. Moreover, protocols for the broadcast control and the narrowcast retrieval must be appropriately defined.

2.3.2 Quadrupole–Dipole Transform

There are several physical implementation methods that can achieve such a transform using optical near-field interactions. One is based on optical excitation transfer between quantum dots via optical near-field interactions [23, 24]. For instance, assume two cubic quantum dots whose side lengths L are a and $\sqrt{2}a$, which we call $\mathrm{QD_A}$ and $\mathrm{QD_B}$, respectively.

Suppose that the energy eigenvalues for the quantized exciton energy level specified by quantum numbers (n_x, n_y, n_z) in a QD with side length L are given by

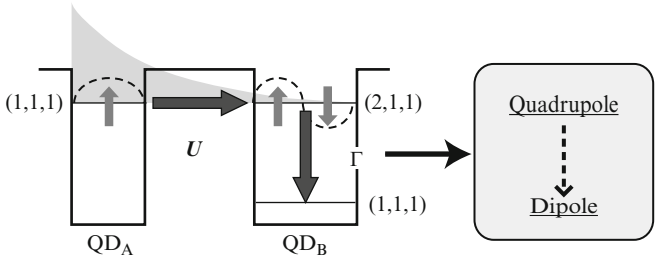

Fig. 2.2 A quadrupole–dipole transform in the transition from the (2,1,1) level to the (1,1,1) level in QD_B. Such a transform is unachievable without the optical near-field interactions between QD_A and QD_B, which allow the (2,1,1) level in QD_B to be populated with excitons

$$E_{(n_x,n_y,n_z)} = E_B + \frac{\hbar^2\pi^2}{2ML^2}(n_x^2 + n_y^2 + n_z^2), \tag{2.1}$$

where E_B is the energy of the exciton in a bulk crystal, and M is the effective mass of the exciton. As shown in Fig. 2.2, there exists a resonance between the level of quantum number (1,1,1) for QD_A and that of quantum number (2,1,1) for QD_B. There is an optical near-field interaction, denoted by U, due to the steep gradient of the electric field in the vicinity of QD_A. Therefore, excitons in QD_A can transfer to the (2,1,1) level in QD_B. Note that such a transfer is prohibited if based on propagating light since the (2,1,1) level in QD_B contains an even number. In other words, near-field excitation can populate even the antisymmetric states of the coupled system, or the dark states, whereas far-field excitation can excite only the symmetric states, that is, the bright states [23]. In QD_B, the exciton relaxes to the lower energy sublevel (1,1,1) with a time constant a, which is faster than the near-field interaction. Therefore, the exciton finally transfers to the (1,1,1) level of QD_B. Also, this sublevel relaxation, or energy dissipation, that occurs at QD_B guarantees unidirectional energy flow from QD_A to QD_B. Here, we can find a quadrupole–dipole transform in the transition from the (2,1,1) level to the (1,1,1) level in QD_B, and such a transform is unachievable without the optical near-field interactions between QD_A and QD_B, which allow the (2,1,1) level in QD_B to be populated with excitons [14,25].

Another way of realizing a quadrupole–dipole transform is based on shape-engineered metal nanostructures, which are the principal concern of this paper. In previous work, we have numerically shown that two metal nanostructures can be designed to exhibit far-field radiation only when their shapes are appropriately configured and when they are closely stacked [21,26]. As discussed in detail below, here we can also find a quadrupole–dipole transform in the sense that individual single planes of the nanostructures work as quadrupoles, but they behave as a dipole when two planes of the nanostructures are appropriately configured. In the following, we discuss the shape design of the nanostructures and their experimental fabrication, and we describe optical characterization of the quadrupole–dipole transform.

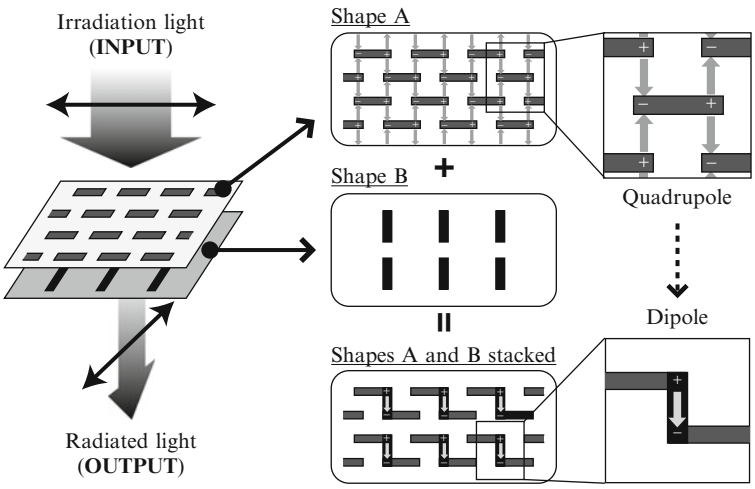

Fig. 2.3 Schematic diagram of nanophotonic matching system. The function is based on a quadrupole–dipole transform via optical near-field interactions, and it is achieved through shape-engineered nanostructures and their associated optical near-field interactions

2.3.3 Nanophotonic Matching

We demonstrate that two nanostructures can be designed to exhibit far-field radiation only under the condition that the shapes of the two structures are appropriately combined and closely stacked. This function of the two nanostructures can be regarded effectively as a *lock* and a *key*, because only an appropriate combination of a lock and a key yields an output signal, namely, far-field radiation [21, 27]. Figure 2.3 shows a schematic diagram of the nanophotonic matching system based on this function.

We design two nanostructural patterns, called *Shape A* and *Shape B* hereafter, to effectively induce a quadrupole–dipole transform via optical near-field interactions. Shape A and Shape B are designed as rectangular units on the xy-plane with constant intervals horizontally (along the x-axis) and vertically (along the y-axis), respectively. When Shape A is irradiated with x-polarized light, surface charges are concentrated at the horizontal edges of each of the rectangular units. The relative phase difference of the oscillating charges between the horizontal edges is π, which is schematically represented by $+$ and $-$ marks in Fig. 2.3. Now, note the y-component of the far-field radiation from Shape A, which is associated with the charge distributions induced in the rectangle. Drawing arrows from the $+$ marks to the $-$ marks along the y-axis, we find that adjacent arrows are always directed oppositely, indicating that the y-component of the far-field radiation is externally small. In other words, Shape A behaves as a quadrupole with regard to the y-component of the far-field radiation. It should also be noted that near-field components exist in the vicinity of the units in Shape A. With this fact in mind, we put the other metal nanostructure, Shape B, on top of Shape A. Through the optical near-fields

in the vicinity of Shape A, surface charges are induced on Shape B. What should be noted here is that the arrows connecting the + and − marks along the y-axis are now aligned in the same direction, and so the y-component of the far-field radiation appears; that is, the stacked structure of Shape A and Shape B behaves as a dipole. Also, Shape A and Shape B need to be closely located to invoke this effect since the optical near-field interactions between Shape A and Shape B are critical. In other words, a quadrupole–dipole transform is achieved through shape-engineered nanostructures and their associated optical near-field interactions.

To verify this quadrupole–dipole transform mechanism brought about by shape-engineered nanostructures, we numerically calculated the surface charge distributions induced in the nanostructures and their associated far-field radiation based on a finite-difference time-domain (FDTD) electromagnetic simulator (*Poynting for Optics*, a product of Fujitsu, Japan). Figure 2.4a schematically represents the design

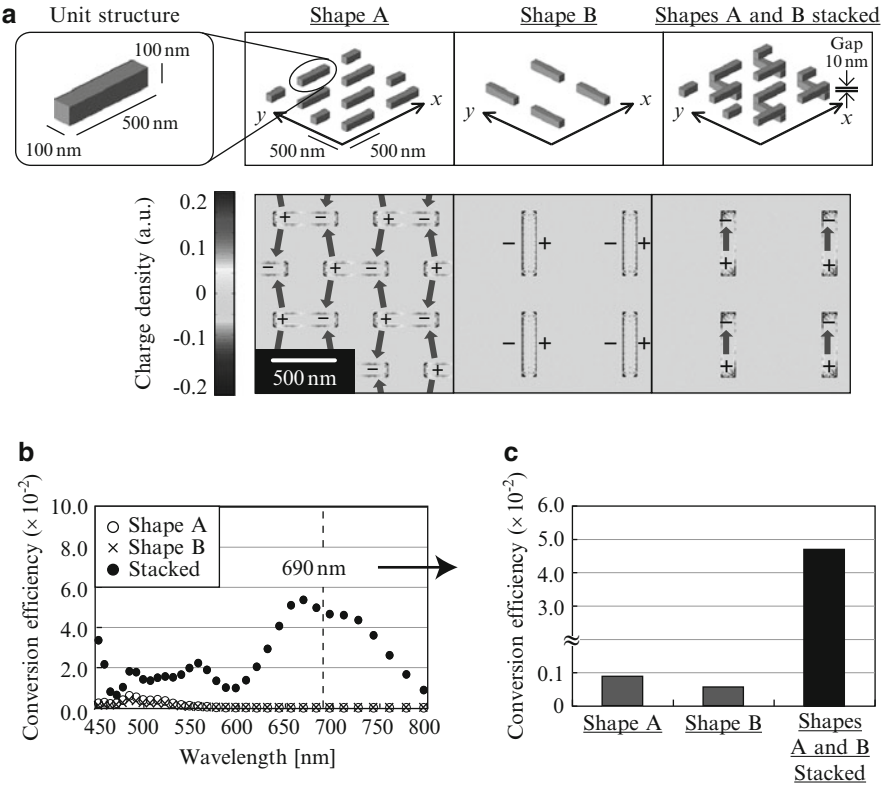

Fig. 2.4 (**a**) Specifications of the three types of nanostructures used in numerical evaluation of the conversion efficiency based on the FDTD method, and corresponding surface charge density distributions induced in each nanostructure. (1) Shape A only, (2) Shape B only, and (3) a stacked structure of Shapes A and B. (**b**) Calculated performance figure of the quadrupole–dipole transform, namely, polarization conversion efficiency, with the three types of nanostructures. (**c**) Selective comparison at a wavelength of 690 nm

of (1) Shape A only, (2) Shape B only, and (3) a stacked structure of Shape A and Shape B, which consist of arrays of gold rectangular units. The length of each of the rectangular units is 500 nm, and the width and height are 100 nm. As the material, we assumed a Drude model of gold with a refractive index of 0.16 and an extinction ratio of 3.8 at a wavelength of 688 nm [28].

When irradiating these three structures with continuous-wave x-polarized input light at a wavelength of 690 nm, the lower figures in Fig. 2.4a show the induced surface charge density distributions (simply called surface charge hereafter) obtained by calculating the divergence of the electric fields. For the Shape A only structure (bottom-left in Fig. 2.4a), we can find a local maximum and local minimum of the surface charges, denoted by the + and − marks. When we draw arrows from the + marks to the − marks between adjacent rectangular units, as shown in Fig. 2.3, we can see that the arrows are always directed oppositely between the adjacent units, meaning that the Shape A only structure behaves as a quadrupole for the y-component of the far-field radiation. For the Shape B only structure (bottom-center in Fig. 2.4a), the charges are concentrated at the horizontal edges of each of the rectangular units, and there are no y-components that could contribute to the far-field radiation. The lower-right figure in Fig. 2.4a shows the surface charge distributions induced in Shape B when it is stacked on top of Shape A. We can clearly see that the charges are induced at the vertical edges of each of the rectangular units, and they are aligned in the same direction. In other words, a dipole arrangement is accomplished with respect to the y-component, leading to a drastic increase in the far-field radiation.

One of the performance figures of the quadrupole–dipole transform is

$$I_{\mathrm{conv}} = I_{y-\mathrm{OUT}} / I_{x-\mathrm{IN}}, \tag{2.2}$$

where $I_{x-\mathrm{IN}}$ and $I_{y-\mathrm{OUT}}$ represent the intensities of the x-component of the incident light and the y-component of the radiated light, respectively. When we radiate a short optical pulse having a differential Gaussian form whose width is 0.9 fs, corresponding to a bandwidth of around 200–1,300 THz, Figure 2.4b shows I_{conv} as a function of the input light wavelength, and Fig. 2.4c compares I_{conv} specifically at 690 nm. I_{conv} appears strongly with the stacked structure of Shapes A and B, whereas it exhibits a small value with Shape A only and Shape B only. We can clearly observe the quadrupole–dipole transform in the optical near-fields as the change of I_{conv} in the optical far-fields.

2.3.4 Experimental Demonstration

In the experiments, we fabricated structures consisting of Shape A only, Shape B only, and Shape A and Shape B stacked. Although the stacked structure should ideally be formed by combining the individual single layer structures, in the following experiment, the stacked structure was integrated in a single sample as a

solid two-layer structure to avoid experimental difficulty in precisely aligning the individual structures mechanically. The fabrication process was as follows.

1. Espacer 300Z and resist solution 2EP-520A were spin coated at a thickness of 350 nm on a sapphire substrate to be subjected to electron-beam (EB) lithography.
2. The first layer (Shape A) was fabricated by EB lithography, and an Au layer was vacuum-evaporate to a thickness of 100 nm.
3. The Espacer layer and EB resist layer (2EP-520A) were removed by lift-off with 2EP-A and acetone. Then an SiO_2 layer was sputtered to a thickness 200 nm to form a gap layer between the first and second layers.
4. The second layer (Shape B) was fabricated in a similar manner to the above processes.

Figure 2.5 schematically represents cross-sectional profiles of these fabrication processes, where (1) Shape A-only structures are fabricated in the first layer, (2) Shape B-only structures are fabricated in the second layer, and (3) stacked structures have Shapes A and B in the first and second layers, respectively. The lower

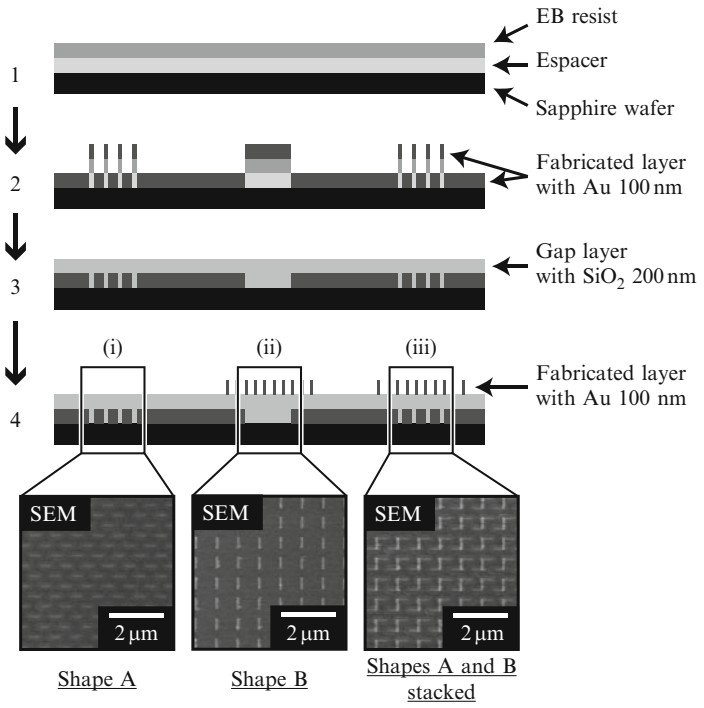

Fig. 2.5 Schematic diagram of the fabrication process of the two-layer nanostructure. The stacked structure was integrated in a single sample as a solid two-layer structure to avoid experimental difficulty in precisely aligning the individual structures mechanically

images in Fig. 2.5 also show scanning electron microscopy (SEM) images of fabricated samples of types (1), (2), and (3). Because the stacked structure was fabricated as a single sample, the gap between Shape A and Shape B was fixed at 200 nm.

The performance of the quadrupole–dipole transform, in terms of the polarization conversion efficiency I_{conv} given by (2.2), was experimentally evaluated by radiating x-polarized light on each of the areas (1), (2), and (3) and measuring the intensity of the y-component in the transmitted light. The light source was a laser diode with an operating wavelength of 690 nm. Two sets of Glan–Thompson prisms (extinction ratio 10^{-6}) were used to extract the x-component for the input light and to extract the y-component in the transmitted light. The intensity was measured by a lock-in controlled photodiode. The position of the sample was controlled by a stepping motor with a step size of 20 μm.

Figure 2.6a shows I_{conv} as a function of the position on the sample, where I_{conv} exhibited a larger value specifically in the areas where the stacked structure of Shapes A and B was located, which agrees well with the calculated result shown in Fig. 2.4c.

The conversion efficiency with the Shape B-only structure is slightly larger than that with the Shape A-only one, as shown in Fig. 2.6a, which exhibits opposite behavior from that obtained in the simulation shown in Fig. 2.4c. Also, the magnitude of the increase in conversion efficiency from the stacked structure of Shapes A and B is not so large compared with that predicted by the simulation in Fig. 2.4c. We attribute these effects mainly to the unintended inhomogeneity of the shapes and layout of the experimental devices, as indicated in the SEM images in Fig. 2.5. Slight rotational misalignment between the irradiated light and the device under study and other factors could also be involved.

Although I_{conv} was larger at the stacked structure, the signals fluctuated within the corresponding area. This was due to the variance of the misalignment between the first layer (Shape A) and the second layer (Shape B), as observed in the SEM images shown in Fig. 2.6b. From Fig. 2.6b, we can see that I_{conv} was larger when the misalignment between Shape A and Shape B was minimized. The variance of the misalignment was presumably due to drift effects in the lithography process during fabrication.

The alignment tolerances were further analyzed as shown below. From the SEM images in Fig. 2.6b, horizontal and vertical misalignments were respectively evaluated as Δx and Δy shown in Fig. 2.7a. Figure 2.7b, c respectively show I_{conv} as a function of the horizontal and vertical misalignments. Solid lines represent calculated results, and the left-hand axis and right-hand axis represent the conversion efficiency of the experimental and calculated results, respectively. Although the absolute values of the efficiency were different between the experiments and simulations, they showed similar dependence on the misalignment. If we define the alignment tolerance as the maximum misalignment that yields 10% of the maximum efficiency, the horizontal and vertical alignment tolerances are respectively estimated to be about 150 and 200 nm.

To analyze the gap dependency of the conversion efficiency, other samples were also fabricated. As shown in Fig. 2.7d, the thicknesses of the SiO_2 gap layer between

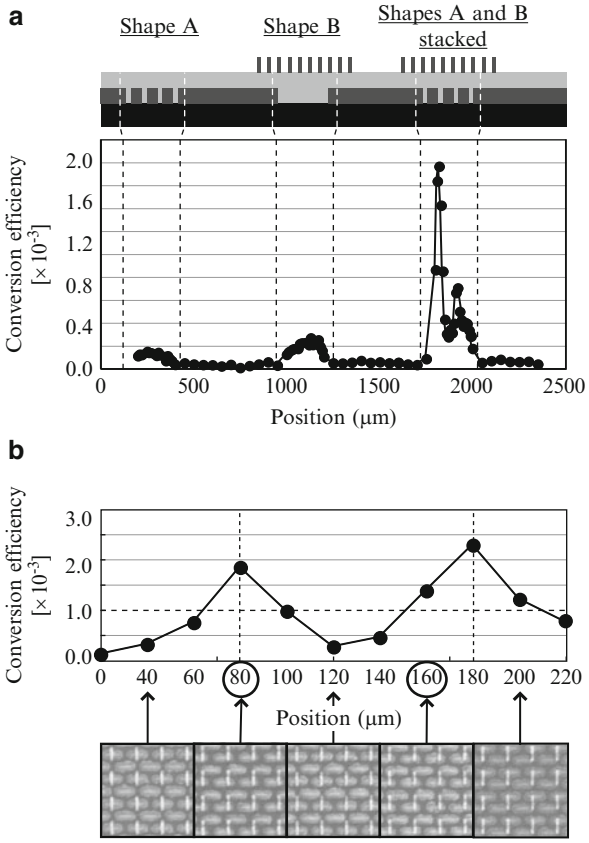

Fig. 2.6 (**a**) Measured conversion efficiency for the three types of nanostructures. Conversion efficiency was larger specifically in the areas where the stacked structure of Shapes A and B was located. (**b**) Conversion efficiency within the area of the stacked structure of Shapes A and B. SEM images are also shown corresponding to the evaluated position. Conversion efficiency was larger when the misalignment between Shape A and Shape B was minimized

the first and second layers were 143, 216, and 363 nm. As shown in Fig. 2.7e, the conversion efficiency decreased as the gap between the layers increased, which also validates the principle of the quadrupole–dipole transform that requires optical near-field interactions between closely arranged nanostructures.

2.3.5 Outlook

Here, we make a few remarks regarding the quadrupole–dipole transform demonstrated in this study. We can engineer many more degrees-of-freedom on the nanometer-scale while using far-field radiation for straightforward characterization.

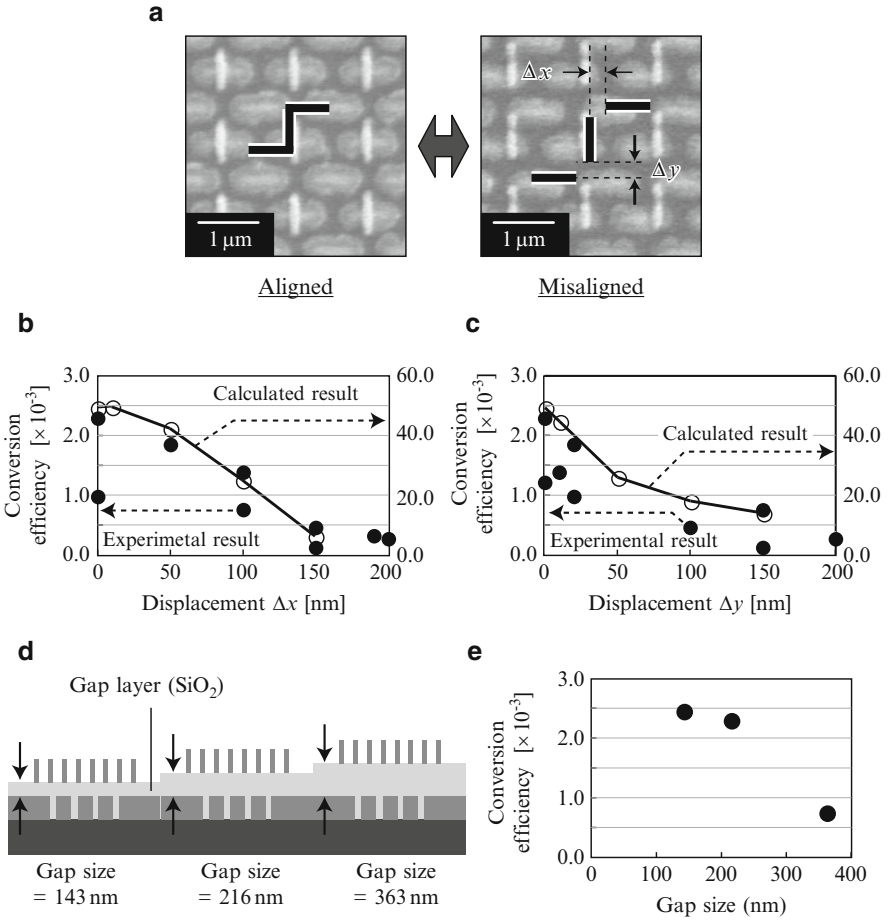

Fig. 2.7 (**a**) Horizontal and vertical misalignments between Shape A and Shape B denoted by Δx and Δy, and (**b**), (**c**), their relations to conversion efficiency. (**d**) Schematic cross-sectional profiles of samples with different gaps. The thickness of the SiO_2 gap layer between the first and second layers was set in three steps. (**e**) The conversion efficiency decreased as the gap increased. The result validates the principle of the quadrupole–dipole transform that requires optical near-field interactions between closely arranged nanostructures

For practical use, on the other hand, more precise fabrication of nanostructures and more precise alignment between the two layers are necessary. Optical near-field lithography would be one solution for the mass production of large-area nanostructures [29, 30]. As for alignment, use of micro electro mechanical systems (MEMS) technologies [31] would be one option to resolve the alignment difficulties.

From a system perspective, the quadrupole–dipole transform can be regarded as a kind of mutual authentication or certification function of two devices, meaning that the authentication of Device A (with Shape A) and Device B (with Shape

B) is achieved through the quadrupole–dipole transform. Because such fine nanostructures are difficult to falsify, the vulnerability of a security system based on this technology is expected to be extremely low.

Another relevant issue is to seek more general theories that account for the relationship between the shapes and layout of nanostructures and their associated hierarchical optical properties at the sub-wavelength scale [32]. Dependence on the internal structures of the materials could be exploited [22]. Also, the dependence on operating wavelength and other physical quantities [33] could be understood possibly in a unified manner. We will explore these issues in future work.

2.4 Nanophotonics-Induced Phase Transition as Magnified-Transcription

2.4.1 Magnified-Transcription of Optical Near-Fields

Here we describe *magnified-transcription* of optical near-fields, whereby their effects are spatially magnified so as to be detected in optical far-fields. Figure 2.8

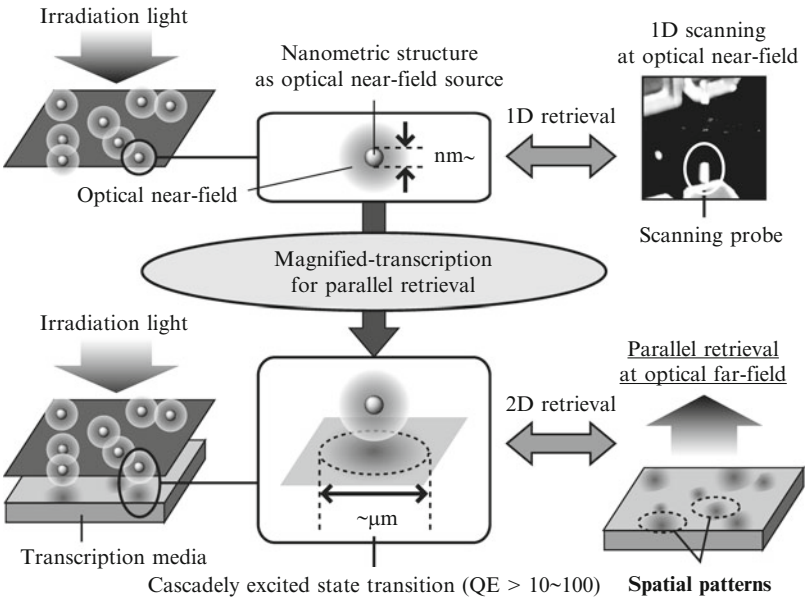

Fig. 2.8 Basic concept and fundamental process of optical parallel data retrieval based on the transcription of optical near-fields. Our fundamental idea is to spatially magnify the distribution of an optical near-field from the nanometric scale to the sub-micrometer scale in the resultant transcribed pattern so that it is observable in the optical far-field

shows a schematic diagram that represents the basic concept of parallel retrieval based on magnified-transcription.

Generally, the 2D distribution of optical near-fields in the vicinity of the surface of a nanostructure in response to far-field light irradiation can be measured by one-dimensional scanning of an optical near-field probe tip, as shown in the upper half of Fig. 2.8. The idea of the work presented here is to spatially magnify the distribution of optical near-fields so that their effects can be detected in optical far-fields, as schematically shown in the lower half of Fig. 2.8. In other words, we transcribe the optical near-field distribution to another layer with a certain magnification factor.

The process of transcription is crucial for the implementation of this concept, and it should originate from the physical attributes associated with the material used. In our proposal, it is necessary to spatially magnify an optical near-field from the nanometric scale to the sub-micrometer scale in the resultant transcribed pattern so that it is observable in the optical far-field. It turns out that the magnification factor in the transcription should be 10–100. Once the spatial pattern is detectable in the far-field, various concepts and technologies common in parallel processing will be applicable, such as fully parallel processing [34], so-called smart pixels, or parallel processing VLSI devices [35].

Several properties of optical near-field sources and transcription media can affect the transcription of spatial patterns. Therefore, it can be said that our proposal retrieves not only the existence or nonexistence of optical near-fields, but also several of their characteristics, such as energy transfer [36] and hierarchy [37]. From this point of view, our proposal is fundamentally different from other recording and retrieving methods, including near-field holography [38], which is concerned only with structural changes in the media.

2.4.2 Photoinduced Phase Transition

A photoinduced phase transition has been observed in several cyano-bridged metal complexes [39]. They exhibit bistable electronic states at room temperature. The energy barrier between these bistable states maintains a photoproduced state even after photo-irradiation is terminated. Also, the state can easily be reset either via optical irradiation or temperature control. Moreover, typical phase transitions are excited in a cascaded manner, meaning that they exhibit high quantum efficiencies.

Concerning the applicability of these features of cyano-bridged metal complexes to the transcription discussed previously, we chose rubidium manganese hexacyanoferrate [40] as a suitable material for the transcription medium. Compounds in this series show a charge-transfer phase transition from Mn^{II} ($S = 5/2$)–NC–Fe^{III} ($S = 1/2$) as the high-temperature (HT) phase to Mn^{III}($S = 2$)–NC–Fe^{II} ($S = 0$) as the low-temperature (LT) phase [41, 42]. The LT phase is a ferromagnet because of ferromagnetic coupling between the Mn^{III} sites ($S = 2$ at the Mn^{III} sites), but the PI phase, which has a similar valence state to the HT phase, is an antiferromagnet ($S = 5/2$ at the Mn^{II} sites and $S = 1/2$ at the Fe^{III} sites). Figure 2.9a shows the

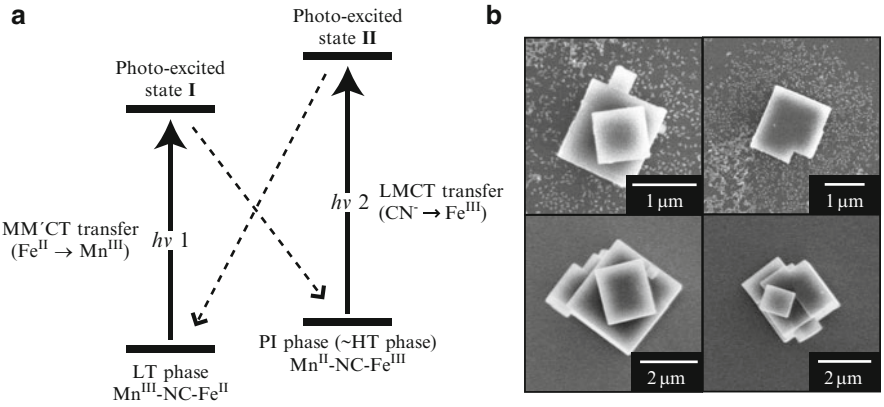

Fig. 2.9 (**a**) Schematic illustration of the visible-light-induced reversible photo-magnetic effect in rubidium manganese hexacyanoferrate. The charge-transfer phase transition is accompanied by a structural change from a cubic to a tetragonal structure due to Jahn–Teller distortion of Mn^{III}. (**b**) Observed SEM images of rubidium manganese hexacyanoferrate in the single crystal state

scheme for reversible charge transfer between the Mn^{III}–NC–Fe^{II} and Mn^{II}–NC–Fe^{III} states and the spin ordering for the LT and HT phases. This charge-transfer phase transition is accompanied by a structural change from a cubic to a tetragonal structure due to Jahn–Teller distortion of Mn^{III}. The maximum value of the quantum efficiency of this type of material has been found to be more than 30 [43].

In their typical optical characterizations, these materials are prepared in bulk form. However, for our transcription purposes, especially for the proof-of-principle experiments shown earlier, it is important to spatially distribute these materials so that we can evaluate the optical responses individually from each material. Therefore, in this paper, we mixed the materials with a dispersant based on an ester surfactant and dispersed the materials as single crystals in the solution. SEM images of single crystals are shown in Fig. 2.9b. The mean size of the single crystals was 1 μm (horizontal) × 1 μm (vertical) × 500 nm (thick).

2.4.3 Experimental Demonstrations

For experimental confirmation of the photoinduced phase transitions, we first measured microscopic optical responses of these single crystals on a sapphire substrate. Figure 2.10a shows the experimental setup. A green laser light source, emitting light at a wavelength of 532 nm with a power density of 45 mW cm^{-2}, was employed for inducing the phase transition from the LT phase to the HT phase [40]. The optical responses of the materials were obtained by a CCD camera (Apogee, AltaU260) before and after 60 min of irradiation. In the characterization processes, the materials were irradiated with a halogen lamp. We alternately inserted three types of band-pass filters to evaluate the spectral responses before and after irradiation. The

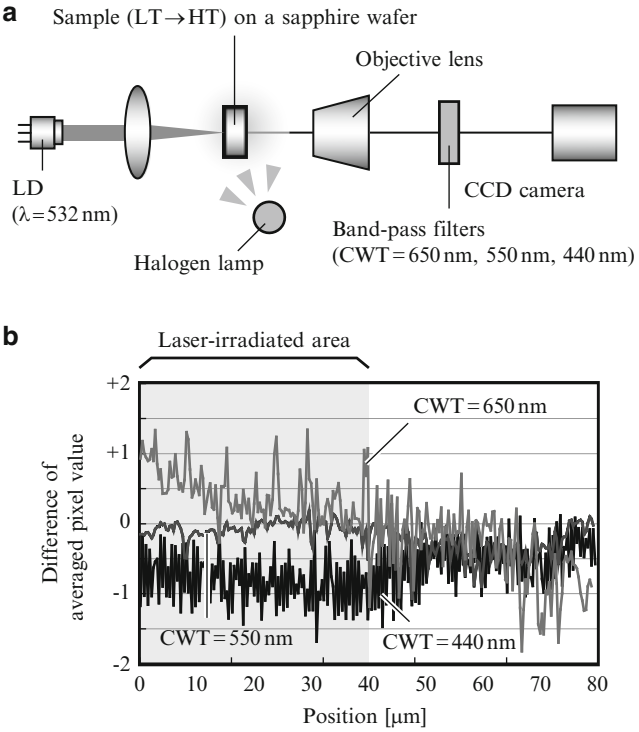

Fig. 2.10 (**a**) Schematic diagram of experimental setup for microspectroscopic detection of photoinduced phase transition. (**b**) Qualitative comparison of optical responses before and after irradiation. The change of the response at each wavelength, particularly at the wavelengths of 440 and 650 nm, in the irradiated area can be clearly observed, whereas the response remains unchanged in the unirradiated area

center wavelengths (CWTs) of the band-pass filters were 650, 550, and 440 nm, and the bandwidth of each filter was 20 nm.

To compare the differences in the images observed before and after irradiation, we calculated average pixel values in the horizontal direction and plotted each value along the vertical direction. Figure 2.10b shows the difference of the two results, before and after the irradiation. The shaded area in the profiles corresponds to the laser-irradiated area. We can clearly observe the change of the response at each wavelength, in particular at the wavelengths of 440 and 650 nm, in the irradiated area, whereas the responses remained unchanged in the unirradiated area. Such changes in the optical response correspond to changes of the dielectric constant found in previous research with bulk materials [40]. The results indicate that the phase transition of each single crystal could be successfully observed as a change of optical response at an appropriate wavelength.

To experimentally demonstrate the transcription of optical near-fields with the materials introduced previously, we employed an NOM setup, as shown in

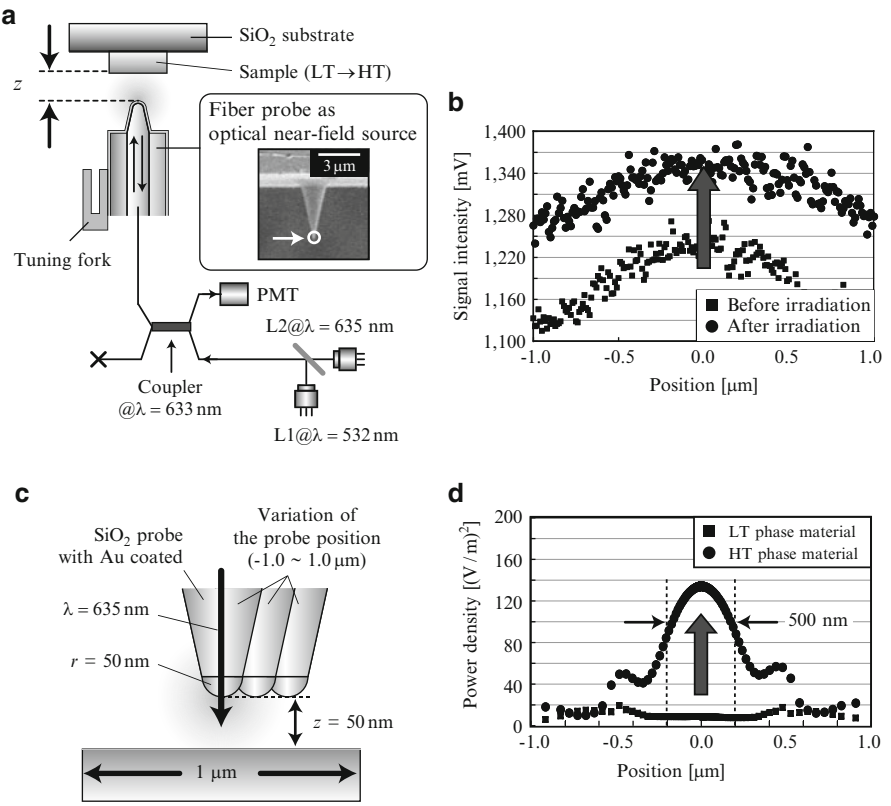

Fig. 2.11 (**a**) Schematic diagram of setup and (**b**) experimental results. (**c**) Schematic diagrams of calculation model for numerical validation of the transcription. (**d**) Numerical results. The signal intensity in the near-field is obviously increased by the irradiation

Fig. 2.11a. It was operated in an illumination-collection setup using an optical fiber probe with a tip radius of 50 nm. A change in the material was induced by laser light with a wavelength of 532 nm (L1). The optical responses from the samples were evaluated micro-spectroscopically using laser illumination with a wavelength of 635 nm (L2). The power of L2 was kept as low as possible to avoid any unintended transitions during observation. The fiber probe tip was positioned close to the target crystal only when L1 was radiated for inducing a transition in the sample. Scattered light from the sample was detected with a photomultiplier tube (PMT) via a fiber probe, and an optical image was constructed from the detected signal. The spatial distributions evaluated with L2 illumination were obtained before and after 15 min irradiation with L1. From these distributions, we compared the differences; Fig. 2.11b shows the results. The detected signal intensity in the near-fields was obviously increased by the L1 irradiation.

Furthermore, for numerical proof, we simulated the difference of the optical response between the LT- and HT-phase materials using FDTD based electromagnetic simulation. As shown in Fig. 2.11c, a nanometric scanning probe with a radius of 50 nm and an illumination light source with an operating wavelength of 635 nm were also included in the calculation model. The electric field intensity was evaluated at the surface of each material. The results are shown in Fig. 2.11d. The power density at the surface of the HT-phase material was much stronger than that of the LT-phase material. This change is similar to the NOM result in Fig. 2.11b. These results also indicate that the increase of scattered light intensity is attributed to the structural change in the rubidium manganese hexacyanoferrate material. From these results, we believe that we have successfully demonstrated the fundamental principle of the transcription of optical near-fields at the scale of a single crystal by using a nanometric fiber probe.

2.4.4 Outlook

We described the concept of transcription of optical near-field distributions for parallel nanophotonic processing, and we experimentally demonstrated its principle with nanometric light irradiation of a single crystal of a metal complex exhibiting a structural change that affects the change in its optical response. Specifically, rubidium manganese hexacyanoferrate was employed as the transcription medium, and we experimentally confirmed that the phenomenon could be induced on the scale of a single crystal. The transcription of optical near-fields that we demonstrated here will be one of the key techniques for implementing proposed parallel nanophotonics processing systems.

These process are valuable system-level functions for implementing nanometric processing systems. Further advances, including the introduction of postprocessing after the transcription and developing an original coding theorem that utilizes several features of nanophotonics, might yield highly integrated, real-time information processing at the scale of optical near-fields.

2.5 Nanophotonic Hierarchical Hologram

2.5.1 Background

Many anti-counterfeiting techniques have been proposed in the fields of security and product authenticity verification [44]. Optical techniques, which represent one kind of anti-counterfeiting, are well-established; for instance, confidential information can be hidden in any of the physical attributes of light, such as phase, wavelength, spatial frequency, or polarization [45–47]. For example, holography, which generates natural three-dimensional images, is the most common anti-counterfeiting technique [48]. In the case of a volume hologram, the surface of the hologram is

ingeniously designed into a complicated structure that diffracts incident light in a specific direction. A number of diffracted light beams can form an arbitrary three-dimensional image. Because these structures are generally recognized as being difficult to duplicate, holograms have been widely used in the anti-counterfeiting of bills, credit cards, etc. However, conventional anti-counterfeiting methods based on the physical appearance of holograms are less than 100% secure [49]. Although they provide ease of authentication, adding another security feature without causing any deterioration in the appearance is quite difficult.

Existing optical devices and systems operate based on several phenomena of *propagating* light. However, the performance is generally limited by the diffraction of light [50]. Reducing the physical scale beyond the scale of the optical wavelength is difficult. The critical dimension of a conventional hologram is also bounded by the diffraction limit, because the function of a conventional hologram is based on the diffraction of light.

However, with advances in nanophotonics, especially in systems utilizing optical near-field interactions, optical devices and systems can be designed at densities beyond those conventionally constrained by the diffraction limit of light [51]. Several nanophotonic device structures and operating principles based on optical near-field techniques have been proposed [1, 52]. Because several physical parameters of propagating light are not affected by nanometric structures, conventional optical responses in the far-field also are not affected by these structures. Essentially, this means that another functional hierarchical level in the optical near-field regime can be added to conventional optical devices and systems without any loss of the primary quality, such as reflectance, absorptance, refractive index, or diffraction efficiency. Here we focus on an embossed hologram as such a conventional optical device. We demonstrated our concept by utilizing a *nanophotonic hierarchical hologram* that works in both optical far- and near-fields [53].

Moreover, we propose embedding a *nanophotonic code*, which is physically a subwavelength-scale shape-engineered metal nanostructure, in the hierarchical hologram to implement a near-mode function [54]. The basic concept of the nanophotonic code and fabrication of a sample device are described. In particular, since our proposed approach involves embedding a nanophotonic code *within* the patterns of the hologram, which is basically composed of one-dimensional grating structures, it yields clear polarization dependence compared with the case where it is not embedded within the hologram or arrayed structures. There are also other benefits with the proposed approach: a major benefit is that we can fully utilize the existing industrial facilities and fabrication technologies that have been developed for conventional holograms, yet adding novel new functionalities to the hologram.

2.5.2 Basic Concept

A nanophotonic hierarchical hologram can be created by adding a nanometric structural change to a conventional embossed hologram. Figure 2.12 shows the basic composition of the hierarchical hologram.

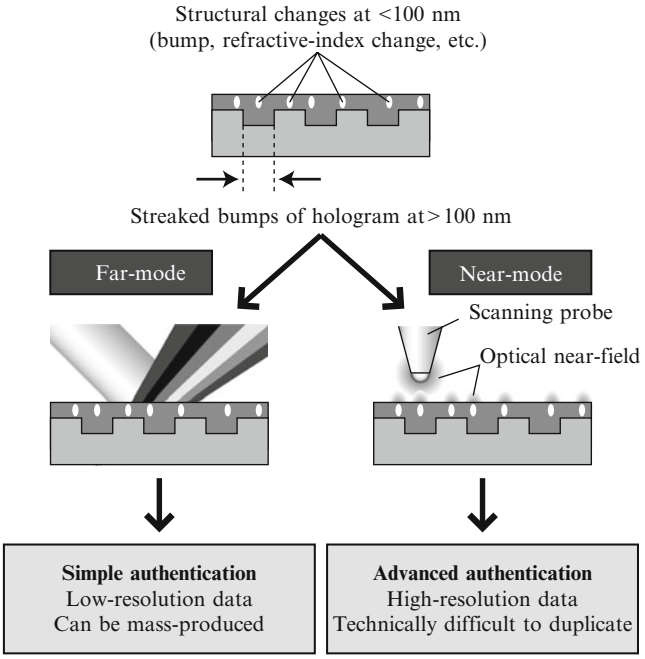

Fig. 2.12 Basic concept of functional hierarchy of hierarchical hologram. In principle, no interference occurs between the two layers, the far-mode and the near-mode

The physical scales of the nanometric structural changes and the elemental structures of the hologram are less than 100 nm and larger than 100 nm, respectively. In principle, a structural change occurring at the subwavelength scale does not affect the optical response functions, which are dominated by propagating light. Therefore, the visual aspect of the hologram is not affected by such a small structural change on the surface. Additional data can thus be written by engineering structural changes in the subwavelength regime so that they are only accessible via optical near-field interactions (we call such information retrieval *near-mode* retrieval) without having any influence on the optical responses obtained via the conventional far-field light (what we call *far-mode* retrieval). By applying this hierarchy, new functions can be added to conventional holograms.

In actual use of the hierarchical hologram, we needed to demonstrate that a nanometric structural change does not affect the optical response in the far-mode retrieval. At the same time, an obvious change must be observed in the near-mode retrieval. We used a commercially available embossed hologram in our demonstration as a sample for nanometric fabrication. Because an embossed hologram is easily mass produced at low cost, it is the type used in most security applications, such as credit cards and bank bills [55]. A 40-nm thick Au layer was coated on the sample surface of the hologram. Then, 40 holes (diameter 80 nm) were fabricated in a $10\,\mu m \times 10\,\mu m$ region using a focused ion beam (FIB) system. Upper

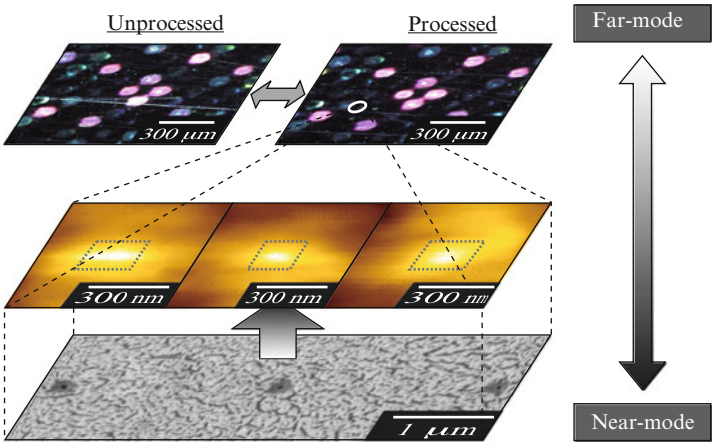

Fig. 2.13 (*Upper*) Observed CCD image of sample hologram. (*Middle*) Magnified image of processed hologram and (*Lower*) corresponding optical response observed with an NOM

images in Fig. 2.13 show optical microscope images of the unprocessed hologram and processed hologram, respectively, which are optical responses of the hierarchical hologram during the far-mode retrieval. The middle images in Fig. 2.13 show an SEM image of three nanometric holes that were fabricated on the processed-hologram. The diameter of each hole was less than 100 nm, and some structural changes were observed on the rim of each hole. No difference was evident in a comparison between the unprocessed hologram and the processed hologram. The compared results indicate the independence of the far-mode retrieval from nanometric fabrication of the hierarchical hologram.

Optical responses obtained in near-mode retrieval were detected using an NOM, which was operated in an illumination-collection mode with a near-field probe having a tip with a radius of curvature of 5 nm. The light source used was a laser diode (LD) with an operating wavelength of 785 nm, and scattered light was detected by a PMT. Magnified SEM images of each hole, that is, the optical responses during the near-mode retrieval, are shown in the lower images in Fig. 2.13. Evident optical responses were observed, which were attributed to an optical near-field generated at the rim of each hole.

The experimental results in Fig. 2.13 show that nanometric fabricated structures do not affect the far-mode observations, but they evidently affect the near-mode observations. These results indicate that the conventional functions of a hologram in the far-field were not adversely affected by adding another functional layer in the near-field. Next, we replaced the embedded hologram with a diffraction grating for quantitative evaluation of the independence between the nanometric fabricated structures and far-mode observation. After fabricating nanometric holes on the surface of the grating, we measured the diffraction efficiency and compared the efficiency with that of a grating with no holes. Figure 2.14a shows a 40-nm thick Au layer that was coated on the surface of the grating (600 lines/mm) and 25 nanometric

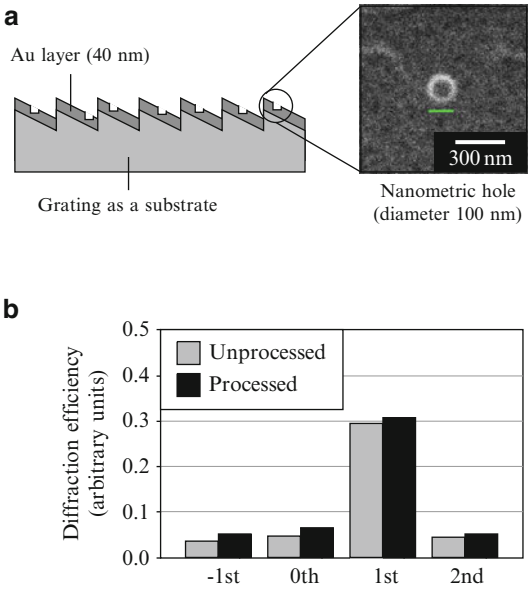

Fig. 2.14 (**a**) Composition of processed grating, and magnified SEM image of nanometric fabricated structure. (**b**) Diffraction efficiencies of unprocessed and processed gratings

holes ($\phi 100\,\text{nm}$) that were fabricated at $100\,\mu\text{m}$ pitch with an FIB system. The processed region was illuminated by the light from the LD ($\lambda = 532\,\text{nm}$), and the diffracted light intensity was measured. Figure 2.14b shows the experimental results. For example, the first-order diffraction intensities of the processed and unprocessed gratings were 30.9% and 29.6%, respectively, showing a relative difference of only about 10%. No large differences were evident in the other diffraction orders either. This means that the nanometric fabricated structure did not have a large effect on the optical devices.

2.5.3 Nanophotonic Code

Our nanophotonic code is defined by induced optical near-fields, which are generated by irradiating a nanometric structure with light. An optical near-field is a non-propagating light field generated in a space extremely close to the surface of a nanometric structure [36]. Because the light distribution depends on several parameters of the structure and the retrieval setup, various types of coding can be considered. Moreover, several novel features of nanophotonics, such as energy transfer [23] and hierarchy [37], may be exploited.

As shown in Fig. 2.15, we created a sample device to experimentally demonstrate the retrieval of a nanophotonic code within an embossed hologram. The entire device structure, whose size was $15\,\text{mm} \times 20\,\text{mm}$, was fabricated by electron-beam lithography on an Si substrate, followed by sputtering a 50 nm-thick Au layer, as schematically shown in the cross-sectional profile in Fig. 2.15b.

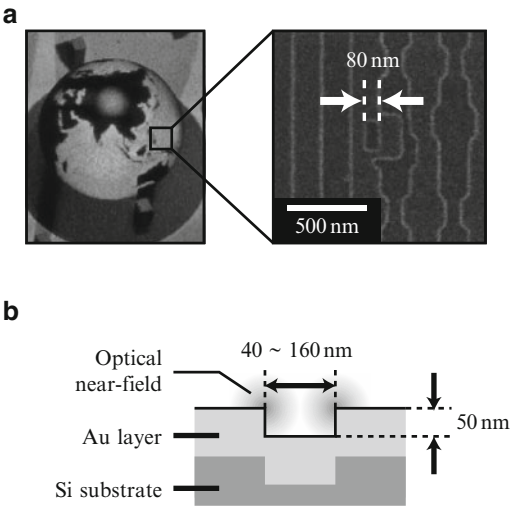

Fig. 2.15 (**a**) Fabrication of a nanometric structure as a nanophotonic code within the embossed structure of Virtuagram®, and SEM images of various designed patterns serving as nanophotonic codes. (**b**) Schematic diagram of fabricated sample device

As indicated in the left-hand side of Fig. 2.15a, we could observe a three-dimensional image of the earth from the device. More specifically, our prototype device was essentially based on the design of *Virtuagram*®, developed by Dai Nippon Printing Co., Ltd., Japan, which is a high-definition computer-generated hologram composed of binary-level one-dimensional modulated gratings, as shown in Fig. 2.15a. Within the device, we slightly modified the shape of the structure so that near-mode information was accessible only via optical near-field interactions. As shown in Fig. 2.15a, square- or rectangle-shaped structures, whose associated optical near-fields correspond to the near-mode information, were embedded in the original hologram structures. We call such embedded nanostructures *nanophotonic codes*. The unit size of the nanophotonic codes ranged from 40 to 160 nm.

Note that the original hologram was composed of arrays of one-dimensional grid structures, spanning along the vertical direction in Fig. 2.15a. To embed the nanophotonic codes, the grid structures were partially modified to implement the nanophotonic codes. Nevertheless, the grid structures remained topologically continuously connected along the vertical direction. On the other hand, the nanophotonic codes were always isolated from the original grid structures. Those geometrical characteristics produce interesting polarization dependence, which is discussed in detail in Sect. 2.5.4.

2.5.4 Numerical Evaluations

First, electric fields at the surface of nanometric structures were numerically calculated by the FDTD method. As shown in Fig. 2.16a, d, two types of calculation models were created to examine polarization dependencies in retrieving the

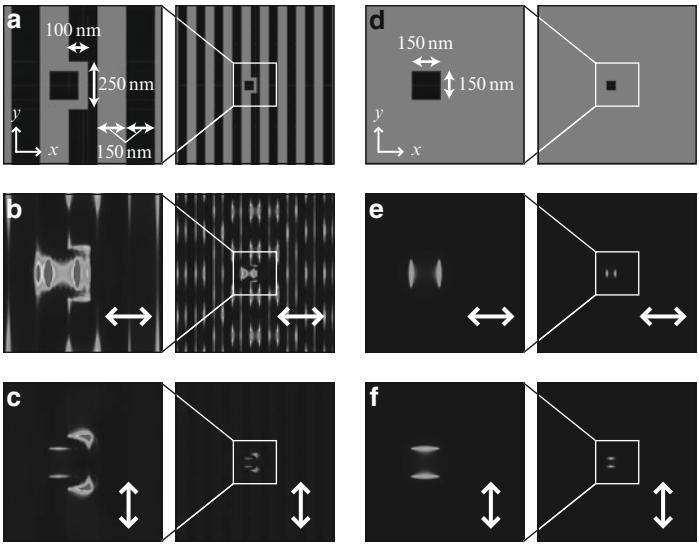

Fig. 2.16 (**a**) Calculation model of embedded nanophotonic code with environmental structures and calculated intensity distribution of electric field produced by (**b**) *x*-polarized input light and (**c**) *y*-polarized input light. (**d**) Calculation model of isolated nanophotonic code and calculated intensity distribution of electric field produced by (**e**) *x*-polarized input light and (**f**) *y*-polarized input light

nanophotonic code. The nanophotonic code was represented by a square-shaped Au structure whose side length was 150 nm and whose depth was 100 nm, shown near the center in Fig. 2.16a, d.

As shown in Fig. 2.16a, the square-shaped structure was embedded in a periodic one-dimensional wire-grid structure, whose pitch was 150 nm, which models the typical structure of an embossed hologram. As shown in Fig. 2.16d, on the other hand, the square-shaped structure, whose size was the same as that in Fig. 2.16a, was not provided with any grid structure. By comparing those two cases, we can evaluate the effect of the environmental structures around the nanophotonic code. Also, we chose the square-shaped structure that is isotropic in both the *x* and *y* directions to clearly evaluate the effects of environmental structures and ignore the polarization dependency originating in the structure of the nanophotonic code itself. Periodic-conditioned computational boundaries were located 1.5 μm away from the center of the square-shaped structure. The wavelength was set to 785 nm.

Figure 2.16b, e, c, f show the electric field intensity distribution on the surface of the structure assuming *x*-polarized and *y*-polarized input light irradiation, respectively. We then investigated how the environmental structures affected the electric fields in the vicinity of the nanophotonic code and the influence of input light polarization. For such purposes, we first evaluated the average electric field intensity in the area of the nanophotonic code, denoted by $\langle I \rangle_{\text{signal}}$, and that in the area including the surrounding areas, denoted by $\langle I \rangle_{\text{env}}$. More specifically, $\langle I \rangle_{\text{signal}}$ represents the

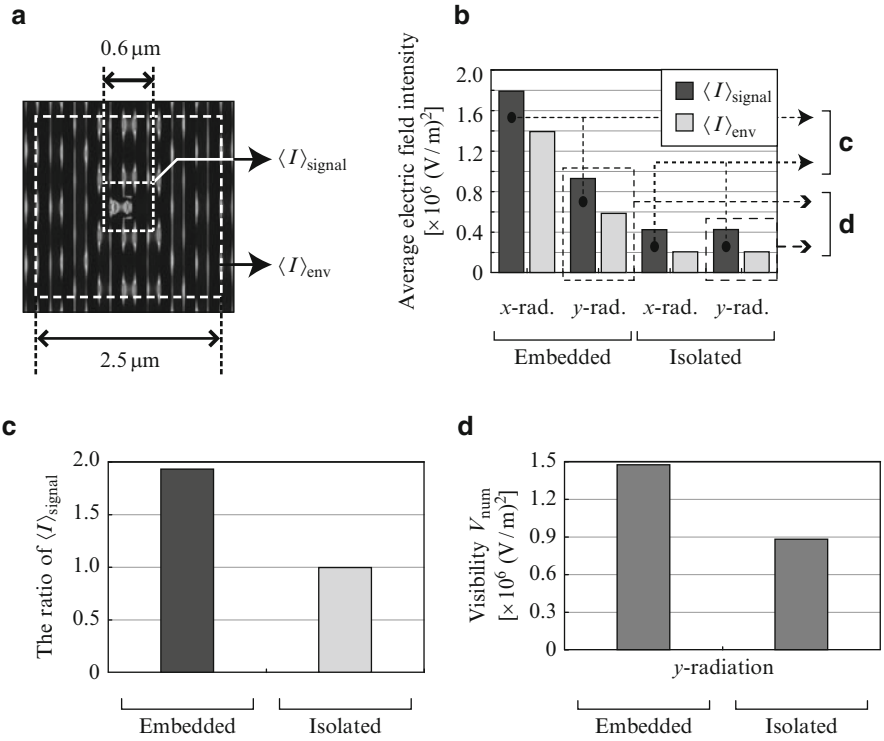

Fig. 2.17 (**a**) Schematic diagram explaining definition of average electric field intensity $\langle I \rangle_{\text{signal}}$ and $\langle I \rangle_{\text{env}}$, and (**b**) their graphical representations in each calculation model. Evident polarization dependency was exhibited in the case of the nanometric code embedded in environmental structures. (**c**) The ratio of $\langle I \rangle_{\text{signal}}$ with *x*-polarized input light to that with *y*-polarized input light for the embedded and isolated structures. (**d**) Numerical visibility V_{num} in two types of models with *y*-polarized input light. The result indicates that the visibility of the nanophotonic code was greatly enhanced by embedding it in the environmental structure

average electric field intensity in the $0.6\,\mu\text{m} \times 0.6\,\mu\text{m}$ area covering the nanophotonic code, as shown by the dotted square in Fig. 2.17a, whereas $\langle I \rangle_{\text{env}}$ indicates that in the $2.5\,\mu\text{m} \times 2.5\,\mu\text{m}$ area marked by the dashed square in Fig. 2.17a. Figure 2.17b summarizes the calculated $\langle I \rangle_{\text{signal}}$ and $\langle I \rangle_{\text{env}}$, respectively shown by the left and right bars.

We first investigated the polarization dependencies. In the case of the nanophotonic code embedded in environmental periodic structures, evident polarization dependency was observed for both $\langle I \rangle_{\text{signal}}$ and $\langle I \rangle_{\text{env}}$. For example, $\langle I \rangle_{\text{signal}}$ with *x*-polarized input light was about two times larger than $\langle I \rangle_{\text{signal}}$ with *y*-polarized input light. On the other hand, the isolated nanophotonic code did not show any polarization dependency. Figure 2.17c compares the ratio of $\langle I \rangle_{\text{signal}}$ with *x*-polarized input light to that with *y*-polarized input light for the embedded and isolated structures.

Second, from the viewpoint of facilitating recognition of the nanophotonic code embedded in the hologram, it is important to obtain a kind of higher *visibility* for the signals associated with the nanophotonic codes. To evaluate such visibility, here we define a figure-of-merit V_{num} as

$$V_{\mathrm{num}} = \frac{\langle I \rangle_{\mathrm{signal}}}{\langle I \rangle_{\mathrm{env}}} \times \langle I \rangle_{\mathrm{signal}}, \tag{2.3}$$

which yields a higher value with higher contrast with respect to $\langle I \rangle_{\mathrm{signal}}$ and $\langle I \rangle_{\mathrm{env}}$ (indicated by the term $\langle I \rangle_{\mathrm{signal}}/\langle I \rangle_{\mathrm{env}}$) and with higher signal intensity (indicated by $\langle I \rangle_{\mathrm{signal}}$). Figure 2.17d shows the calculated V_{num} in the case of *y*-polarized light input to the two types of models. The result indicates that the nanophotonic code embedded in the environmental structure is superior to that of the isolated code, in terms of the visibility defined by (2.3).

We consider that such a polarization dependency and the visibility of nanophotonic codes are based on the environmental grid structures that span along the vertical direction. The input light induces oscillating surface charge distributions due to coupling between the light and electrons in the metal. In the present case, the *y*-polarized input light induces surface charges along the vertical grids; since the grid structure continuously exists along the *y*-direction, there is no chance for the charges to be concentrated. However, in the area of the embedded nanophotonic code, we can find structural discontinuity in the grid; this results in higher charge concentrations at the edges of the embedded nanophotonic code.

On the other hand, the *x*-polarized input light sees structural discontinuity along the horizontal direction due to the vertical grid structures, as well as in the areas of the nanophotonic codes. It turns out that charge concentrations occur not only in the edges of the nanophotonic codes but also at other horizontal edges of the environmental grid structures. In contrast to these nanophotonic codes embedded in holograms, for the isolated square-shaped nanophotonic codes, both *x*- and *y*-polarized input light have equal effects on the nanostructures.

These mechanisms indicate that such nanophotonic codes embedded in holograms could also exploit these polarization and structural dependences, not only for retrieving near-mode information via optical near-field interactions. For instance, we could facilitate near-mode information retrieval using suitable input light polarization and environmental structures.

2.5.5 Experimental Demonstration

In the experimental demonstration, optical responses during near-mode observation were detected using an NOM. A schematic diagram of the detecting setup is shown in Fig. 2.18a, in which the NOM was operated in an illumination-collection mode with a near-field probe having a tip with a radius of curvature of 5 nm. The fiber probe was connected to a tuning fork. Its position was finely regulated by sensing a shear force with the tuning fork, which was fed back to a piezoelectric actuator. The

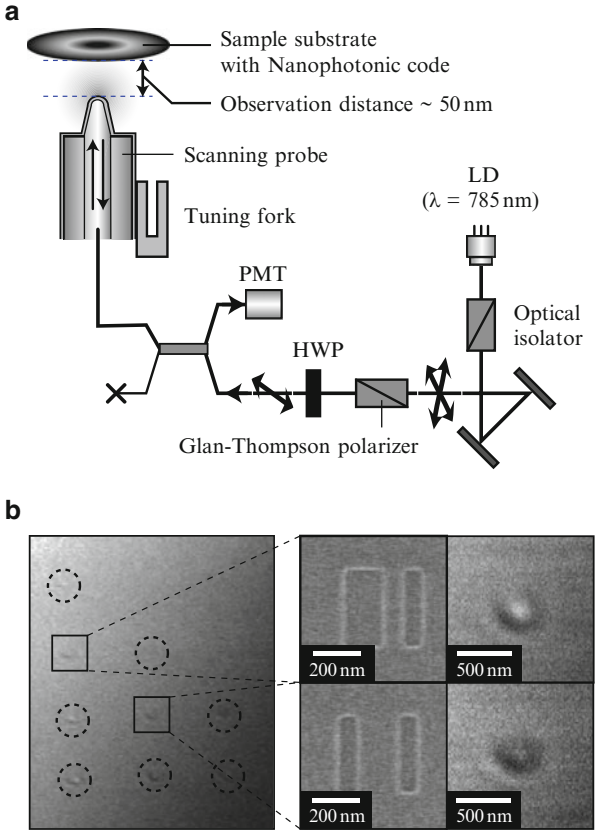

Fig. 2.18 (**a**) Schematic diagram of the experimental setup for retrieving a nanophotonic code, and (**b**) basic retrieval results

observation distance between the tip of the probe and the sample device was set at less than 50 nm. The light source used was an LD with an operating wavelength of 785 nm, and scattered light was detected with a PMT. A Glan–Thompson polarizer (extinction ratio 10^{-6}) selected only linearly polarized light as the radiation source, and a half-wave plate (HWP) rotated the polarization.

Figure 2.18b summarizes the experimental results obtained in retrieving nanophotonic codes which were *not* embedded in the hologram. In this demonstration, different shapes of nanophotonic codes were formed at the positions marked by the dashed circles in Fig. 2.5b. For the first step of our demonstration, the device was irradiated with randomly polarized light by removing the polarizer from the experimental setup. Clear near-field optical distributions that depended on the structures of the nanophotonic codes were obtained.

Figures 2.19 and 2.20 show other retrieved results of nanophotonic codes that were embedded in the hologram and *not* embedded in the hologram, respectively,

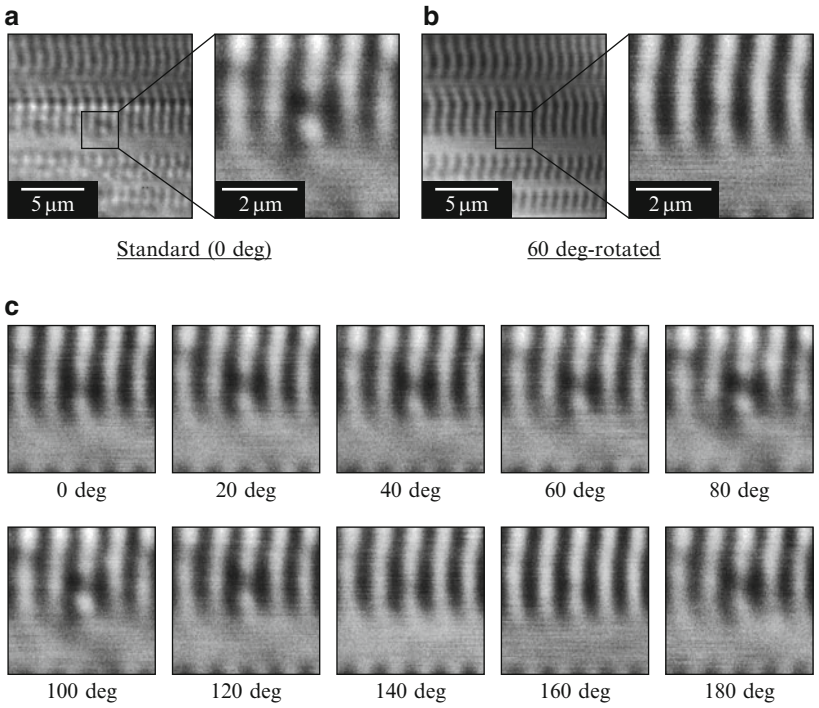

Fig. 2.19 Observed NOM images of optical intensity distributions of retrieved nanophotonic code embedded in environmental structures with (**a**) standard polarization and (**b**) polarization rotated by 60°, and (**c**) NOM images observed by radiating light with various polarizations

using a linearly polarized radiation source. Figure 2.19a, b respectively show observed NOM images of the nanophotonic code embedded in the hologram with a standard polarization (defined as 0° polarization) and 60°-rotated polarization. Figure 2.19c summarizes the NOM images obtained with input polarizations rotated by 0–180° at 20-degree intervals. Also, Fig. 2.20a–c show the NOM images of the nanophotonic code which was not embedded in the hologram. As is evident, in the case of the nanophotonic code embedded in the hologram, clear polarization dependence was observed; for example, from the area of the nanophotonic code located in the center, a high-contrast signal intensity distribution was obtained with polarizations around 80°.

To quantitatively evaluate the polarization dependency of the embedded nanophotonic code, we investigated two kinds of intensity distribution profiles from the NOM images observed. One is a horizontal intensity profile along the dashed line in Fig. 2.21a, which crosses the area of the nanophotonic code, denoted by $I(x)$, where x represents the horizontal position. The other was also an intensity distribution as a function of horizontal position x; however, at every position x, we evaluated the average intensity along the vertical direction within a range of 2.5 μm, denoted by $\langle I(x)\rangle_{\mathrm{env}}$, which indicates the environmental signal distribution. When a higher

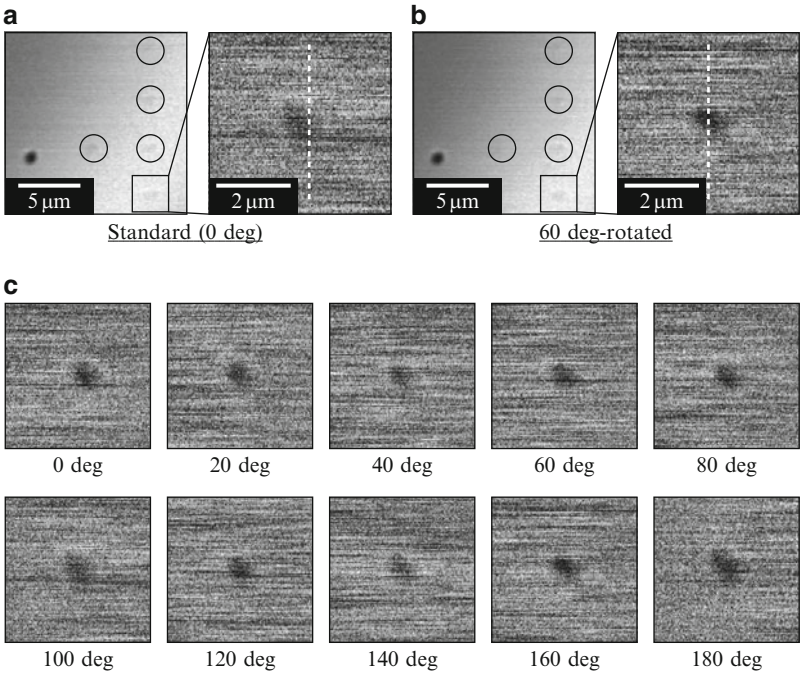

Fig. 2.20 Observed NOM images of optical intensity distributions of retrieved isolated nanophotonic code with (**a**) standard polarization and (**b**) polarization rotated by 60°, and (**c**) NOM images observed by radiating light with various polarizations

intensity is obtained selectively from the area of the nanophotonic code, the difference between $I(x)$ and $\langle I(x)\rangle_{\text{env}}$ can be large. On the other hand, if the intensity distribution is uniform along the vertical direction, the difference between $I(x)$ and $\langle I(x)\rangle_{\text{env}}$ should be small. Thus, the difference between $I(x)$ and $\langle I(x)\rangle_{\text{env}}$ indicates the visibility of the nanophotonic code. We define an experimental visibility V_{exp} as

$$V_{\text{exp}} = \sum_{x} \left| I(x) - \langle I(x)\rangle_{\text{env}} \right|. \tag{2.4}$$

Figure 2.21b shows V_{exp} as a function of input light polarization based on the NOM results shown in Figs. 2.19c and 2.20c. The nanophotonic code embedded in the hologram exhibited much greater polarization dependency, as shown as "in a hologram" in Fig. 2.21b, where the maximum V_{exp} was obtained at 80° input polarization, whereas only slight polarization dependency was observed with the isolated nanophotonic code, as shown as "w/o a hologram" in Fig. 2.21b. Such polarization dependence in retrieving the nanophotonic code agrees well with the results of the simulations in Fig. 2.16.

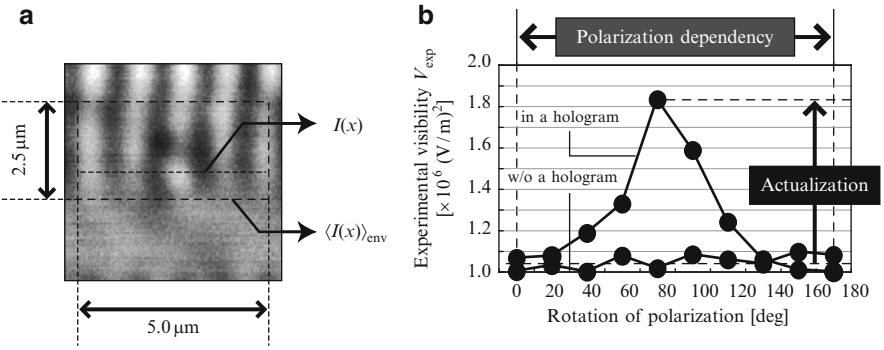

Fig. 2.21 (**a**) Schematic diagram explaining definition of $I(x)$ and $\langle I(x)\rangle_{\mathrm{env}}$, and (**b**) calculated experimental visibility V_{exp} of embedded nanophotonic code and that of isolated nanophotonic code, showing actualization of optical response as evident visibility and its polarization dependency

2.5.6 Outlook

In this section, we described the basic concept of a nanophotonic hierarchical hologram and a nanophotonic code embedded in a hologram as an implementation of a hierarchical hologram, and we demonstrated its features by numerical simulations, experimental fabrication of prototype devices, and optical characterization. Our concept can be applied not only to a hologram but also to any other media, such as lenses and jewelry. Adding extra functions creates value-added media with only a slight impact on the primary functions. However, a trade-off occurs between the nanometric fabrication conditions (e.g., size and pitch) and the impact on the primary functions. We are currently investigating these trade-offs for several types of media in actual use. Moreover, the number of layers can be increased in the near-mode observation to further extend the hierarchical function. An optical near-field interaction between multiple nanometric structures produces a characteristic spatial distribution depending on the size, the alignment, etc. Therefore, various optical signal patterns can be observed depending on the size of the fiber probe, and another layer can be added in the near-mode observation [32, 37].

One of the most notable characteristics of our proposed approach is embedding a nanophotonic code within the patterns of a hologram composed of one-dimensional grating structures; it yields clear polarization dependence compared with an isolated nanophotonic code that is not embedded within a grid structure. These features were successfully demonstrated both numerically and experimentally. Also, because embedding and retrieval of a nanophotonic code requires highly advanced technical know-how, this approach can also improve the strength of anti-counterfeiting measures.

Our results indicated that the environmental structure provides interesting polarization dependency, and more interestingly, facilitates the retrieval of near-field information. In our future research, we may come to understand the relation between

the retrieved optical intensity distributions and the design of the nanometric structures, including their environmental conditions. Such insights should allow us to propose, for instance, an optimized strategy for implementing nanophotonic codes, or a strategy robust to errors that possibly occur in the fabrication and/or retrieval processes [56]. Moreover, a simpler method for retrieving the nanophotonic code is required, without using optical fiber probe tips [22]. These aspects are currently being investigated by the authors.

2.6 Summary

In this review, we have described the basic concepts and experimental demonstrations of some proposals for probe-free nanophotonics and have demonstrated the potential of nanophotonics for application to far-field systems without using any probe-scanning method. Probe-free nanophotonics is an innovative proposal for sparking explosive expansion of the applications of nanophotonics. An important point is that, if the probe-scanning process can be eliminated, we could adopt nanophotonics as a fundamental technique for implementing, on the nanometric scale, several of the parallel processing tasks that have been the subject of fundamental research in the field of optical computing since the invention of laser technology.

Although the capabilities of classical optical computing have been restricted by the diffraction limit of light, in the scale from sub-micron to nanometer, the primacy of electrical processing over optical processing has not been clearly demonstrated. This scale is conventionally called the *mesoscopic* scale, and it is still interesting in several research fields, such as physics, biology, materials science, information science, and so on. It is likely that some aspects of our ideas will also need to be discussed in view of this scale because the extraction of an output from the optical near-field scale to the optical far-field scale, one of the fundamental processes in our concept, occurs via an *optical mesoscopic scale*. In light of this, we strongly expect that our proposals will lead not only to progress in nanophotonics but also to the establishment and development of new research fields.

Acknowledgements The authors thank the members of the Ohtsu Research Group in the Department of Electrical Engineering and Information Systems, School of Engineering, the University of Tokyo, and also thank Prof. Ohkoshi, Dr. Tokoro, and Dr. Takeda of the Department of Chemistry, School of Science, the University of Tokyo, for their valuable contributions to our collaborative research. These works were supported in part by a comprehensive program for personnel training and industry–academia collaboration based on projects funded by the New Energy and Industrial Technology Development Organization (NEDO), Japan, the Global Center of Excellence (G-COE) Secure-Life Electronics project, and Special Coordination Funds for Promoting Science and Technology sponsored by the Ministry of Education, Culture, Sports, Science and Technology (MEXT), Japan.

References

1. M. Ohtsu, K. Kobayashi, T. Kawazoe, S. Sangu, T. Yatsui, IEEE J. Sel. Top. Quant. Electron. **8**(4), 839 (2002)
2. M. Naruse, T. Miyazaki, T. Kawazoe, K. Kobayashi, S. Sangu, F. Kubota, M. Ohtsu, IEICE Trans. Electron. **E88-C**(9), 1817 (2005)
3. T. Nishida, T. Matsumoto, F. Akagi, H. Hieda, A. Kikitsu, K. Naito, J. Nanophoton. **B**, 011597 (2007)
4. E. Ozbay, Science **311**, 189 (2006)
5. M. Ohtsu, J. Nanophoton. **1**, 011590 (2007)
6. M. Naruse, T. Kawazoe, T. Yatsui, S. Sangu, K. Kobayashi, M. Ohtsu, *Progress in Nano-Electro-Optics V* (Springer, Berlin, 2006)
7. S. Mononobe, *Near-Field Nano/Atom Optics and Technology* (Springer, Berlin, 1998)
8. U. Maheswari Rajagopalan, S. Mononobe, K. Yoshida, M. Yoshimoto, M. Ohtsu, Jpn. J. Appl. Phys. **38**(12A), 6713 (1999)
9. Y. Inao, S. Nakasato, R. Kuroda, M. Ohtsu, Microelectron. Eng. **84**, 705 (2007)
10. T. Kawazoe, M. Ohtsu, Y. Inao, R. Kuroda, J. Nanophoton. **1**, 011595 (2007)
11. T. Yatsui, K. Hirata, W. Nomura, Y. Tabata, M. Ohtsu, Appl. Phys. B **93**, 55 (2008)
12. K. Kobayashi, S. Sangu, T. Kawazoe, A. Shojiguchi, K. Kitahara, M. Ohtsu, J. Microsc. **210**, 247 (2003)
13. T. Kawazoe, K. Kobayashi, K. Akahane, M. Naruse, N. Yamamoto, M. Ohtsu, Appl. Phys. B **84**, 243 (2006)
14. T. Yatsui, S. Sangu, T. Kawazoe, M. Ohtsu, S.-J. An, J. Yoo, Appl. Phys. Lett. **90**(22), 223110 (2007)
15. W. Nomura, T. Yatsui, T. Kawazoe, M. Ohtsu, J. Nanophoton. **1**, 011591 (2007)
16. W. Nomura, T. Yatsui, T. Kawazoe, M. Naruse, M. Ohtsu, Appl. Phys. B **100**, 181 (2010)
17. T. Yatsui, Y. Ryu, T. Morishima, W. Nomura, T. Kawazoe, T. Yonezawa, M. Washizu, H. Fujita, M. Ohtsu, Appl. Phys. Lett. **96**(13), 133106 (2010)
18. U. Schendel, *Introduction to Numerical Methods for Parallel Computers* (Ellis Horwood, New York, 1984)
19. H.H. Hopkins, Proc. Roy. Soc. **A217**, 408 (1953)
20. N. Tate, W. Nomura, T. Yatsui, T. Kawazoe, M. Naruse, M. Ohtsu, Nat. Comput. (Proceedings in Information and Communications Technology) **2**, 298 (2010)
21. M. Naruse, T. Yatsui, T. Kawazoe, N. Tate, H. Sugiyama, M. Ohtsu, Appl. Phys. Exp. **1**, 112101 (2008)
22. N. Tate, W. Nomura, T. Yatsui, M. Naruse, M. Ohtsu, Appl. Phys. B **96**(1), 1 (2009)
23. M. Ohtsu, K. Kobayashi, T. Kawazoe, T. Yatsui, M. Naruse (eds.), *Principles of Nanophotonics* (Taylor and Francis, Boca Raton, 2008)
24. T. Kawazoe, K. Kobayashi, J. Lim, Y. Narita, M. Ohtsu, Phys. Rev. Lett. **88**, 067404 (2002)
25. T. Kawazoe, K. Kobayashi, M. Ohtsu, Appl. Phys. Lett. **86**, 103102 (2005)
26. M. Naruse, T. Yatsui, H. Hori, M. Yasui, M. Ohtsu, J. Appl. Phys. **103**, 113525 (2008)
27. N. Tate, H. Sugiyama, M. Naruse, W. Nomura, T. Yatsui, T. Kawazoe, M. Ohtsu, Opt. Exp. **17**, 11113 (2009)
28. D.W. Lynch, W.R. Hunter, *Handbook of Optical Constants of Solids* (Academic, Orlando, 1985)
29. M. Naya, I. Tsurusawa, T. Tani, A. Mukai, S. Sakaguchi, S. Yasutani, Appl. Phys. Lett. **86**, 201113 (2005)
30. H. Yonemitsu, T. Kawazoe, K. Kobayashi, M. Ohtsu, J. Lumin. **122–123**, 230 (2007)
31. P.-Y. Chiou, A.T. Ohta, A. Jamshidi, H.-Y. Hsu, M.C. Wu, IEEE J. Microelectromech. Syst. **17**, 525 (2008)
32. M. Naruse, T. Inoue, H. Hori, Jpn. J. Appl. Phys. **46**, 6095 (2007)
33. S. Zhang, D.A. Genov, Y. Wang, M. Liu, X. Zhang, Phys. Rev. Lett. **101**, 047401 (2008)
34. J. Tanida, Y. Ichioka, Appl. Opt. **27**(14), 2926 (1988)

35. M. Ishikawa, A. Morita, N. Takayanagi, High speed vision system using massively parallel processing, in *Proceedings of IEEE International Conference on Intelligent Robots and Systems*, 373 (1992)
36. M. Ohtsu, T. Kawazoe, T. Yatsui, M. Naruse, IEEE J. Sel. Top. Quant. Electron. **14**(6), 1404 (2008)
37. M. Naruse, T. Yatsui, W. Nomura, N. Hirose, M. Ohtsu, Opt. Exp. **13**(23), 9265 (2005)
38. B. Lee, J. Kang, K.-Y. Kim, Proc. SPIE **4803**, 220 (2002)
39. O. Sato, S. Hayami, Y. Einaga, Z.Z. Gu, Bull. Chem. Soc. Jpn. **76**(3), 443 (2003)
40. H. Tokoro, T. Matsuda, T. Nuida, Y. Morimoto, K. Ohoyama, E.D.L.D. Dangui, K. Boukheddaden, S. Ohkoshi, Chem. Mater. **20**, 423 (2008)
41. S. Ohkoshi, H. Tokoro, M. Utsunomiya, M. Mizuno, M. Abe, K. Hashimoto, J. Phys. Chem. B **106**, 2423 (2002)
42. H. Tokoro, S. Ohkoshi, T. Matsuda, K. Hashimoto, Inorg. Chem. **43**, 5231 (2004)
43. H. Tokoro, T. Matsuda, K. Hashimoto, S. Ohkoshi, J. Appl. Phys. **97**, 10M508 (2005)
44. W.F. Fagan (ed.), *Optical Security and Anti-Counterfeiting systems* (Society of Photo Optical Instrumentation Engineers, WA, 1990)
45. B. Javidi, J.L. Horner, Opt. Eng. **33**, 1752 (1994)
46. P. Refregier, B. Javidi, Opt. Lett. **20**, 767 (1995)
47. G.A. Rakuljic, V. Leyva, A. Yariv, Opt. Lett. **17**, 1471 (1992)
48. R.L. Van Renesse (ed.), *Optical Document Scanning* (Altech House Optoelectronics Library, 1998)
49. S.P. McGrew, Proc. SPIE, Optical Security and Anticounterfeiting Systems **1210**, 66 (1990)
50. G.S. Zhdanov, M.N. Libenson, G.A. Martsinovskii, Phys-Usp **41**, 719 (1998)
51. M. Ohtsu, Proc. SPIE **3749**, 478 (1999)
52. T. Yatsui, K. Itsumi, M. Kourogi, M. Ohtsu, Appl. Phys. Lett. **80**, 2257 (2002)
53. N. Tate, W. Nomura, T. Yatsui, M. Naruse, M. Ohtsu, Opt. Exp. **16**, 607 (2008)
54. N. Tate, M. Naruse, T. Yatsui, T. Kawazoe, M. Hoga, Y. Ohyagi, T. Fukuyama, M. Kitamura, M. Ohtsu, Opt. Exp. **18**, 7497 (2010)
55. I. Lancaster (ed.), *Holopack Holoprint Guide Book* (Reconnaissance International Publishers and Consultants, UK, 2000)
56. M. Naruse, H. Hori, K. Kobayashi, M. Ishikawa, K. Leibnitz, M. Murata, N. Tate, M. Ohtsu, J. Opt. Soc. Am. B **26**, 1772 (2009)

Chapter 3
Self-Formation of Semiconductor Quantum Dots

Koichi Yamaguchi

Abstract We reviewed the self-formation control of InAs/GaAs quantum dots (QDs) by molecular beam epitaxy. Uniform InAs/GaAs QDs were demonstrated by self size-limiting effect, the optimized capping growth, and the closely-stacked growth using the nanoholes. High-density InAs QDs were achieved by Sb-mediated growth. In addition, an intermittent growth method was presented for ultra-low density InAs QDs. Furthermore, the vertical and in-plane arrangements of InAs/GaAs QDs were attempted by using the strain-controlled underlying layers. One-dimensional QD chains were spontaneously formed along the [1–10] direction on the GaAs/InGaAs/GaAs(001) buffer layers. Two-dimensional arrangement of InAs QDs was demonstrated by using GaAsSb/GaAs(001) buffer layers.

3.1 Introduction

Recent progress in epitaxial semiconductor growth techniques, such as molecular beam epitaxy (MBE) and metalorganic chemical vapor deposition (MOCVD), has enabled the fabrication of semiconductor nanostructures having low-dimensional electronic characteristics. In particular, semiconductor quantum dots (QDs) are expected to enable the development of high-performance next-generation optoelectronic devices based on zero-dimensional quantum confinement. Self-assembled QD growth using a Stranski–Krastanov (SK) growth mode has been actively studied since about 1990, and self-assembled QDs have attracted much attention in nanophotonics. To develop novel nanophononic QD devices, the QD structure must be precisely controlled. The controlled self-formation of QD structures remains an open challenge.

K. Yamaguchi
Department of Engineering Science, The University of Electro-Communications,
1-5-1 Chofugaoka, Chofu, Tokyo 182-8585, Japan
e-mail: kyama@ee.uec.ac.jp

M. Ohtsu (ed.), *Progress in Nanophotonics 1*, Nano-Optics and Nanophotonics,
DOI 10.1007/978-3-642-17481-0_3,

This chapter focuses on control techniques for self-assembled InAs/GaAs QDs by MBE. Section 3.2 introduces the basics of the self-formation of QDs using the SK growth mode. Section 3.3 introduces the uniform formation of QDs, based on a self-size limiting effect, capping growth on QDs, and closely-stacked growth using nanoholes. In Sect. 3.4, the control of quantum energy levels is discussed, and adjustment of growth conditions and post-growth annealing are introduced. Section 3.5 treats density control of QDs. Control of high density QDs can be realized in an Sb-mediated growth method, and low-density QDs can be controlled by an intermittent growth method. In Sect. 3.6, vertical and in-plane arrays of QDs are introduced.

3.2 Stranski–Krastaov Growth of Quantum Dots

Thin film growth can be classified into three modes; Frank–van der Merwe (FM) mode, which results in 2-dimensional (2D) growth, Volmer–Weber (VM) mode, which forms 3D islands, and Stranski–Krastanov (SK) mode. The SK mode is a combination of the FM and VW modes, that is, 3D island growth occurs, followed by 2D growth. The SK mode frequently appears in the hetero-epitaxial growth of lattice mismatched materials, such as Ge/Si and InAs/GaAs. In 1985, self-assembled InAs QDs were first demonstrated using the SK growth mode [1].

During the initial growth in SK mode, the free energy of the 2D growth is always lower than that of the 3D growth. However, as the growth proceeds, this free energy relationship inverts because of excess strain energy due to lattice mismatch between the materials. Therefore, a growth mode transition from 2D to 3D growth occurs spontaneously, as shown in Fig. 3.1. After further growth, dislocations form because

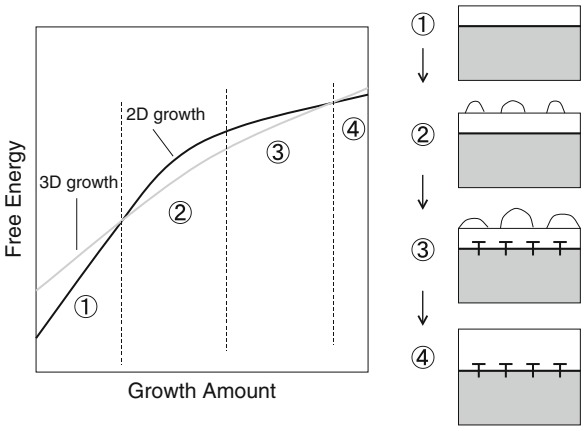

Fig. 3.1 In typical SK growth, free energy vs. growth amount for 2D and 3D growth. As the growth proceeds, the growth mode transits from 2D mode (①) to 3D mode (②). Schematic diagrams show the change of the thin film structure. At ③, dislocations generate at the heterointerface

of excess strain energy. Hence, to fabricate coherent 3D islands with high crystal quality, the extent of growth must be controlled precisely [2]. With sufficient control of the growth, self-assembled QDs can be fabricated using SK growth techniques.

In MBE growth, reflection high energy electron-beam diffraction (RHEED) is frequently used for real-time monitoring of the growth surface. In self-assembled QD growth using the SK mode, RHEED monitoring is a useful tool to control the growth. Figure 3.2 shows changes in the RHEED pattern and diffraction-beam intensity as a function of growth time for InAs growth on GaAs. When the InAs coverage exceeds the critical thickness for the growth mode transition (about 1.75 monolayers (ML)), the RHEED pattern changes from a streak pattern to a spot pattern, and the diffraction-beam intensity increases rapidly [3]. By in situ RHEED observation, we can precisely control the extent of growth. However, since the 3D islanding proceeds quickly, control of the QD structure formation is very difficult during the growth. Therefore, the SK growth conditions and the growth sequence should be modified to control the QD structures.

Figure 3.3a shows an atomic force microscopy (AFM) image of 2D and 3D InAs islands with 1.8 ML of coverage. InAs islands are often observed near step edges, which are preferential sites to reduce the strain energy. Figure 3.3b shows the relationship between the lateral size and height of InAs islands grown on GaAs with various InAs coverages ranging from 1.6 ML to 3.0 ML. During the initial growth, the 2D islands spread laterally, maintaining an island height of about 2 ML. As the growth proceeds, the island height increases rapidly, indicating a growth mode transition. 3D dots are spontaneously formed, and fluctuate in size [4]. In the design of QD devices, well-controlled QD structures are highly desirable for the realization of high performance and new functionality. For example, uniform QDs with a narrow size distribution are required for some QD devices, such as QD lasers.

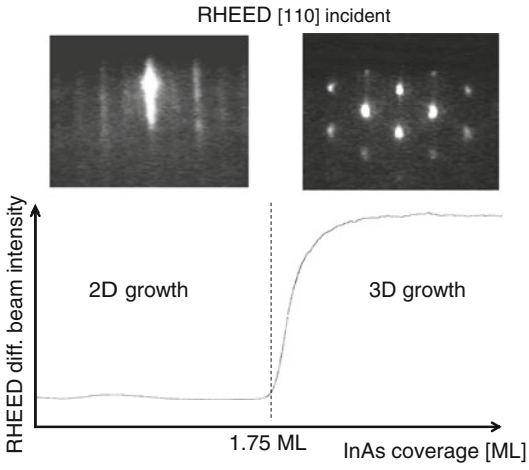

Fig. 3.2 InAs coverage dependence of RHEED diffraction-beam intensity in InAs/GaAs hetero-epitaxy. critical thickness for growth mode transition was about 1.75 ML. RHEED pattern changed from streak to spot pattern at the critical thickness

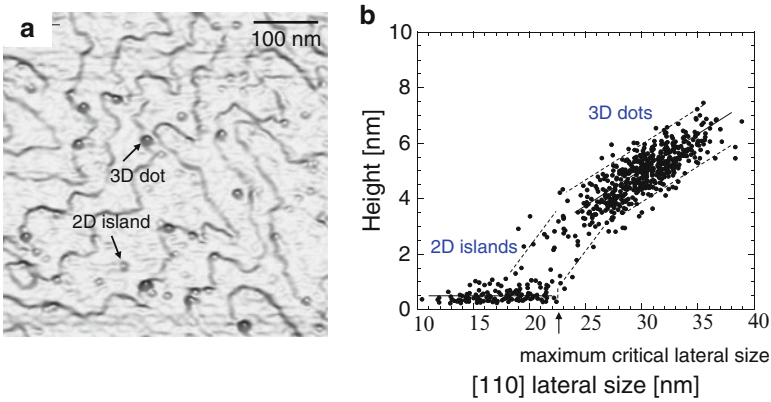

Fig. 3.3 AFM image of 2D and 3D InAs islands with 1.8 ML coverage (**a**). Relationship between height and [110] lateral size of InAs islands (**b**)

3.3 Uniform Formation of Quantum Dots

As described in Sect. 3.2, the SK growth technique is a powerful tool for the fabrication of self-assembled QDs. However, fluctuation of the QD structure causes inhomogeneous broadening of the QD energy levels, and presents a critical problem in the development of certain device applications, such as QD lasers. In this section, three methods for improving the uniformity of the QD structure are described: self size-limiting growth (Sect. 3.3.1), capping growth (Sect. 3.3.2), and closely-stacked growth (Sect. 3.3.3).

3.3.1 Self Size-Limiting Growth of Uniform InAs/GaAs Quantum Dots

QD structure strongly depends on the SK growth conditions, and there have been many reports concerning their growth condition dependencies [5]. To reduce the size fluctuation of InAs/GaAs QDs, a low growth rate [6] and low arsenic pressure conditions [7] are effective because of the resulting enhanced surface migration. In particular, the above growth conditions induce a saturation of QD size, which is called a self size-limiting effect. A typical result of the self size-limiting phenomenon is shown in Fig. 3.4, which shows the lateral size and height of InAs QDs as a function of InAs coverage. When the InAs coverage is larger than the critical thickness for the growth mode transition, the lateral size and height of the 3D dots immediately saturate [8]. Recently, such self size-limiting of InAs/GaAs QDs has also been observed using in situ X-ray diffraction (XRD) analysis [9]. This limiting of lateral size may be attributed to a compressive strain at the island edges near the wetting layer [10].

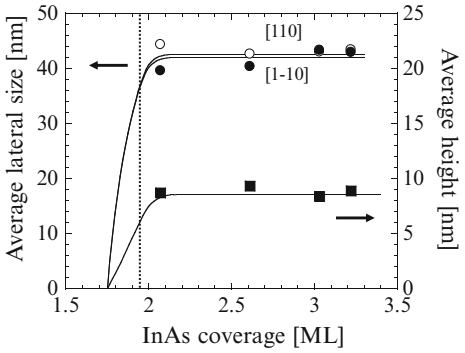

Fig. 3.4 Average lateral size and average height of the InAs 3D islands as a function of the InAs coverage

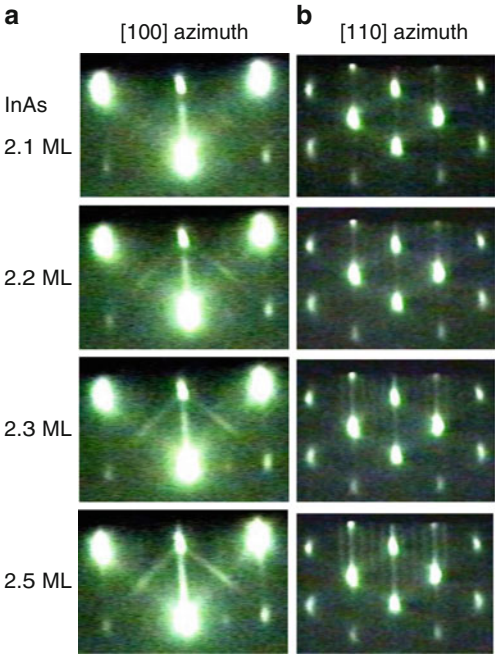

Fig. 3.5 RHEED patterns taken along the [100] azimuth (**a**) and the [110] azimuth (**b**) as a function of the InAs coverage

The incorporation of In adatoms is suppressed at the strained island edges. However, since the top area of the 3D islands is relaxed, the height limiting cannot be due to the strain.

To study the self limiting of the height, the RHEED pattern was monitored during InAs growth. Figure 3.5a shows RHEED chevron patterns obtained using a [100] incident electron-beam. The chevron pattern provides some information regarding the formation of a micro-facet on the side walls of the QDs. For more than 2.1 ML of InAs coverage, a 45° chevron pattern clearly appeared, indicating {110} facet formation [11]. Therefore, the InAs QDs had a pyramidal shape with {110} facets, as shown in Fig. 3.6a, a typical AFM image of an InAs QD. The RHEED patterns for the [110] incident beam are shown in Fig. 3.5b. As the growth proceeds beyond

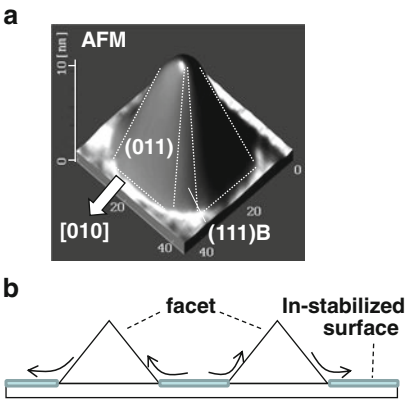

Fig. 3.6 AFM image of InAs QD with limited size and {110} facets (**a**). Schematic diagram of the size-limited QDs surrounded with stable facets (**b**). The wetting layer was covered with In-stabilized surface

2.2 ML, a (4×) streak pattern appears, that is, the RHEED pattern changed from a (1×1) spot pattern to a (4×2) streak pattern with a (1×1) spot [11]. Once limited dots with {110} facets are formed, In adatoms are no longer incorporated into the limited dots. Therefore, the dot height is spontaneously limited by the formation of stable facets. As a result, incoming In adatoms are accumulated on the wetting layer (Fig. 3.6b). Excess In adatoms cause the (4×2) streak pattern, which reveals the In-stabilized surface.

The self size-limiting phenomenon, described above, plays an important role in the improvement of size uniformity. Figure 3.7 shows photoluminescence (PL) spectra of the InAs QDs as a function of InAs coverage. InAs QDs were embedded in the GaAs capping layers, as described in Sect. 3.3.2. At low coverage, the PL spectrum width is very large (a large size distribution). As the InAs coverage increased, a low-energy PL peak (1.05 eV) was enhanced and the high-energy components were suppressed. This coverage dependence of the PL spectrum can be explained by the self size-limiting effect, and uniform QDs can be obtained.

Figure 3.8 shows in-plane distributions of InAs QDs (for 1.8 ML (Fig. 3.8a) and 2.5 ML (Fig. 3.8b) of coverage). In this experiment, the substrates were not rotated during the MBE growth, and the InAs coverage was evaluated at the center of the substrate using RHEED. The critical thickness for the 2D–3D transition was 1.75 ML, and the InAs growth at 1.8 ML was insufficient to trigger the size-limiting effect. Hence, a large distribution of InAs QDs was observed for 1.8 ML of coverage (Fig. 3.8a). On the other hand, for 2.5 ML of coverage (Fig. 3.8b), the in-plane uniformity of QD size and density improved because of the size-limiting effect.

Figure 3.9 shows an AFM image of uniform InAs QDs, grown at a low growth rate and low arsenic pressure, under the self size-limiting effect. The standard deviations of the sizes of these QDs were 4% for the lateral size and 8% for the height. These values reveal narrower size distributions than growth under conventional SK growth conditions [7].

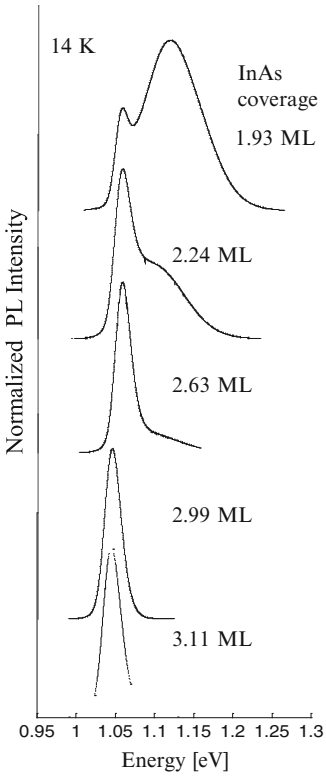

Fig. 3.7 PL spectra of InAs QDs with various InAs coverage (1.93, 2.24, 2.63, 2.99 and 3.11 ML). PL temperature was 14 K

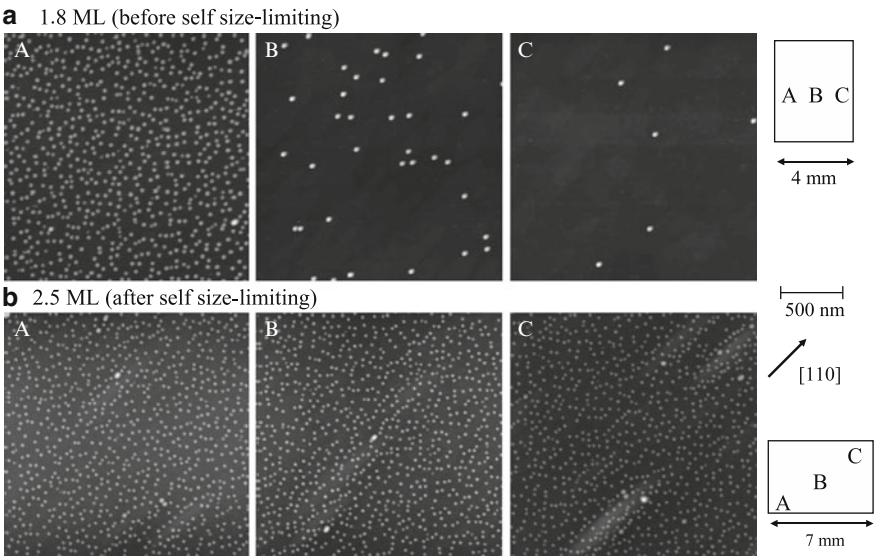

Fig. 3.8 AFM images of InAs QDs, measured at different positions (A, B, C) on the substrate. The InAs were grown respectively at 1.8 ML coverage (**a**) and 2.5 ML coverage (**b**). In this growth, the substrate was not rotated

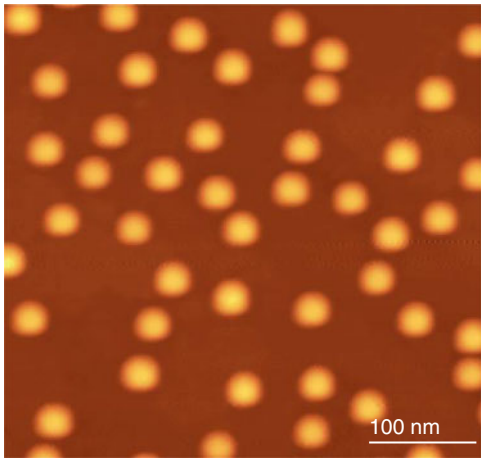

Fig. 3.9 AFM image of uniform InAs QDs with limited size

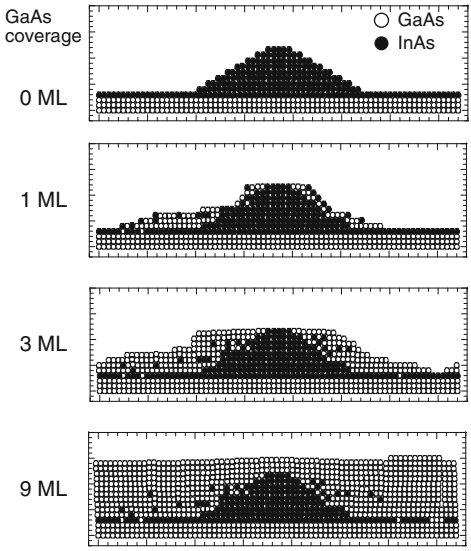

Fig. 3.10 Calculated cross-sectional images of InAs *dots*, embedded by GaAs capping layers with 0 ML, 1 ML, 3 ML, and 9 ML coverages, respectively. The capping growth process was calculated by using kinetic Monte-Carlo method. The base length and height of the *dots* were given respectively at 33 ML and 8 ML. The substrate temperature of the capping growth was 450°C, and the growth rate was 0.56 ML s^{-1}

3.3.2 Capping Growth of Uniform InAs/GaAs Quantum Dots

For device applications, QDs are usually embedded within capping layers, which suppress undesirable electronic states near the QDs. It should be noted here that capping growth often modifies the QD structure [12]. Figure 3.10 shows InAs-QD structures with GaAs capping layers, which were calculated using a kinetic Monte-Carlo method [13]. The surface segregation and surface desorption of InAs, depending on the strain, were included in this calculation. These effects modified the dot shape and induced the intermixing of GaAs and InAs during the GaAs capping

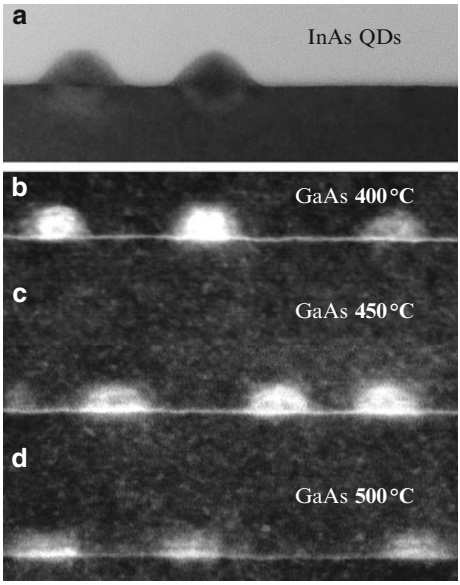

Fig. 3.11 $(1\bar{1}0)$ Cross-sectional STEM images of InAs QDs without capping layer (**a**) and with GaAs capping layers, which were grown at 400°C (**b**), 450°C (**c**), and 500°C (**d**), respectively

growth [14]. When the growth temperature was increased, the growth rate decreased and the strain increased, enhancing the surface segregation and desorption effects. Therefore, the growth conditions and the growth structure of the capping layer are very important for the fabrication of a uniform QD structure of high crystal quality.

Figure 3.11 shows cross-sectional scanning transmission electron microscopy (STEM) images of InAs QDs with GaAs capping layers, grown at 400°C (Fig. 3.11b), 450°C (Fig. 3.11c), and 500°C (Fig. 3.11d). As mentioned above, the dot height decreased with increasing growth temperature because of surface segregation and desorption of the InAs. This modification of the QD structure strongly affected the inhomogeneous broadening in the quantum energy level.

Figure 3.12 shows the relationships between the PL properties of InAs QDs and the growth temperature of the GaAs capping layer. For temperatures below 450°C, the poor crystal quality of the GaAs layer drastically decreased the PL intensity. However, higher temperature growth induced a blue shift and broadening of the PL spectra. Therefore, at the intermediate temperature of 450°C, the low growth rate and low arsenic pressure in the GaAs capping growth were optimized to obtain uniform QD structures of high crystal quality. As shown in Fig. 3.13, a narrow PL linewidth of 17.6 meV was achieved.

The extensive inhomogeneous broadening of the QDs, which causes overlapping of the second state of a QD with the ground state of other QDs, prevents accurate measurement. This problem can be overcome by adopting the above uniform QD samples. For instance, a phonon relaxation bottleneck [15], spin Pauli blocking [16], and spin relaxation dynamics [17] were clearly observed.

Next, InGaAs capping growth on InAs QDs is described. InAs QDs in a GaAs matrix have a large compressive strain. Hence, the excess strain often modifies the

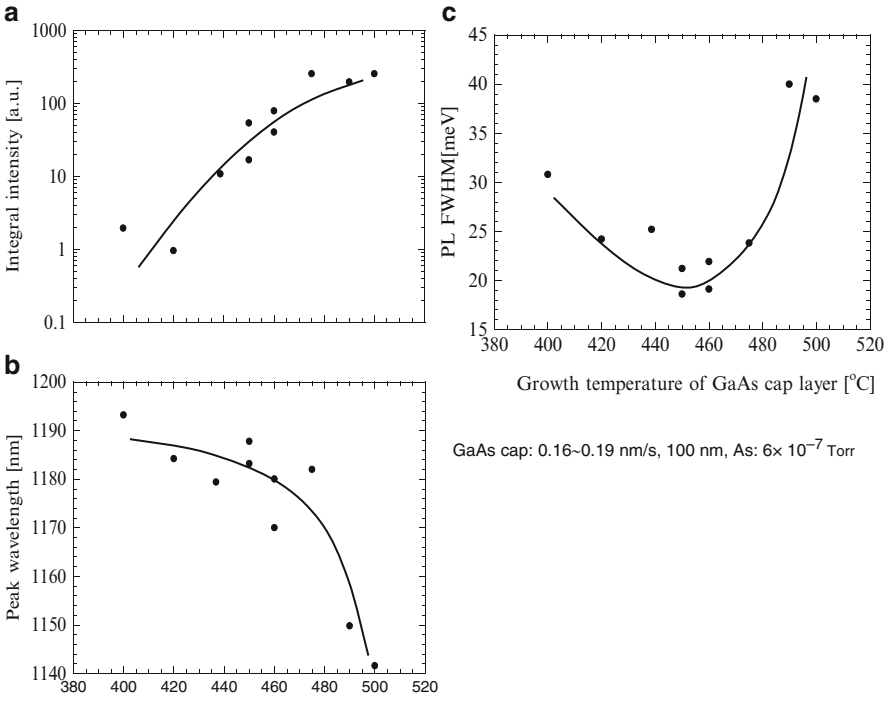

Fig. 3.12 PL properties (integral intensity (**a**), peak wavelength (**b**) and FWHM (**c**)) of InAs QDs as a function of growth temperature of GaAs capping layer. PL was measured at 12 K

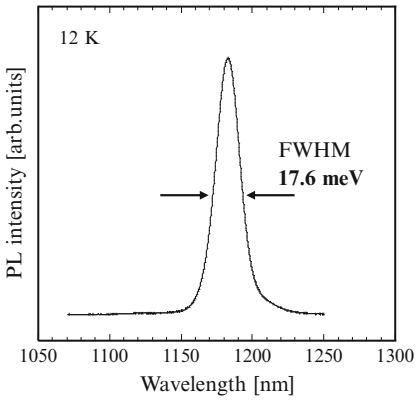

Fig. 3.13 PL spectrum of uniform InAs QDs. PL was measured at 12 K

dot structure during the capping growth. In addition, the accumulated strain often induces dislocations near the hetero-interface. InGaAs capping growth on InAs QDs reduces the strain, and as a result, the crystal quality improves and the decrease in dot height is suppressed [18]. Figure 3.14 shows PL spectra of InAs QDs (2.3 ML

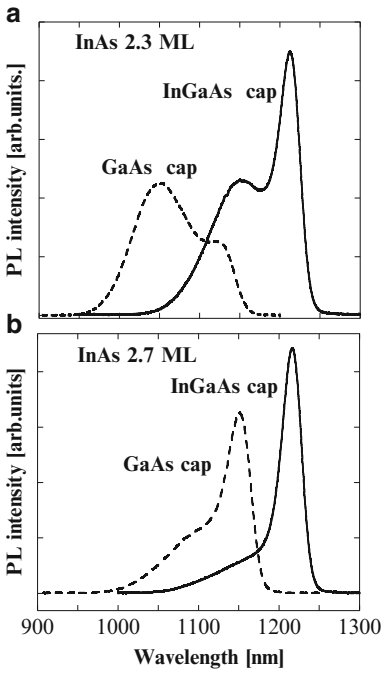

Fig. 3.14 PL spectra of InAs QDs with GaAs and InGaAs capping layers. The InAs coverage was 2.3 ML (**a**) and 2.7 ML (**b**). PL temperature was 12 K

(Fig. 3.14a) and 2.7 ML (Fig. 3.14b)), covered by a GaAs capping layer and an InGaAs capping layer, respectively. For the InGaAs capping layers, the PL spectra shifted to a lower energy, and the inhomogeneous broadening became narrower, compared with GaAs capping layer spectra [19]. Strain-reduced InGaAs capping growth is a useful method for improvement of size uniformity and crystal quality.

3.3.3 Closely-Stacked Growth of Uniform InAs/GaAs Quantum Dots

A strong coupling between neighboring QDs forms QD molecules, which have many attractive properties arising from interaction between the QDs [20]. To fabricate QD molecules, closely stacked growth of the QDs has been actively investigated. In this growth technique, a spacing layer between two QD layers must be controlled precisely. In this section, the closely stacked growth of uniform InAs QDs is described. In particular, the upper InAs-QD layers were stacked through self-formed nanoholes in GaAs spacer layers onto underlying InAs-QD layers.

After the uniform growth of InAs QDs by the self size-limiting effect (Fig. 3.15a), a 10-nm-thick GaAs capping layer was grown, as shown in Fig. 3.15b. On the GaAs surface, there were ridge structures and small dips, located above the embedded InAs QDs (Fig. 3.15d) [21]. By thermal annealing at 500°C for 5 min, the ridges

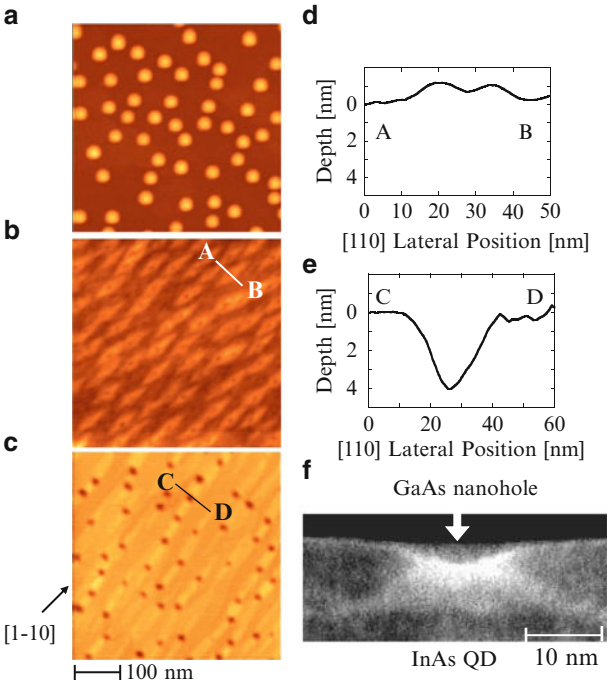

Fig. 3.15 AFM images of InAs QDs without capping layer (**a**) and with 10-nm-thick GaAs capping layer (**b**, **c**). AFM image of Fig. 3.15c was obtained after thermal annealing at 500°C for 5 min. Line profiles of (**d**) and (**e**) show the ridge structure (A–B in (**b**)) and nanohole structure (C–D, in (**c**)) just above the InAs QDs. Figure 3.15f indicates cross-sectional STEM image of the embedded InAs QDs with GaAs nanohole capping layer

elongated along the $[1\bar{1}0]$ direction, and nanoholes were spontaneously formed (Fig. 3.15c) [22]. Figure 3.15e shows a line profile of a nanohole, which was approximately 4 nm deep. From the cross-sectional STEM image (Fig. 3.15f), it was determined that the nanohole was located just above an embedded InAs QD. In addition, the nanohole density was almost identical to the QD density. The self-formation of GaAs nanoholes and the change in the GaAs ridges can be explained as follows. Since the strained GaAs surface layer near InAs dots is energetically unstable, thermal annealing induces desorption of unstable GaAs molecules. During the annealing, desorbed GaAs molecules (or Ga atoms) migrate on the surface, and are preferentially incorporated into $[1\bar{1}0]$ steps. As a result, nanoholes are formed just above dots, and the ridges flatten and lengthen along the $[1\bar{1}0]$ direction.

Next, InAs QDs were grown selectively on GaAs nanoholes to fabricate strongly coupled QD molecules [23]. Figure 3.16 shows AFM images of InAs islands grown on a GaAs-nanohole spacer layer. For 1.6 ML of InAs coverage (Fig. 3.16a), InAs was randomly incorporated into the nanoholes. Hence, the size fluctuation was very large, as shown in Fig. 3.16b. This random incorporation was caused by a longer surface migration distance of In adatoms, compared with the separation distance

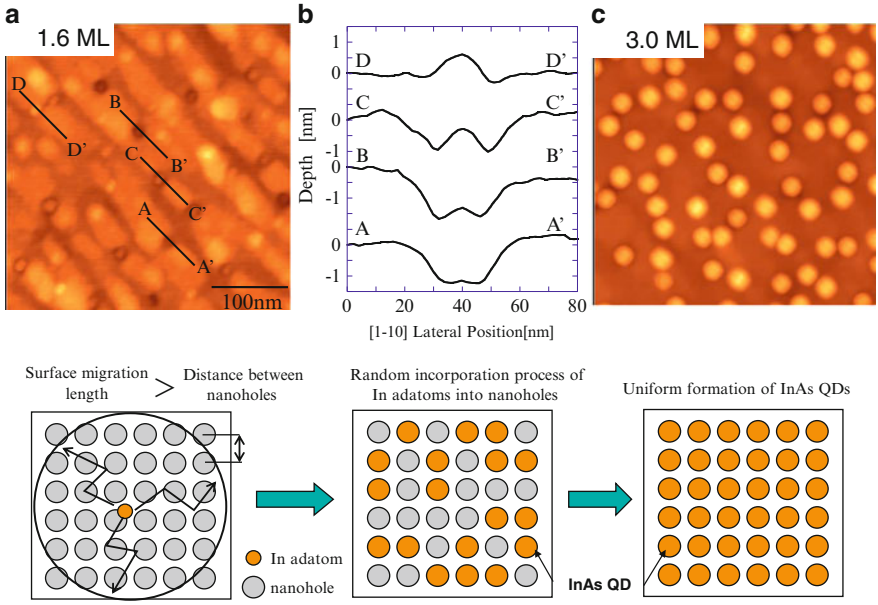

Fig. 3.16 AFM images of second InAs islands with 1.6 ML (**a**, **b**) and 3.0 ML (**c**), which were grown on GaAs nanoholes. Fig. 3.16b shows line profiles at various positions of the nanoholes in (**a**). Insert of schematic diagram indicates selective formation process of second InAs QDs on nanoholes. Uniform first InAs QDs were embedded under nanoholes

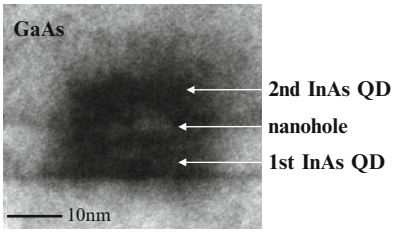

Fig. 3.17 Cross-sectional STEM image of closely stacked InAs QD. The second QD was combined with the first QD through the GaAs nanohole

between the nanoholes. As the InAs coverage increased, the InAs islands formed more uniformly. Particularly, the self size-limiting of the second InAs QDs gave uniform InAs QD-molecules (Fig. 3.16c).

In Fig. 3.17, a cross-sectional STEM image of a uniform InAs QD-molecule is presented, and the second InAs QDs are closely stacked on the first QDs through the GaAs nanoholes. Figure 3.18 shows low-temperature (12 K) PL spectra of uniform InAs QD-molecules, excited at 4 W cm^{-2} (Fig. 3.18a) and 4 mW cm^{-2} (Fig. 3.18b) of Ar+ laser power density. Not only ground states but also first excited states were observed at high excitation power density (4 W cm^{-2}). The energy separation between the quantum levels was about 64 meV, and the PL linewidth was 16.1 meV. At low excitation power density (4 mW cm^{-2}), a narrow PL linewidth of 13.2 meV was successfully obtained.

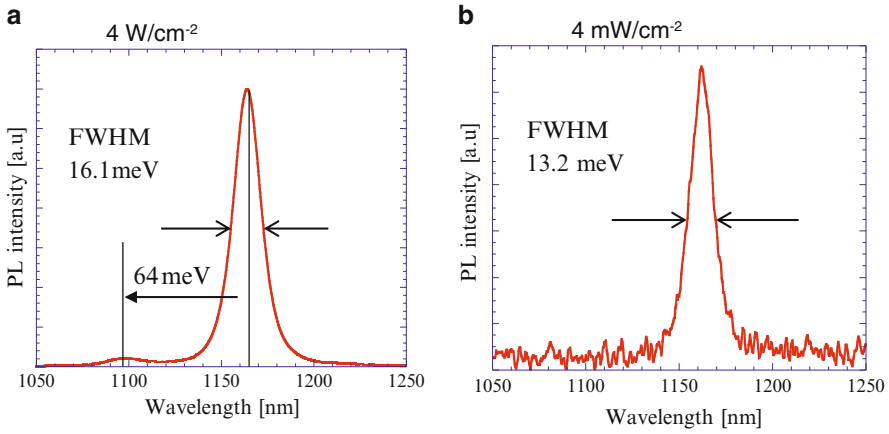

Fig. 3.18 Low-temperature (12 K) PL spectra of closely stacked InAs QDs. Excitation power density was 4 W cm^{-2} (**a**) and 4 mW cm^{-2} (**b**). PL sub-peak based on the first excited states was observed for high excitation power density (**a**)

3.4 Control of Quantum Energy Level

Control of QD energy levels is needed for various device applications. For example, for optical fiber communication systems, QD structures must be designed to have optical wavelengths of 1.3 and 1.55 μm. The quantum energy levels of the QDs can be adjusted by modification of the QD structures, material composition, and/or size. The QD size can be changed by adjusting the SK growth conditions. Generally, higher growth temperatures, lower growth rates, and lower arsenic pressures result in the formation of larger QDs with lower quantum energy levels. However, changing the SK growth conditions frequently provides a different QD density. On the other hand, the post-growth thermal annealing of QDs has been investigated as a means to modify QD structure [24–27], and it is possible to control the quantum energy levels using post-growth annealing. In this section, we present results from the post-growth annealing of uniform InAs QDs in a GaAs matrix, and discuss the control of QD energy levels and an intermixing effect between In and Ga atoms.

In this experiment, as-grown InAs QDs revealed narrow PL spectra, about 20 meV wide. Following the MBE growth of a uniform InAs QD sample, a 420-nm thick SiO_2 film was deposited on the sample surface by rf-sputtering at 250°C. Then, the SiO_2-capped QD sample was annealed at 700°C in a nitrogen atmosphere. Figure 3.19 shows PL spectra of the uniform InAs QDs as a function of annealing time. As the annealing time increased, the PL spectra shrank and shifted toward a higher energy because of the changes in the QD structure. It is well known that modification of the dot structure due to annealing is mainly caused by interdiffusion of III-group materials [28–30]. The blue shift and narrowing of the PL spectra can be explained by broadening of the In composition profile due to In–Ga interdiffusion. In particular, III-group atomic vacancies enhanced the interdiffusion.

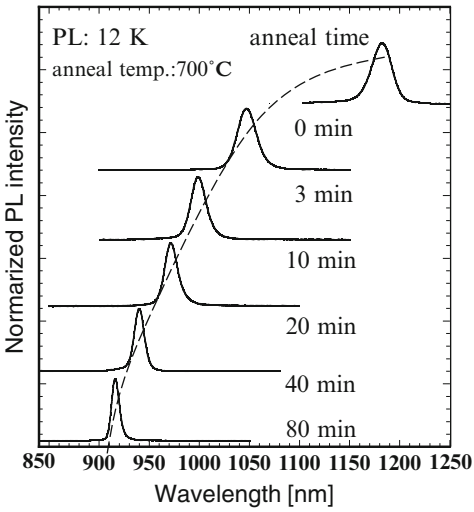

Fig. 3.19 PL spectra (12 K) of InAs QDs as a function of thermal annealing time. The annealing temperature was 700°C

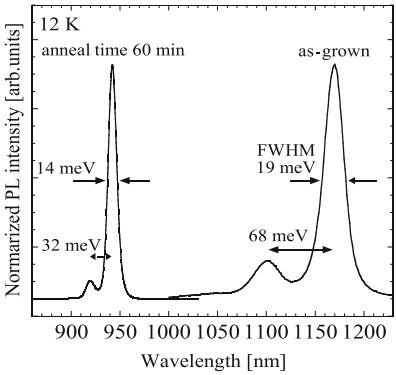

Fig. 3.20 PL spectra (12 K) of as-grown InAs QDs and annealed InAs QDs. Low-energy and high-energy PL peaks were based on the transitions from ground states and first excited states of their QDs, respectively

In general, III-group vacancies existed near the SiO_2/GaAs interface because of the interface reaction and surface damage induced by sputtering of the SiO_2 capping film [28, 31]. As a result, the PL peak wavelength at 12 K shifted from 1,180 nm (at 0 min) to 910 nm (at 80 min). This demonstrates the availability of wide control over the quantum energy level ($E = 312$ meV) by post-growth thermal annealing. In addition, an extremely narrow PL linewidth of 13 meV was obtained after 80 min of annealing. However, in the annealed QDs, the energy separation between the ground state and the first excited state became narrower, as shown in Fig. 3.20.

Figure 3.21 shows (110) cross-sectional STEM images of InAs QDs, annealed at 700°C for 0 min (Fig. 3.21a), 40 min (Fig. 3.21b), and 80 min (Fig. 3.21c). From Fig. 3.21a–c the lateral size (L) of the QDs, the thickness of the wetting layer (W), and the total height (D) were measured, and the results are plotted in Fig. 3.22 as a function of annealing time. Broadening of the InAs/GaAs heterointerface due

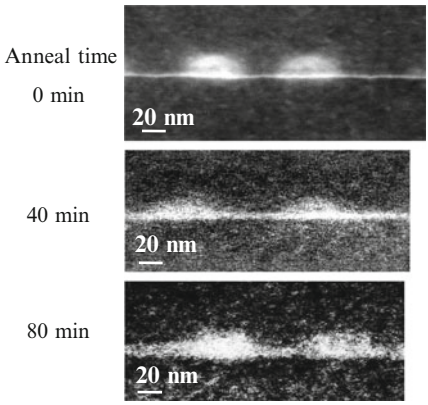

Fig. 3.21 (110) Cross-sectional STEM images of as-grown InAs QDs (**a**) and annealed InAs QDs, which were annealed for 40 min (**b**) and 80 min (**c**), respectively

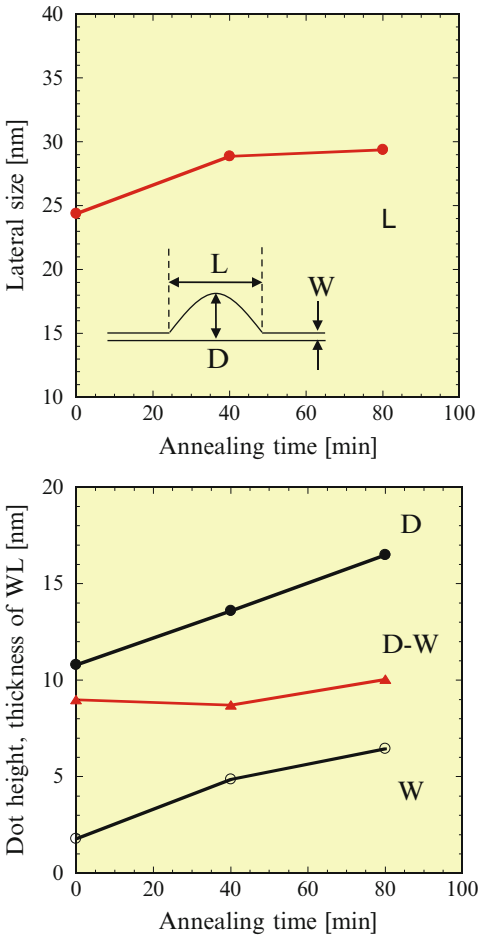

Fig. 3.22 (110) Lateral size (L) and height (D) of InAs QDs and wetting layer thickness (W) as a function of the annealing time. Annealing temperature was 700°C

to the annealing was clearly observed. However, the increment of the total height (D) was almost the same as the broadening width of the wetting layer in the vertical direction: the net height of the QD (D – W) did not depend on the annealing time. As the annealing time increased, the lateral size of the QD increased, and then saturated. It is probable that the In–Ga interdiffusion was enhanced by the strain. Since the compressive strain in the QD was relaxed by the broadening of the heterointerface, the interdiffusion effect weakened with increasing annealing time. However, as mentioned above, post-growth annealing is a useful tool for increasing QD energy levels.

3.5 Density Control of Quantum Dots

In the application of QDs to semiconductor lasers and solar cells, high-density QDs are expected to improve performance. In conventional SK growth of QDs, the QD density can be changed by adjusting the growth conditions. In general, low growth temperatures, high arsenic pressures, and high growth rates of InAs/GaAs QDs provide a high QD density. However, the crystal quality and uniformity of the high-density QDs is very important. In particular, the coalescence of neighboring QDs occurs easily for high-density QDs because of the short separation distance between the QDs. Dislocations are usually observed in the giant dots that result from this coalescence. Therefore, coalescence should be suppressed to maintain a high crystal quality. In Sect. 3.5.1, Sb-mediated growth of high-density InAs/GaAs QDs is presented to resolve the trade-off relationship between high density, uniformity, and crystal quality.

On the other hand, low QD density is desirable for some devices that use individual QDs, such as single-photon sources. However, precise control of low-density QDs is difficult because the growth mode transition from 2D to 3D occurs rapidly. To realize low-density growth, the surface concentration of adatoms should be suppressed, and the supply amount of growth materials should be precisely controlled. In Sect. 3.5.2, an intermittent growth method is presented for the controlled formation of low-density InAs/GaAs QD.

3.5.1 Sb-Mediated Growth of High-Density InAs/GaAs Quantum Dots

As described in Sect. 3.3.1, a low growth rate and a low arsenic pressure can enhance surface migration, and, as a result, produce highly-uniform InAs/GaAs QDs at a low density, as shown in Fig. 3.23a. Therefore, growth conditions opposite to those employed for high-density growth induce large size fluctuations (Fig. 3.23b). In addition, under high-density conditions (Fig. 3.23b), many giant dots appeared due to coalescence. In 2004, Yamaguchi et al. reported an Sb-mediated SK growth

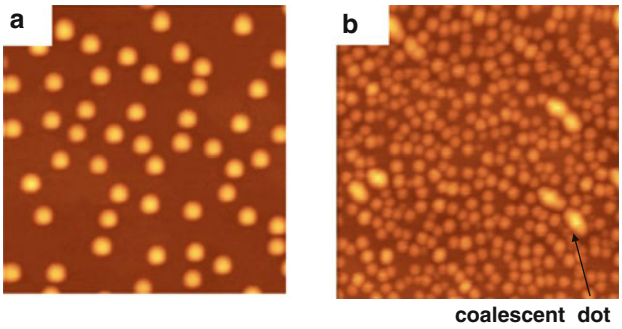

Fig. 3.23 AFM images of low-density InAs QDs (**a**) and high-density InAs QDs (**b**). (**a**): growth temperature of 500°C, growth rate of 0.035 ML s^{-1}, arsenic pressure of 3×10^{-6} Torr, (**b**): 480°C, 0.070ML s^{-1}, 6×10^{-6} Torr)

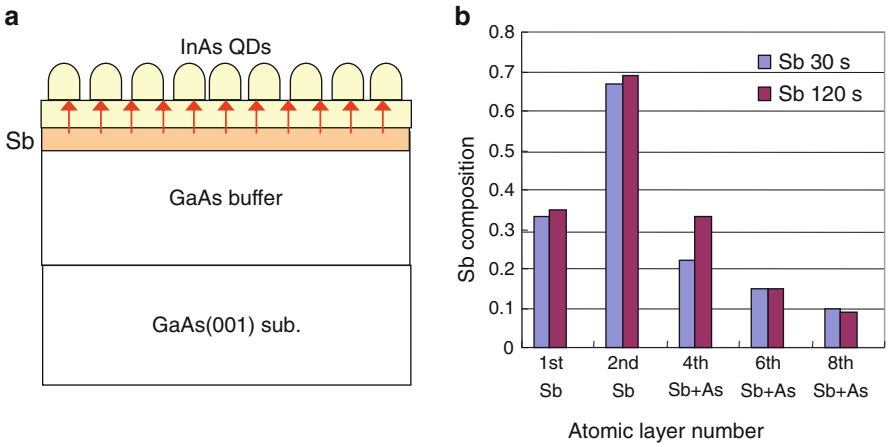

Fig. 3.24 Sample structure of high-density InAs QDs on Sb/GaAs(001) (**a**). Sb composition profiles of Sb-irradiated GaAs surface layers (**b**). Sb-irradiation time was 30 and 120 s

method using Sb-containing GaAs buffer layers of high-density InAs QDs [32, 33]. In this growth, the coalescence of the QDs was effectively suppressed. Figure 3.24a shows a schematic diagram of the growth structure in this Sb-mediated growth of InAs QDs. Prior to the InAs growth, an Sb flux was irradiated onto the GaAs buffer layer. The RHEED pattern changed from (2×4) to (1×3) or (2×3), which indicated an Sb-stabilized surface. Figure 3.24b shows the Sb composition profiles of an Sb-irradiated GaAs surface, measured by X-ray crystal truncation rod (CTR) scattering. From the CTR scattering, it was found that the Sb-stabilized surface layer was composed from the Sb bi-layer with 30% (first) and 60% (second) in coverage [34]. Furthermore, 3-ML-thick GaAsSb alloy layers were formed beneath the surface.

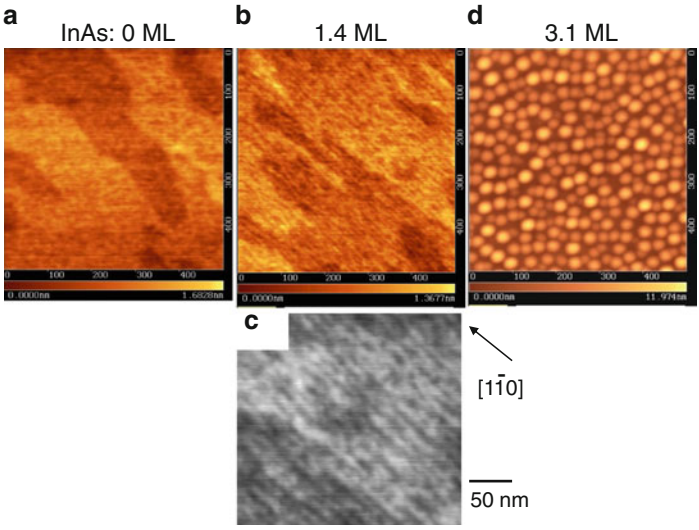

Fig. 3.25 AFM images of Sb-irradiated GaAs surface (**a**) and InAs islands with different coverage of 1.4 ML (**b**, **c**) and 3.1 ML (**d**)

After Sb irradiation of the GaAs buffer layer, InAs was grown on the surface. Figure 3.25 shows AFM images of the Sb-irradiated GaAs surface (Fig. 3.25a) and InAs islands with 1.4 ML (Fig. 3.25b, c) and 3.1 ML (Fig. 3.25d) of InAs coverage on the Sb-irradiated GaAs buffer layers. Although the Sb-irradiated GaAs layer (Fig. 3.25a) had an atomically flat surface, 2-dimensional wire-like structures appeared on the InAs wetting layer (Fig. 3.25b, c). These wire-like structures were about 2 ML in height and were aligned in the [1$\bar{1}$0] direction.

Figure 3.26 shows the in-plane lattice spacing of InAs grown on GaAs and Sb/GaAs layers as a function of InAs coverage. The in-plane lattice spacings were measured using RHEED during the growth. During normal InAs/GaAs SK growth, the InAs has the same in-plane lattice spacing as the GaAs because of the coherent growth. However, the wire-like InAs structures on the Sb/GaAs layer revealed a large in-plane lattice spacing, which was caused by Sb incorporation. That is, surface segregation of Sb adatoms occurred during the InAs growth [35, 36], and the segregated Sb atoms were incorporated into the InAs wetting layer. According to Bennett's report, similar wire-like structures were observed in Sb-containing compound semiconductor (ex. InSb, AlSb,) growth on GaAs [37]. Therefore, InAsSb growth occurred during the InAs growth on Sb/GaAs, and the wire-like structures were spontaneously formed because of strain relaxation. In general, it is well known that, in the SK growth of Ge/Si and InGaAs/GaAs, Sb surfactant suppresses 3D nucleation [38, 39]. However, such wire-like structures provide many step sites, which are preferential sites for 3D nucleation. As a result, high-density InAs QDs were formed, as shown in Fig. 3.25d [40].

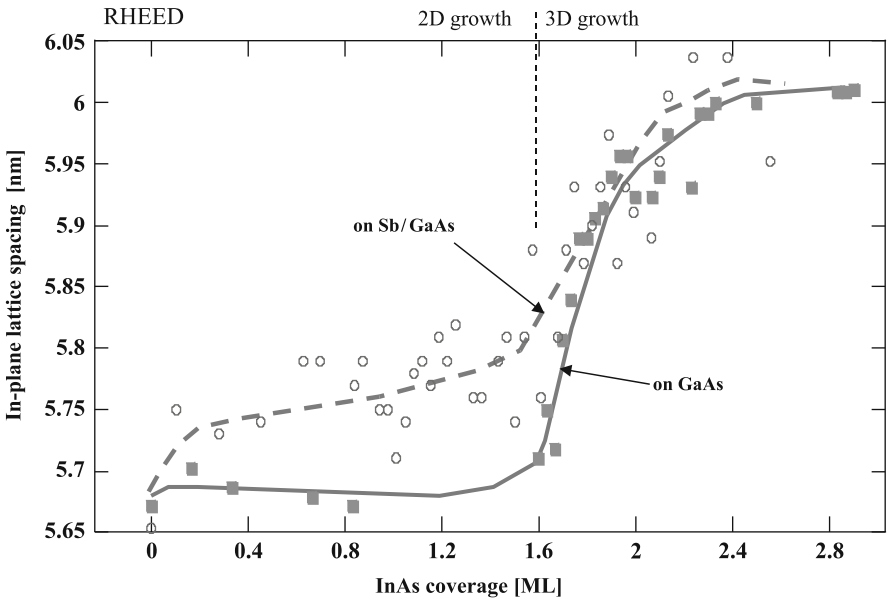

Fig. 3.26 InAs coverage dependence of In-plane lattice spacing of InAs layers, grown respectively on Sb/GaAs and on GaAs. In-plane lattice spacing was evaluated from RHEED pattern

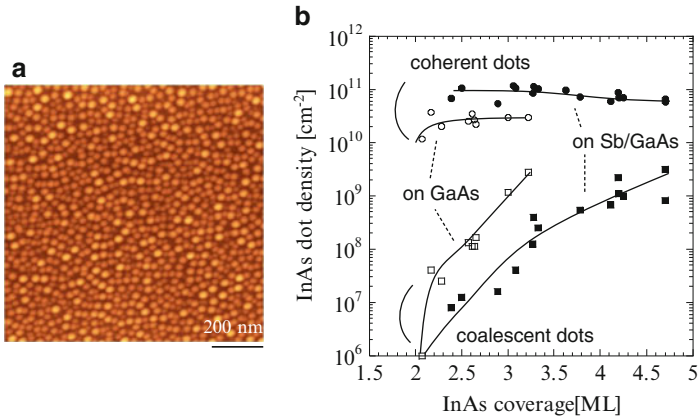

Fig. 3.27 AFM image of high-density InAs QDs on Sb/GaAs (**a**). Relationship between InAs dot density (coherent dots, coalescent dots) and InAs coverage (**b**). InAs dots were grown on GaAs and on Sb/GaAs, respectively

Figure 3.27a shows an AFM image of high-density InAs QDs on Sb/GaAs. The QD density was 1×10^{11} cm^{-2}. There are no giant dots in this image, and it is possible that the segregated Sb surface atoms suppressed QD coalescence. Figure 3.27b shows the coherent QD density and the coalescent dot density for InAs on GaAs and InAs on Sb/GsAs as a function of InAs coverage. The InAs growth conditions

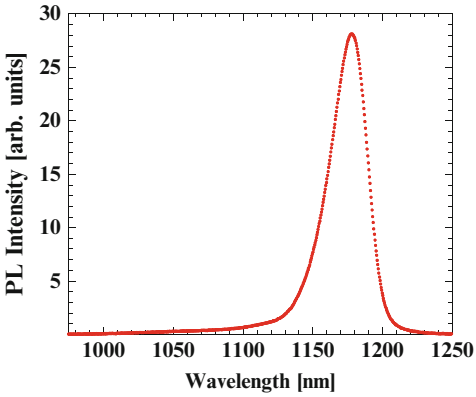

Fig. 3.28 PL spectrum of high-density and high-uniformity InAs QDs, grown on Sb/GaAs

were the same in both cases. In this experiment, the coherent QD density of the Sb/GaAs buffer layer was about three times higher than in a conventional GaAs buffer layer. However, the coalescent dot density on Sb/GaAs was one-tenth of that on GaAs. Figure 3.28 shows a narrow PL spectrum of high-density InAs QDs on Sb/GaAs. The QD density was $1 \times 10^{11}\,\mathrm{cm}^{-2}$, and the PL linewidth was about 28 meV. This Sb-mediated SK growth using Sb-containing GaAs buffer layers is a powerful method for obtaining high-density, high-uniformity InAs QDs with a high crystal quality.

3.5.2 Intermittent Growth of Low-Density InAs/GaAs Quantum Dots

In conventional SK growth, the QD density can be reduced by adjusting the growth conditions, such as by using a lesser extent of growth, a higher growth temperature, and/or a lower growth rate. However, reduction to below $10^8\,\mathrm{cm}^{-2}$ is very difficult because 3D islanding occurs rapidly, and the density increases drastically. Figure 3.29 shows RHEED diffraction-beam intensity vs. growth time for InAs growth on GaAs. In this experiment, the InAs growth was stopped just after the growth mode transition. However, the RHEED diffraction-beam intensity continued to increase despite the growth interruption, and the RHEED spot pattern developed, indicating that the initial 3D islanding was not controllable. In conventional SK growth, since the growth is easily limited by surface strain, the growth species often accumulates at the surface. Hence, even during the growth interruption, residual surface species formed 3D nuclei and/or were incorporated into 3D nuclei.

To precisely control low-density QD growth, an intermittent growth method was proposed [41]. In this growth method, 0.3-ML thick InAs was grown intermittently after 1.5 ML of coverage (wetting layer). The growth was interrupted for 2 (or 3) min between each intermittent growth phase. Figure 3.30 shows RHEED patterns and

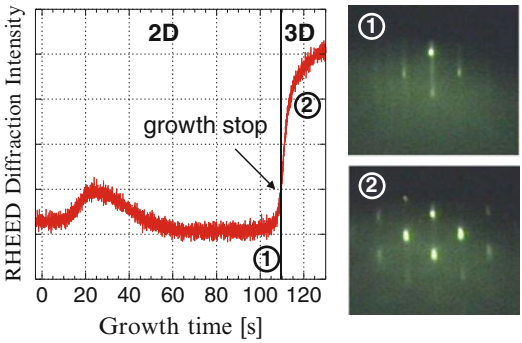

Fig. 3.29 RHEED diffraction-beam intensity as a function of growth time (including growth interruption time). The In flux was stopped at 110 s, and then the growth was interrupted. RHEED patterns were obtained at 105 s (①) and at 120 s (②)

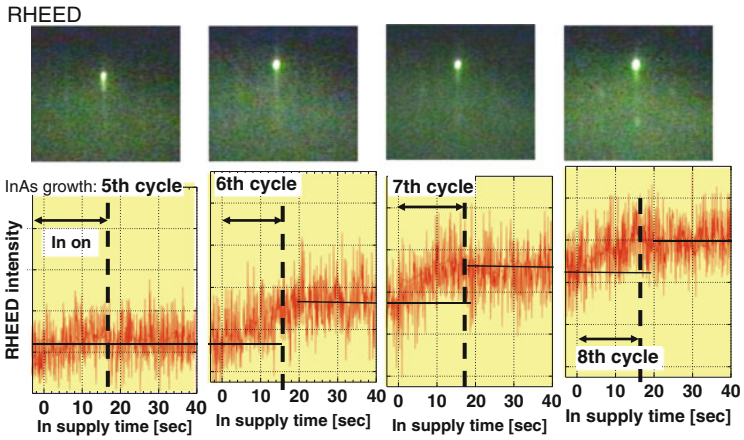

Fig. 3.30 RHEED patterns and RHEED diffraction-beam intensity as a function of intermittent growth cycle number. At each growth cycle, In flux was supplied for 16 s. For more than sixth cycle, diffraction-beam intensity slightly increased during the In supply, and then the intensity was almost kept constant during the growth interruption

diffraction beam intensity as a function of the InAs growth cycle number. Until the fifth cycle, the diffraction beam intensity did not change. At the sixth cycle, the diffraction beam intensity increased slightly, and this increased intensity was maintained during the growth interruption. This indicates that the initial 3D islanding was maintained. In the seventh and eighth cycles, similar changes in the RHEED diffraction-beam intensity and a slight spot pattern were observed. Therefore, the QD density can be controlled by adjusting the number of growth cycles.

Figure 3.31 shows relationships between QD density and the number of growth cycles for two different conditions. As the cycle number increases, the QD density increases monotonically. At 0.018 ML s^{-1} (and G.I. for 3 min), the increase in

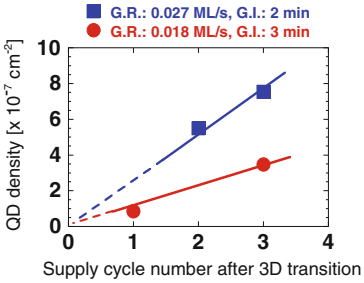

Fig. 3.31 Relationship between InAs-QD density and supply cycle number after 2D–3D transition. (*Filled square*: InAs growth rate of 0.027 ML s^{-1}, growth interruption time of 2 min. *Filled circle*: 0.018 ML s^{-1}, 3 min) The QD density for one supply cycle was 2.5×10^7 cm^{-2} for *filled square* and 1.0×10^7 cm^{-2} for *filled circle*

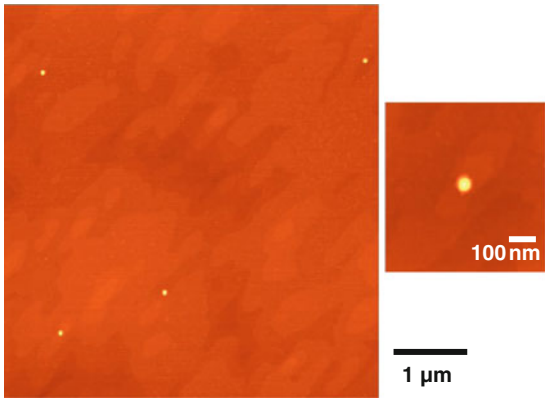

Fig. 3.32 AFM images of low-density InAs QDs with 5.5×10^7 cm^{-2}, grown by the intermittent growth

the QD density per cycle was 1.0×10^7 cm^{-2}. Therefore, InAs QDs with an ultra-low density of 10^7–10^8 cm^{-2} can be controlled step-by-step using an intermittent growth technique. Figure 3.32 shows AFM images of ultra-low density InAs QDs with a density of 5.5×10^7 cm^{-2}. From the RHEED chevron pattern, {110} facets were confirmed on the side walls of the QDs.

Figure 3.33 shows a macroscopic PL spectrum of InAs QDs with an ultra-low density of $5–8 \times 10^7$ cm^{-2}. The substrate was rotated during the 2D growth, and was fixed for observation of the RHEED diffraction-beam intensity during the intermittent growth. A PL peak appeared at about 1,195 nm, and the linewidth was 18 meV, which indicates uniform QD structures. Figure 3.34 shows a microscopic PL spectrum of ultra-low density InAs QDs. There were probably several InAs QDs within the excitation laser spot, which was about 3 μm in diameter. The PL spectrum reveals two peaks due to exciton emissions from two individual QDs with different size. The PL linewidth indicates homogeneous broadening of about 0.9 meV, which was limited in this PL setup. Ultra-low density QDs prepared by intermittent growth are useful to evaluate the characteristics of single QDs.

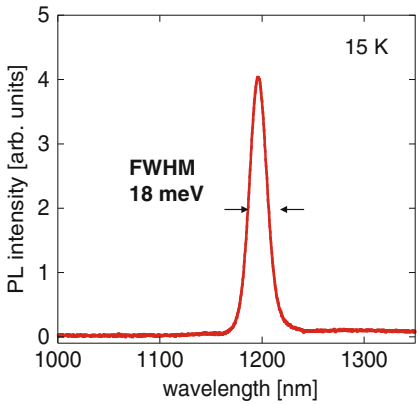

Fig. 3.33 A macroscopic PL spectrum of low-density InAs QDs with 5–8 × 10^7 cm^{-2}, grown by the intermittent growth. PL was measured at 15 K

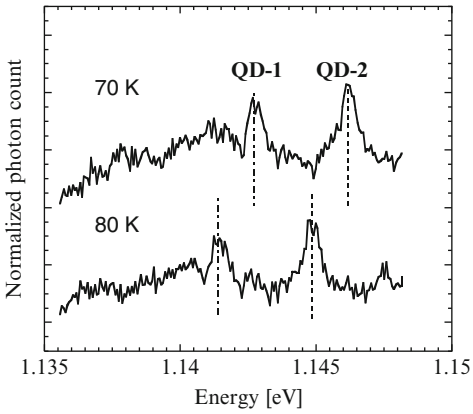

Fig. 3.34 Microscopic PL spectra of low-density InAs QDs, grown by the intermittent growth. PL was measured at 70 and 80 K

3.6 Quantum Dot Array

A QD array structure enables electronic and optical interaction between neighboring QDs. Recently, exciton interactions between QDs have become desirable for certain novel devices [42]. In normal SK growth, the 3D islands are randomly deposited on a surface. However, the self-formation of arranged QDs can be achieved by modification of the underlying layers. In this section, the self-arrangement of vertical and in-plane InAs/GaAs QDs is described.

3.6.1 Vertical Array of InAs/GaAs Quantum Dots

The vertical alignment of QDs has been already demonstrated via stacking growth of QDs with thin spacer layers [43]. For InAs/GaAs QDs, the GaAs capping layer just above the InAs QDs has a tensile strain. Therefore, stacked InAs QDs are preferentially grown above the embedded QDs. Figure 3.35 shows the relative

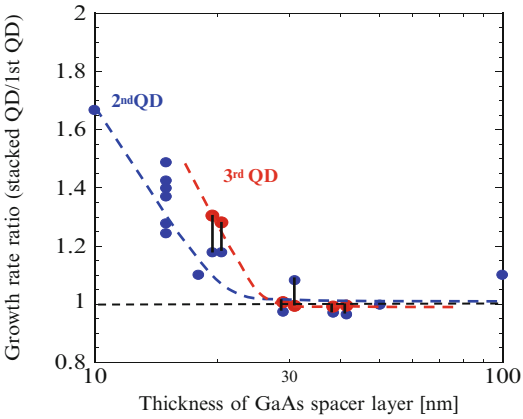

Fig. 3.35 Growth rate ratio of stacked InAs QDs for first QDs as a function of thickness of GaAs spacer layer

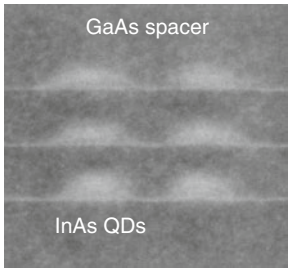

Fig. 3.36 A cross-sectional STEM image of three-stacked InAs QDs. Thickness of the GaAs spacer layer was 15 nm

growth rate of stacked InAs QD layers (second and third QDs) for that of the first QD layer as a function of the thickness of the GaAs spacer layers. In this experiment, the height of the first QD was about 10 nm. When the thickness of the spacer layer was increased above 30 nm, the growth rate of the stacked QD layer was almost the same as that of the first layer. This indicates that the strain interaction of the stacked QDs through the spacer layers becomes weak for spacer layers thicker than 30 nm [44]. When the spacer thickness was decreased below 30 nm, the stacking growth rate was enhanced. In this case, InAs was easily deposited just above the embedded QDs.

Figure 3.36 shows a cross-sectional STEM image of triple-stacked InAs QDs with a 15-nm thick GaAs spacer layer. The stacked QDs are vertically aligned. For closely stacked QDs, it is possible to form an electronic coupling between the stacked QDs. Thus, vertical alignment of the QDs can be obtained by the stacking growth technique using thin spacer layers. It should be noted that the structure of the stacked QDs was different than that of the underlying QDs. Figure 3.37 shows cross-sectional STEM images of double-stacked InAs QDs with different coverage of the second InAs layer (2.5 ML (Fig. 3.37a), 3.3 ML (Fig. 3.37b)). The coverage of the first QDs was 2.5 ML. Since the thickness of the GaAs spacer layer was 15 nm, the second QDs were stacked just above the first QDs. Although the RHEED chevron pattern revealed (110) facets during the first QD growth, high index planes

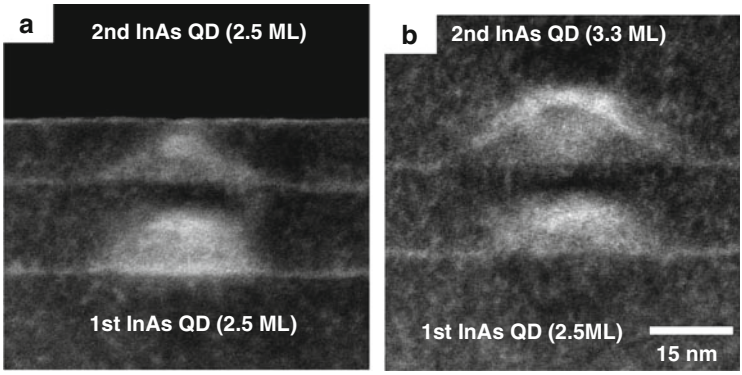

Fig. 3.37 Cross-sectional STEM images of double-stacked InAs QDs with different second-InAs coverage of 2.5 ML (**a**) and 3.3 ML (**b**). The first-InAs coverage was 2.5 ML

of (136) or (137) were observed for 2.5-ML thick second InAs layer coverage (Fig. 3.37a). In this stacking growth, a second InAs layer coverage of more than 3 ML was needed to obtain the same QD shape with (110) facets. However, the volume of the second QDs was larger than that of the first QDs, as shown in Fig 3.37b. This modification of the stacked QDs can be attributed to strain interaction with the underlying QDs.

To achieve vertical alignment of the QDs without strain interaction, strain compensation layers were introduced as a spacer layer between the stacked QDs [45]. For example, an InGaAsP spacer layer was used in the stacking growth of InAs QDs on InP substrates. In this growth system, 60 QD layers were vertically stacked [46]. For InAs QDs on a GaAs substrate, a GaNAs spacer layer was investigated to reduce the residual strain [47].

3.6.2 In-Plane Arrays of InAs/GaAs Quantum Dots

In-plane ordering of QDs has been demonstrated by the selective growth of QDs on patterned substrates [48]. In other studies, the self-formation of in-plane arranged QDs has been attempted using a stacked growth technique [49, 50] or high index plane substrates [51]. For site control and arrangement of QDs, strain control of the underlying buffer layers is important. 1D and 2D in-plane arrangements of InAs QDs on GaAs(001) substrates are described below.

The nucleation of 3D islands is related to the surface strain and surface undulation of the underlying buffer layers. Thereby, strained buffer layers have been used for the selective growth of QDs: InP QDs on an InGaP/GaAs buffer layer [52], Ge dots on an SiGe/Si buffer layer [53], and InAs QDs on an InGaAs/GaAs buffer layer [54]. Figure 3.38 shows AFM images of InAs QDs on a conventional GaAs buffer layer (Fig. 3.38a), and on a GaAs(70–80 nm)/$In_{0.16}Ga_{0.84}As$(175 nm)/GaAs

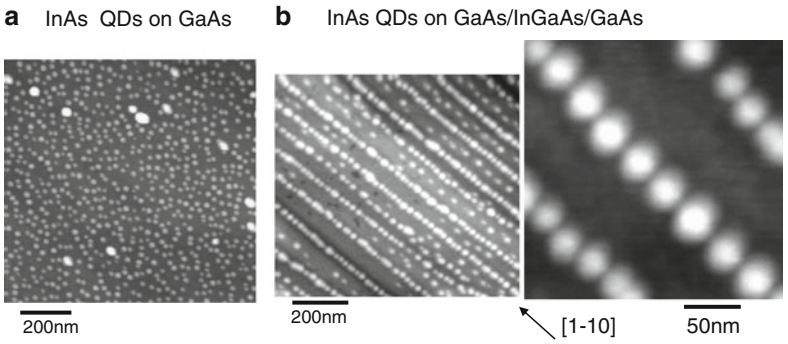

Fig. 3.38 AFM images of InAs QDs, grown, respectively, on GaAs buffer layer (**a**) and on GaAs/InGaAs/GaAs buffer layer (**b**). InAs QD chains were aligned along [1 $\bar{1}$ 0] direction on the GaAs/InGaAs/GaAs (**b**)

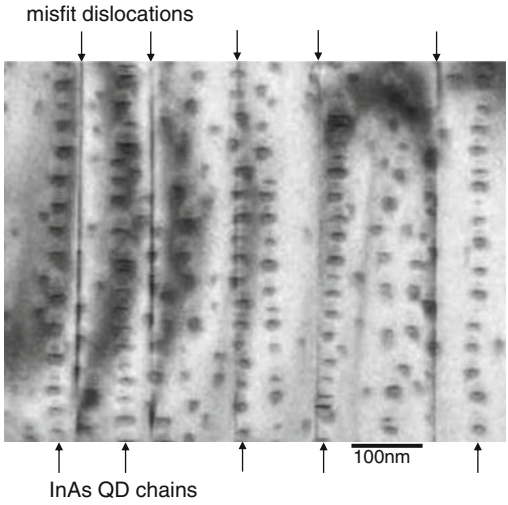

Fig. 3.39 A plan-TEM image of InAs QDs/GaAs/InGaAs/GaAs sample. In this image, QD chains and misfit dislocations were observed

buffer layer (Fig. 3.38b). In the conventional SK growth, 3D InAs islands were randomly deposited on the GaAs buffer layers (Fig. 3.38a). However, with a GaAs/InGaAs/GaAs buffer layer (Fig. 3.38b), the InAs QDs were periodically aligned in the [1$\bar{1}$0] direction [55]. The periodic distance between the QD chains ranged from 100 to 150 nm. The self-formation of the QD chain structure can be attributed to misfit dislocations at the InGaAs/GaAs heterointerface.

Figure 3.39 shows a planar TEM image of InAs QD chains on a GaAs/InGaAs/GaAs buffer layer. The image reveals misfit dislocation lines at the upper GaAs/InGaAs heterointerface. No threading dislocations were observed in the buffer layer. Misfit dislocations were preferentially generated along the [1$\bar{1}$0]

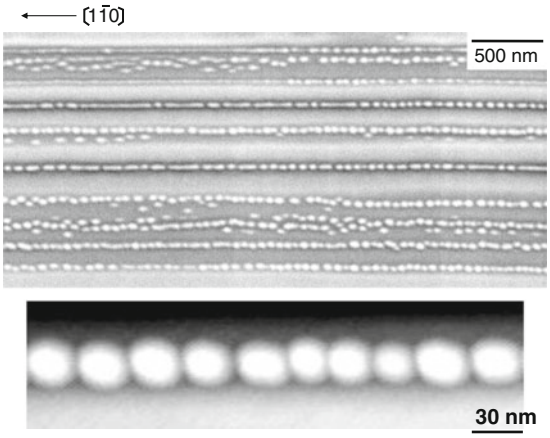

Fig. 3.40 SEM and AFM images of InAs QD chains grown on GaAs/InGaAs/GaAs buffer layer. Length of the QD chains were several micro-meters

direction, as opposed to the [110] direction, because of the anisotropic residual strain in the buffer layer [56]. The [1$\bar{1}$0] misfit dislocations were arranged in an orderly manner, and had a lateral spacing of about 100–150 nm. The lateral ordering of the misfit dislocations was mainly due to periodic corrugation of the InGaAs layer. As shown in Fig. 3.39, the periodic QD chains aligned near the misfit dislocation lines along the [1$\bar{1}$0] direction. In addition, the line number of the QD chains was almost the same as that of the misfit dislocations. Therefore, the lateral ordering of the misfit dislocations probably induced the self-formation of periodic QD chains. By optimizing the growth conditions, uniform InAs QD chains several micrometers in length were demonstrated on GaAs/InGaAs/GaAs buffer layers [57], as shown in Fig. 3.40. Figure 3.41 shows PL spectra of normal InAs QDs on a GaAs buffer layer (Fig. 3.41a), and those of InAs QD chains on a GaAs/InGaAs/GaAs buffer layer (Fig. 3.41b). The InAs QDs and GaAs capping layers of both samples were grown under the same growth conditions. The PL peak of the InAs QD chains was at 1,200 nm, which was longer than that of the normal InAs QDs. The PL linewidth of the QD chains (about 47 meV) was wider than that of the normal QDs (about 24 meV). The red shift and broadening in the PL spectra of the QD chains were mainly attributed not only to size fluctuation of the QDs, but also to the lateral coupling of QDs along the chain.

The self-formation of a 2D QD array is more difficult in conventional SK growth without stacked layer structures and high-index plane substrates. In addition, high QD density and high uniformity of the QD structure are required for the fabrication of 2D-arranged QDs. In 2007, the 2D self-arrangement of high-density InAs QDs was demonstrated using GaAsSb/GaAs(001) buffer layers [58]. Figure 3.42 shows AFM images of 2D and 3D InAs islands on GaAs(2 ML)/GaAsSb(10 ML, Sb flux ratio of 0.13)/GaAs(001) buffer layers. For 1.45 ML of InAs coverage (Fig. 3.42a), a number of small islands were formed, and several [010] steps

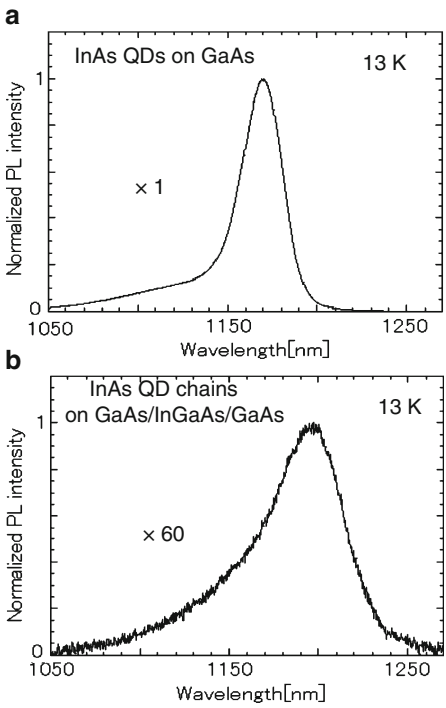

Fig. 3.41 PL spectra of InAs QDs on GaAs buffer layer (**a**) and InAs QD chains on GaAs/InGaAs/GaAs buffer layer (**b**). Both InAs QDs were embedded by GaAs capping layers. PL was measured at 13 K

appeared in addition to the [1$\bar{1}$0] steps. When the InAs coverage was above 1.5 ML, the growth mode shifted from 2D to 3D growth. After the InAs growth at 1.6 ML (Fig. 3.42b), the initial dots were formed near the step edges. In addition, many holes and grooves of nanometer size were observed. The diameter of the nanoholes and the width of the nanogrooves were about 20–30 nm. The depths of these nanoholes and nanogrooves were less than about 3 nm, indicating that the nanoholes and the nanogrooves were formed in the strained GaAsSb buffer layer and did not reach the underlying GaAs layer. Therefore, the formation of the nanoholes and nanogrooves was caused by desorption of the unstable, highly-strained GaAsSb during the InAs growth. In Fig. 3.42b, most of the nanoholes and nanogrooves are located next to the dots. In particular, 1D dot chains were formed along the [010] step edges. As the InAs growth proceeded, the dot density increased, and the density of nanoholes and nanogrooves also increased (Fig. 3.42c). The high dot density area coincided with the high nanohole density area. This suggests that the dot formation induced nanohole formation, because the InAs dots stressed the GaAsSb layer; the dot essentially played the role of a stressor. In addition, the desorbed GaAsSb from the nanoholes reformed small Sb-containing islands near the nanoholes. In fact, small 2D islands were observed beside the nanoholes (Fig. 3.42b, c). Such Sb-containing 2D islands would provide preferential sites for 3D nucleation. Therefore, it is also possible that the nanoholes induced nearby dot formation. Furthermore, for 2.0 ML of coverage (Fig. 3.42c), remarkably, a 2D arrangement of InAs dots

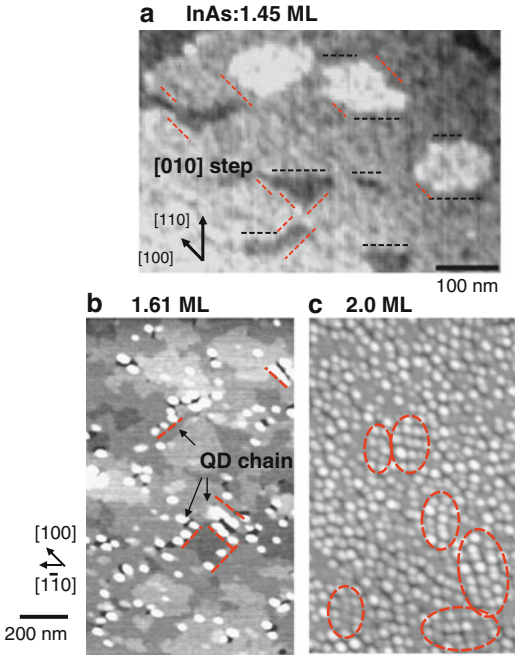

Fig. 3.42 AFM images of 2D and 3D InAs islands grown on GaAs/GaAsSb/GaAs buffer layer. InAs coverage were 1.45 ML (**a**), 1.61 ML (**b**), and 2.0 ML (**c**)

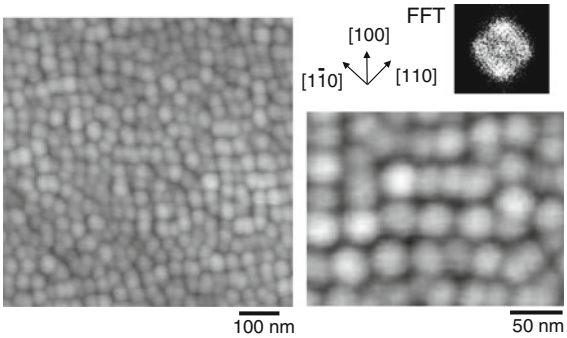

Fig. 3.43 AFM images of 2D array of InAs QDs, grown on GaAs/GaAsSb/GaAs buffer layer. InAs coverage was 2.6 ML. Inset is a fast Fourier transform (FFT) image, which indicates 2D periodic pattern of squared QD array for ⟨010⟩ direction

was partially formed. In the in-plane-arranged area, the dots mainly aligned along the [010] direction. Therefore, on the basis of these results and considerations, it can be concluded that the in-plane arrangement of the dots originated from the dot chains and nanogrooves, which were aligned along the [010] edges. Figure 3.43 shows AFM images of in-plane InAs QDs with 2.6 ML of coverage, grown on a

GaAs/GaAsSb/GaAs(001) buffer layer. The inset is a fast Fourier transform (FFT) image of the AFM image, which indicates 2D periodic pattern of squared QD array for the ⟨010⟩ direction. The QD density was about 1×10^{11} cm^{-2}, and the QDs were partially arranged along the ⟨010⟩ direction. Control of the [010] step structure is important for the wide-area 2D arrangement of QDs.

3.7 Conclusion

In this chapter, we reviewed the growth characteristics and optical properties of InAs/GaAs QDs grown by MBE. To develop novel nanophotonic QD devices, precise control of the QD structure is required. Based on SK mode growth of InAs/GaAs QDs, the growth conditions, the growth structures, and post-growth annealing were extensively investigated for the achievement of narrow inhomogeneous broadening and wide control of the QD density and energy levels. Uniform InAs/GaAs QDs were achieved by the self size-limiting effect, optimized capping growth, and closely-stacked growth using nanoholes. High-density InAs QDs with a narrow size distribution were formed by Sb-mediated growth, which is an attractive method for suppressing QD coalescence. For ultra-low density InAs QDs, an intermittent growth method was presented, and the QD density was precisely controlled by real time RHEED observation. Furthermore, vertical and in-plane arrangements of InAs/GaAs QDs were attempted by using strain-controlled underlying layers. Stacked growth produced vertically aligned QDs. 1D InAs-QD chains were spontaneously formed along the [1$\bar{1}$0] direction on GaAs/InGaAs/GaAs(001) buffer layers, and a 2D arrangement of InAs QDs was demonstrated using GaAsSb/GaAs(001) buffer layers.

References

1. L. Goldstein, F. Glas, J.Y. Marzin, M.N. Charasse, G. Le Roux, Appl. Phys. Lett. **41**, 1099 (1985)
2. D.J. Eaglesham, M. Cerullo, Phys. Rev. Lett. **4**, 1943 (1990)
3. A.M. Ceschin, J. Massies, J. Cryst. Growth **114**, 693 (1991)
4. K. Yamaguchi, T. Kaizu, K. Yujobo, Y. Saito, J. Cryst. Growth **237–239**, 1301 (2002)
5. D. Bimberg, M. Grundmann, N.N. Ledentsov, in chapter 4, *Growth and Structural Characterization of Self-Organized quantum dots*. Quantum Dot Heterostructures (Wiley, New York, 1999)
6. R. Murray, D. Childs, S. Malik, P. Siverns, C. Roberts, J. Hartmann, P. Stavrinou, Jpn. J. Appl. Phys. **38**, 528 (1999)
7. K. Yamaguchi, K. Yujobo, T. Kaizu, Jpn. J. Appl. Phys. **39**, L1245 (2000)
8. K. Yamaguchi, T. Kaizu, K. Yujobo, Y. Saito, J. Cryst. Growth **237–239**, 1301 (2002)
9. M. Takahasi, T. Kaizu, J. Mizuki, Appl. Phys. Lett. **88**, 101917 (2006)
10. A.-L Barabási, Appl. Phys. Lett. **70**, 2565 (1997)
11. T. Kaizu, K. Yamaguchi, Jpn. J. Appl. Phys. **42**, 4166 (2003)
12. J.M. García, G. Medeiros-Ribeiro, K. Schmidt, T. Ngo, J.L. Feng, A. Lorke, J. Kotthaus, P.M. Petroff, Appl. Phys. Lett. **71**, 2014 (1997)

13. Y. Saito, R. Ohtsubo, K. Yamaguchi, Inst. Phys. Conf. Ser. **170**, 531 (2002)
14. P.B. Joyce, T.J. Krzyzewski, P.H. Steans, G.R. Bell, J.H. Neave, T.S. Jones, Surf. Sci. **492**, 345 (2001)
15. T. Kitamura, R. Ohtsubo, M. Murayama, T. Kuroda, and K. Yamaguchi, A. Tackeuchi: Phys. Status Solidi (C0) 1165 (2003)
16. M. Murayama, R. Ohtsubo, T. Kitamura, T. Kuroda, K. Yamaguchi, A. Tackeuchi, Phys. Status Solidi (C0) 1145 (2003)
17. A. Tackeuchi, R. Ohtsubo, K. Yamaguchi, M. Murayama, T. Kitamura, T. Kuroda, T. Takagahara, Appl. Phys. Lett. **84**, 3576 (2004)
18. K. Mukai, M. Sugawara, Appl. Phys. Lett. **74**, 3963 (1999)
19. S. Tonomura, K. Yamaguchi, J. Appl. Phys. **104**, 054909 (2008)
20. M. Bayer, P. Hawrylak, K. Hinzer, S. Fafard, M. Korkusinski, Z.R. Wasilewski, O. Stern, A. Forchel, Science **291**, 451 (2001)
21. P.B. Joyce, T.J. Krzyzewski, G.P. Bell, T.S. Jones, Appl. Phys. Lett. **79**, 3615 (2001)
22. T. Satoh, K. Yamaguchi, J. Appl. Phys. **44**, 2672 (2005)
23. N. Tsukiji, K. Yamaguchi, J. Cryst. Growth. **301–302**, 849 (2006)
24. A.O. Kosogov, P. Werner, U. Goesele, N.N. Ledentsov, D. Bimberg, V.M. Ustinov, A. Yu Egorov, A.E. Zhukov, P.S. Kopev, N.A. Bert, Appl. Phys. Lett. **69**, 3072 (1996)
25. S.J. Xu, X.C. Wang, S.J. Chua, C.H. Wang, W.J. Fan, J. Jiang, X.G. Xie, Appl. Phys. Lett. **42**, 3335 (1998)
26. A. Babinski, J. Jasinski, R. Bozek, A. Szepielow, J.M. Baranowski, Appl. Phys. Lett. **79**, 2576 (2001)
27. Y. Kobayashi, K. Yamaguchi, Appl. Surf. Sci. **244**, 88 (2005)
28. D. Bhattacharyya, A. Saher Helmy, A.C. Bryce, E.A. Avrutin, J.H. Marsh, J. Appl. Phys. **88**, 4619 (2000)
29. R. Leon, Y. Kim, C. Jagadish, M. GaI, J. Zou, D.J.H. Cockayne, Appl. Phys. Lett. **69**, 1888 (1996)
30. S. Malik, C. Roberts, R. Murray, M. Pate, Appl. Phys. Lett. **71**, 1987 (1997)
31. O.P. Kowalski, C.J. Hamilton, S.D. McDougall, J.H. Marsh, A.C. Bryce, C.C. Button, J.S. Roberts, Appl. Phys. Lett. **72**, 581 (1998)
32. K. Yamaguchi, T. Kanto, Self-Assembled InAs Quantum Dots on GaSb/GaAs(001) Layers by Molecular Beam Epitaxy. *14th International Conference on Crystal Growth/12th International Conference on Vapor Growth and Epitaxy (ICCG-14/ICVGE-12)*, Grenoble, 9–13 Aug 2004, T03-3, p. 644
33. K. Yamaguchi, T. Kanto, J. Cryst. Growth **275**, e2269 (2005)
34. K. Yamaguchi, T. Kaizu, K. Yujobo, Y. Saito, J. Cryst. Growth **237–239**, 1301 (2002)
35. R. Magri, A. Zunger, Phys. Rev. B **65**, 165302 (2002)
36. T. Nakai, K. Yamaguchi, Jpn. J. Appl. Phys. **44**, 3803 (2005)
37. B.R. Bennett, B.V. Shanabrook, P.M. Thibado, L.J. Whitman, R. Magno, J. Cryst. Growth **175/176**, 888 (1997)
38. B. Voigtlander, A. Zinner, T. Weber, H.P. Bonzel, Phys. Rev. B **51**, 7583 (1995)
39. T. Matsuura, T. Miyamoto, T. Kageyama, M. Ohta, Y. Matsui, T. Furuhata, F. Koyama, Jpn. J. Appl. Phys. **43**, L605 (2004)
40. T. Ohta, T. Kanto, K. Yamaguchi, Jpn. J. Appl. Phys. **45**, 3427 (2006)
41. P. Pachakapat, K. Yamaguchi, Self-Formation Control of Low-Density InAs Quantum-Dots. *The 34th International Symposium on Compound Semiconductors (iscs2007)*, Kyoto, 15–18 Oct 2007, p. 172
42. M. Ohtsu, T. Kawazoe, T. Yatsui, M. Naruse, IEEE J. Sel. Top. Quant. Electron. **14**, 1404 (2008)
43. J. Tersoff, C. Teichert, M.G. Lagally, Phys. Rev. Lett. **76**, 1675 (1996)
44. Y. Suzuki, T. Kaizu, K. Yamaguchi, Physica **E 21**, 555 (2004)
45. K. Akahanea, N. Ohtania, Y. Okada, M. Kawabe, J. Cryst. Growth **245**, 31 (2002)
46. K. Akahane, N. Yamamoto, M. Tsuchiya, Appl. Phys. Lett. **93**, 041121 (2008)
47. R. Oshima, A. Takata, Y. Okada, Appl. Phys. Lett. **93**, 083111 (2008)

48. S. Kiravittaya, O.G. Schmidt, Appl. Phys. Lett. **86**, 206101 (2005)
49. G. Springholz, V. Holy, M. Pinczoltis, G. Bauer, Science **282**, 734 (1998)
50. G.S. Solomon, Appl. Phys. Lett. **84**, 2073 (2004)
51. K. Akahane, T. Kawamura, K. Okino, H. Koyama, S. Lan, Y. Okada, M. Kawabe, Appl. Phys. Lett. **73**, 3411 (1998)
52. K. Hausler, K. Eberl, F. Noll, A. Trampert, Phys. Rev. B **54**, 4913 (1996)
53. Y.H. Xie, S.B. Samavedam, M. Bulsara, T.A. Langdo, E.A. Fitzgerald, Appl. Phys. Lett. **71**, 3567 (1997)
54. K. Yamaguchi, E. Waki, H. Hasegawa, Jpn. J. Appl. Phys. **36**, L871 (1997)
55. K. Yamaguchi, K. Kawaguchi, T. Kanto, Jpn. J. Appl. Phys. **41**, L996 (2002)
56. K.L. Kavanagh, M.A. Capano, L.W. Hobbs, J.C. Barbour, P.M.J. Maree, W. Schaff, J.W. Mayer, D. Pettit, J.M. Woodall, J.A. Stroscio, R.M. Feenstra, J. Appl. Phys. **64**, 4843 (1988)
57. T. Kanto, K. Yamaguchi, Jpn. J. Appl. Phys. **44**, 7690 (2005)
58. T. Kanto, K. Yamaguchi, J. Appl. Phys. **101**, 094901 (2007)

Chapter 4
Near-Field Optical Imaging of Wavefunctions and Optical Fields in Plasmonic Nanostructures

Kohei Imura and Hiromi Okamoto

Abstract Plasmonic nanostructures exhibit unique optical properties, and fundamental studies of these structures are relevant to wide range of research areas, both fundamental and applied. Potential applications of the plasmonic nanostructures originate from their ability to confine (and sometimes propagate as well) optical fields in nanometer scales, and are closely related to the static and dynamic properties of plasmonic waves. In this chapter, visualization of wavefunctions and optical fields in plasmonic nanostructures using near-field linear and non-linear optical methods is described.

4.1 Introduction

The unique colors of noble metal nanoparticles have been used as dyes for various items since ancient times. Red and yellow colors in stained glasses arise from the scattering and absorption of light by gold and silver nanoparticles, respectively. These optical properties of noble metal nanoparticles originate from the collective oscillation of free electrons (plasma) known as plasmons [1–3]. Whereas plasma in bulk material cannot be optically excited because of the momentum mismatch between photons and electrons [4], plasmons in nanoparticles, the sizes of which are smaller than those of the wavelengths of light, are optically excited because the momentum mismatch is compensated by the spatial frequency of the nanoparticle and also by the highly distorted optical field in the vicinity of the nano-particle. Optically excited plasmons are hybrid modes of optical fields and

K. Imura (✉)
Department of Chemistry and Biochemistry, School of Advanced Science and Engineering, Waseda University, 3-4-1 Okubo, Shinjuku, Tokyo 169-8555, Japan
and
PRESTO, Japan Science and Technology Agency, 4-1-8 Honcho, Kawaguchi, Saitama 332-0012, Japan
e-mail: imura@waseda.jp

M. Ohtsu (ed.), *Progress in Nanophotonics 1*, Nano-Optics and Nanophotonics,
DOI 10.1007/978-3-642-17481-0_4,

the electronic oscillations and thus are called as plasmon-polaritons [5]. Herein, the plasmon-polariton is simply called a plasmon for convenience.

Plasmons induce a large polarization in the nanoparticle and confine the optical field on a nanometer scale. The confinement results in the enhancement of the field. The enhanced optical field has been used to amplify Raman scattering from molecules adsorbed on the nanoparticle [6]. Since the discovery of surface enhanced Raman scattering (SERS) [7–9], much research has been devoted to developing chemical- and biological-sensors based on SERS because the vibrational bands in Raman spectra are useful for the identification of molecules. In 1997, single molecule sensitivity SERS was reported [10, 11]. Since then, the research area has been further pursued to attain ultimate sensitivity for sensing applications and also to elucidate the enhancement mechanism of the SERS. Currently, applications of the enhanced field are expanding from sensing [12] to nano-optical devices [13–15], imaging [16, 17], and novel photochemical reactions [18, 19]. Plasmon-based materials also have a large impact on basic science [20–27]. The negative refractive index of meta-materials and super resolution using plasmons have been reported [28, 29], for example.

As described above, plasmons have attracted much attention not only in applied science but also in basic science. For understanding and controlling the functions of plasmons, it is essential to reveal the spatial features of plasmon wavefunctions and optical fields. To study the spatial characters of a certain object, an optical microscope is useful in many occasions. The spatial resolution of optical microscopes is limited to about 1 μm in the visible range, however [30, 31]. Spatial features of plasmon wavefunctions are smaller than that achieved by optical microscopy, and thus optical microscopy cannot be useful for the visualization of plasmon wavefunctions and optical fields. Visualization of the smaller features beyond the resolution of optical microscopy is feasible by means of the recently developed near-field optical methods [32–34]. Near-field optical microscope images the object using the optical contrast mechanism very different from those of conventional microscope [35]. The conventional microscope uses an objective lens with a high numerical aperture (NA) to achieve high resolution. However, because a lens is used, the diffraction of light is always involved [30], and thus the spatial resolution is limited by the diffraction limit of light. Near-field optical microscopes, on the other hand, do not use lenses, and thus their spatial resolution is not limited by the diffraction limit. Near-field optical microscopes can achieve much higher spatial resolutions down to the 10-nm level [36, 37], and possess the potential to visualize wavefunctions of elemental excitations [38–40]. In this review, visualization of plasmon wavefunctions and optical fields using various near-field optical methods will be described.

4.2 Optical Properties of Nanoparticles

Optical properties of nanoparticles can be elucidated by solving the electromagnetic wave equations, considering the boundary conditions near the nanoparticles. In 1908, Mie formulated vector wave equations for spherical nanoparticles and

obtained rigorous solutions for them [41]. This is known as Mie theory. Mie theory predicts the scattering and absorption properties of spherical nanoparticles regardless of the particles' size and the material. For example, Mie theory predicts that a spherical gold nanoparticle of a diameter of 20 nm shows a plasmon resonance near 520 nm and that the resonance shifts to the longer wavelength side with the increase of the diameter. The theory also predicts that the scattering and absorption cross-sections scale linearly and quadratically with the particle volume, respectively. These predictions are confirmed to be correct experimentally.

As long as small spherical nanoparticles ($<\lambda/20$) are concerned, dipolar approximation is applicable to obtain optical properties, instead of solving the complex vector wave equations. As a typical example, here we consider a spherical nanoparticle of diameter a illuminated by a plane wave. Upon illumination, polarization is induced in the nanoparticle and is proportional to the incident field (E_0), the dielectric constant of the surrounding material, and the polarizability of the nanoparticle as follows.

$$P = \epsilon_{\mathrm{m}} \alpha E_0 \tag{4.1}$$

The polarizability can be obtained by considering the boundary conditions of the scalar potential near the particle,

$$\alpha = 4\pi a^3 \frac{\epsilon - \epsilon_{\mathrm{m}}}{\epsilon + 2\epsilon_{\mathrm{m}}} \tag{4.2}$$

The induced polarization re-radiates the electromagnetic energy into the far-field. Extinction and scattering cross-sections are given by the following relations, respectively.

$$C_{\mathrm{ext}} = k\,\mathrm{Im}(\alpha) \tag{4.3}$$

$$C_{\mathrm{sca}} = \frac{k^4}{6\pi} |\alpha|^2 \tag{4.4}$$

Because the extinction cross-section is a sum of the absorption and the scattering cross-sections, the absorption cross-section is obtained by subtracting the scattering from the extinction.

$$C_{\mathrm{abs}} = C_{\mathrm{ext}} - C_{\mathrm{sca}} \tag{4.5}$$

For a smaller nanoparticle, the scattering cross-section is much smaller than the absorption cross-section, and thus $C_{\mathrm{abs}} \sim C_{\mathrm{ext}}$. From (4.2)–(4.4), it is revealed analytically that the absorption and scattering cross-sections are proportional to the particle volume and its square, respectively.

Mie theory gives the rigorous solutions of wave equations only for spherical nanoparticles. For particles with other shapes like ellipsoids, Mie theory cannot be applied, and treatment with the dipolar approximation is useful to discuss the optical properties of the particle qualitatively. By taking the shape-dependent depolarization factor into account, the polarizability of the ellipsoid can be obtained as a form similar to that of the sphere [42].

$$\alpha = V \frac{\epsilon - \epsilon_{\mathrm{m}}}{\epsilon_{\mathrm{m}} + L_i(\epsilon - \epsilon_{\mathrm{m}})}, \tag{4.6}$$

where V is the volume of the ellipsoid and L_i is the geometrical factor for one of the semi-principle axes of the spheroid.

$$L_1 + L_2 + L_3 = 1 \tag{4.7}$$

The geometrical factors satisfy the above relation, and thus for a sphere in which three principal axes are identical, L_i is equal to 1/3. Substitution of $L_1 = 1/3$ in (4.6) yields the same formula as that of (4.2).

The spheroid is a special kind of ellipsoid in which two principal axes are identical to each other, and therefore only one of the geometrical factors is independent. For a prolate spheroid ($L_1 < L_2 = L_3$), the geometrical factor is obtained by the following equations [43].

$$L_1 = \frac{1 - e^2}{e^2}\left(-1 + \frac{1}{2e}\ln\frac{1+e}{1-e}\right) \tag{4.8}$$
$$e^2 = 1 - \frac{b^2}{a^2},$$

where a and b denote half-lengths of the major and minor axes of the spheroid, respectively. As is understood from (4.8), the geometrical factor changes with the aspect ratio (a/b) of the prolate spheroid. For an oblate spheroid ($L_1 = L_2 < L_3$), similarly, the geometrical factor is dependent on the aspect ratio (a/c where c is half-length of the minor axis).

$$L_1 = \frac{g(e)}{2e^2}\left(\frac{\pi}{2} - \tan^{-1} g(e)\right) - \frac{g^2(e)}{2} \tag{4.9}$$
$$g(e) = \left(\frac{1 - e^2}{e^2}\right)^{1/2}, \quad e^2 = 1 - \frac{c^2}{a^2}$$

When the particle size becomes comparable to the wavelength of light, a retardation effect occurs and has to be taken into account in analysis [44]. Radiation damping becomes significant as the particle volume increases. These factors can be taken into account in the following equation.

$$\alpha = V \frac{1}{\dfrac{\epsilon - \epsilon_{\mathrm{m}}}{\epsilon_{\mathrm{m}} + L_i(\epsilon - \epsilon_{\mathrm{m}})} - \dfrac{k^2}{b}\dfrac{V}{4\pi} - \dfrac{2}{3}ik^3\dfrac{V}{4\pi}} \tag{4.10}$$

On the right-hand side of the equation, the second and third terms in the denominator denote the retardation and radiation damping effects, respectively.

For particles with other shapes, the optical properties are numerically calculated by solving the Maxwell equations. For this purpose, the finite-difference

time-domain (FDTD) method [45], discrete dipole approximation (DDA) method [46], Green dyadic methods [47, 48], etc., have been developed. FDTD calculation is based on the time-evolution of the electromagnetic wave in the scattering system, and dynamical information of the electromagnetic wave can be obtained in addition to static properties. However, the discretization of the scatterer sometimes induces artifacts due to a finite size of the mesh, and thus careful operation is required to extract the genuine optical properties of the particle.

4.2.1 Optical Properties of Ensemble of Nanoparticles

Figure 4.1 shows extinction spectra for spherical gold nanoparticles, with diameters of 20 and 100 nm, suspended in water. Gold nanoparticles with diameters of 20 and 100 nm exhibit broad extinction bands near 520 and 580 nm, respectively. Spectral features of the particles are well reproduced by Mie theory (Fig. 4.1b), and the bands are assigned to plasmon resonances. As mentioned, Mie theory gives rigorous solutions for spherical nanoparticles, and thus discrepancy between the observation and

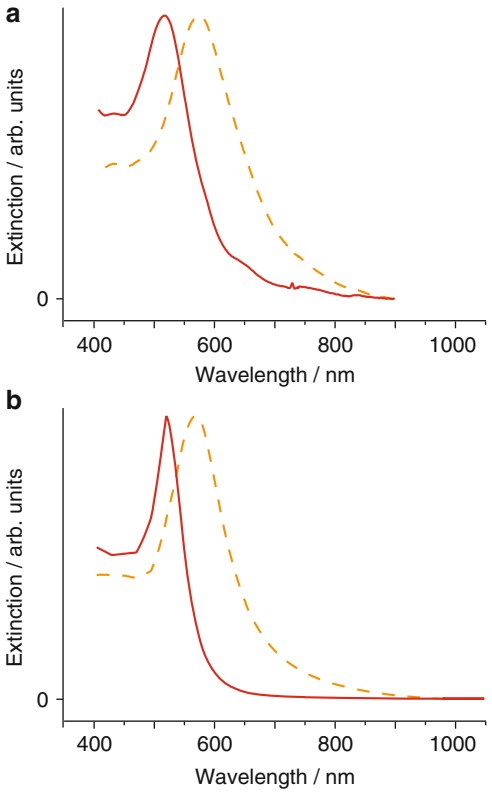

Fig. 4.1 Far-field extinction spectra of spherical gold nanoparticles in water solution. *Solid line*: 20 nm. *Dotted line*: 100 nm. (**a**) Observation and (**b**) calculation by Mie theory

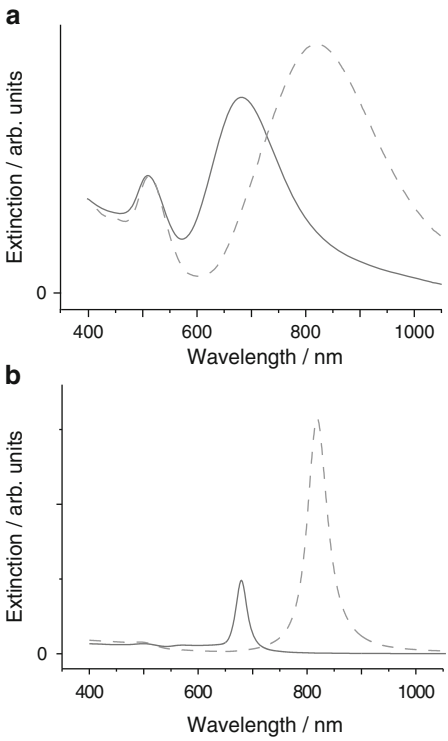

Fig. 4.2 Far-field extinction spectra of gold nanorods in water solution. *Solid line*: aspect ratio ∼3. *Dotted line*: aspect ratio ∼4. (**a**) Observation and (**b**) calculation by (4.6)–(4.8)

calculation is attributable to inhomogeneity (distribution of the size and shape) of the sample.

Figure 4.2 shows extinction spectra of gold nanorods in water. The spectrum shows two bands in the visible to near-infrared region. The peak position of the intense band appearing in the near-infrared region depends on the aspect ratio of the nanorod and shifts toward the longer wavelength side with the increase of the aspect ratio, while the other band appearing near 520 nm depends little on the aspect ratio. The extinction band observed in the long-wavelength region is assigned to the plasmon resonance polarized along the long axis of the nanorod. The other band near 520 nm is assigned to the plasmon resonance polarized across the long axis of the nanorod. These are called longitudinal and transverse plasmon modes, respectively. The dependence of the aspect ratio on the longitudinal plasmon resonance is qualitatively reproduced by simulations using (4.6)–(4.8), as shown in Fig. 4.2b. The observed bandwidths are broader than the calculated ones because of the inhomogeneity of the sample.

Extinction spectra of single silver nanodisks have been reported [49]. The spectra shows an extinction band in the visible to near-infrared region that shifts toward the longer wavelength with the increment of the aspect ratio defined as (diameter)/(thickness), similar to the gold nanorods. The spectral bandwidth is broader than the gold nanorods. Since the sample is a single nanoparticle, the broad

bandwidth is not due to the inhomogeneity of the sample but due to the volume damping effect. The observed spectral features are well reproduced by the DDA simulations. In the simulation, the extinction band was assigned to the plasmon mode excited on the surface of the disk.

4.3 Plasmon Wavefunctions

Spectral features of spherical nanoparticles, nanorods, and disks have been discussed in relation to plasmon resonances. The plasmon resonances considered so far are the lowest dipolar mode, where free electrons in the particles oscillate collectively in a single direction concerted with the optical field. The amplitude of the electronic oscillation as a function of the position represents the wavefunction of the plasmon. The plasmon wavefunction of the dipolar mode extends over the nanoparticles and does not show any nodal planes. In addition to the dipolar mode, higher plasmon modes can be excited in nanoparticles. Plasmon wavefunctions of the higher modes, where the direction of the collective oscillation is reversed, show nodal planes in nanoparticles. Longitudinal plasmon wavefunctions for gold nanorods are schematically shown in Fig. 4.3. Arrows in the nanorod indicate the directions of the oscillations of free electrons. Similar to the wavefunctions of a "particle in a box," there are higher modes in addition to the dipolar mode. The mode with one node at the center is the second-lowest mode to the dipolar mode. Wavefunctions of the transverse plasmons show periodic oscillations across the long axis of the nanorod. Plasmon resonance frequency of the mode is only little dependent on the order of the mode, and many modes are spectrally overlapped. On the other hand, for longitudinal plasmons, the plasmon resonances are spectrally well separated, and thus selective excitation of the individual mode is feasible. Since the spatial features of the plasmon wavefunction are finer than the diffraction limit of light, only near-field optical methods have the ability to visualize them optically.

4.4 Principle of Wavefunction Visualization

In physics and chemistry, phenomena are always linked to the wavefunctions of elementary excitations, and thus understanding the wavefunctions is of prime importance. Molecular wavefunctions are indispensable for understanding molecular properties. Photo-excitation processes of molecules and chemical reaction routes are also elucidated from the view of the wavefunctions. Spatial scales of wavefunctions are generally very small, and direct visualization of wavefunctions requires very high spatial resolution. The first visualization of electronic wavefunctions was demonstrated with a scanning tunneling microscope (STM). Scanning tunneling microscopy visualizes electronic wavefunctions of an object with atomic-scale

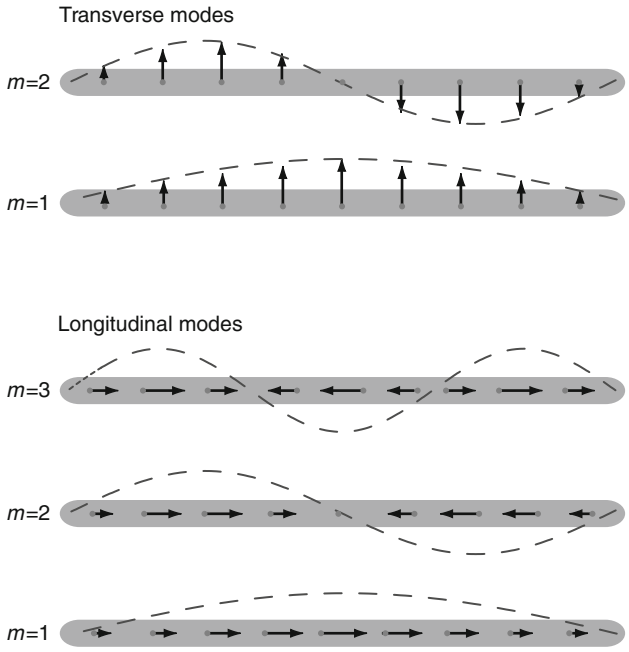

Fig. 4.3 Schematic drawing of plasmon modes. *Arrows* indicate the amplitude of free electron oscillation. *Dotted lines* indicate plasmon wave functions

spatial resolution. In optics, to realize the ultimate resolution like that of STM, several breakthroughs may still be needed. However, wavefunctions of elementary excitations such as excitons and plasmons can be visualized if a sufficiently high spatial resolution is achieved. Near-field optical microscopy is promising for this purpose. Wide spectral range and compatibility with dynamic measurements are the great advantages of optical methods and allow one to study materials properties from broad points of view. Here, the principles of visualization of wavefunctions using a near-field optical microscope will be briefly described in comparison with that of STM.

STM detects electric currents due to tunnel electrons between the sample and the probe tip. Tunneling probability at the tip position is dependent on the overlap of electronic wavefunctions between the sample and the tip. Because the wavefunction of the electron at the tip is localized on a single atom, STM visualizes the electronic local density-of-states (LDOS) of the sample at tip position $\overrightarrow{r}$ and energy E with atomic resolution [50, 51]. Operation principles of a near-field optical microscope is similar to that of an STM [52, 53]. Instead of using tunnel electrons as in an STM, a near-field optical microscope uses tunnel photons between the sample and the near-field probe tip and visualizes photonic LDOS at position $\overrightarrow{r}$ and frequency ω. In general, LDOS is defined by the following equation [54].

$$\rho(\overrightarrow{r}, \omega) = \sum_n \delta(\omega - \omega_n)\phi_n(\overrightarrow{r})\phi_n^*(\overrightarrow{r}), \tag{4.11}$$

where ϕ_n is a set of orthogonal wavefunctions of electromagnetic modes and ω_n denotes the resonance frequency of an eigenstate n. From (4.11), it is acceptable that, under resonance $\omega \approx \omega_n$, LDOS is approximately equal to the square amplitude of the wavefunction $|\phi_n|^2$. Because near-field optical microscopy observes the photonic LDOS, it enables visualization of the wavefunctions of elementary excitations resonant with the incident photons. The near-field methods have been utilized to visualize wavefunctions of exciton and biexcitons photo-excited in a quantum dot [55] and wavy patterns arising from photonic modes in optical corrals [56]. In the following, visualization of wavefunctions of plasmons using similar operational principles will be described.

4.5 Near-Field Optical Microscope

Since the first demonstration of near-field optical imaging in the early 1990s [34], the near-field optical microscope has expanded its application area from basic to applied science and become an indispensable tool in imaging the optical properties of objects with high spatial resolution. The operational principles of the near-field optical microscope were first proposed by Synge in 1928 [57]. Synge suggested the use of a tiny aperture created in an opaque screen. When the screen is illuminated from its backside, a localized optical field is created in the close vicinity of the aperture. High spatial resolution can be achieved if the localized photons interact with the object, and then the resulting scattered photons are detected. Near-field optical microscopes using a tiny aperture are called aperture-type near-field microscopes. A localized optical field can also be created at the tip of a metal needle with external illumination. Near-field optical microscopes using this type of the optical field are called scattered-type near-field microscopes. Both types of near-field microscope have advantages and disadvantages, and we need to select one of them, considering the sample condition and the information to be obtained. Detailed operational principles have been well described in the references [35, 58]. In this review, we deal only with the experimental results taken by the aperture-type near-field optical microscope.

4.5.1 Instrumentation of Near-Field Optical Microscope

Figure 4.4 shows schematic diagrams of an aperture-type near-field optical microscope. The apparatus consists of a light source, a sample scanner, a near-field probe, a control unit, and a detection system. A light source is chosen from various lasers and discharge lamps depending on the spectroscopic purposes. For example, a Xe

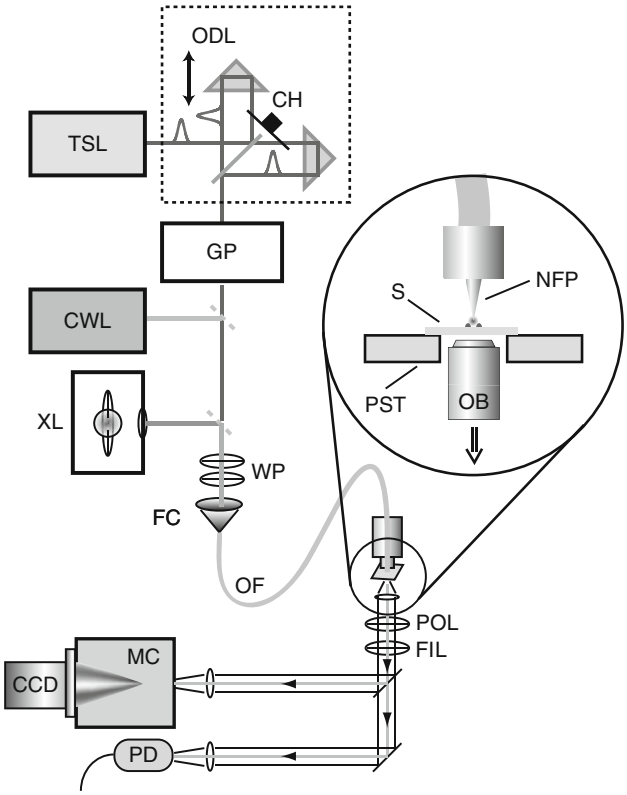

Fig. 4.4 Schematic diagram of an aperture-type scanning near-field optical microscope. *TSL* Ti:Sapphire laser, *GP* Grating pair, *ODL* Optical delay line, *CH* Mechanical chopper wheel, *CWL* CW laser, *XL* Xe lamp, *WP* Wave plates, *FC* Fiber coupler, *OF* Optical fiber, *S* Sample substrate, *NFP* Near-field probe, *PST* Piezo driven stage, *OB* Objective lens, *POL* Polarizer, *FIL* Optical filter, *MC* Monochromator, *CCD* Charge coupled device, *PD* Photodiode

lamp (XL) is used for transmission measurements, and continuous wave lasers (CWL) are used for Raman and fluorescence measurements. Aperture-type near-field optical probes (NFP) are used for local illumination and are prepared by chemical etching followed by metal coating and aperture fabrication. The aperture size of the probe tip is several tens of nanometer confirmed by SEM observation of the tip and/or near-field fluorescence images of single molecules using the tip. Figure 4.5 shows a scanning electron microscope (SEM) image of an aperture near-field probe-tip. The aperture, where the glass part is exposed outside of the metal film, appears as a dark spot at the tip of the probe. An optical near-field is created at the aperture by coupling the photons from a light source to the other end of an optical fiber of the near-field probe. A sample is dispersed on a transparent glass or silica substrate by spin-coating a colloidal solution. The sample substrate (S) is installed on the piezo-driven stage (PST) for lateral scanning. The piezo-stage with

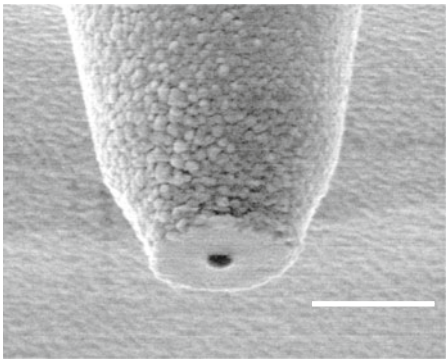

Fig. 4.5 Scanning electron micrograph of an aperture near-field probe. Scale bar: 400 nm

a closed-loop feedback system for position regulation is advantageous in improving the stability and reproducibility of the sample positioning. Because the optical near-field is localized in the vicinity of the near-field aperture, the near-field aperture should be kept in close vicinity to the sample surface while scanning the sample. A shear-force feedback mechanism was utilized for this purpose and enables the regulation of the tip-sample distance within several nm [35]. The regulation signal can be used for extracting topographic information of the sample. This enables simultaneous observation of topography and the optical image of the sample. To take the optical image, the sample is illuminated locally through the aperture of the near-field probe, and the transmitted light and/or luminescence from the sample is detected. To collect the light from the sample effectively, an objective lens (OB) with a high NA is used. The detection system adopts either a multichannel or single channel detector taking the required sensitivity and the purposes into consideration.

4.5.2 Time-Resolved and Non-Linear Measurements

By combining near-field optical microscopy with pulsed laser sources, time-resolved and non-linear measurements become possible. Several research groups have succeeded in attaining picosecond time resolution and subwavelength spatial resolution at the same time [59–63]. To excite non-linear processes, short pulse duration is essential. Although higher time resolution in the femtosecond regime is sometimes desired for time-resolved near-field observation, the simple combination of a near-field optical microscope with an ultrashort pulsed laser source does not allow us to achieve very high time resolution. This is because the pulses delivered from the laser source are seriously broadened as the pulses propagate in optical media due to the group velocity dispersion (GVD) of the material. In an aperture near-field optical microscope, the pulses travel through an optical fiber tens of cm in length, and the pulse duration is broadened to several picosecond at the aperture of the near-field probe even if the initial pulse duration is about 100 fs. By compensating for the GVD with a grating pair (GP) before the pulses couple to the fiber, the

GVD effect can be cancelled out, and the original pulse width can be recovered at the aperture of the near-field probe. In this way, high time resolution can be achieved while retaining the high spatial resolution of a near-field optical microscope. For time-resolved and non-linear near-field measurements, a mode-locked Ti:Sapphire oscillator (TSL) is useful as a light source. Amplified lasers, which are frequently used for far-field time-resolved measurements, are not compatible with the aperture near-field probe because pulses with high power break the near-field tip easily by thermal effects. Moderate peak power is desirable for combination with aperture near-field probes.

Time-resolved near-field pump-probe measurements are feasible by the apparatus shown in Fig. 4.4. The optical beam from the laser is split into pump and probe beams by a beam splitter. One of the two beams is introduced to a reflector mounted on a motor-driven stage and the other to a reflector mounted on a fixed stage. The two beams are coupled again collinearly by the beam splitter and introduced to the downstream. The delay time between the pump and the probe pulses is adjusted by the optical path difference of the beams, which is controlled by the movable stage. Transient optical response induced by the pump pulse is observed by the probe pulse using the one-color equal pulse correlation (EPC) method. To detect the transient signal effectively, a phase sensitive detection scheme is useful, where the pump and the probe beams are modulated at different frequencies, and the signal is detected as the difference of the modulation frequencies. Dynamic information at the tip position can be obtained by monitoring the transient signal as a function of the delay time, and time-resolved image can be obtained by scanning the sample while monitoring the transient signal [64].

4.6 Photonic Local Density-of-States Calculation

In near-field observation, the contrasts of the optical and topographic images often do not match well. This originates from the fact that the optical contrast reflects photonic LDOS at the tip position on the sample, which does not necessarily coincide with the topography. However, artifacts sometimes contribute to the image as well. The artifacts mostly arise from up-and-down motions of the near-field probe tip as the tip follows the topography of the sample surface (topographic artifact) [65]. The artifact interferes seriously with the genuine optical signal and makes correct interpretation of the image difficult. To interpret the observed optical contrast appropriately, special care must be taken. In this respect, comparison of the observed optical image with calculated photonic LDOS maps is beneficial in many cases. Here the method of photonic LDOS calculations based on the Green dyadic method is briefly described.

Analysis of the photonic LDOS relies on electromagnetic wave equations derived from Maxwell's equations. Electromagnetic properties of the scatterer can be evaluated by solving the vector wave equations, where the boundary condition near the scatterer is appropriately taken into account. The vector wave equation at

position $\overrightarrow{r}$ and angular frequency ω is given as

$$-\nabla\times\nabla\times\overrightarrow{E}(\overrightarrow{r},\omega)+\frac{\omega^2}{c^2}\epsilon_{\mathrm{ref}}\overrightarrow{E}(\overrightarrow{r},\omega)+\frac{\omega^2}{c^2}\epsilon_{\mathrm{s}}\overrightarrow{E}(\overrightarrow{r},\omega)=0, \tag{4.12}$$

where ϵ and ϵ_{ref} are the dielectric constants of the scatterer and reference medium, respectively. The equation can be rewritten with the Green dyadic of the scatterer $\overleftrightarrow{G}$.

$$\begin{aligned}-\nabla\times\nabla\times\overleftrightarrow{G}(\overrightarrow{r},\overrightarrow{r}',\omega)+\frac{\omega^2}{c^2}\epsilon_{\mathrm{ref}}\overleftrightarrow{G}(\overrightarrow{r},\overrightarrow{r}',\omega)+\frac{\omega^2}{c^2}\epsilon_{\mathrm{s}}\overleftrightarrow{G}(\overrightarrow{r},\overrightarrow{r}',\omega)\\ =\delta(\overrightarrow{r}-\overrightarrow{r}'),\end{aligned} \tag{4.13}$$

where $\delta(\overrightarrow{r}-\overrightarrow{r}')$ is the delta function. The Green dyadic in the scattering system can be obtained with the aid of the discretized Dyson equation by referencing the Green dyadic of the homogeneous medium $\overleftrightarrow{G_0}$ [66].

$$\overleftrightarrow{G}(\overrightarrow{r},\overrightarrow{r}',\omega)=\overleftrightarrow{G_0}(\overrightarrow{r},\overrightarrow{r}',\omega)+\overleftrightarrow{G_0}(\overrightarrow{r},\overrightarrow{r}',\omega)\frac{\omega^2}{c^2}(\epsilon_{\mathrm{ref}}-\epsilon_{\mathrm{s}})\overleftrightarrow{G}(\overrightarrow{r},\overrightarrow{r}',\omega) \tag{4.14}$$

The Green dyadic is correlated with the photonic LDOS as follows.

$$\rho(\overrightarrow{r},\omega)=-\frac{1}{\pi}\mathrm{Im}[\mathrm{Tr}\,\overleftrightarrow{G}(\overrightarrow{r},\overrightarrow{r},\omega)] \tag{4.15}$$

Once the Green dyadic of the scattering system is obtained, the scattered field can be calculated using the Lippmann–Schwinger equation

$$\overrightarrow{E}(\overrightarrow{r})=\overrightarrow{E_0}(\overrightarrow{r})+k^2\int_\Omega \mathrm{d}\overrightarrow{r}'\overleftrightarrow{G}(\overrightarrow{r},\overrightarrow{r}',\omega)[\epsilon_{\mathrm{ref}}(\overrightarrow{r})-\epsilon_{\mathrm{s}}(\overrightarrow{r}',\omega)]\cdot\overrightarrow{E_0}(\overrightarrow{r}'), \tag{4.16}$$

where the integration should be taken over the volume of the scatterer.

4.7 Near-Field Transmission Measurements [67–69]

Transmission measurement enables us to gain spectroscopic information with a wide spectral range, and thus is generally useful for understanding the basic properties of some materials. However, the near-field version of transmission spectroscopy has not been well utilized partly because of the low light throughput of the near-field probe as well as interference from topographic artifacts as mentioned in the last section. The chemical etching method for near-field probe tip fabrication improves

the throughput of the probe greatly [58], and facilitates the transmission spectral measurement practicable level. As for topographic artifacts, pseudo-constant-height mode operation, where the tip travels in a horizontal plane above the substrate, reduces the artifacts to a considerable extent [69, 70], which partially removes this problem. These techniques enable us to obtain reliable spectroscopic information from the near-field transmission measurements.

In far-field measurements, the transmission spectrum is defined as the intensity spectrum for the sample $I(\lambda)$ divided by the intensity spectrum of the reference $I_0(\lambda)$. Instead, the near-field transmission spectrum is obtained by $(I-I_0)/I_0$, where I and I_0 represent the intensity spectrum taken at the sample location and that at the bare substrate, respectively.

4.7.1 Near-Field Transmission Measurement of Spherical Gold Nanoparticles [67]

Figure 4.6a shows a typical near-field transmission spectrum of a single spherical gold nanoparticle (diameter 100 nm). Positive and negative signs in the vertical axis correspond to the reduction and enhancement of transmitted light intensity with respect to that taken at the bare substrate. The spectrum shows a minimum and a maximum at 580 and 730 nm, respectively. Near-field transmission images taken at these wavelengths show reversed optical contrast to each other as shown in Fig. 4.6b, c. The reduction peak observed at 580 nm is very close to the plasmon resonance of the spherical nanoparticle. On the other hand, the transmission enhancement peak appears rather far from the resonance. The enhancement cannot be ascribed to luminescence from the particle because the quantum efficiency of gold is extremely low. The enhanced transmission is attributed to an "antenna effect" of the particle, where the nanoparticle extracts photons from the aperture of the near-field probe and scatters them into the far-field. In the aperture-type near-field microscope, near-field photons are localized at the aperture and can interact with the object only when the object enters the near-field region. During the interaction, the photons are first coupled to the object, and then they are either damped in the object or re-radiated toward far-field. The wavelength-dependent coupling between the near-field and the far-field is described by the "near-field scattering" spectrum [71], which can be calculated based on Mie theory. On the other hand, there is a propagating (far-field) radiation component emanating from the aperture, which is also scattered and absorbed by the particle. The spectral behavior of this far-field component is also given by Mie theory. The observed transmission spectrum is considered to be composed of these near-field and far-field scattering components. The spectrum simulated using this idea reproduces the enhancement and reduction of transmission and shows good qualitative agreement with the observation. The peak observed near 580 nm can thus be assigned to the dipolar plasmon resonance of the spherical particle.

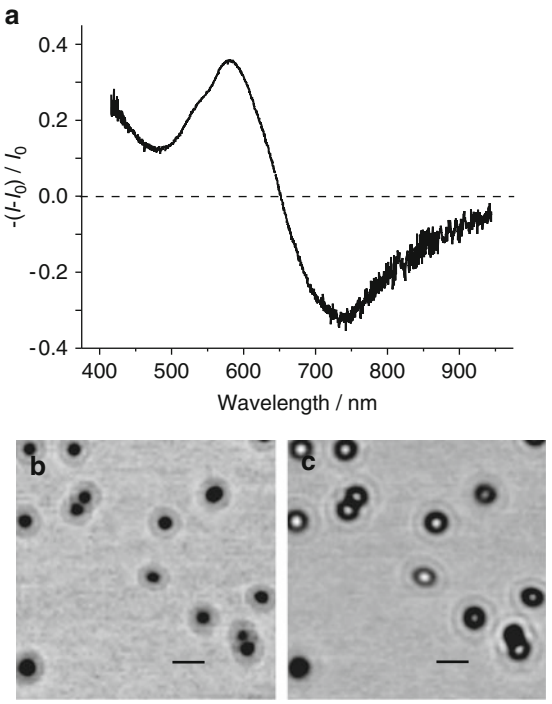

Fig. 4.6 (**a**) Near-field transmission spectrum of a spherical gold nanoparticle (diameter 100 nm). (**b**,**c**) Near-field transmission images taken at 580 and 720 nm, respectively. Scale bar: 100 nm

4.7.2 Near-Field Transmission Measurement of Gold Nanorods [68]

Near-field optical microscopy provides simultaneous observation of topography and optical images, and a direct comparison between the morphology of the sample and optical properties is feasible. Figure 4.7a shows the topography of a short nanorod obtained using a near-field microscope. The topography of the sample is broadened because of the finite size of the tip curvature. The dimensions of the nanorod were estimated from the topography image by taking the tip-broadening effect into account and were determined to be 30 nm in diameter and 180 nm in length. Figure 4.7b shows a near-field transmission spectrum of the nanorod taken at its end part (cross point in Fig. 4.7a). The spectrum shows two major peaks at 530 and 850 nm (denoted as bands A and B, respectively) and a minor peak at 690 nm. The polarization dependence of band A shows the maximum extinction as the incident field is parallel to the short axis of the nanorod. In contrast, the polarization dependence of band B shows the maximum extinction as the field is parallel to the long axis of the nanorod. Based on the polarization dependencies, bands A and B are assigned to transverse and longitudinal plasmon resonances, respectively.

Figure 4.7c, d show near-field transmission images of the nanorod taken at 532 and 780 nm, respectively. The dark parts correspond to reduction of the transmission due to the absorption and scattering of light. The image reflects the transition

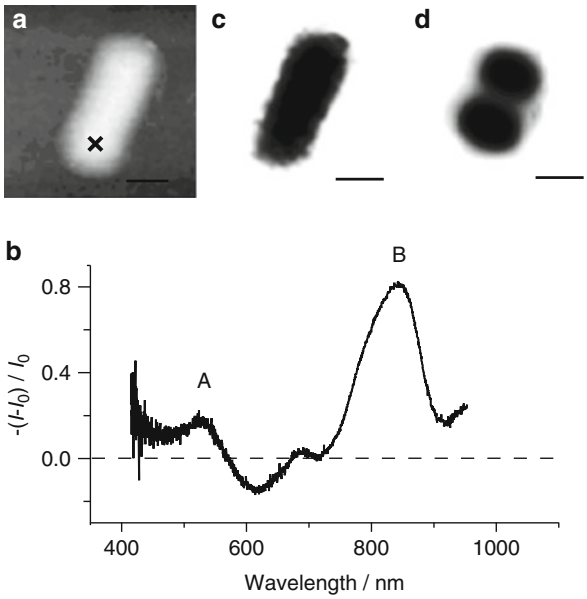

Fig. 4.7 (**a**) Topography of a short gold nanorod (diameter 30 nm, length 180 nm). (**b**) Near-field transmission spectrum taken at the cross point in (**a**). (**c**,**d**) Near-field transmission images taken at 532 and 780 nm, respectively. Scale bars: 100 nm

probability at the tip position. The images observed at 532 and 780 nm are markedly different from each other. The image obtained at 532 nm shows a spatial feature similar to that of the topography image. On the other hand, the image obtained at 780 nm shows an oscillating feature along the long axis of the nanorod. The oscillating feature is well reproduced by the photonic LDOS calculation and is attributed to the square of the amplitude of the wavefunction associated with a longitudinal plasmon mode resonant with the incident wavelength. The wavefunction shows a node at the center of the nanorod and is assigned to $m = 2$ mode in Fig. 4.3, which is the second-lowest dipolar mode. The dipolar mode appears at a wavelength longer than 1 μm. The observed minor peak at 690 nm can be assigned to $m = 3$ mode based on the LDOS calculation as well as the spatial feature of the observed transmission image. As the resonant frequency of the transverse plasmon mode is weakly dependent on mode number (m in Fig. 4.3), the band A may originate from various transverse modes. Consequently, the spatial feature in Fig. 4.7c may be attributable to the overlap of many transverse plasmon-mode wavefunctions.

Plasmon modes with odd parity characters are dipolar forbidden because no polarization is created upon photo-excitation. Observation of the odd plasmon mode in Fig. 4.7d indicates that the optically forbidden mode becomes optically allowed by the local illumination of the near-field. It is also noted that observation of the wavefunction image indicates that the coherence of the polarization wave extends from the tip position to the whole area of the nanorod.

Figure 4.8a shows the near-field transmission spectrum of a longer nanorod (diameter 20 nm, length 510 nm). Compared with the transmission spectrum of the short nanorod, many plasmon resonances are observable in the spectral region longer than 600 nm. Peak positions of the plasmon resonances are well reproduced by the calculated photonic DOS spectrum in Fig. 4.8b, which was obtained by spatially integrating the LDOS along the nanorod. The peaks are only visible when the incident field is polarized along the long axis of the nanorod and are assigned to longitudinal plasmon resonances. Transmission images at the plasmon resonances are shown in Fig. 4.9a–c along with the corresponding calculated LDOS maps in Fig. 4.9d–f. Periodic oscillating features along the long axis of the nanorod are again observed and are assigned to plasmon wavefunctions with the mode numbers $m = 5$, 6, and 7. It should be noted that the period of spatial oscillation becomes longer as the wavelength of observation increases.

The resonance energy and the wave vector of the plasmon can be obtained from the extinction peak wavelength of the transmission spectrum and the spatial oscillation period of the image of the nanorod, respectively. By plotting the wave vector of the plasmon vs. the resonance photon energy, the dispersion relation of the plasmon in the nanorod can be determined. Figure 4.10 shows the dispersion relation determined from near-field transmission measurements of various nanorods with

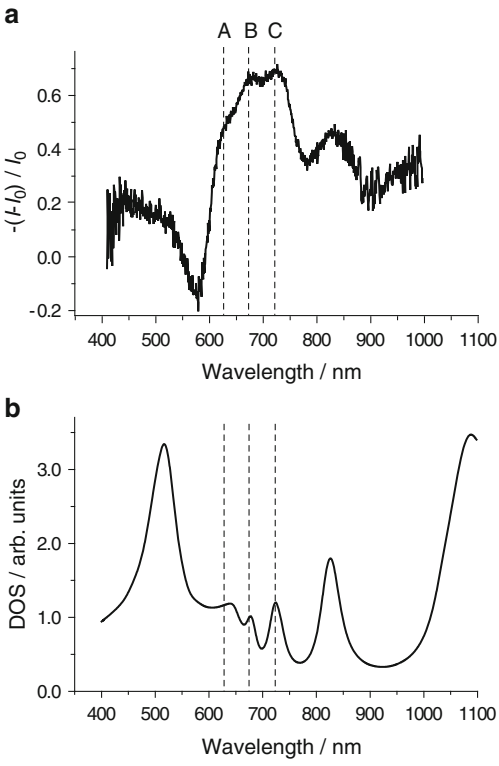

Fig. 4.8 (**a**) Near-field transmission spectrum of a long gold nanorod (diameter 20 nm, length 510 nm). *Dotted lines* indicate plasmon resonances. (**b**) Calculated density-of-states (DOS) spectrum of the gold nanorod

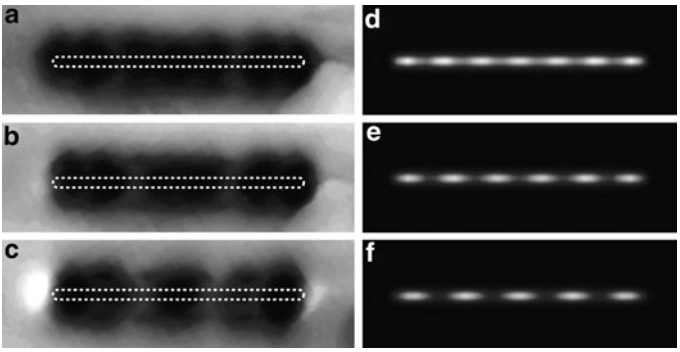

Fig. 4.9 (**a**–**c**) Near-field transmission images of the gold nanorod (diameter 20 nm, length 510 nm, the same rod as Fig. 4.8) obtained near the plasmon resonances shown in Fig. 4.8a: (**a**) 647–666 nm, (**b**) 666–686 nm, (**c**) 705–725 nm. *Dotted lines*: approximate shape of the nanorod. (**d**–**f**) Calculated local density-of-states images of the nanorod at (**d**) 636 nm, (**f**) 679 nm, and (**g**) 722 nm, respectively

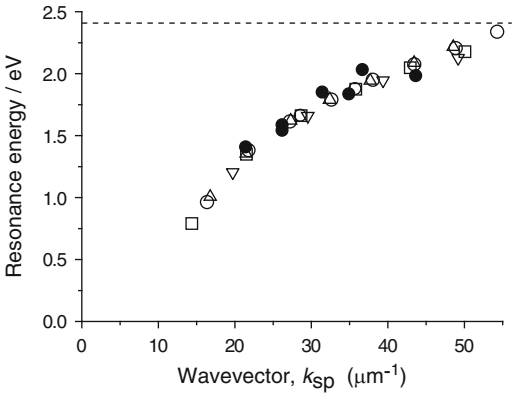

Fig. 4.10 Dispersion relation of single gold nanorods (diameter 20 nm). *Closed circles*: observations. *Open symbols*: calculations. *Dotted horizontal line* indicates the transverse plasmon resonance

different lengths and the same diameter. The results show that the dispersion relation follows a single dispersion curve regardless of the length of the nanorod if the diameter is the same. The dispersion relation obtained by the DOS calculation also follows the same curve and converges to a value close to the resonance energy of the transverse plasmon. A similar result was also reported by far-field measurements for gold nanowires fabricated by electron beam lithography [72]. The dispersion relation of the plasmons excited in silver nanorods was also determined in the same manner [73]. The dispersion relation of silver nanorods follows a single curve regardless of the length of the rod, but the dispersion curve depends on the diameter of the rod. The dispersion curve shifts toward the higher energy side as the diameter increases. The shift has the same origin in the aspect-ratio dependence as that of the resonance wavelength found in the far-field measurement of the nanorods [74] and is attributed to the depolarization effect in the nanorod.

4.8 Time-Resolved Measurement [64]

Photo-excited plasmons decay quickly within a few femtosecond to a few tens of femtosecond, and various energy dissipation processes occur after that [75, 76]. In the case of noble metals, hot electrons are created by electron–electron (e–e) collisions within a few hundreds femtosecond, and the electron distribution is cooled down within several picosecond by the e–e and electron–phonon (e–ph) scattering processes [43, 77]. The photo-excitation energy is finally released to the heat bath through the phonon–phonon scattering process. Since plasmons are the collective oscillation of free electrons, plasmonic properties are correlated with the electronic distribution and thus the energy dissipation processes. In the case of nanoparticles, as the particle size becomes comparable to the mean-free path of free electrons, the electron-surface scattering may also have some influence on the e–e and e–ph processes. To understand electronic and nonlinear properties of plasmonic materials, dynamics of free electrons after photo-excitation is of special importance. Time-resolved measurements give direct information for that. Far field studies on colloidal solutions of gold nanoparticles have elucidated decay dynamics of the e–e and e–ph processes [78–80]. The information obtained suffers from the inhomogeneity of the sample, however, and is ensemble-averaged over many particles with various sizes and shapes. Time-resolved microscopy enables us to give direct access to the dynamics of single particles. By using a confocal microscope, a single particle study becomes feasible and gives valuable information about dynamics and nonlinearity [81, 82]. Though confocal microscopy can achieve very high time resolution (15 fs) [83], the spatial resolution of the conventional microscope is limited to sub-microns, and thus position-dependent dynamics on the nanostructures cannot be directly investigated. The combination of near-field microscopy with time-resolved methods achieves high time resolution of less than 100 fs with a higher spatial resolution in a wide spectral range for various samples under ambient conditions. A typical example for the study of gold nanoparticles is described below. Time-resolved photoemission electron microscope (PEEM) also enables ultrafast measurements with a high spatial resolution under high vacuum. By using the two-photon excitation scheme of the PEEM process, propagation of the excited plasmon in metal films was visualized [84, 85].

We describe here the result of ultrafast near-field measurements on a gold nanorod (diameter 30 nm, length 300 nm). In the polarized near-field transmission spectrum, the nanorod (Fig. 4.11a, b) shows a longitudinal plasmon resonance at 750 nm. A near-field transmission image taken at 750 nm shows two dark spots on both sides and a node at the center of the nanorod (Fig. 4.11c).

The spatial feature is in excellent agreement with the calculated photonic LDOS at the excitation wavelength. The spatial feature of the image is assigned to the plasmon wavefunction of $m = 2$ mode. Similarly, a near-field transmission image taken at 900 nm (Fig. 4.11d) is assigned the plasmon wavefunction of $m = 1$ mode. To examine the ultrafast dynamics in the nanorod, the one-color EPC method was adopted, with near-infrared pulses as the excitation sources. At the excitation wavelength, both the $m = 1$ and $m = 2$ modes were excited at the same time. In EPC, the

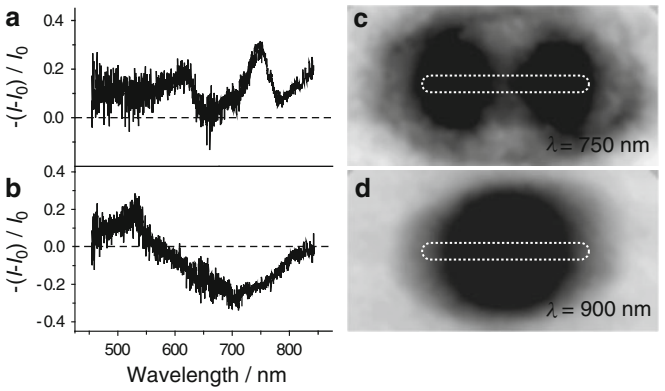

Fig. 4.11 (**a**,**b**) Polarized near-field transmission spectrum of a gold nanorod (diameter 30 nm, length 300 nm); polarization parallel (**a**) and across (**b**) to the long axis of the nanorod. (**c**), (**d**) Polarized near-field transmission images obtained at 750 and 900 nm, respectively. Polarization is parallel to the long axis of the nanorod. *Dotted lines*: approximate shape of the nanorod

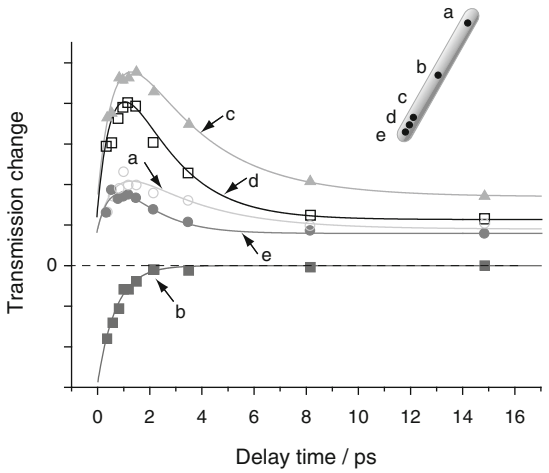

Fig. 4.12 Transient transmission signal traces obtained in the gold nanorod (diameter 30 nm, length 300 nm). *Solid curves* indicate double (for **a**, **c**–**e**) and single (for **b**) exponential fits. Inset: observed positions in the nanorod

pump pulse induces the transient absorption in the nanorod, and the probe pulse is used to detect the transient transmission change. Ultrafast dynamics in the nanorod can be investigated by detecting the transmission change as a function of pump-probe delay time. Figure 4.12 shows the pump-probe time-resolved traces taken at various positions in the nanorod. Depending on the position on the nanorod, the time-resolved signal shows the induced and bleached absorption. Because the e–e and e–ph processes in noble metals occur at different time scales in the femtosecond to picosecond regime, the observed pump-probe trace was analyzed by double exponential functions. The results of the analysis are summarized in Table 4.1. The fast component with a time constant of 600 fs was observed in the entire nanorod and

Table 4.1 Time constants of relaxation after photo-excitation in the nanorod obtained from double exponential fits

Position	t_{fast}/ps	t_{slow}/ps
a	0.6	2.8
b	0.6	–
c	0.6	2.8
d	0.6	1.8
e	0.6	1.5

is attributed to the e–e scattering. The slow component with a ps-time constant was observed everywhere except at the center and is attributed to the e–ph scattering. The picosecond component varies from 2.4 to 1.5 ps depending on the position on the nanorod, and becomes faster toward the end of the nanorod. The short lifetime at the end and the position dependence may indicate that the electron-surface scattering has some influence on the dynamics of the e–ph scattering. However, the far-field studies using ensembles of colloidal solutions concluded that the electron-surface scattering is of great significance only for nanoparticles smaller than 10 nm, which is contradictory to the interpretation above [86–88]. Further investigation is underway to clarify the position-dependent energy dissipation processes observed in the near-field measurements.

The spatio-temporal behavior of the nanorod can be visualized by detecting the transmission change at a fixed delay time while scanning the nanorod position to obtain a near-field transmission image. Figure 4.13a shows the transient transmission image of the nanorod at a 600 fs delay. Dark and bright parts in the image correspond to the reduction (bleached absorption) and enhancement (induced absorption) of the transmission induced by the pump pulse. Interestingly, both bleached and induced absorptions are observed in the single nanorod. To reveal the origin of the spatial feature, an electromagnetic simulation was performed [89]. In the simulation, the electronic temperature in the nanorod was assumed to be homogeneously elevated upon photo-excitation. An ultrafast study of gold films reported that the heat transport in a 300 nm thick gold film occurs within 300 fs [77,90]. If the heat transport mechanism in the nanorod is similar to that in the metal film, it is reasonable to consider that the electronic temperature in the nanorod is homogeneously increased and equilibrated within 600 fs. It may also be reasonable to consider that the transient transmission change at each position arises from the LDOS change due to the elevation of the electronic temperature, since the static near-field transmission images are well reproduced by the LDOS maps as shown in the previous section. Thus, we assume that the transient transmission change ΔI is proportional to the difference between LDOS at room temperature and that at elevated temperature.

$$\Delta I(\overrightarrow{r}, \omega) = \rho(\overrightarrow{r}, \omega, T + \Delta T) - \rho(\overrightarrow{r}, \omega, T), \tag{4.17}$$

where ΔT denotes the electronic temperature change induced by the pump pulse. The temperature dependence of the LDOS originates from the variation of the dielectric function of the material and induces variation of the spatial feature of the LDOS. Figure 4.13b shows the simulated image based on (4.16). Bright and dark parts in the image correspond to the increase and decrease of the LDOS,

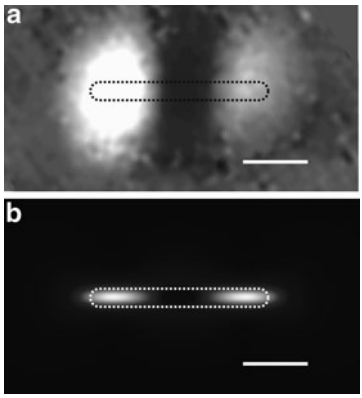

Fig. 4.13 (**a**) Near-field transient transmission image of the nanorod taken at delay time of 600 fs. (**b**) Simulated transient transmission image of the nanorod. *Dotted lines*: approximate shape of the nanorod. Scale bars: 100 nm

respectively. The spatial feature calculated is well correlated to the observed image. Upon elevation of the electronic temperature, plasmon resonance energies of both $m = 1$ and $m = 2$ modes are shifted to the red, which makes the contributions of these modes to the image at the probe wavelength different from those at room temperature. The increased LDOS in both sides and the decreased LDOS at the center arise from this effect. Transient images of other nanorods with different diameters and/or lengths sometimes show reversed optical contrasts. Also, in such cases, the images are well reproduced in terms of variation of the LDOS under elevated electronic temperature. These results indicate that the transient image of the nanorod arises from the deformation of plasmon wavefunctions induced by a rise in electronic temperature in the nanorod.

Ultrafast dynamics investigated here are the phenomena that occur after the plasmons are completely dephased. Spatio-temporal dephasing dynamics of plasmon waves is of prime importance in attaining a deeper understanding of plasmons. For this purpose, ultimately high time resolution (several femtosecond), which is shorter than the lifetime of the plasmon, is required and is still a challenge for near-field optical microscopy to achieve.

4.9 Non-Linear Measurements

Non-linear optical methods have various advantages over linear methods [91]. Spatial resolution, optical contrast, and, occasionally, signal-to-noise ratio can be improved in the non-linear measurements with respect to those of the linear measurements. In addition, the non-linear methods often enable us to obtain information that is not accessible by linear methods. Since high peak power is essential to excite the non-linear processes, a pulse laser with a short pulse width is frequently used. For excitation of the non-linear processes, spatial confinement and focusing of light is helpful. Combination of the near-field method and the short pulse laser source enables effective excitation of non-linear processes, such as two-photon induced photoluminescence (PL), second harmonic generation (SHG), and so forth in nanomaterials.

The quantum yield of PL from gold is extremely low [92]. This is because the excited energy decays very rapidly through non-radiative processes before the excited energy decays by radiating photons to the far-field. Recently, many research groups reported that the PL from gold is significantly enhanced when the PL is excited by two-photon absorption [93–97]. The two-photon absorption process in materials occurs via either simultaneous or sequential photon absorptions. The two-photon signal intensity scales with the square of the incident power, in contrast to the one-photon signal where the intensity scales linearly with the incident power. Thus, two-photon-induced PL (TPI-PL) is more sensitive to the optical field than one-photon PL. Near-field TPI-PL of gold holds great potential in visualizing the enhanced optical field in the vicinity of gold nanostructures. TPI-PL of gold has been applied in, for example, white-light continuum generation [98] and bioimaging [99–101]. In this section, visualization of the optical fields for single gold nanoparticles [93, 102, 103] and their assembly [104–107] using near-field TPI-PL is described.

The PL process of gold begins with the excitation of an electron in the d band to the sp band above the Fermi level and the creation of a hole in the d band [108, 109]. PL is radiated after a manifold of collision processes occur when the electron–hole pair recombines. With near-field irradiation of infrared light pulses (800 nm), some gold nanoparticles emit strong PL in the visible spectral range. From the incident power dependence of the PL intensity, it was confirmed that the PL was excited by two-photon absorption. Spherical gold nanoparticles show no TPI-PL, but the gold nanorod exhibits strong TPI-PL. Figure 4.14a shows a typical spectrum of TPI-PL from a single gold nanorod. TPI-PL shows two bands near 550 and 620 nm. The relative intensity of the two bands varies depending on the size and shape of the particle. However, the peak positions of the two bands show little dependence. Based on the band-structure calculation of gold [110], the photon energies of these two bands are in good agreement with the band gap energies between the d-band and the Fermi energy levels near the L and X symmetric points, respectively. The two bands are thus assigned to radiative recombination of an electron in the sp band near the Fermi energy level and a hole in the d band near these symmetric points (Fig. 4.14b, c). Polarization characteristics of PL for these bands are also consistent with the emission mechanism described above and the crystalline structure of the gold. Incident polarization dependence of the TPI-PL intensity indicates that the two-photon process occurs through the sequential absorption of photons via the intermediate state. Time-resolved measurements for the TPI-PL revealed that the lifetime of the intermediate state is shorter than several tens of femtosecond.

4.9.1 Gold Nanorods

Visualization of the optical field is feasible by detecting the PL intensity while scanning the sample surface laterally. Optical images obtained in this way reflect the excitation probability at the tip position (we should note that the observed image

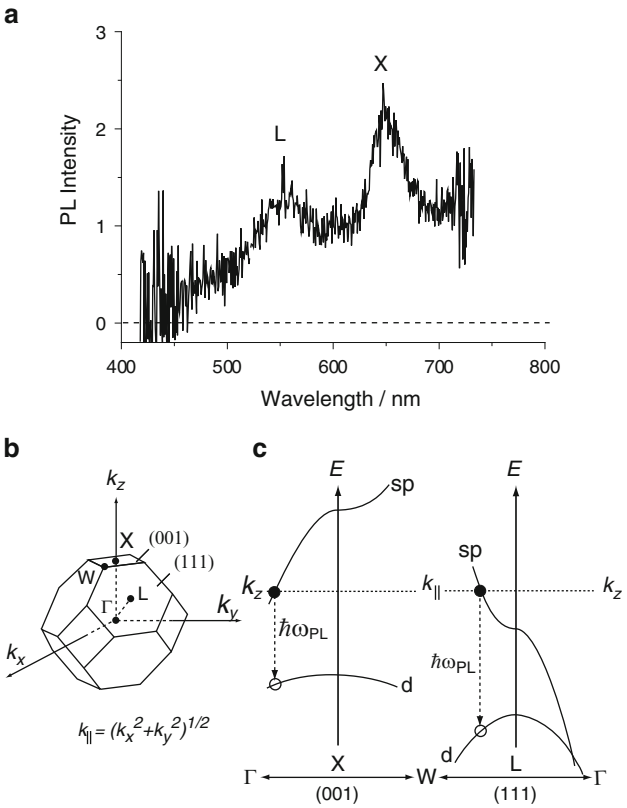

Fig. 4.14 (**a**) Two-photon induced photoluminescence from a single gold nanorod. (**b**) Symmetry points and axes in the first Brilloiun zone of gold. (**c**) Band structures of gold near the X and L symmetric points. The notations sp and d denote, respectively, the sp conduction band and the d valence band. The *dashed line*: Fermi energy level. $\hbar\omega_{PL}$: photon energy of photoluminescence radiated through recombination of an electron–hole pair

is not the map of PL intensity itself). Figure 4.15 shows the two-photon excitation images of single gold nanorods. Similar to the transmission image (Fig. 4.9), periodic spatial oscillation along the long axis of the nanorod is found in Fig. 4.15a. The period of the oscillation depends on the incident wavelength and becomes longer with increasing wavelength. By comparing with the calculated photonic LDOS map, the observed oscillating feature is attributable to the plasmon wavefunction resonant with the incident photons. As mentioned before, the two-photon process is very sensitive to the optical field strength, and the image reflects the enhanced optical fields in the vicinity of the nanorods. In the present case, the PL signal was enhanced because of the resonance between the incident field and the plasmon mode of the nanorod, which was confirmed by the excitation wavelength dependence. Some gold nanorods show different spatial features in which the optical fields are enhanced only at the end parts of the nanorod, as shown in Fig. 4.15b. It is known that the

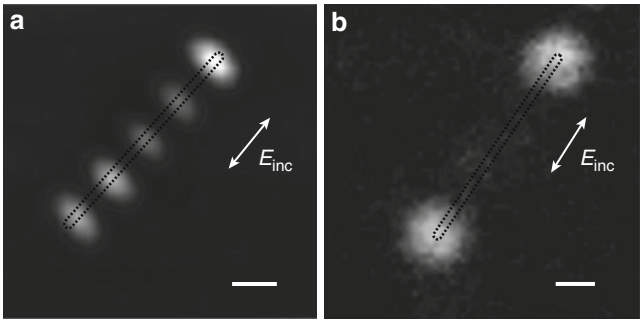

Fig. 4.15 Two-photon excitation images of single gold nanorods. (**a**) diameter 20 nm, length 540 nm, (**b**) diameter 21 nm, length 565 nm. The images are taken at 780 nm excitation. *Dotted lines*: approximate shape of the nanorod. Scale bars: 100 nm

optical field enhancement occurs at sharp corners or edges of metal nanostructures. This is known as the "lightning rod effect" [111–113]. The effect is mainly determined by the geometry of the sample and shows little dependence on the incident wavelength. In Fig. 4.15b, the lightning rod effect is dominant over the plasmon-mode resonance enhancement. Difference between Fig. 4.15a, b may originate from the difference in the resonance conditions of the nanorods or from microscopic structures created at the end-edges of the nanorod.

4.9.2 Gold Nonoplates [103]

Near-field TPI-PL excitation imaging is applicable to various shapes of nanoparticles. Two-dimensional structures such as nanoplates are of fundamental interest in optical-field imaging because the excited plasmons may extend over the nanoparticles as two-dimensional waves. The TPI-PL intensities of gold nanoplates are found to be, in general, more intense than those of gold nanorods. Single gold triangles show one or two orders of magnitude more intense PL compared to gold nanorods. The optical field enhancement in the nanotriangles is also interesting in relation to SERS. Figure 4.16a shows a near-field two-photon excitation image of a single nanotriangle. The dotted line in the figure shows the approximate shape of the particle estimated from the topography image. The two-photon excitation image shows that the excitation probability is highly localized near one of the apexes of the triangle. It is noted that the lightning rod effect was operative at the sharp corners or at the edges and was observed in the nanorod (Fig. 4.15b). In Fig. 4.16a, however, the enhanced field observed is located at the inner part of the triangle. In addition, it was found that the excitation probability (i.e., the PL intensity) is very sensitive to the excitation wavelength. As described before, the lightning rod effect shows little wavelength dependence, but the plasmon-mode resonance effect shows strong wavelength dependence. It is likely that in the triangle the plasmon resonance effect is dominant over the lightning rod effect. The calculated optical field image in Fig. 4.16b is in excellent agreement with the observation, and the spatial feature

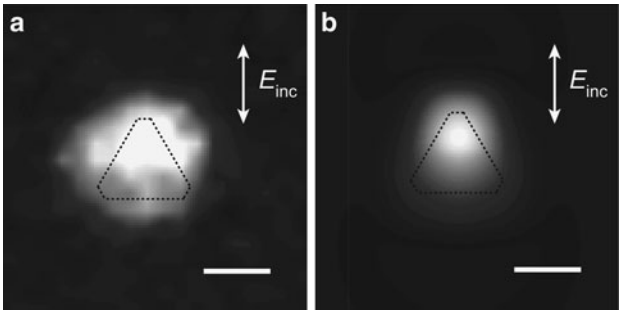

Fig. 4.16 (**a**) Two-photon excitation image of a triangular gold nanoplate (thickness 18 nm, base length 160 nm). (**b**) Calculated optical field distribution near the triangle. *Arrows* indicate the incident polarization. *Dotted lines*: approximate shape of the triangle. Scale bars: 100 nm

found in the image is assigned to the plasmon wavefunction resonantly excited with the incident wavelength. The location of the enhanced optical field can be controlled from one apex to the other by rotation of the incident-field polarization. This fact indicates that the plasmon mode is degenerated as a pair of two-dimensional waves with a degenerate resonance frequency, and one of the waves can be selectively visualized by the polarized incident light.

4.9.3 Dimeric Nanoparticles [104, 105]

Assemblies of nanoparticles exhibit very unique properties which are very different from those of single nanoparticles. The unique properties sometimes originate in near-field interactions between elemental excitations such as excitons and plasmons. Near-field interactions between optical fields and molecules also give rise to remarkable phenomena such as SERS [114]. Signal enhancement of SERS is 10^4–10^6-fold on roughened metal surfaces or on isolated metal particles [6, 12]. Noble metal nanoparticle dimers were predicted theoretically to exhibit extraordinarily enhanced optical fields at the junctions of the dimers [115–117]. In the late 1990s, SERS with single-molecule level sensitivity was reported experimentally [10, 11], and since then, noble metal nanoparticle dimers have been studied extensively as prototypical systems to theoretically examine the mechanism of the enhancement. Figure 4.17a, b show typical examples of calculated optical field intensity maps for a gold nanosphere dimer. When the incident field is polarized across the interparticle axis of the dimer (Fig. 4.17a), the field is only slightly enhanced. This is because plasmons excited in the individual particles do not interact with each other through the gap. On the contrary, when the incident field is polarized along the inter-particle axis of the dimer, the optical field is significantly enhanced at the junction. The enhancement mechanism can be explained by considering the near-field interaction of plasmons in the dimer. As the incident field is parallel to

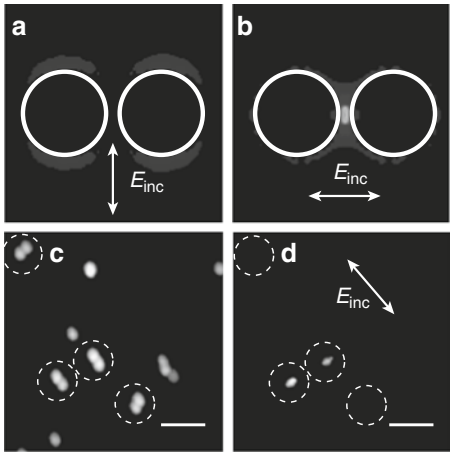

Fig. 4.17 (**a**,**b**) Calculated optical field distributions near a dimer of spherical gold nanoparticles (diameter 100 nm). *Arrows* indicate the incident polarization. (**c**) Topography of single and aggregated gold nanoparticles. (**d**) Two-photon excitation image of the sample (**c**) taken with incident polarization indicated by the *arrow*. Scale bars: 100 nm

the dimer axis, particle plasmons excited in individual particles interact with each other through the space at the junction, and a new plasmon resonance ("dimer plasmon" mode) is formed. The dimer plasmon amplifies the optical field greatly up to four orders of magnitudes because of the Coulombic interaction at the junction. In SERS, signal enhancement is operative not only for the incident field but also for the scattering radiation, and thus, signal enhancement is approximately proportional to the fourth power of the field enhancement. The enhancement of SERS thus reaches 10^{11}–10^{13} in the highest case. If the optical field localized at the interstitial site is visualized in real space, it is highly advantageous in the detailed investigation of SERS mechanisms. Near-field TPI-PL imaging is promising for this purpose. Visualization of the enhanced fields is important not only for understanding the SERS mechanism, but also for applications of the field enhancement to photochemical reactions. Recently, it has been reported for noble metal nanoparticle dimers that the multi-photon polymerization reaction is promoted predominantly at the junction of the dimer [18].

Figure 4.17c shows a typical topography image of dimeric and isolated gold nanoparticles prepared on a cover slip. From the SEM observation of the sample, particles in the aggregate do not directly contact each other but are separated by a few nanometer to 10 nm. A two-photon excitation image of the sample is shown in Fig. 4.17d. The image obtained sensitively reflects the optical field distribution of the sample. The optical field of the sample was greatly enhanced at the dimers (and at the trimer) in comparison with the isolated nanoparticles. Among four dimers in the sample, two dimers whose axes were parallel to the polarization of the incident light exhibited huge enhancements at the interstitial sites of the dimers. The other two dimers, whose axes are perpendicular to the incident field, showed only little

enhancement. These observations are in excellent agreement with the theoretical predictions illustrated in Fig. 4.17a, b.

To examine the influence of the localized optical field on Raman enhancement, dimeric gold nanospheres doped with Raman active dye molecules were investigated. Figure 4.18a shows the topography of the sample and Fig. 4.18b the near-field excited Raman spectrum for dimer A. Raman scattering excited at the interstitial site of the dimer shows very high intensity as shown in Fig. 4.18b. Most of the bands observed are assigned to vibrational modes of the dye molecule [118]. Raman active sites can be visualized by monitoring one of the vibrational bands while the sample position relative to the probe is scanned. Figure 4.18c shows the observed near-field Raman excitation image, and the Raman active site is localized at the junction. Raman signal is strongest as the incident field is polarized along the inter-particle axis of the dimer. The location of the Raman active site spatially overlaps well with the alternatively visualized optical field in the near-field TPI-PL experiment [105]. These results are consistent with the proposed SERS mechanism described above. The average number density of dye molecules was about 100 molecules μm^{-2}, which means only several molecules were excited at the near-field probe tip. From this figure, the Raman enhancement factor is estimated to be even greater than 10^{10} at the most intense sites. Furthermore, Raman signals fluctuate at a time scale of a few seconds, which suggests that the Raman signal originates from a very small number of molecules. These observations indicate that single-molecule level sensitivity has been achieved in this near-field SERS experiment, where optical field enhancement at the junction of the dimer is essential for the giant Raman signal.

4.9.4 Larger Assemblies of Nanoparticles [106, 107]

In many-body assemblies of nanoparticles, a number of inter-particle near-field interactions are involved and may give further unique properties. Many-particle assemblies have been paid much attention in relation to the development of the

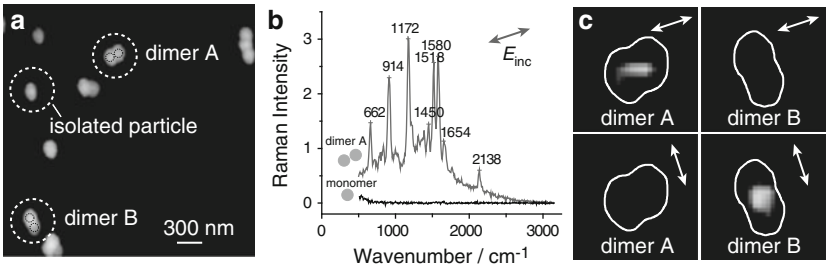

Fig. 4.18 (**a**) Topography of single and aggregated gold nanoparticles. (**b**) Near-field Raman spectra taken at dimer 1 and the isolated particle indicated in (**a**). Excitation wavelength is 785 nm. (**c**) Polarized near-field Raman excitation images of the dimer 1 and dimer 2. *Arrows* indicate the incident polarization. *Solid curves*: approximate shape of the dimer

SERS active substrates. Various protocols have been reported for the preparation of the assemblies with close-packed forms [119–121]. Most of them give moderate SERS enhancements on the order of 10^6–10^8, which are much lower than those needed for single-molecule level sensitivity. The results may indicate that a simple increase of the particle number in the assembly is not enough to attain the ultimate field enhancement. To clarify the reason for this finding, visualization of the optical field is one of the most straightforward methods.

Figure 4.19b shows a near-field two-photon excitation image of an island-like assembly of gold nanospheres (diameter 100 nm). Because the topography image obtained simultaneously with the near-field image is not clear enough to discuss fine details of the nanostructures, such as the interparticle separation of the nearly touching nanoparticles, SEM observation of the sample is of great use to gain finer information of the nanostructure. From the SEM image in Fig. 4.19a, the interparticle distances were found to be less than 10 nm for the close-packed portion. The optical-field image in Fig. 4.19b reveals that the enhanced field is non-uniformly distributed over the island-like assembly. The enhancement is more significant at the rim of the assembly than at the inner part. The difference between the inner part and the rim may originate from the delocalization character of plasmon excitations in the assembly. At the inner part, particles are surrounded by many particles, and excited plasmons may propagate in all of the directions though the near-field interactions. On the other hand, at the rim part, particles are only partially surrounded by the other particles. Localization of the excited plasmon may be stronger in this case because the plasmon propagation into the surroundings is geometrically restricted compared with that at the inner part.

From close inspection of the image, it is found that the highest enhancement occurs at the isolated dimer (A), and the enhancement observed at the rim or at the defect sites in the assembly is lower. This observation implies that the enhancement is the highest in the dimer and becomes lower with increasing size of the assembly. The finding may have some correlation with the relatively low SERS enhancement reported in close-packed assemblies. Plasmon localization at the rim of the assembly may have some similarities with photon localizations at the boundaries of photonic

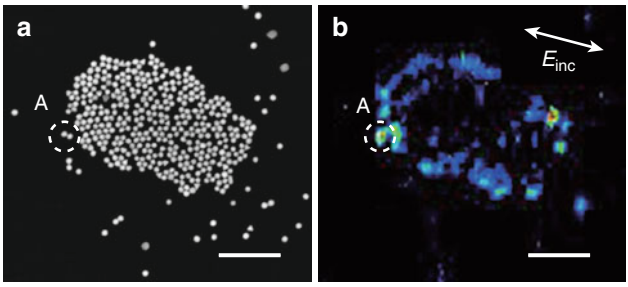

Fig. 4.19 (**a**) SEM image of an assembly of spherical gold nanoparticles (diameter 100 nm). (**b**) Near-field two-photon excitation image of the assembly. Scale bars: 1 μm

crystals [122]. To understand the mechanism of the localization, detailed analysis using theoretical calculation will be informative.

Near-field observation of the optical field distribution in the nanostructures reveals a wealth of information about the enhancement mechanism of the optical field and will give useful guidelines to design a desirable SERS substrate. It is also practically important to consider the potential applications of the confined optical fields to nano-optical devices, bioimaging, and photochemical reactions.

4.10 Summary

In this review, the visualization of plasmon wavefunctions and optical fields using near-field methods was described. Longitudinal plasmon wavefunctions visualized for single gold nanorods showed periodic spatial oscillations along the long axis of the nanorod. The periods of the oscillations depended on the excitation wavelength and became longer with the increase of the excitation wavelength. Spatial features of the plasmon wavefunctions and their resonance energy dependencies were similar to those in the "particle in a box." The number of nodes in the wavefunction increased with the increment of the eigen energy of the plasmon mode. Spatio-temporal behaviors of the plasmon wavefunction upon photo-excitation were also discussed. Visualized transient transmission images of the nanorod showed characteristic spatial features that were different from the static plasmon wavefunction images. The observed transient image was understood as a variation of plasmon wavefunctions due to the elevation of the electronic temperature in the nanorod.

The optical fields excited in various nanostructures were visualized with the non-linear near-field imaging technique. The optical field strength in the nanorod was found to be larger than that in the spherical nanoparticle and was effectively enhanced either by the resonance excitation of a plasmon mode or by the lightning rod effect. In the case of the dimer of nanoparticles, the near-field interaction of plasmons excited in the individual nanoparticles induced extraordinarily large enhancements of the optical field with respect to that of the isolated nanoparticle. The optical field induced in the interstitial site of the dimer was found to enhance Raman scattering from molecules, and the sensitivity was close to the single-molecule level. For the larger assembly, the optical field was larger at the rim of the assembly than at the internal positions of the assembly. The distribution of the optical fields in the assembly was discussed in relation to the spatial localization character of the plasmons.

In the near future, dynamic visualization of plasmon wavefunctions will become more important. Experimentally, however, imaging with time resolutions shorter than the lifetime of a plasmon ($<$20 fs) is a challenge. On the other hand, electromagnetic field calculation has fewer barriers and is feasible. Calculation protocols with high precision, high reliability, and reasonable computational cost are expected to be developed and applied to reveal the dynamic features of plasmon wavefunctions.

Basic studies on plasmons and their related materials will influence wider research areas in fundamental and applied fields. Among them, applications of plasmonic optical fields to photochemical reactions have a large impact in photo- and material-sciences. For instance, the interaction between localized optical (or plasmon) fields with molecular electronic wavefunctions may enhance photochemical reaction rates, which is sometimes forbidden under the far-field irradiation of light. It has a potential to open up new chemical reaction routes beyond the dipolar approximation. Such novel photochemical reactions shed new light on photo- and material-sciences.

Acknowledgements The authors thank Dr. T. Nagahara, Dr. J. K. Lim, Dr. N. Horimoto, Dr. T. Shimada, Dr. M. K. Hossain, and Prof. M. Kitajiama for their many essential contributions to this work. The authors also thank the Equipment Development Center of IMS for collaboration in construction of the near-field optical microscope. This work was supported by the Sumitomo foundation, the Research Foundation for Opto-Science and Technology, Grants-in-Aid for Scientific Research (Grant Nos. 16350015, 16750017, 17655011, 17034062, 18205004, 18685003, 19049015, and 22225002) and the Asian CORE program from the Japan Society for the Promotion of Science and from the Ministry of Education, Culture, Sports, Science, and Technology.

References

1. M. Kerker, *The Scattering of Light and Other Electromagnetic Radiation* (Academic, New York, 1969)
2. U. Kreibig, M. Vollmer, *Optical Properties of Metal Clusters* (Springer, Berlin, 1995)
3. C.F. Bohren, D.R. Huffman, *Absorption and Scattering of Light by Small Particles* (Wiley, New York, 1998)
4. R.H. Ritchie, Surf. Sci. **34**, 1 (1973)
5. S. Kawata, *Near-field Optics and Surface Plasmon Polaritons* (Springer, Berlin, 2001)
6. M. Moskovits, Rev. Mod. Phys.**57**, 783 (1985)
7. M. Fleishmann, P.J. Hendra, A.J. McQuillan, Chem. Phys. Lett. **26**, 163 (1974)
8. D.J. Jeanmaire, R.P. Van Duyne, J. Electroanal. Chem. **84**, 1 (1978)
9. M.G. Albrecht, J.A. Creighton, J. Am. Chem. Soc. **99**, 5215 (1997)
10. S. Nie, S.R. Emory, Science **275**, 1102 (1997)
11. K. Kneipp, Y. Wang, H. Kneipp, L.T. Perelman, I. Itzkan, R.R. Dasari, M.S. Feld, Phys. Rev. Lett. **78**, 1667 (1997)
12. G.C. Schatz, R.P. Van Duyne, *Handbook of Vibrational Spectroscopy* (Wiley, New York, 2002)
13. S.A. Maier, M.L. Brongersma, P.G. Kik, S. Meltzer, A.A.G. Requicha, H.A. Atwater, Adv. Mater. **13**, 1501 (2001)
14. N.F. van Hulst, Nature **448**, 141 (2007)
15. N. Engheta, Science **317**, 1698 (2007)
16. R.M. Stöckle, Y.D. Suh, V. Deckert, R. Zenobi, Chem. Phys. Lett. **318**, 131 (2000)
17. N. Hayazawa, Y. Inouye, Z. Sekkat, S. Kawata, Chem. Phys. Lett.**335**, 369 (2001)
18. K. Ueno, S. Juodkazis, T. Shibuya, Y. Yokota, V. Mizeikis, K. Sasaki, H. Misawa, J. Am. Chem. Soc. **130**, 6928 (2008)
19. Y. Tsuboi, R. Shimuzu, T. Shoji, N. Kitamura, J. Am. Chem. Soc. **131**, 12623 (2009)
20. E. Pordan, C. Radloff, N.J. Halas, P. Nordlander, Science **302**, 419 (2003)
21. W.L. Banes, A. Dereux, T.W. Ebbesen, Nature **424**, 824 (2003)
22. E. Ozbay, Science **311**, 189 (2006)
23. R. Zia, M.L. Bringersma, Nat. Nanotech. **2**, 426 (2007)

24. N. Fang, H. Lee, C. Sun, X. Ahang, Science **308**, 534 (2005)
25. M. Aeschlimann, M. Bauer, D. Bayer, T. Brixner, F.J. Garcia de Abajo, W. Pfeiffer, M. Rohmer, C. Spindler, F. Stteb, Nature **446**, 301 (2007)
26. A.V. Akimov, A. Mukherjee, C.L. Yu, D.E. Chang, A.S. Zibrov, P.R. Hemmer, H. Park, M.D. Lukin, Nature **450**, 402 (2007)
27. S. Kim, J. Jin, Y.-J. Kim, I.-Y. Park, Y. Kim, S.-W. Kim, Nature **453**, 757 (2008)
28. H.J. Lezec, J.A. Dionne, H.A. Atwater, Science **316**, 430 (2007)
29. R. Liu, C. Ji, J.J. Mock, J.Y. Chin, T.J. Cui, D.R. Smith, Science **323**, 366 (2009)
30. E. Abbe, Ark. Mikrosk. Anat. **9**, 413 (1873)
31. M. Born, E. Wolf, *Principles of Optics* (Cambridge University Press, Cambridge, 1999)
32. D.W. Pohl, D. Denk, M. Lanz, Appl. Phys. Lett. **44**, 651 (1984)
33. U. Durig, D.W. Pohl, F. Rohner, J. Appl. Phys. **59**, 3318 (1986)
34. E. Betzig, J.K. Trautman, T.D. Harris, J.S. Weiner, R.L. Kostelak, Science **251**, 1468 (1991)
35. L. Novotony, B. Hecht, *Principle of Nano-Optics* (Cambridge University Press, Cambridge, 2006)
36. N. Hosaka, T. Saiki, Opt. Rev. **13**, 262 (2006)
37. T. Taubner, R. Hillenbrand, K. Keilmann, Appl. Phys. Lett. **85**, 5064 (2004)
38. H. Okamoto, K. Imura, Sur. Sci. Rep. **84**, 199 (2009)
39. K. Imura, H. Okamoto, Bull. Chem. Soc. Jpn. **81**, 659 (2008)
40. H. Okamoto, K. Imura, J. Mater. Chem. **16**, 3920 (2006)
41. G. Mie, Ann. Phys. **25**, 377 (1908)
42. R. Ganz, Ann. Phys. **37**, 881 (1912)
43. S. Link, M.B. Mohamed, M.A. El-Sayed, J. Phys. Chem. B **103**, 3073 (1999); S. Link, M.A. El-Sayed, J. Phys. Chem. B **109**, 10531 (2005)
44. M. Meier, A. Wokaun, Opt. Lett. **8**, 581 (1983)
45. A. Taflove, S.C. Hagness, *Computational Electrodynamics: The Finite-Difference Time-Domain Method*, 3rd edn. (Aetech House, Norwood, MA, 2005)
46. B.T. Drain, P.J. Flatau, J. Opt. Soc. Am. A **11**, 1491 (1994)
47. C. Girard, A. Dereux, Rep. Prog. Phys. **59**, 657 (1996)
48. J.-J. Greffet, R. Carminati, Prog. Sur. Sci. **56**, 133 (1997)
49. L. Gunnarsson, T. Rindzevicius, J. Prikulis, B. Kasemo, M. Käll, J. Phys. Chem. B **109**, 1079 (2005)
50. M.F. Crommie, C.P. Lutz, D.M. Eigler, Nature **363**, 524 (1993)
51. A. Nilius, T.W. Wallis, W. Ho, Science **297**, 1853 (2002)
52. G. Colas des Francs, C. Girard, J.-C. Weeber, C. Chiane, T. David, A. Dereux, Phys. Rev. Lett. **86**, 4950 (2001)
53. R.Y. Chiao, P.G. Kwiat, A.M. Steinberg, Physica B **175**, 257 (1991)
54. E.N. Economou, *Green's Function in Quantum Physics* (Springer, Berlin, 1983)
55. K. Masuda, T. Saiki, S. Nomura, M. Mihara, Y. Aoyagi, S. Nair, T. Takagahara, Phys. Rev. Lett. **91**, 177401 (2003)
56. C. Chicanne, T. David, R. Quidant, J.C. Weeber, Y. Lacroute, E. Bourillot, A. Dereux, Phys. Rev. Lett. **88**, 097402 (2002)
57. E.H. Synge, Philos. Mag, **6**, 356 (1928)
58. M. Ohtsu, *Near-Field Nano/Atom Optics and Technology* (Springer, Berlin, 1998)
59. S. Smith, N. Christian, R. Holme, B. Orr, R. Kopelman, T. Norris, Ultramicroscopy **71**, 213 (1998)
60. B.A. Nechay, U. Siegner, M. Achermann, H. Bielefeldt, U. Keller, Rev. Sci. Instrum. **70**, 2758 (1999)
61. T. Guenther, C. Lienau, T. Elsaesser, M. Glanemann, V. Martin Axt, T. Kuhn, Phys. Rev. Lett. **89**, 057401 (2002)
62. T. Nagahara, K. Imura, H. Okamoto, Rev. Sci, Instrum. **75**, 4528 (2004)
63. M. Labardi, M. Zavelani-Rossi, D. Polli, G. Cerullo, M. Allegrini, S. De Silvestri, O. Svelto, Appl. Phys. Lett. **86**, 031105 (2005)
64. K. Imura, T. Nagahara, H. Okamoto, J. Phys. Chem. B **108**, 16344 (2004)
65. B. Hecht, H. Bielefeldt, Y. Inouye, D.W. Pohl, L. Novotny, J. Appl. Phys. **81**, 2492 (1997)

66. P.M. Morse, H. Feshbash, *Methods of Theoretical Physics* (McGraw-Hill, New York, 1953)
67. K. Imura, T. Nagahara, H. Okamoto, Chem. Phys. Lett. **400**, 500 (2004)
68. K. Imura, T. Nagahara, H. Okamoto, J. Chem. Phys. **122**, 154701 (2005)
69. K. Imura, H. Okamoto, Opt. Lett. **31**, 1474 (2006)
70. C.E. Jordan, S.J. Stranick, L.J. Richter, R.R. Cavanagh, J. Appl. Phys. **86**, 2785 (1999)
71. B.J. Messinger, K. Ulrich von Raben, R.K. Chang, P.W. Barber, Phys. Rev. B **24**, 649 (1981)
72. G. Schider, J.R. Krenn, A. Hohenau, H. Ditlbacher, A. Leitner, F.R. Aussenegg, Phys. Rev. B **68**, 155427 (2003)
73. J.K. Lim, K. Imura, T. Nagahara, S.K. Kim, H. Okamoto, Chem. Phys. Lett. **41**, 412 (2005)
74. S. Link, M.A. El-Sayed, J. Phys. Chem. B **103**, 8410 (1999)
75. H. Petek, G. Ogawa, Prog. Surf. Sci. **56**, 239 (1997)
76. J.-Y. Bigot, V. Halté, J.-C. Merle, A. Daunois, Chem. Phys. **251**, 181 (2000)
77. C.-K. Sun, F. Vallée, L. Acioli, E.P. Ippen, J.G. Fujimoto, Phys. Rev. B **48**, 12365 (1993)
78. J.H. Hodak, A. Henglein, G.V. Hartland, J. Phys. Chem. B **104**, 9954 (2000)
79. C. Voisin, D. Christofilos, P.A. Loukakos, N. Del Fatti, F. Vallée, J. Lermé, M. Gaudry, E. Cottancin, M. Pellarin, B. Broyer, Phys. Rev. B **69**, 195416 (2004)
80. M. Hu, G.V. Hartland, J. Phys. Chem. B **106**, 7029 (2002)
81. O.L. Muskens, N. Del Fatti, F. Vallée, Nano Lett. **6**, 552 (2006)
82. M. Pelton, M. Liu, S. Park, N.F. Scherer, P. Guyot-Sionnest, Phys. Rev. B **73**, 155419 (2006)
83. D. Brinks, F.D. Stefani, F. Kulzer, R. Hildner, T.M. Taminiau, Y. Avlasevich, K. Müllen, N.F. van Hulst, Nature **465**, 905 (2010)
84. A. Kubo, K. Onda, H. Petek, Z. Sun, Y.S. Jung, H.K. Kim, Nano Lett. **5**, 1123 (2005)
85. A. Kubo, N. Pontius, H. Petek, Nano Lett. **7**, 470 (2007)
86. A. Stella, M. Nisoli, S. De Silvesti, O. Svelto, G. Lanzani, P. Cheyssac, R. Kofman, Phys. Rev. B **53**, 15497 (1996)
87. T.V. Chahbazyan, I.E. Perakis, J.-Y. Bigot, Phys. Rev. Lett. **81**, 3120 (1998)
88. C. Voisin, D. Christofilos, N. Del Fatti, F. Vallée, B. Prével, E. Cottancin, J. Lérme, M. Pellarin, M. Broyer, Phys. Rev. Lett. **85**, 2200 (2000)
89. K. Imura, H. Okamoto, Phys. Rev. B **77**, 041401 (R) (2008)
90. S.D. Brorson, J.G. Fujimoto, E.P. Ippen, Phys. Rev. Lett. **59**, 1962 (1987)
91. N. Bloembergen, *Nonlinear Optics* (World Scientific, Singapore, 1996)
92. A. Mooradian, Phys. Rev. Lett. **22**, 185 (1969)
93. K. Imura, T. Nagahara, H. Okamoto, J. Am. Chem. Soc. **126**, 12730 (2004)
94. P.J. Schuck, D.P. Fromm, A. Sundaramurthy, G.S. Kino, W.E. Moerner, Phys. Rev. Lett. **94**, 017402 (2005)
95. R.A. Farrer, F.L. Butterfield, V.W. Chen, J.T. Fourkas, Nano Lett. **5**, 1139 (2005)
96. A. Bouhelier, R. Bachelot, G. Lerondel, P. Royer, G.P. Wiederrecht, Phys. Rev. Lett. **95**, 267405 (2006)
97. A. Hohenau, J.R. Krenn, J. Beermann, S.I. Bozhevolnyi, S.G. Rodrigo, L. Martin-Moreno, F. Garcia-Vidal, Phys. Rev. B **73**, 155404 (2006)
98. M. Mühlschlegel, H.-J. Eisler, O.J.F. Martin, B. Hecht, D.W. Pohl, Science **308**, 1607 (2005)
99. H. Wang, T.B. Huff, D.A. Zweifel, W. He, P.S. Low, A. Wei, J.-X. Cheng, Proc. Nat. Acad. Sci. USA **102**, 15752 (2005)
100. N.J. Durr, T. Larson, D.K. Smith, B.A. Korgel, K. Sokolov, A. Ben-Yakar, Nano Lett. **7**, 945 (2007)
101. Y. Jiang, N.N. Horimoto, K. Imura, H. Okamoto, K. Matsui, R. Shigemoto, Adv. Mater. **21**, 2309 (2009)
102. K. Imura, T. Nagahara, H. Okamoto, J. Phys. Chem. B **109**, 13214 (2005)
103. K. Imura, T. Nagahara, H. Okamoto, Appl. Phys. Lett. **88**, 023104 (2006)
104. K. Imura, H. Okamoto, M.K. Hossain, M. Kitajima, Chem. Lett. **35**, 78 (2006)
105. K. Imura, H. Okamoto, M.K. Hossain, M. Kitajima, Nano Lett. **6**, 2173 (2006)
106. T. Shimada, K. Imura, M.K. Hossain, H. Okamoto, M. Kitajima, J. Phys. Chem. C **112**, 4033 (2008)
107. M.K. Hossain, T. Shimada, M. Kitajima, K. Imura, H. Okamoto, Langmuir **24**, 9241 (2008)
108. G.T. Boyd, Z.H. Yu, Y.R. Shen, Phys. Rev. **33**, 7923 (1986)

109. P. Apell, R. Monreal, S. Lundqvist, Phys. Scr. **38**, 174 (1988)
110. R. Rosei, Phys. Rev. B **10**, 474 (1974); M. Guerrrisi, R. Rosei, P. Winsemius, Phys. Rev. B **12**, 557 (1975)
111. J.I. Gersten, J. Chem. Phys. **72**, 5779 (1980)
112. J. Gersten, A. Nitzan, J. Chem. Phys. **73**, 3023 (1980)
113. P.F. Liao, A. Wokaun, J. Chem. Phys. **76**, 751 (1982)
114. A.M. Michaels, M. Nirmal, L.E. Brus, J. Am. Chem. Soc. **121**, 9932 (1999)
115. H. Xu, J. Aizpurua, M. Käll, P. Apell, Phys. Rev. E **62**, 4318 (2000)
116. E. Hao, G.C. Schatz, J. Chem. Phys. **120**, 357 (2004)
117. T.E. Talley, J.B. Jackson, C. Oubre, N.K. Grady, C.W. Hollars, S.M. Lane, T.R. Huser, P. Nordlander, N.J. Halas, Nano Lett. **5**, 1569 (2005)
118. H. Watanabe, N. Hayazawa, Y. Inouye, S. Kawata, J. Phys. Chem. B **109**, 5012 (2005)
119. H. Wang, C.J. Levin, N.J. Halas, J. Am. Chem. Soc. **127**, 14992 (2005)
120. J.A. Fan, C. Wu, K. Bao, J. Bao, R. Bardhan, N.J. Halas, V.N. Manoharan, P. Nordlander, G. Shvets, F. Capasso, Science **328**, 1135 (2010)
121. T. Kodo, F. Matsumoto, K. Nishio, H. Masuda, Chem. Lett. **37**, 466 (2008)
122. N. Nedyalkov, T. Sakai, T. Miyanishi, M. Obara, Appl. Phys. Lett. **90**, 123106 (2007)

Chapter 5
Simple Approaches for Constructing Metallic Nanoarrays on a Solid Surface

Hidenobu Nakao

Abstract This chapter concerns simple experimental approaches for constructing metallic nanoarrays on a solid surface for applications to miniaturized optical devices, sensors, and single-molecule detection. Simple interface (air–liquid) movement leads to the controlled formation of one-dimensional (1D) nanoarrays of DNA or its nanofiber without special equipment. The assembly of metallic nanoparticles onto DNA can be driven by electrostatic binding of newly prepared gold nanoparticles with positive charges, leading to the formation of 1D metallic nanoarrays. Finally, the fabrication and patterning of metallic nanoarrays achieved with transfer printing techniques are described.

5.1 Introduction

Metal nanoparticles (MNPs) such as Au or Ag can confine light (electromagnetic fields) to their dimensions on the order of or smaller than the wavelength. Such properties, called localized plasmon resonances (LPRs), are based on interactions between electromagnetic radiation and conduction electrons at metallic interfaces or in metallic nanostructures, leading to an enhanced optical near field of subwavelength dimension below the optical diffraction limit [1]. LPRs of MNPs are tunable throughout the visible and near-infrared region of the spectrum as a function of particle size, shape, aggregation state, and local environment [1]. When MNPs are organized in closely spaced arrays, their LPR peak is shifted towards lower energy and the bandwidth increases because the dielectric constant of the surrounding MNPs is increased [1–3]. Since such a one-dimensional (1D) MNP array can exhibit coupled modes due to near-field interactions between adjacent MNPs, it is possible to propagate electromagnetic waves (light) with a transverse

H. Nakao
Nano-Architecture Group, National Institute for Materials Science, Namiki 1-1, Tsukuba, Ibaraki 305-0044, Japan
e-mail: NAKAO.hidenobu@nims.go.jp

M. Ohtsu (ed.), *Progress in Nanophotonics 1*, Nano-Optics and Nanophotonics,
DOI 10.1007/978-3-642-17481-0_5,

confinement below the diffraction limit (plasmon waveguides). Researchers have developed plasmon waveguides that operate well below the optical diffraction limit, $\lambda/2$, down to $\lambda/20$ [1–5]. Incident radiation on one particle gives rise to plasmon oscillation, which can induce plasmon oscillations in neighboring MNPs that are sufficiently close. The light coupled through nanoparticle plasmons can then propagate along the array, around corners, and through T junctions. Molecules absorbed by the surface of the array undergo a surface-enhanced Raman scattering (SERS) effect, enhancing its Raman signal [6–8]. This process has attracted much attention, due to its potential applications in miniaturized optical devices, sensors, and single-molecule detection via SERS [9–13]. Thus, constructing various architectures of ordered MNPs and investigating the light localized in such architectures should be of great interest.

To utilize these arrays for the above applications, we must know their precise assembly and patterning on solid surfaces. Here, we describe our own approach for fabricating 1D MNP arrays on surfaces. In our assembly, highly aligned DNA molecules or nanofibers on a surface are used as a 1D template and can be driven by simple interface (air–liquid) movement. Positively charged MNPs can be explored to produce MNPs that have strong binding properties with DNA strands, leading to highly aligned 1D metallic nanoarrays on surfaces. Furthermore, preparation and patterning of metallic nanoarrays with long-range order are presented using DNA nanofibers and transfer-printing (TP) techniques. Finally, optical applications that take advantage of light fields localized on prepared metallic nanoarrays are discussed.

5.2 Assembling MNPs in One Dimension

Controlling assemblies of MNPs is useful for numerous sensing or electronic applications. 1D array of MNPs strongly absorbs light of specific wavelengths with polarizations parallel to the long axes oriented in the same direction, thus exhibiting useful properties for photonic applications. In general, MNPs can be organized using bottom-up approaches based on self-assembly. Simple self-assembly strategies introduce functional groups (ligands) onto MNPs, as specific physical and chemical affinities such as covalent or noncovalent (van der Waals, hydrophobic, or electrostatic) interactions can be exploited to achieve precise self-assembly of MNPs. With alkanethiol molecules, preferential binding of thiols to the {111} surface is obtained [14, 15].

5.2.1 Chemical Self-Assembly

Gold nanorods (AuNRs) with various aspect ratios have {111} at each end and {100} at their sides (Fig. 5.1). The most popular synthetic method for such AuNRs

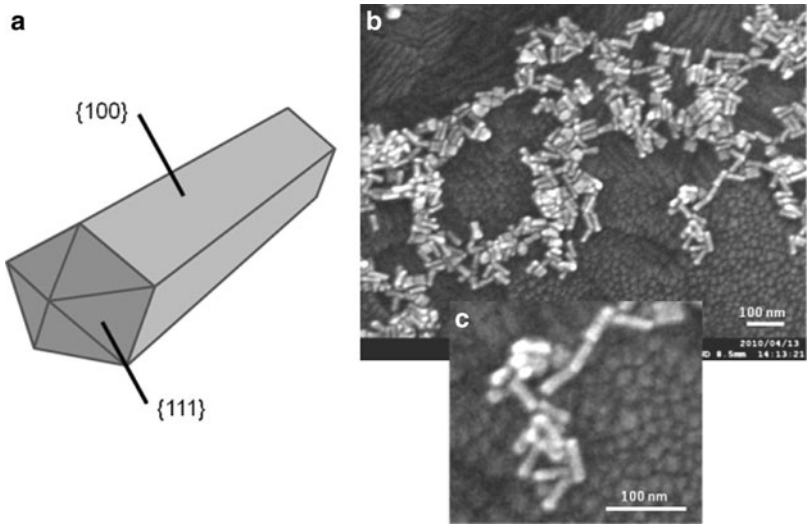

Fig. 5.1 (**a**) Schematic of three-dimensional (3D) morphology of a gold nanorod. (**b**) SEM image of the gold nanorod with the aspect ratio of 3.5. (**c**) Enlarged image of (**b**) (courtesy of Dr. K. Tsukamoto)

is that of seed-mediated nanoparticle growth in the presence of surfactant, as introduced by the Murphy group [9]. In the seed-mediated growth method, cetyltrimethyl ammonium bromide (CTAB) used as surfactant can form a bilayer around AuNR rather than a micellar form, and prefers to bind with the {100} longitudinal side surface of the AuNR rather than the {111} end surface (Fig. 5.2). Thus, the {111} side faces of AuNRs are more exposed and accessible to the alkanethiols, preferentially binding to such faces. In several reports, alkanethiols were introduced onto the {111} side faces of AuNRs through hydrogen bonds [16] between alkanethiol molecules, or through binding of biomolecules [17] to the alkanethiol layer, resulting in a "head-to-tail" chainlike formation of AuNR aggregates.

An alternative strategy for assembling AuNRs is to use "side-to-side" formation between {100} longitudinal side surfaces capped with the cationic CTAB bilayer. Simple concentration of AuNR solutions leads to preferential "side-to-side" assembly [18]. This process is entropically driven, in part by release of water and counterions from the interface of adjacent AuNRs. Other side-to-side assemblies of AuNRs can also be prepared in a pH-dependent manner [19]. In this case, AuNRs capped with the cationic CTAB bilayer are incubated with adipic acid ($HOOC(CH_2)_4COOH$). At pH values below the pKa of carboxylic acid, no particular assembly of nanorods is observed, but at pH 7–8, the deprotonated adipic acid acts as a short rigid bridge between AuNRs. As described above, 1D arrays of MNPs can behave as waveguides with high field confinement. Recent work suggests that light propagation between adjacent particles can be increased by changing the geometry to the "side-to-side" formation of nanorods [2, 3].

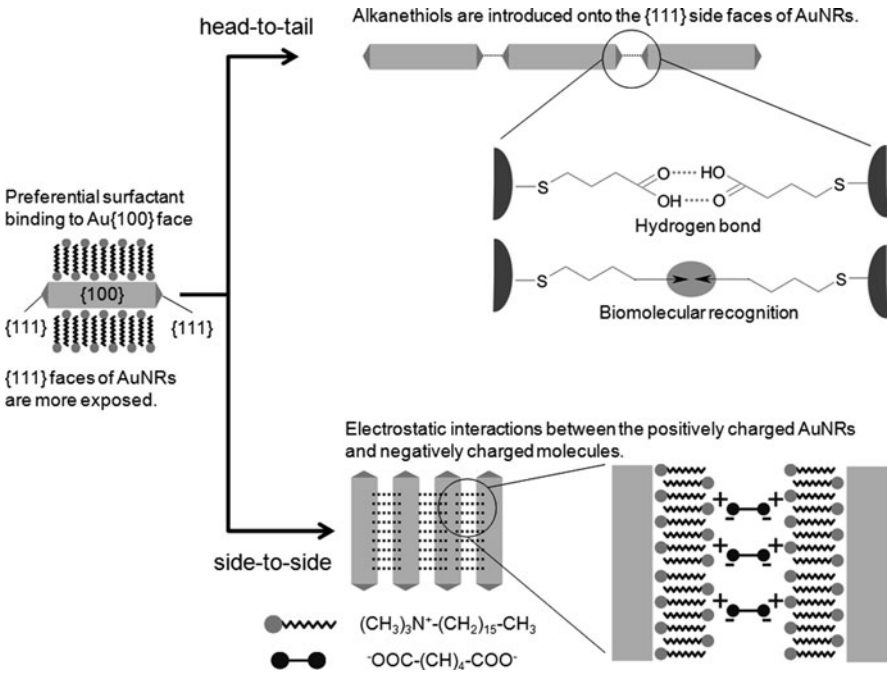

Fig. 5.2 Schematic of "head-to-tail" and "side-to-side" assemblies of gold nanorods

Furthermore, De Vries et al. reported a simple method to place target molecules specifically at two diametrically opposed positions in the molecular coating of MNPs [20, 21]. This approach is based on functionalization of the polar singularities that must form when a curved surface is coated with ordered monolayers, such as a phase-separated mixture of ligands. The molecules placed at these polar defects were used as chemical handles to form 1D AuNP chains.

5.2.2 Physical Means

Current lithography methods and microcontact printing can either directly produce arrays of MNP [2, 3, 22] or predefine a surface (geometrically, chemically, or electrostatically) to assist the assembly of MNPs on a surface [23–26]. Scanning probe nanolithography techniques with a local interaction between the probe and the substrate have been applied to patterning of self-assembly monolayers. One such technique is dip-pen nanolithography [27], where an atomic microscope tip is utilized as a pen to deposit general organic molecules directly onto solid substrates without any complicated processing steps (Fig. 5.3a). Barsotti et al. chemically directed mercaptopropionic acid-protected AuNPs onto the mercaptohexadecanoic acid lines, prepatterned by dip-pen nanolithography [28].

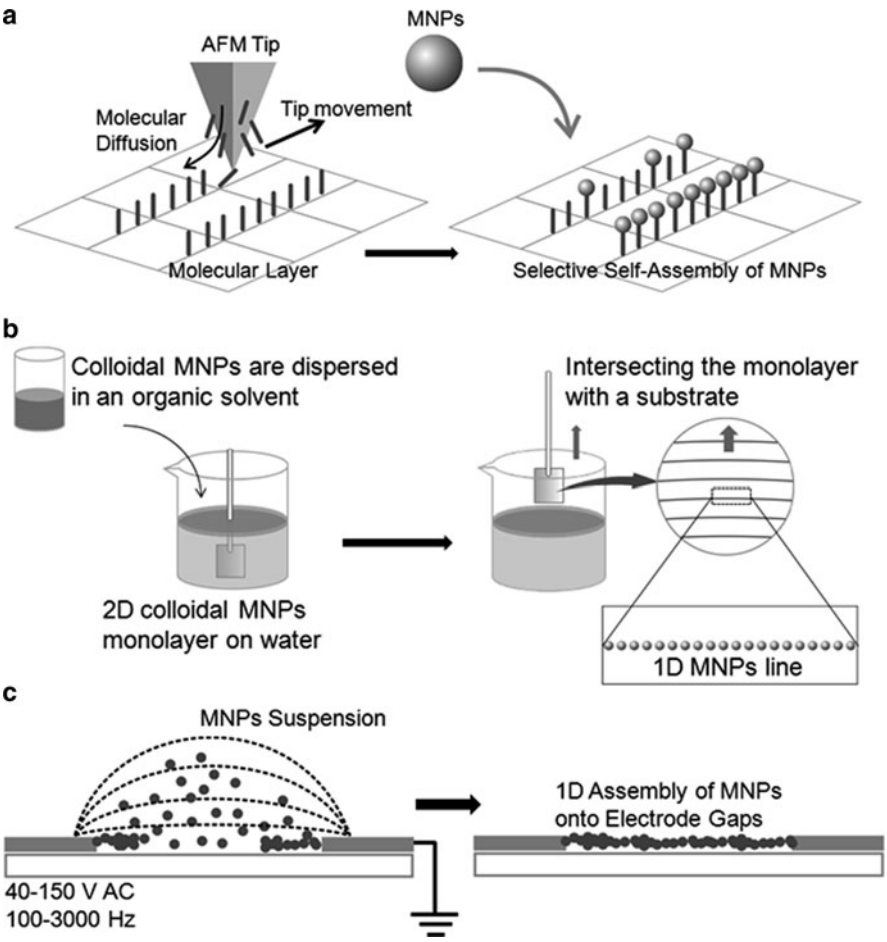

Fig. 5.3 Physical approaches for fabricating 1D MNP arrays on surfaces. (**a**) MNPs are deposited or self-organized on the patterns fabricated with dip-pen nanolithography. (**b**) 1D MNP arrays of particles can be deposited on the substrate upon lifting through a stick–slip motion of the contact line. (**c**) Microwires of MNPs are assembled in an alternating electric field between two electrodes

In different MNP assembly approaches, interfaces such as gas–solid and liquid–liquid play important roles. The Langmuir–Blodgett technique is a typical interfacial assembly process [29–31]. Surface-protected MNPs are generally made to float over a water surface using hydrophobic interactions. At the water–air interface, MNPs form a monolayer, which is slowly compressed and transferred during compression, using horizontal or vertical lift-off, to substrates such as silicon (Fig. 5.3b). Using this technique, uniform 1D arrays of MNPs with sizes ranging from a few nanometers to a few micrometers can be readily produced with tunable particle density. Thus, 1D arrays or films of various well-ordered MNPs can be achieved [32].

Furthermore, an alternating electric field (dielectrophoresis) assembly of particles also gives composite wire-like structures, for example, if AuNPs are used [33–35]. AuNPs with a diameter of 10–20 nm are assembled via dielectrophoresis into long wires of micrometer thickness (Fig. 5.3c). Mertig's group reported 1D palladium nanowires grown from an aqueous palladium salt solution by dielectrophoresis, which have a thickness of 5–10 nm and a length of up to several micrometers [36].

5.2.3 Template-Assisted Assembly

Directional organization using suitable templates is the best approach for creating 1D assemblies. Various templates are available to achieve this purpose. Linear soft templates (e.g., organic polyelectrolytes [37–39] and biomolecules [40–43]) and hard templates (e.g., inorganic wires [44–47] and crystal step edges [48,49]) are utilized for creating 1D MNP assemblies. For linear electrolytes acting as 1D scaffolds, Minko et al. reported Pd nanoparticles assembled onto cationic poly(2-polyvinyl pyridine) P2VP scaffolds, first by absorbing $PdCl_4$ anions onto the polyelectrolyte, via electrostatic interactions, followed by chemical reduction [50]. Like polyelectrolytes, biomolecules such as DNA, or proteins, they are useful 1D templates. Their structures can be manipulated, and MNPs can be specifically located on their surfaces. For example, attaching AuNPs to linear or tile-like DNA structures creates fascinating nanoarchitectures [51–56].

5.3 Highly Aligned DNA as Templates for 1D Assembly of MNPs

DNA has a well-defined structure for the bottom-up construction of artificial nanostructures and networks in one, two, and three dimensions [57–63]. In particular, the specificity of Watson–Crick base pairing enables the programming of its intramolecular and intermolecular associations, and then makes use of its unique molecular recognition and self-assembly capabilities to construct DNA-based architectures. Having a diameter of 2 nm and a virtually infinite length, providing a large variety of binding sites for different metal ions, and having remarkable mechanical properties, DNA constitutes an ideal template for organizing metallic and semiconductor nanoparticles into 1D assemblies. Metallic wires grown on DNA have been observed to possess peculiar transport properties both at room temperature and at low temperature and are thus good candidates for optoelectronic applications.

5.3.1 Stretching and Aligning DNA Molecules on Surfaces

Since DNA molecules in solution have the conformation of a random coil, they must be stretched and aligned on surfaces to create templates of 1D arrays. Generally, DNA molecules have been stretched and aligned at the macroscopic or single-molecule level by hydrodynamic flow [64–66], meniscus forces [67–71], electric field [72, 73], atomic force microscopy (AFM) [74, 75], optical trapping [76], or magnetic tweezers [77]. Surface modifications (e.g., silanization [67–70] and poly-L-lysine modification [78] of substrate surfaces) have also been utilized to facilitate the fixation and the stretching of DNA molecules using the above methods. Though controlling the interaction between DNA molecules and surfaces is very important for stretching and aligning DNA molecules, the interaction mechanism at the chemical structure level has not been sufficiency investigated.

We have reported a useful technique for reproducibly stretching and aligning DNA on surfaces. The point of this technique is controlling the interaction between surfaces and DNA using a polymer coating [79]. Chemical structures of the coating polymers selected in this study are presented in Fig. 5.4. A solution of 5 μL of DNA (4.5 ng μL^{-1}) in TE buffer (10 mM Tris–HCl and 1 mM EDTA, pH = 8) was deposited on such polymer-coated glass surfaces, and its droplet was then sucked up using pipette. When a droplet of DNA solution on a surface is sucked up, the surface tension at the moving air–water interface is sufficient to stretch and align the molecules along the central direction of the droplet (Fig. 5.5).

The stretching of DNA on surfaces coated with various polymers was examined. We observed fluorescence microscopic images of DNA deposited on various

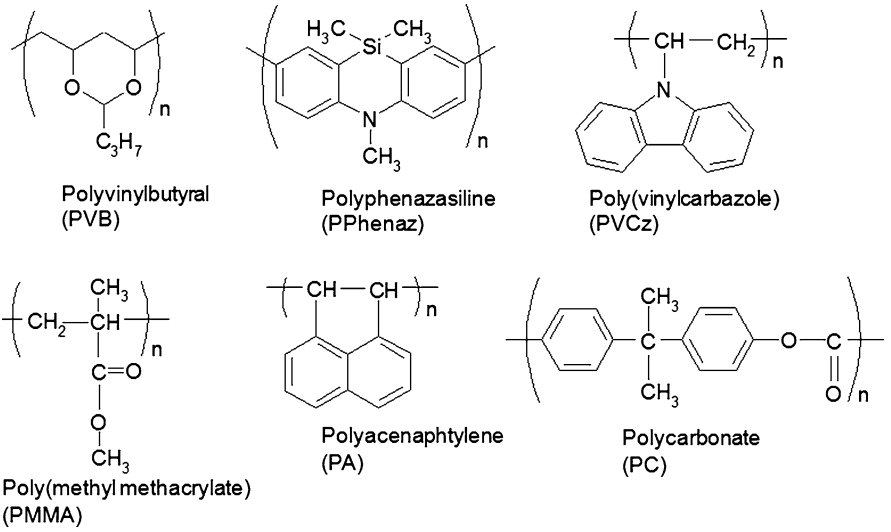

Fig. 5.4 Chemical structures of polymers in this study

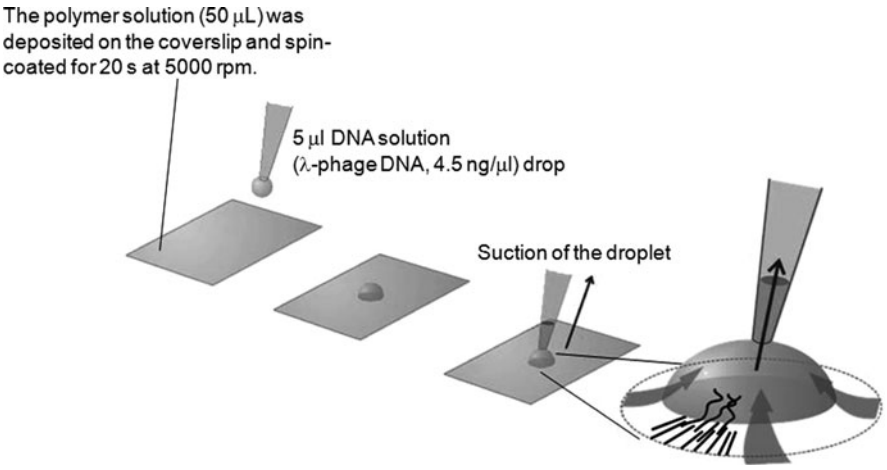

Fig. 5.5 Procedure of DNA stretching and alignment on surfaces

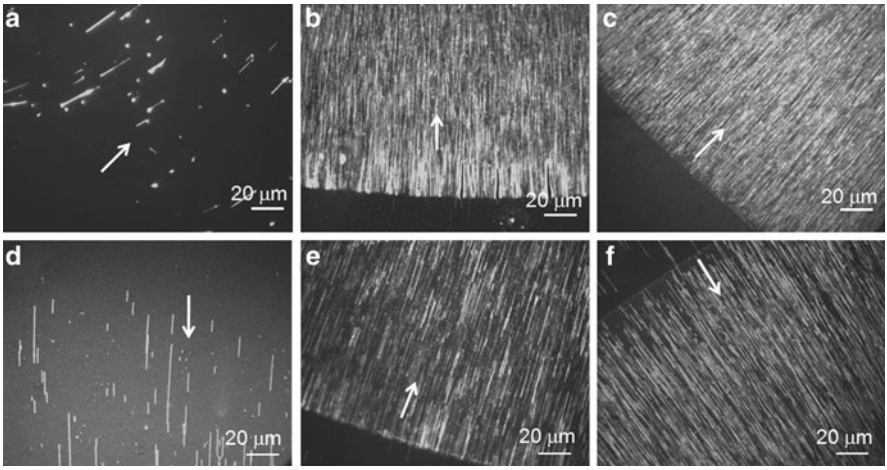

Fig. 5.6 Fluorescence microscopic images of DNA stretched on various polymer-coated surfaces. (**a**) PVB-coated glass. (**b**) PPhenaz-coated glass. (**c**)PVCz-coated glass. (**d**) PMMA-coated glass. (**e**) PA-coated glass. (**f**) PC-coated glass. The *arrow* indicates the central direction of the droplet. Reprinted with permission from [79] and [80]. Copyright (2010) by the American Chemical Society and the Japan Society for Analytical Chemistry

polymer-coated coverslips (Fig. 5.6). On uncoated surfaces, the observed image revealed that only a few molecules were partially stretched and that many molecules were aggregated. Because the glass surface has strong polar groups, it seems that DNA interacts with the surface strongly and nonspecifically. However, DNA molecules were not sufficiently fixed on PVB-coated surfaces (Fig. 5.6a). PVB-coated glasses have hydrophobic surfaces, so that the interactions of DNA having

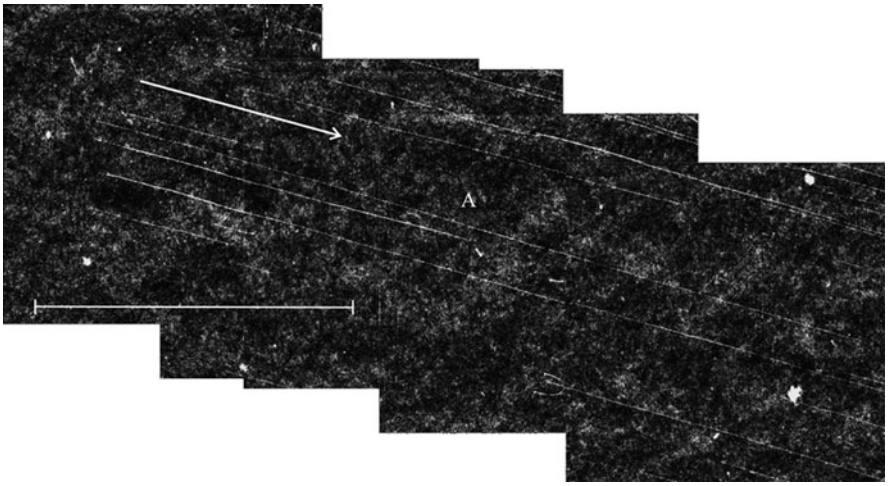

Fig. 5.7 AFM image of DNA stretched on PPhenaz-coated glass in a wide-range scan. DNA molecules are stretched and aligned in the direction of the *arrow* in the figure. The *white bar* denotes 10 μm. Height scale is 3 nm. Reprinted with permission from [79]. Copyright (2010) by the American Chemical Society

negative charges or hydrophilic groups with these surfaces are very weak. In contrast, the observed DNA molecules on PVCz- and PPhenaz-coated coverslips were sufficiently fixed and stretched (Fig. 5.6b, c). In addition, these images demonstrate that DNA molecules are stretched and aligned in a central direction of the DNA droplet. Thus, it seems that PVCz- and PPhenaz-coated coverslips are useful for depositing and imaging well-stretched DNA. Fluorescence microscopy images reveal that the length of the well-stretched DNA on PPhenaz surface was $23.7 \times 3.4\,\mu m$ ($n = 35$), and that of the PVCz surface was $23.1 \times 3.8\,\mu m$ ($n = 30$).

The AFM image of well-stretched DNA on PPhenaz-coated coverslip is shown in Fig. 5.7. The length of the DNA denoted segment A was 24.8 μm, and its height was ~1 nm. This length is similar to the average length of a single λ-DNA stretched on PPhenaz or PVCz surfaces, suggesting that the AFM image of segment A corresponds to a single λ-DNA. This idea is also supported by the fact that the observed height of the DNA is consistent with the height of a single double-stranded DNA imaged by AFM in a previous study [81, 82]. Although the DNA stretched on PPhenaz or PVCz was longer than the crystallographic length of the 48.5-kb λ-DNA (~16.5 μm), the length is close to that (26.5 μm) [69] on polystyrene obtained by Bension et al. Because the stretching force applied by the interface motion on hydrophobic surfaces is stronger than that on hydrophilic surfaces, the DNA is more stretched on PPhenaz and PVCz having hydrophobicity similar to that of polystyrene. DNA was almost the same on both polymers. Furthermore, the root mean square (RMS) roughness of the uncoated coverslip decreased from 5.013 to 0.319 nm after coating with PPhenaz and to 0.512 nm after coating with PVCz. It should be noted that these polymer coatings enabled the attainment of adequate AFM images of DNA on conventional coverslips.

Although PVCz and PPhenaz have hydrophobicity similar to that of PVB, DNA molecules sufficiently fixed and stretched on both surfaces. The results suggest that these polymers have a specific interaction with DNA. To understand the interactions between these polymers and DNA, we examined their absorption spectral properties. When we added DNA molecules to a solution (mixture of TE buffer (pH) 8.0: THF 1:1) containing PPhenaz, the absorption band at 390 nm, which is attributed to the π–π^* transition of PPhenaz, decreased gradually. Such a decrease in absorbance indicates strong interaction between the electronic state of the polymer and that of the DNA base. Consequently, it seems that these spectral changes are characteristic of an interaction (e.g., π-stacking) between aromatic compounds and DNA [83–85]. We observed a similar phenomenon for PVCz. From the molecular viewpoint, their aromatic amine units are planar or almost planar, favoring the insertion of polymer units into the hydrophobic interior of the DNA base stack. We, therefore, assume that DNA attaches to surfaces through π-stacking between aromatic amines in polymers and base pairs in DNA. In addition, the λ-phage DNA used in this study was linear DNA with 12-base-long sticky ends, which expose the hydrophobic π-core (bases) on both ends of the helix. Since such positions have a strong affinity with surfaces, DNA molecules are preferentially anchored at either end [69]. Consequently, effective DNA stretching and fixations are achieved on surfaces. By using polymers containing π-units other than aromatic amines, we found that such polymers effectively stretch and fix DNA molecules on surfaces (Fig. 5.3e, f). Thus, the above results strongly indicate that π–π interaction is the important factor for DNA stretching and fixations in our system.

5.3.2 Assembling AuNPs onto Aligned DNA Molecules

The interaction of MNPs with DNA is a well-known phenomenon [86–89], and single- or double-strand DNA is decorated by MNPs, which can easily be imaged by transmission electron microscopy (TEM) or AFM [90–92]. Various surface-functionalized AuNPs have been prepared to attach AuNPs securely to DNA molecules. In numerous studies, such AuNPs were prepared by surface modifications with cationic thiols [54, 55, 92] or intercalators [93, 94]. The 1D chains of AuNPs coated with cationic trimethyl(mercaptoundecyl) ammonium monolayers were electrostatically assembled along DNA molecules in solution by the relative molar quantities of AuNPs and DNA base pairs. Since psoralen acts as a specific intercalator for A–T base pairs, the functionalized AuNPs were assembled onto the pA–pT ds-DNA [93]. Furthermore, UV irradiations induced the reaction between the psoralen units and the thymine of DNA, and then covalently fixed AuNPs to the DNA.

Recently, we reported a one-step preparation of surface-functionalized AuNPs without ligand exchange [95]. Novel surface-functionalized AuNPs (AN-AuNPs) were prepared based on the conventional reduction of $HAuCl_4$ using aniline as a reducer, so that the AN-AuNPs had a positive charge and an aromatic ring on

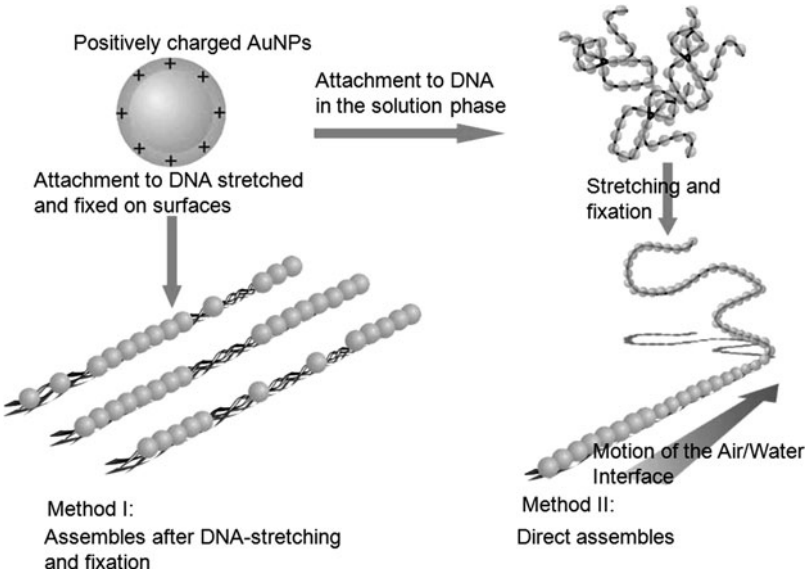

Fig. 5.8 Procedure of assembling AN-AuNPs onto DNA. Reprinted with permission from [95]. Copyright (2010) by the American Chemical Society

the surface (due to the formation of oxidized aniline during preparation), which resulted in their electrostatic binding to the negatively charged phosphate backbone of DNA. Characterization of prepared particles by electrophoresis analysis, zeta-potential measurements, and UV measurements revealed the presence of positive charges on their surfaces. We then experimented with assemblies of AN-AuNPs organized on DNA molecules. Two different procedures were used here (Fig. 5.8). In method I, DNA was stretched and fixed on the surface according to the above method, which resulted in highly aligned DNA patterns formed on surfaces. Next, DNA molecules were treated with AN-AuNP solution for 5 min, and then rinsed in water.

Before treatment with AN-AuNPs, the height (diameter) of DNA molecules imaged by AFM on the surface was $\sim$1.0 nm, which agreed well with that of a single double-stranded DNA in the previous description. After treatment with AN-AuNPs, AFM observation revealed that many DNA molecules on the surfaces had contiguous particles with raised height, indicating that the observed heights of DNA molecules were 2.14×0.35 nm. The majority of particles that can be distinguished from the background are 1.56×0.21 nm. Consequently, it is reasonable that the increased DNA molecule heights after treatment were caused by particle deposition. In method II, we prepared a mixture of AN-AuNP solution and λ-DNA solution, and incubated the mixture for 30 min. Next, samples were stretched and fixed on surfaces according to the above method. It was very interesting to note that AN-AuNPs with larger interparticle spacing were assembled along the DNA molecules in a necklace-like formation. Since the DNA molecules

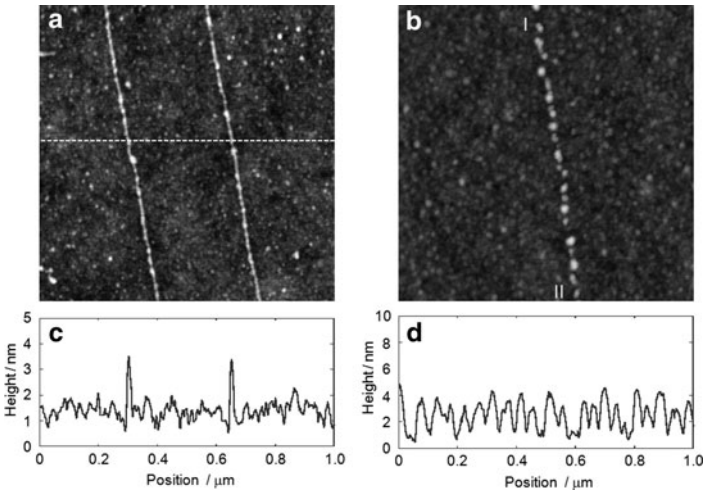

Fig. 5.9 AFM images of highly ordered assemblies of AN-AuNPs on DNA molecules using (**a**) method I and (**b**) method II. Image sizes are 1 μm × 1 μm. The height scale is 5 nm. (**c**) Scan profile along the white line of the image (**b**). (**d**) Scan profile along particles line from I to II in image (**b**). Reprinted with permission from [95]. Copyright (2010) by the American Chemical Society

(to which AN-AuNPs were already attached) were stretched significantly by surface tension, interparticle spacing was greater. Figure 5.9 presents AFM images of AN-AuNP-attached DNA molecules by two methods. By depositing different MNPs in interparticle spacing, it should be possible to tune the electrical or optical properties of linear arrays. Most recently, a one-step process achieved raspberry-[96] and mushroom-like aggregates [97] of AN-AuNPs that have 3D structures on a nano-order level. DNA templates should be also helpful in aligning such aggregates, which produce metallic nanoarrays having significant electrical and optical properties.

As described above, many DNA molecules were sufficiently stretched and fixed on PPhenaz-coated surfaces by the π–π interaction between π-conjugated units in polymer and base pairs in DNA. To enhance the solubility of PPhenaz in polar solvent such as water and interactions with DNA having negative charges, PPhenaz having alkylammonium salts on the N atom (PPhenaz-TMA) was synthesized (Fig. 5.10), directly forming π-conjugated polymer functionalized DNA (PPhenaz-TMA/DNA) nanowires [98]. AFM observations revealed structural changes of PPhenaz-TMA/DNA nanowires before and after treatments of $AuCl_4^-$ (Fig. 5.11). Au depositions along PPhenaz-TMA/DNA nanowires could be also clarified by using scanning near-field optical microscope (SNOM). Before treatment, the AFM topographic image of PPhenaz-TMA/DNA nanowires was observed, but the SNOM image of those was not observed (Fig. 5.12a, b). However, the SNOM image of PPhenaz-TMA/DNA nanowires after treatment was clearly observed, synchronizing exactly with its AFM topographic image (Fig. 5.12c, d). The observed SNOM image after treatment originates from near-field plasmon coupling between the probing tip

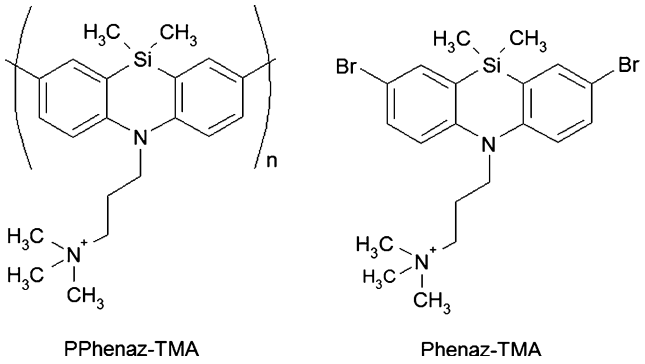

Fig. 5.10 Chemical structures of PPhenaz-TMA and Phenaz-TMA

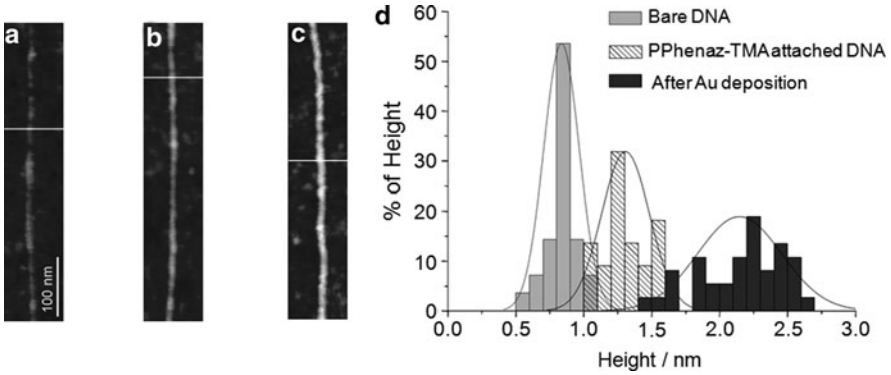

Fig. 5.11 Structural changes of DNA molecules induced by treatments. (**a**) AFM images of bare DNA. (**b**) AFM image of PPhenaz-TMA-attached DNA. (**c**) AFM image of PPhenaz-TMA-attached DNA after Au deposition. The height scale is 5 nm. (**d**) Histograms showing the height distributions of DNA induced by treatments

and the AuNPs on PPhenaz-TMA/DNA nanowires, which leads to enhanced light scattering.

Phenaz-TMA-attached AuNPs (Phenaz-TMA/AuNPs) have also been prepared by photochemical reduction of $AuCl_4^-$ with 365 nm UV light in the presence of Phenaz-TMA [80]. Since Phenaz-TMA (Fig. 5.10), which is the monomer unit of PPhenaz-TMA, has an oxidation potential of +1.245 V (vs. SHE) [99], it cannot directly reduce $AuCl_4^-$, which has a reduction potential of +1.002 V (vs. SHE) [100]. However, Phenaz-TMA excited by photoreaction has greater reduction power, thus leading to a spontaneous electron transfer from excited Phenaz-TMA (oxidation) to $AuCl_4^-$ (reduction). The photochemical formation of Phenaz-TMA/AuNPs was monitored by taking UV–vis absorption spectra as a function of irradiation time (Fig. 5.13a). As the $HAuCl_4$ solution was added, the absorption spectra of Phenaz-TMA resulted in a long tail on the long wavelength side (350–400 nm) of the peak. Au(III) gives stable complexes with C, N, P, S, or even O-donor

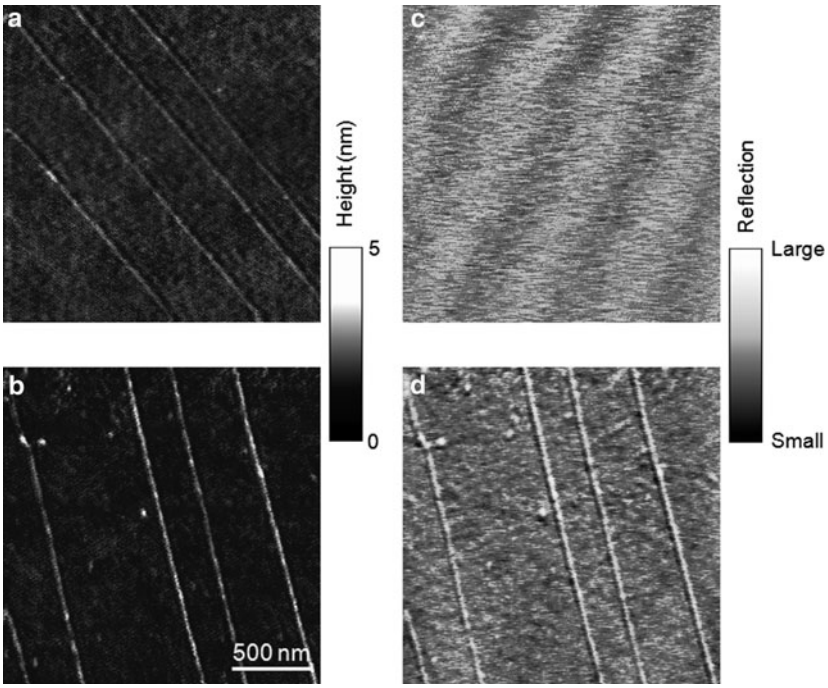

Fig. 5.12 AFM and SNOM images of PPhenaz-TMA/DNA nanowires before and after immersion in an Au^{3+} solution. (**a**) AFM topographic image and (**b**) SNOM image of PPhenaz-TMA/DNA nanowires before treatment. (**c**) AFM topographic image and (**d**) SNOM image of PPhenaz-TMA/DNA nanowires after treatment. Reprinted with permission from [98]. Copyright (2010) by the American Chemical Society

ligands [101]. The resulting long tail on 350–400 nm suggests the formation of Au(III)–Phenaz–TMA complex. Thus, an effective electron transfer for reducing $AuCl_4^-$ can be achieved with 365 nm UV light. Consequently, an absorption peak at 535 nm was clearly observed and increased with increasing irradiation time. This absorption peak is attributed to the surface plasmon resonance (SPR) absorbance band of AuNPs. After a certain irradiation time (10 min in this case), the UV absorption spectrum reached a state of stagnation because of the completion of photoreduction. The TEM micrograph indicated that the prepared Phenaz-TMA/AuNPs were 5–20 nm in diameter (Fig. 5.13b).

The interaction between Phenaz-TMA/AuNPs and DNA was subsequently examined. Figure 5.14a illustrates a typical DNA titration of Phenaz-TMA/AuNP solution. As DNA was gradually added, the SPR band intensity gradually increased, and the peak maximum shifted toward lower energy. The binding of Phenaz-TMA/AuNPs to DNA brings them close together, modifying their local environment and changing SPR absorbance. Phenaz-TMA has alkylammonium salts on the N atom; additionally, it is oxidized during the preparation of AuNPs. Nanoparticles were electrostatically bound to the negatively charged phosphate backbone of DNA

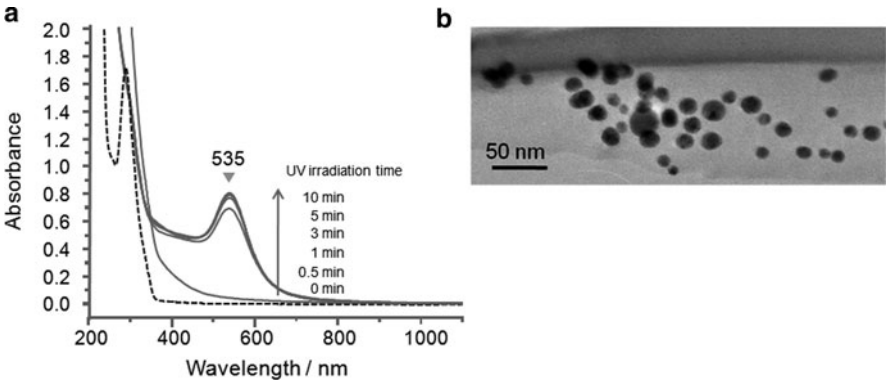

Fig. 5.13 (**a**) Absorption spectra corresponding to the growth of the Phenaz-TMA/AuNPs by photochemical reduction. A 3 mL aqueous solution containing Phenaz-TMA (150 nmol mL^{-1}) and $AuCl_4^-$ (150 nmol mL^{-1}) was irradiated by 365 nm UV light with 6 × 8 W. *Dashed line* is the spectrum of Phenaz-TMA without $AuCl_4^-$ before UV irradiation. (**b**) TEM image of prepared Phenaz-TMA/AuNPs. Reprinted with permission from [80]. Copyright (2010) by the Japan Society for Analytical Chemistry

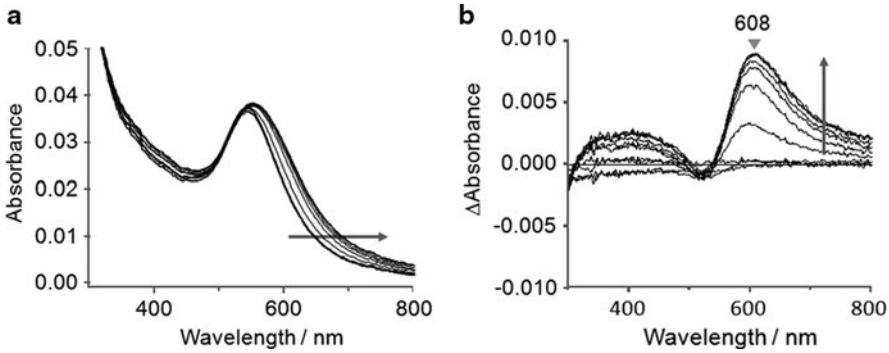

Fig. 5.14 (**a**) Absorption spectra taken during titration of Phenaz-TMA/AuNPs with λ-DNA and (**b**) their difference spectra. Here 0, 5, 10, 15, 20, 25, 30, 35, 40, 45, and 50 μL of DNA (4.5 ng μL^{-1}) solutions were added to 3 mL of Phenaz-TMA/AuNP (143 μg mL^{-1}) aqueous solution. Reprinted with permission from [80]. Copyright (2010) by the Japan Society for Analytical Chemistry

by using Phenaz-TMA/AuNPs with a positively charged protecting monolayer. Figure 5.14b also indicates differences in spectra changes. The absorption peak at 608 nm increases with an increase in DNA additions, suggesting the SPR of AuNPs assembled onto DNA molecules. Also, a mixture of Phenaz-TMA/AuNPs and DNA incubated for 1 h was stretched and fixed on surfaces. AFM observations revealed that 1D arrays of particles with a diameter of 5–10 nm formed on surfaces (Fig. 5.15).

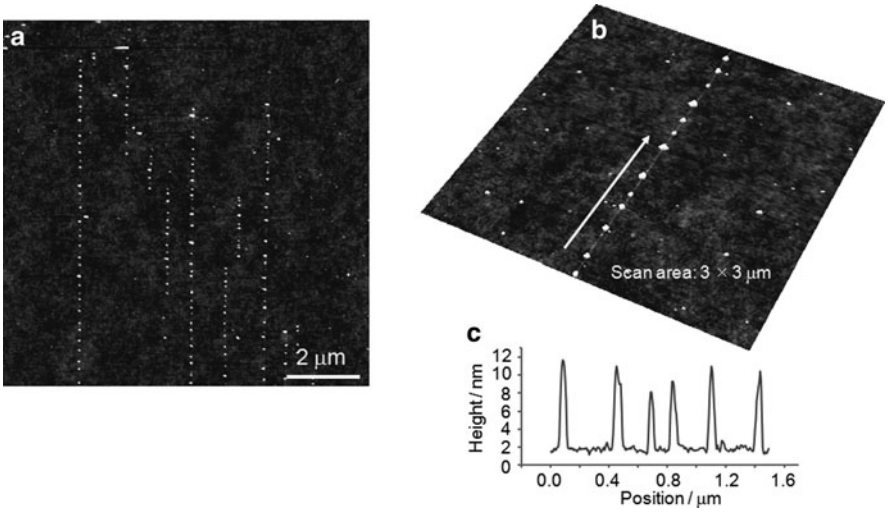

Fig. 5.15 AFM images of Phenaz-TMA/AuNPs assembled on DNA. (**a**) Image in a large scan range. (**b**) Image in a smaller scan range. (**c**) Scan profile along the *white arrow* in image (**b**)

5.4 Fabrication and Patterning of Metallic Nanoarrays with Long-Range Order

Although DNA is an ideal 1D template to fabricate metallic nanoarrays, the length of prepared arrays essentially depends on that of the original DNA. For example, λ-DNA having a theoretical length of 16.5 μm is usually used as such a template. Since a 1D template with a greater geometrical aspect ratio leads to metallic nanoarrays with a larger scale, they can be easily manipulated during microscope observations, measuring their electrical and optical properties and sensing molecule interactions on them via SERS. Long DNA can be produced with some effort using a biochemical (enzymatic) technique such as polymerase chain reaction (PCR). In particular, rolling circle amplification (RCA) [102–104] can be used to produce a long single strand of DNA (>70 kb or more) [105], which has a repeating sequence with a designed repeat unit on the order of 100 bases, and these repeat units can be addressed by hybridization to their complementary DNA sequence. The applicability of RCA for preparing DNA with periodic binding motifs has been demonstrated for arranging MNPs and binding proteins [106, 107]. However, thus far, RCA and assembly reactions have been carried out solely in the liquid phase in a reaction tube. Such long DNA strands seem to be problematic for stretching and aligning on surfaces because of their intertwined state in solution.

5.4.1 *Preparation of Longer Metallic Nanoarrays with DNA Nanofibers*

Most recently, we have developed a simple method to create highly aligned DNA nanofibers on a surface [108]. This method is based on the processes of solvent vapor-induced buildup and controlled drying front movement, and forms parallel aligned DNA nanofibers exceeding several hundred micrometers in length and 40 nm in diameter on a poly(dimethylsiloxane) (PDMS) sheet. Thus, this process leads to a DNA nanostrand that is much longer than the contour length of λ-DNA (16.5 μm) and facilitates manipulation of a single nanofiber under microscope observation, measuring its electrical and optical properties, and connecting it to electrode pads. Various MNPs could also be attached to such nanofibers, forming metallic nanoarrays with a longer scale.

The formation process for long metallic nanoarrays with DNA nanofibers is illustrated in Fig. 5.16 [80, 109]. First, a mixture of Phenaz-TMA/AuNPs and λ-DNA in a TE buffer (pH = 8) solution was added to 8 μL of ethanol. This solution was then deposited on a PDMS sheet, which was tilted at 15° during solvent evaporation to move the drying front downwards. Solvent evaporation leads to a decrease in the volume of the solution, leaving behind line patterns. Line patterns of metallic nanoarrays were formed when DNA with AuNPs attached was continuously deposited at the highly concentrated finger positions. Metallic nanoarrays also exceed several hundred micrometers in length and can be made within 30 min.

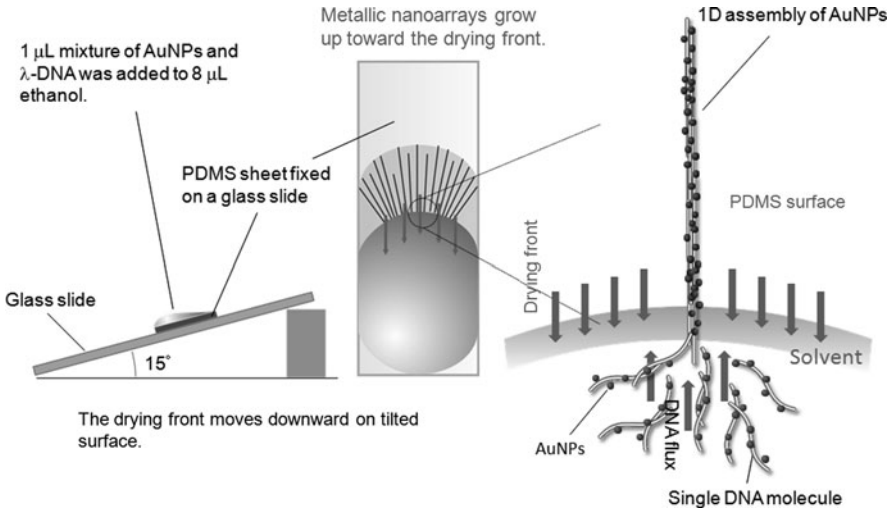

Fig. 5.16 Procedure of solvent vapor-induced assembly for generating metallic nanoarrays. Reprinted with permission from [80]. Copyright (2010) by the Japan Society for Analytical Chemistry

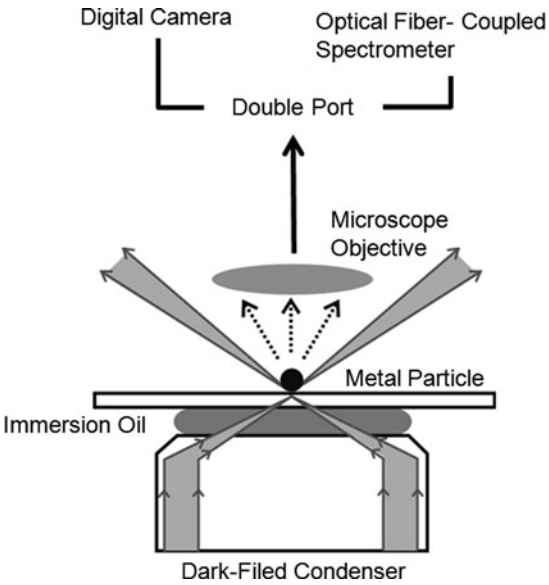

Fig. 5.17 Schematic diagram of the experiment setup for dark-field imaging and spectroscopy

Dark-field optical microscopy enables the observation of the LPR of single MNPs. In dark-field optical microscopy, only the light scattered by the structure under study is collected in the detection path, while directly transmitted light is blocked using a dark-field condenser. Dark-field light scattering images were acquired using a NIKON ECLIPSE 80i with a dark-field condenser and a NIKON Power shot A640 digital camera. The scattering spectra from the sample were collected by a miniature grating spectrometer (USB2000+, spectral resolution 3.67 nm), which was connected to the microscope using an optical fiber (core diameter 50 μm). Typical acquisition times were 5 s. Scattering spectra were corrected for spectral variations in system response and white-light intensity distribution through division by bright-field spectra recorded through the sample. The collection volume is nearly diffraction-limited (cross-sectional area $\sim$1 μm^2) for the 100$\times$ objective/fiber combination used here. Figure 5.17 schematically illustrates the setup.

Figure 5.18 is a dark-field optical microscope image depicting metallic nanoarrays on a PDMS sheet prepared by the above method. Many reddish lines originating from the plasmon resonance of AuNPs assembled on DNA nanofibers are clearly observed. Despite curvature of the lines at the edges of the surface due to the shape of the meniscus movement, they were aligned parallel to the moving drying front of the solvent. In general, individual spheres of AuNPs are observed as green particles originating from its LPR colors [110]. Before DNA attachment, many greenish spots were observed (Fig. 5.19a), and their scattering spectra exhibited a maximum peak at 570 nm (as indicated by spectra 1 and 2 in Fig. 5.19c). Thus, these spots denote isolated AuNPs. However, we observed a significant color change (reddish) in each of the spots along the DNA chains after DNA attachment (Fig. 5.19b). When two or more particles are brought into near-field interaction, the spectrum exhibits

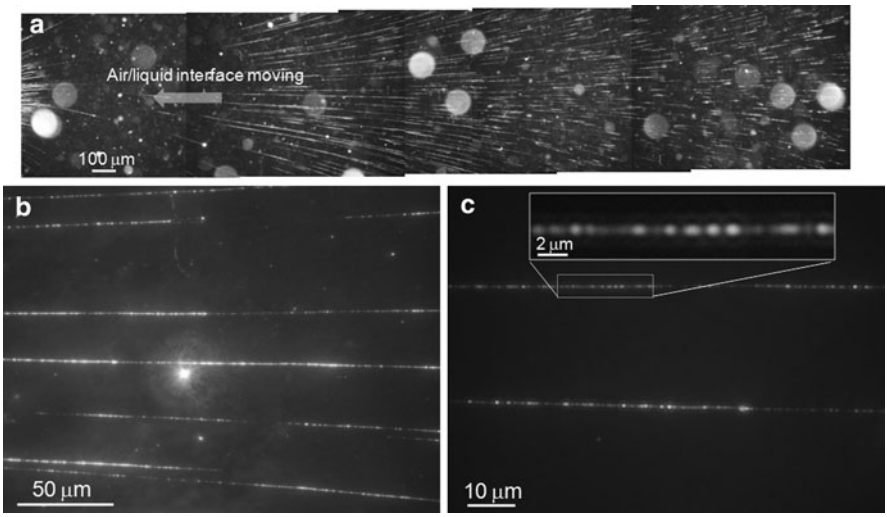

Fig. 5.18 Dark-field optical microscopy images of long metallic nanoarrays prepared with a DNA nanofibers as template. (**a**) Large-area image of metallic nanoarrays. (**b**) Enlarged image with 40× objective. (**c**) Enlarged image with 100× objective. The drying front moved from right to left. Reprinted with permission from [109]. Copyright (2010) by the Japan Society for Analytical Chemistry

a clear red shift (Fig. 5.19d) [1, 111]. Each spot along the DNA cannot be resolved because of their diffraction-limited spots. However, the color change is clear, as can also be seen from the corresponding scattering spectra exhibiting a maximum peak at 650 nm (as indicated by spectra 3 and 4 in Fig. 5.18c). Consequently, these results strongly indicate that many particles were assembled along the DNA. Figure 5.20a presents an AFM image of metallic nanoarrays on the PDMS surface. The observed height (diameter) of metallic nanoarrays was 30–40 nm, which was similar to that of bare DNA nanofibers (Fig. 5.20b). It is significant that DNA nanofibers with AuNPs attached have granulated nanostructures originating from AuNP attachments along them. Enlarged optical and AFM images (Figs. 5.18c and 5.20a) indicate that AuNPs are nonuniformly attached over the entire nanofiber. Further optimizations of the pH or ion strength in solution would achieve more efficient formations of metallic nanoarrays.

As described above, when MNPs are organized in closely spaced arrays, their LPR peak shifts towards lower energy, and an increase in bandwidth is observed because the dielectric constant of the surrounding MNPs is increased. Such interparticle spacing therefore serves as highly localized light fields for enhancing SERS. Termed “hot spots” these highly confined fields also enable increasing fluorescent emission, albeit with more modest enhancement factors. Furthermore, since a 1D particle array can exhibit coupled modes due to near-field interactions between adjacent MNPs, it is possible to propagate electromagnetic waves (light) with a transverse confinement below the diffraction limit (plasmon waveguides). For our

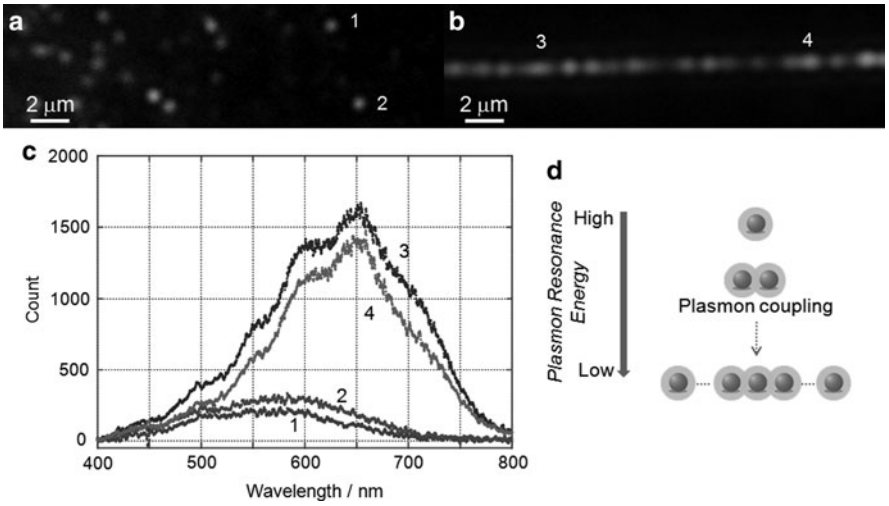

Fig. 5.19 Dark-field optical microscopy images of Phenaz-TMA/AuNPs (**a**) before attaching DNA and (**b**) after attaching DNA. (**c**) Scattering spectra of spots 1, 2, 3 and 4 in both images. (**d**) Schematic diagram of plasmon resonance energy induced by near-field coupling between MNPs

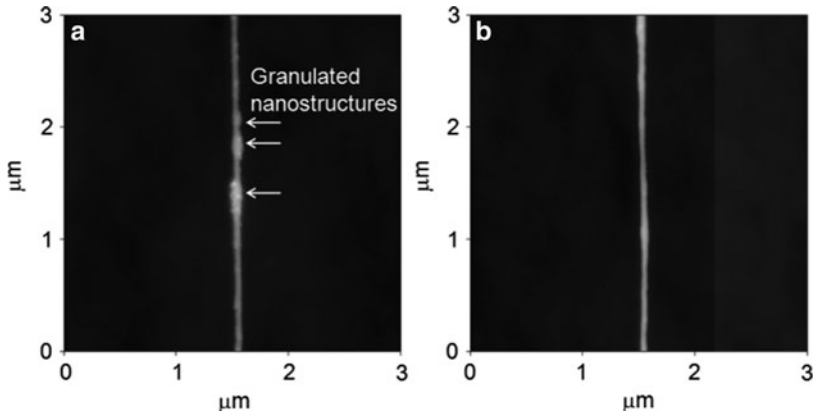

Fig. 5.20 AFM images of (**a**) metallic nanoarrays and (**b**) bare DNA nanofibers on PDMS surface. The height scale is 60 nm. Reprinted with permission from [80]. Copyright (2010) by the Japan Society for Analytical Chemistry

several-hundred-micrometer-long 1D metallic nanoarray, such optical properties can be easily examined by microscopy. We observed dark-field optical images of our metallic nanoarrays under light polarization. The scattering light intensity of metallic nanoarrays is stronger when the light is polarized parallel to the arrays but weaker for vertical polarization (Fig. 5.21a, b). Furthermore, the scattering intensity exhibited a cosine-like dependence on the polarization angle (Fig. 5.21c).

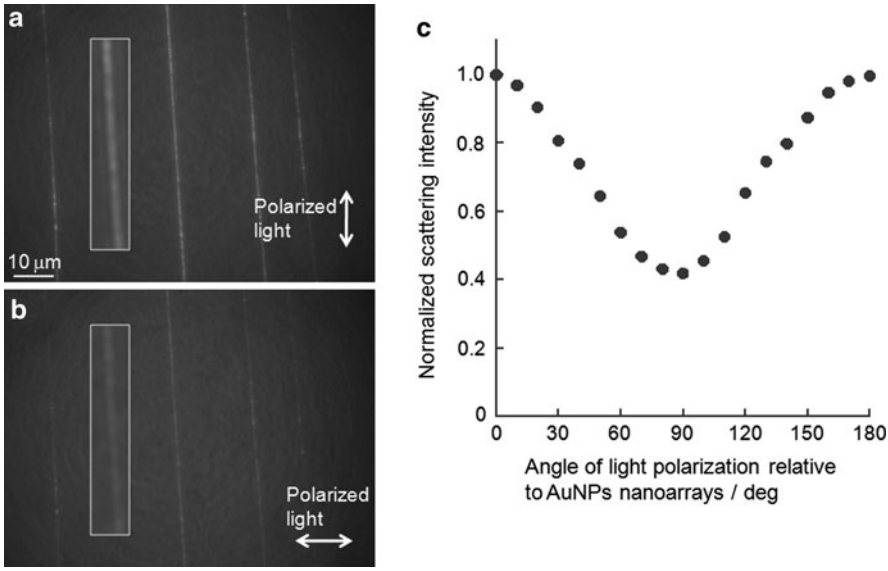

Fig. 5.21 (**a**, **b**) Polarized dark-field optical microscopy images of metallic nanoarrays. *Arrows* indicate the directions of polarized illumination. (**c**) Scattering light intensities from metallic nanoarrays as a function of the angle between the arrays and the polarization. The angle is 0° when the illumination polarization is parallel to the arrays. Reprinted with permission from [109]. Copyright (2010) by the Japan Society for Analytical Chemistry

The enhancement of the light field localized in gaps between MNPs also strongly depends on incident light polarization [112]. We also obtained spectra for some spots along the metallic nanoarray under light polarization (Fig. 5.22). A strong anisotropy was observed for all observed spots in Fig. 5.23. Furthermore, the spectra had multiple peaks in different polarizations. Polarization parallel to the uniaxial alignment of ordered MNPs enhances light field localization in gaps between MNPs, leading to strong light scattering from ordered MNPs. In contrast, polarization vertical to the uniaxial alignment does not enhance light field localization. Thus, the above result indicates that the alignment of AuNPs onto DNA nanofibers was preferentially uniaxial to the fiber axis. The intensity ratio was >2, and this contrast could be further improved by increasing the uniformity of AuNPs attaching to DNA nanofibers.

5.4.2 Transfer Printing of Metallic Nanoarray

We have reported that stretched DNA molecules and nanofibers initially present on the PDMS sheet were transferred onto another surface using TP [108, 113]. Furthermore, by repeating TP onto the same surface, it was possible to realize a

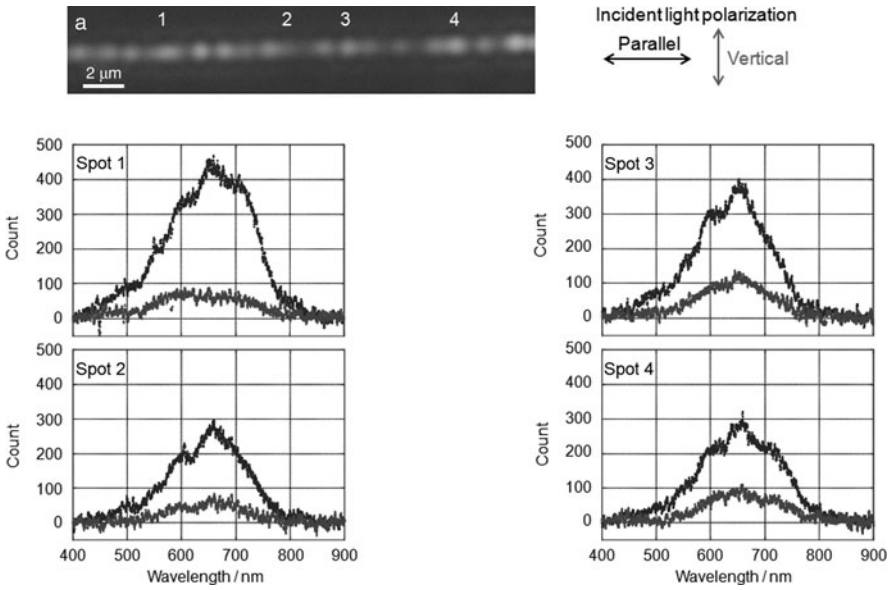

Fig. 5.22 Scattering spectra of spots 1, 2, 3, and 4 along the metallic nanoarray under light polarization. The *black line* is the spectrum measured with polarization parallel to the arrays. The *gray line* is the spectrum with polarization vertical to the arrays

two-dimensional (2D) assembly of stretched DNA molecules and nanofibers. We also demonstrated the TP of 2D patterns of metallic nanoarrays onto surfaces. To assemble the patterns, we first transferred metallic nanoarrays onto a coverslip and then overlapped the other PDMS sheet to which metallic nanoarrays were fixed onto the first one (Fig. 5.23a). Since the glass surface has polar groups stronger than those on the hydrophobic surface of PDMS, such arrays containing hydrophilic groups could be easily transferred from a PDMS surface to a glass surface. The dark-field micrograph of 2D metallic nanoarray patterns is depicted in Fig. 5.23b.

The main advantages of TP are that metallic nanoarrays can be printed in the desired position on the substrate, and that they can be integrated on the same substrate by repeating the TP process. For example, metallic nanoarrays on the PDMS sheet can be printed onto electrode gaps (Fig. 5.24). Thus, the TP method allows the integration and more complex patterning of metallic nanoarrays, and thus would facilitate fabrications for electronic/optical devices. By creating topological micropatterns on PDMS, it is also possible to achieve higher-ordered patterns of metallic nanoarrays.

5.5 Conclusions

In this chapter we have presented our recent works on constructing metallic nanoarrays with a DNA template. Our methods first require DNA stretching and fixation on surfaces. We have demonstrated that surface coating with polymers containing

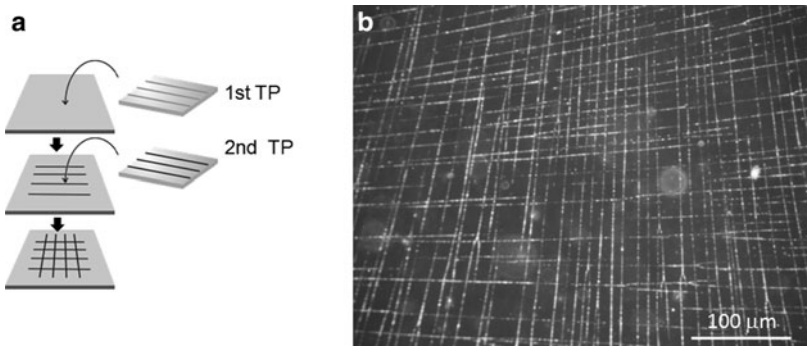

Fig. 5.23 (**a**) Procedure of TP for creating a 2D pattern of metallic nanoarrays. (**b**) Dark-field optical micrograph of 2D metallic nanoarrays. Reprinted with permission from [80]. Copyright (2010) by the Japan Society for Analytical Chemistry

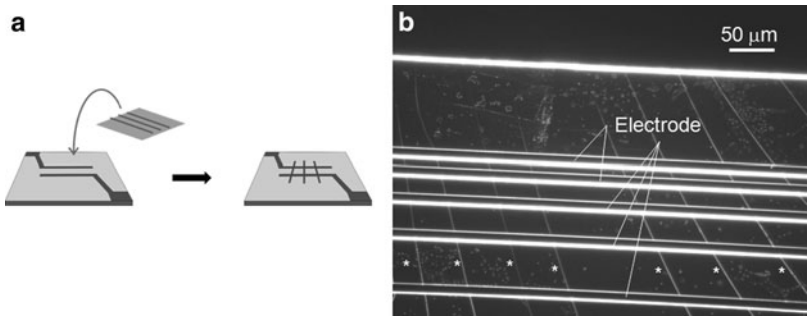

Fig. 5.24 (**a**) Procedure for fixing metallic nanoarrays onto electrode gaps. (**b**) Dark-field optical micrograph of metallic nanoarrays transferred onto microelectrode gaps. Transferred metallic nanoarrays are indicated by the *asterisk* in image (**b**)

π-conjugation units enhances DNA stretching and fixation on surfaces, due to the π–π interaction (π-stacking) between aromatic amines in polymers and base pairs in DNA molecules. Such polymer coating also enables adequate optical microscopy and AFM observation of well-stretched DNA on conventional coverslips. The next step is attaching MNPs to DNA. The AN-AuNPs prepared here strongly interacted with DNA. Two different assembly methods were employed. Consequently, continuous depositions and necklace-like depositions of AN-AuNPs along DNA molecules were achieved. The two approaches used in this study enabled different formations of metallic arrays of AN-AuNPs. Specifically, linear arrays of AN-AuNPs with interparticle spacing could be organized onto DNA molecules in a necklace-like formation. Furthermore, Phenaz-TMA/AuNPs were prepared by photochemical reduction of $AuCl_4^-$ with 365 nm UV light in the presence of Phenaz-TMA. Phenaz-TMA/AuNPs also demonstrated strong interaction with DNA. DNA nanofibers were useful for constructing metallic nanoarrays with a long-range order. UV–vis spectroscopy and dark-field optical microscopic observations revealed assemblies of

Phenaz-TMA/AuNPs on DNA and the LPR color changes involved. Furthermore, it was possible to create 2D patterns of metallic nanoarrays by the TP technique. Our methods summarized here do not require any special equipments, and should provide a useful system for investigating the electromagnetic (light) field localized between MNPs.

Many applications of metallic nanoarrays enhance light fields localized between MNPs. A linear array of closely spaced MNPs can be viewed as a chain of interacting dipoles, which supports traveling polarization waves. This suggests applications of metallic nanoarrays as waveguides with high field confinement, which would facilitate the realization of nano-optical devices. In the field of analytical chemistry, one promising application is optical sensors, and single-molecule detection via SERS has been reported. Gold nanospheres, immobilized on top of 1-mercaptobenzoic acid monolayers, yielded a SERS enhancement factor of 10^7, while other anisotropic shapes had enhancement factors of 10^8–10^9 [114]. Our highly anisotropic metallic nanoarrays therefore serve as highly localized light fields for enhancing SERS. In addition to SERS, surface-enhanced fluorescence has also been reported for molecules near the surfaces of MNPs [115–118]. While molecular fluorescence is quenched within 5 nm of the metal particle surface, at distances of 10 nm or greater, fluorescence is enhanced up to 100-fold by the localized electric field and increased intrinsic decay of the fluorophore [115–118]. Our metallic nanoarrays can also be restructured by the TP technique, and integrated into a desired position on various substrates, such as glass or silicon. Therefore, our method will advance the fabrication of nano-optical devices and optical sensor chips for single-molecule detection.

Acknowledgements The author is grateful for all the contributions from their collaborators, with special thanks to Dr. H. Hayashi (Nagoya Municipal Industrial Research Institute), Prof. H. Shiigi (Osaka Prefecture University), Mr. H. Karasawa, and Prof. F. Iwata (Shizuoka University). The author thanks Dr. H. T. Miyazaki (National Institute for Materials Science), Dr. S. Sugiyama and Dr. T. Ohtani (National Agricultural and Food Research Organization) for the many most useful and inspiring scientific discussions. Financial support for these studies was provided by Iketani Science and Technology Foundation and Grants-in-Aid for Basic Sciences from the Ministry of Education, Science, Sports and Culture, Japan (No. 18710106, No. 18310089 and No. 22550136).

References

1. S.A. Maier, *Plasmonics: Fundamentals and Application* (Springer, Berlin, 2007)
2. S.A. Maier, M.L. Brongersma, P.G. Kik, S. Meltzer, A.A.G.Requichia, H. Atwater, Adv. Mater. **13**, 1501 (2001)
3. S.A. Maier, P.G. Kik, H.A. Atwater, S. Meltzer, E. Harel, B.E. Koel, A.A. Requichia, Nat. Mater. **2**, 229 (2003)
4. W. Nomura, T. Yatsui, M. Ohtsu, Appl. Phys. Lett. **86**, 181108 (2005)
5. T. Yatsui, W. Nomura, M. Ohtsu, Nano Lett. **5**, 2548 (2008)
6. R. Garrell, Anal. Chem. **61**, 401A (1989)
7. A. Campion, P. Kambhampati, Chem. Soc. Rev. **27**, 241 (1998)
8. K. Kneipp, H. Kneipp, I. Itzkan, R.R. Dasari, M.S. Feld, Chem. Rev. **99**, 2987 (1999)

9. J. Murphy, T.K. Sau, A.M. Gole, C.J. Orendorff, J. Gao, L. Gou, S.E. Hunyadi, T. Li, J. Phys. Chem. B **109**, 13857 (2005)
10. B.P. Khanal, E.R. Zubarev, Angew. Chem. Int. Ed. **46**, 2195 (2007)
11. M.E. Stewart, C.R. Anderton, L.B. Thompson, J. Maria, S.K. Gray, J.A. Rogers, R.G. Nuzzo, Chem. Rev. **108**, 494 (2008)
12. P.K. Jain, X. Huang, I.H. El-Sayed, M.A. El-Sayed, Acc. Chem. Res. **41**, 1578 (2008)
13. S. Yamada, Anal. Sci. **25**, 1059 (2009)
14. C.X. Yu, J. Irudayaraj, Anal. Chem. **79**, 572 (2007)
15. J.Y. Chang, H.M. Wu, H. Chen, Y.C. Ling W.H. Tan, Chem. Commun. 1092 (2005)
16. K.G. Thomas, S. Barazzouk, B.I. Ipe, S.T.S. Joseph, P.V.J. Kamat, Phys. Chem. B **108**, 13066 (2004)
17. K.K. Caswell, J.N. Wilson, U.H.F. Bunz, C.J. Murphy, J. Am. Chem. Soc. **125**, 13914 (2003)
18. N.R. Jana, L.A. Gearheart, S.O. Obare, C.J. Johnson, K.J. Edler, S. Mann, C.J. Murphy, J. Mater. Chem. **12**, 2909 (2002)
19. C.J. Orendorff, P. Hankins, C.J. Murphy, Langmuir **21**, 2022 (2005)
20. G.A. DeVries, M. Brunnbauer, Y. Hu, A.M. Jackson, B. Long, B.T. Neltner, O. Uzun, B.H. Wunsch, F. Stellacci, Science **315**, 358 (2007)
21. A.M. Jackson, J.W. Myerson, F. Stellacci, Nat. Mater. **3**, 330 (2004)
22. Q.H. Wei, K.H. Su, S. Durant, X. Zhang, Nano Lett. **4**, 1067 (2004)
23. C.R. Barry, N.Z. Lwin, W. Zheng, H.O. Jacobs, Appl. Phys. Lett. **83**, 5527 (2003)
24. L.M. Demers, D.S. Ginger, S.J. Park, Z. Li, S.W. Chung, C.A. Mirkin, Science **296**, 1836 (2002)
25. Y. Cui, M.T. Bjork, J.A. Liddle, C. Sonnichsen, B. Boussert, A.P. Alivisatos, Nano Lett. **4**, 1093 (2004)
26. Y. Yin, Y. Lu, Y. Xia, J. Am. Chem. Soc. **123**, 771 (2001)
27. S. Hong, R. Eby, S. Myung, B.Y. Lee, S.G. Rao, J. Jang, in *Dip-Pen Nanolithography*, ed. by P. Samorí. Scanning Probe Microscopies Beyond Imaging (Wiley, New York, 2006), pp. 141–174
28. R.J. Barsotti Jr., F. Stellacci, J. Mater. Chem. **16**, 962 (2006)
29. S.W. Chung, G. Markovich, J.R. Heath, J. Phys. Chem. B **102**, 6685 (1998)
30. R.P. Sear, S.-W. Chung, G. Markovich, W.M. Gelbart, J.R. Heath, Phys. Rev. E **59**, R6255 (1999)
31. P. Yang, F. Kim, Chem. Phys. Chem. **3**, 503 (2002)
32. J. Huang, A.R. Tao, S. Connor, R. He, P. Yang, Nano Lett. **6**, 524 (2006)
33. K.D. Hermanson, S.O. Lumsdon, J.P. Williams, E.W. Kaler, O.D. Velev, Science **294**, 1082 (2001)
34. S.O. Lumsdon, D.M. Scott, Langmuir **21**, 4874 (2005)
35. K.H. Bhatt, O.D. Velev, Langmuir **20**, 467 (2004)
36. N. Ranjan, H. Vinzelberg, M. Mertig, small **12**, 1490 (2006)
37. W.A. Lopes, H.M. Jaeger, Nature **414**, 735 (2001)
38. D. Wyrwa, N. Beyer, G. Schmid, Nano Lett. **2**, 419 (2002)
39. T. Reuter, O. Vidoni, V. Torma, G. Schmid, L. Nan, M. Oleiche, L. Chi, H. Fuchs, Nano Lett. **2**, 709 (2002)
40. J.D. Hartgerink, E. Beniash, S.I. Stupp, Science **294**, 1684 (2001)
41. J.D. Hartgerink, E. Beniash, S.I. Stupp, Proc. Natl. Acad. Sci. USA **99**, 5133 (2002)
42. M. Reches, E. Gazit, Science **300**, 625 (2003)
43. L. Li, S.I. Stuppe, Angew. Chem. Int. Ed. **44**, 1833 (2005)
44. L.W. Yin, Y. Bando, Y.C. Zhu, D. Golberg, M.S. Li, Adv. Mater. **16**, 929 (2004)
45. W.Q. Han, A. Zettl, Nano Lett. **3**, 681 (2003)
46. Y. Wang, Z. Tang, X. Liang, L.M. Liz-Marzán, N.A. Kotov, Nano Lett **4**, 225 (2004)
47. G. Ren, Y. Xing, Nanotechnology **17**, 5596 (2006)
48. F. Favier, E.C. Walter, M.P. Zach, T. Benter, R.M. Penner, Science **293**, 2227 (2001)
49. M. P. Zach, K.H. Ng, R.M. Penner, Science **290**, 2120 (2000)
50. S. Minko, A. Kiriy, G. Gorodyska, M. Stamm, J. Am. Chem. Soc. **124**, 10192 (2002)
51. O. Harnack, W.E. Ford, A. Yasuda, J.M. Wessels, Nano Lett. **2**, 919 (2002)

52. K. Keren, M. Krueger, R. Gilad, G. Ben-Yoseph, U. Silvan, E. Braun, Science **72**, 297 (2002)
53. M. Mertig, L.C. Ciacchi, R. Seidel, W. Pompe, A.D. Vita, Nano Lett. **2**, 841 (2002)
54. M.G. Warnerd, J.E. Hutchison, Nature Mater. **2**, 272 (2003)
55. T. Yonezawa, S. Onoue, S. Kimizuka, Chem. Lett. 1172 (2002).
56. J.D. Le, Y. Pinto, N.C. Seeman, K. Musier-Forsyth, T.A. Taton, R.A. Kiehl, Nano Lett. **4**, 2343 (2004)
57. P. Alivisatos, K.P. Johnson, X.G. Peng, T.E. Wilson, C.J. Loweth, M.P. Bruchez, P.G. Schultz, Nature **382**, 609 (1996)
58. R. Elghanian, R.C. Mucic, R.L. Letsinger, C.A. Mirkin, Science **277**, 1078 (1997)
59. N.C. Seeman, Trends Biotechnol. **17**, 437 (1999)
60. H. Yan, S.H. Park, G. Finkelstein, J.H. Park, T.H. LaBean, Science **301**, 1882 (2003)
61. Y. He, T. Ye, M. Su, C. Zhang, A.E. Ribbe, W. Jinag, C. Mao, Nature **452**, 198 (2008)
62. E.S. Andersen, M. Dong, M.M. Nielsen, K. Jahn, R. Subramani, W. Mamdouh, M.M. Golas, B. Sander, H. Stark, C.L.P. Oliveira, J.S. Pedersen, V. Birkedal, F. Besenbacher, K.V. Gothelf, J. Kjems, Nature **459**, 73 (2009)
63. S.M. Douglas, H. Dietz, T. Liedl, B. Hogberg, F. Graf, W.M. Shih, Nature **459**, 414 (2009)
64. C. Erler, M. Mertig, J. Vac. Sci. Technol. B **27**, 939 (2009)
65. K. Otobe, T. Ohtani, Nucleic Acid Res. **29**, e109 (2001)
66. H. Yokota, D.A. Nickerson, B.J. Trask, G. Van Den Engh, M. Hirst, I. Sadowski, R. Aebersold, Anal. Biochem. **264**, 158 (1998)
67. D. Bensimon, A.J. Simon, V. Croquette, A. Bension, Phys. Rev. Lett. **74**, 4754 (1995)
68. X. Michalet, R. Ekong, F. Fougerousse, S. Rousseaux, C. Schurra, N. Hornigold, M. Slegtenhorst, J. Wolfe, S. Povey, J.S. Beckmann, A. Bensimon, Science **277**, 1518 (1997)
69. J.F. Allemand, D. Bensimon, L. Jullien, A. Bensiom, V. Croquette, Biophys. J. **73**, 2064 (1997)
70. A. Bensimon, A. Simon, A. Chiffaudel, V. Croquette, V. Heslot, D. Bensimon, Science **265**, 2096 (1994)
71. Y. Okahata, T. Kobayashi, K. Tanaka, Langmuir **12**, 1326 (1996)
72. P.A. Smith, C.D. Nordquist, T.N. Jackson, T.S. Mayer, Appl. Phys. Lett. **77**, 1399 (2000)
73. X. Liang, K.J. Morton, R.H. Austin, S.Y. Chou, Nano Lett. **7**, 3774 (2007)
74. M. Rief, H. Clausen-Schaumann, H.E. Gaub, Nature Struct. Biol. **6**, 346 (1999)
75. J. Hu, Y. Zhang, H. Gao, M. Li, U. Hartman, Nano Lett. **2**, 55 (2002)
76. Y. Arai, R. Yasuda, K. Akashi, Y. Harada, H. Miyata, K. Kinosita Jr., H. Itoh, Nature **399**, 446 (1999)
77. S.B. Smith, L. Finzi, C. Bustamante, Science **258**, 1122 (1992)
78. A.T. Woolley, R.T. Kelly, Nano Lett. **1**, 345 (2001)
79. H. Nakao, H. Hayashi, T. Yoshino, S. Sugiyama, K. Otobe, T. Ohtani, Nano Lett. **2**, 475 (2002)
80. H. Nakao, Anal. Sci. **25**, 1387 (2009)
81. J.M. Kim, T. Ohtani, S. Sugiyama, T. Hirose, H. Muramatsu, Amal. Chem. **73**, 5984 (2001)
82. T. Thundat, D.P. Allison, R.J. Warmack, Nucleic Acids Res. **22**, 4224 (1994)
83. T. Yamamoto, T. Shimizu, E. Kurokawa, React. Func. Polym. **43**, 79 (2000)
84. D. Yang, T. Strode, H.P. Spielmann, A.H.J. Wang, T.G. Burke, J. Am. Chem. Soc. **120**, 2979 (1998)
85. Y.-F. Song, P. Yang, Polyhedron **20**, 501 (2001)
86. A. Kumar, M. Pattarkine, M. Bhadhade, A.B. Mandale, K.N. Ganesh, S.S. Datar, C.V. Dharmadhikari, M. Sastry, Adv. Mater. **13**, 341 (2001)
87. J. Richter, R. Seidel, R. Kirsch, M. Mertig, W. Pompe, J. Plaschke, H.K. Schackert, Adv. Mater. **12**, 507 (2000)
88. W.E. Ford, O. Harnack, A. Yasuda, J.M. Wessels, Adv. Mater. **13**, 1793 (2001)
89. D. Zanchet, C.M. Micheel, W.J. Parak, D. Gerion, A.P. Alivisatos, Nano Lett. **1**, 32 (2001)
90. M. Mertig, L.C. Ciacchi, R. Seidel, W. Pompe, A. De Vita, Nano Lett. **2**, 841 (2002)
91. Y. Liu, W. Meyer-Zaika, S. Franzka, G. Schmid, M. Tsoli, H. Kuhn, Angew. Chem. Int. Ed. **4**, 95 (2003)
92. G. Wang, R.W. Murray, Nano Lett. **4**, 95 (2004)

93. F. Patolsky, Y.Weizmann, O. Lioubashevski, I. Willner, Angew. Chem. Int. Ed. **41**, 2323 (2002)
94. G. Wang, J. Zhang, R.W. Murray, Anal. Chem. **74**, 4320 (2002)
95. H. Nakao, H. Shiigi, Y. Yamamoto, T. Tokonami, T. Nagaoka, S. Sugiyama, T. Ohtani, Nano Lett. **3**, 1391 (2003)
96. H. Shiigi, Y. Yamamoto, N. Yoshi, H. Nakao, T. Nagaoka, Chem. Commun. 4288 (2006)
97. H. Shiigi, R. Morita, Y. Yamamoto, S. Tokonami, H. Nakao, T. Nagaoka, Chem. Commun. 3615 (2009)
98. H. Nakao, H. Hayashi, F. Iwata, H. Karasawa, S. Sugiyama, T. Ohtani, Lamgmuir **21**, 7945 (2005)
99. H. Nakao, H. Hayashi, K. Okita, Anal. Sci. **17**, 545 (2001)
100. A.J. Bard, R. Parsons, J. Jordan, *Standard Potentials in Aqueous Solution* (Dekker, New York, 1985)
101. M.C. Gimeno, in *The Chemistry of Gold*, ed. by A. Lagna. Modern Supramolecular Gold Chemistry (Wiley, New York, 2008) pp. 41–48
102. G.T. Walker, M.C. Little, J.G. Nadeau, D.D. Shank, Proc. Nati. Acad. Sci. USA **89**, 392 (1992)
103. A. Fire, S.-Q. Xu, Proc. Nati. Acad. Sci. USA **92**, 4641 (1995)
104. H. Takahashi, K. Yamamoto, T. Ohtani, S. Sugiyama, BioTechniques **47**, 609 (2009)
105. L. Blanco, A. Bernad, J.M. Lázaro, G. Martin, C. Garmendia, M. Salas, J. Biol. Chem. **264**, 8935 (1989)
106. S. Beyer, P. Nickels, F.C. Simmel, Nano Lett. **5**, 719 (2005)
107. O.I. Wilner, S. Shimron, Y. Weizmann, Z.-G. Wang, I. Willner, Nano Lett. **9**, 2040 (2009)
108. H. Nakao, T. Taguchi, H. Shiigi, K. Miki, Chem. Commun. 1858 (2009)
109. H. Nakao, H. Hayashi, H. Shiigi, K. Miki, Anal. Sci. **25**, 1175 (2009)
110. C. Sonnichsen, T. Franzl, T. Wilk, G. von Plessen, J. Feldmann, O. Wilson, P. Mulvaney, Phys. Rev. Lett. **88**, 77402 (2002)
111. J. Prikulis, F. Svedberg, M. Käll, J. Enger, K. Ramser, M. Goksör, D. Hanstorp, Nano Lett. **4**, 115 (2004)
112. H. Xu, E.J. Bjerneld, M. Käll, L. Börjesson, Phys. Rev. Lett. **83**, 4357 (1999)
113. H. Nakao, M. Gad, S. Sugiyama, K. Otobe, T. Ohtani, J. Am. Chem. Soc. **125**, 7161 (2003)
114. C.J. Orendorff, A. Gole, T.K. Sau, C.J. Murphy, Anal. Chem. **77**, 3261 (2005)
115. K. Sokolov, G. Chumanov, T.M. Cotton, Anal. Chem. **70**, 3898 (1998)
116. J. Malicka, I. Gryzczynski, J.R. Lakowicz, Anal. Chem. **75**, 4408 (2003)
117. A. Parfenov, I. Gryzczynski, J. Malicka, C.D. Geddes, J.R. Lakowicz, J. Phys. Chem. B **107**, 8829 (2003)
118. J.R. Lakowicz, C.D. Geddes, I. Gryzczynski, J. Malicka, Z. Gryzczynski, K. Aslan, J. Lukomski, E. Matveera, J. Zhang, R. Badugn, J.J. Huang, Fluorescence **14**, 425 (2004)

Chapter 6
Assembly and Immobilization of Metal Nanoparticles

Nao Terasaki and Tetsu Yonezawa

Abstract This paper reviews recent progress of chemical preparation of metal nanoparticles and their assembly formation processes. Various metal and semiconductor nanoparticles have been intensively studied according to their unique properties controlled by their sizes. One predicted that nanoparticles with the diameter in the range of 1–10 nm would display specific electronic structures, which reflect the electronic band structure ("quantum size effect"). For example, some metal nanoparticles in these sizes show photoemission. The melting points of these nanosized metal particles are extremely lower than the bulk. Gold, silver, and copper nanoparticles show their specific absorption, plasmon absorption, which is also used for surface plasmon resonance (SPR). To use their unique properties as materials, not only the control of their structures and sizes but also controlled formation of low dimensional assembly of these nanoparticles are highly important. Ordered assembly of such nanoparticles give their unique and interesting functions, such as sensing, electron tunneling, information stage and so forth. From this viewpoint, we would like to discuss hereafter a couple of fundamental preparation processes of metal nanoparticles and various assemble techniques.

6.1 Introduction

The science and technology of metal nanoparticles are well established during the past several decades from the viewpoints of both fundamental and applied aspects [1–3]. Researches on metal nanoparticles are the subject of one of the most

N. Terasaki
Measurement Solution Research Center, National Institute of Advanced Industrial Science and Technology (AIST), 807-1, Shuku-machi, Tosu, Saga 841-0052, Japan
e-mail: nao-terasaki@aist.go.jp

T. Yonezawa (✉)
Division of Materials Science and Engineering, Faculty of Engineering, Hokkaido University, Kita 13, Nishi 8, Kita-ku, Sapporo, Hokkaido 060-8628, Japan
e-mail: tetsu@eng.hokudai.ac.jp

M. Ohtsu (ed.), *Progress in Nanophotonics 1*, Nano-Optics and Nanophotonics,
DOI 10.1007/978-3-642-17481-0_6,

important themes in the resent nanotechnology. For example, the fields of catalysis [4, 5], electronics [6, 7], medical sciences [8, 9], information storage [10], biorecognition [11–13], sensors [14,15], and mass analyses [16–18] are good targets of nanoparticle technology. However, it is also one of the subjects of the oldest themes in science. Colloidal gold nanoparticles have a long history in the field of physical chemistry. In the fourth century, the Romans made the Lycurgus cup, which can be actually found in the British Museum [19]. The color of this cup can be explained by the plasmon absorption of gold nanoparticles. Scientific studies of metallic gold nanoparticles began in 1857 by Michael Faraday [20,21]. From then, various preparative techniques of nanoparticles of gold and other metals have been proposed. We will pick up the representative three processes in this chapter, that is, the citrate reduction process, sodium borohydrate-reduction to generate thiol-stabilized nanoparticles, and alcohol reduction. Although there have already been a number of excellent review articles and books available in this field, this chapter will focus mainly on the assembly formation and application of such nanoparticle assemblies. A great deal of excitement has been generated from the controlled/ordered assemblies of nanoparticles. Surface modification, long range interaction among nanoparticles, positioning of nanoparticles will be discussed in Sect. 6.3 of this chapter.

6.2 Preparation of Metal Nanoparticles

Preparation of metal nanoparticles can be largely divided into two categories, that is, the bottom-up process and the break-down (top-down) process Fig. 6.1 [22]. Breakdown process is subdivision of bulk materials into nanosize. This process is very simple but size control of nanoparticles is relatively difficult. The bottom-up process includes the aggregation of metal atoms or molecules as the precursor of nanoparticles. This process can also be divided into two categories, the chemical reduction and the physical vacuum process (Fig. 6.2). In the former process, reduction of metal ions by chemical or physical process to form metal atoms is included. The aggregation of atoms is usually controlled by addition of some organic molecules, such as metal coordinating molecules, surfactants as well as polymers. In the latter process, metal ingots are heated to evaporate in a vacuum chamber to form metal atom vapor. Among these various processes, chemical reduction has become quite familiar because its easiness to control the particle size, its low initial cost (no expensive apparatus is needed), as well as its high reproducibility.

6.2.1 Preparation of Metal Nanoparticles by Chemical Reduction [23]

Among the conventional processes of nanoparticle preparation, chemical reduction of precursor ions by organic acids can be the most popular process. Other preparation processes of nanoparticles by chemical reduction are described in detail

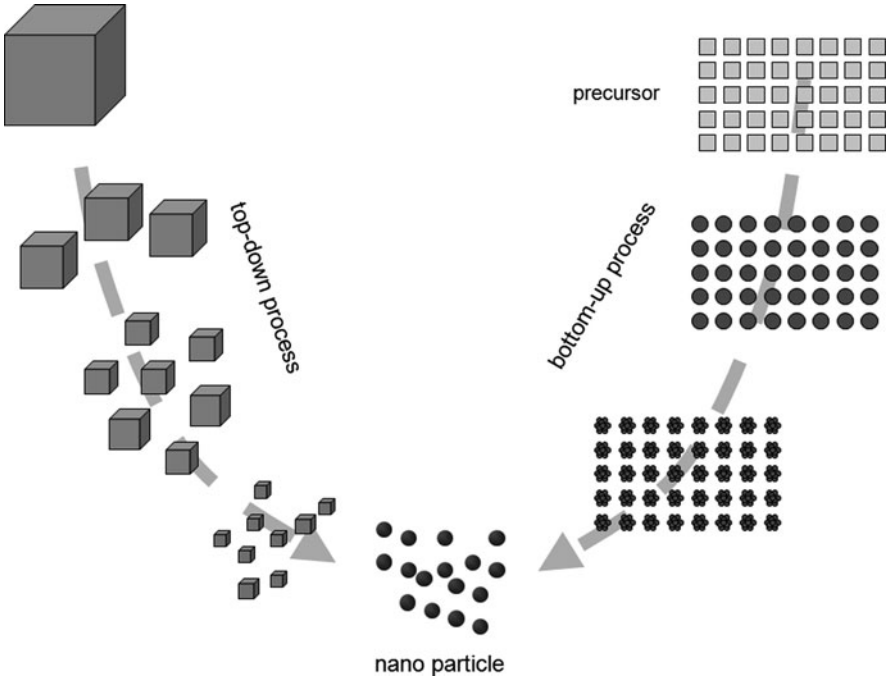

Fig. 6.1 Schematic illustration of the preparation processes of metal nanoparticles: (*right*) the bottom-up process and (*left*) the top-down process

in the previous reviews [23–25]. citrate reduction or isoascorbic acid reduction of tetrachloroaureic (III) acid ($HAuCl_4$) is very useful. Turkevich introduced this process in 1951 [26], and Frens improved this process to control the particle size in a wide range [27]. This process is intensively used for preparation of aqueous dispersion of gold nanoparticles for bioscience because these particles are stabilized relatively loose molecules, organic acids. Citrate reduction with water soluble thiols has also been proposed. Simultaneous addition of 3-mercaptopropionic acid and citrate acid gives relatively larger thiol-stabilized gold nanoparticles, whose sizes could be readily controlled by stabilizer/gold ratios (Fig. 6.3) [28].

To obtain smaller sized particles, sodium borohydride ($NaBH_4$)-reduction of metal salts in the presence of thiol molecules is proposed [29–31]. This is called Brust method which is firstly reported in 1994 (Fig. 6.4) [29]. This is a quite facile process to obtain small and uniform gold and other metal nanoparticles. Especially, organosol of gold nanoparticles can be readily prepared in a two-phase system by phase transfer of the corresponding metal ions from aqueous phase to organic phase with a phase-transfer surfactant (Fig. 6.5). The particle size can be controlled by gold/thiol ratios, and furthermore the particle size can be enlarged by thermal treatment of these thiol-stabilized gold nanoparticles. Brust and co-workers

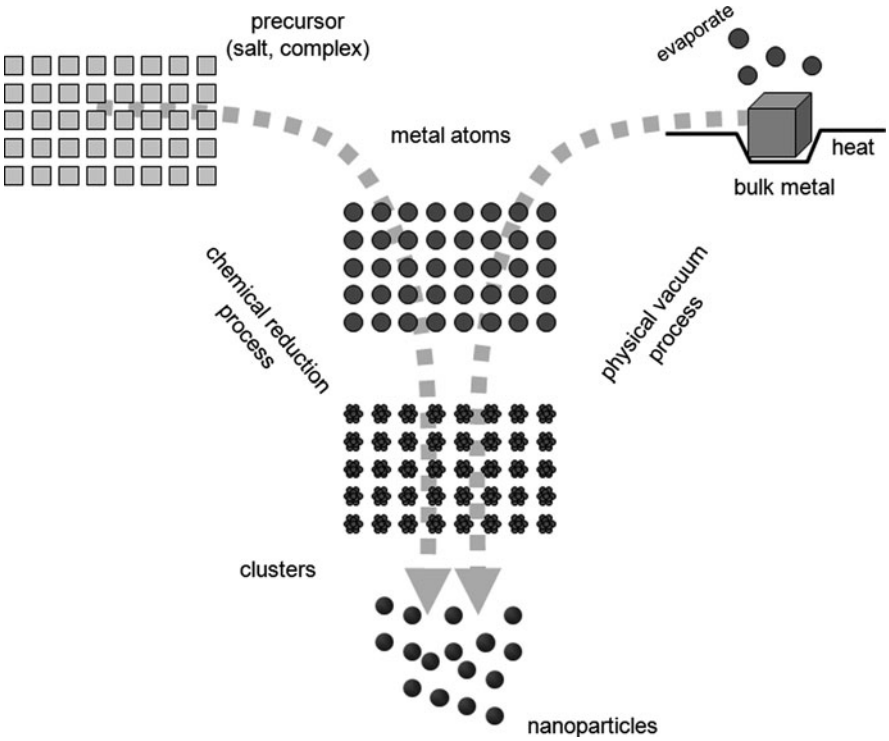

Fig. 6.2 Schematic illustration of the bottom-up preparation processes of metal nanoparticles: (*left*) the chemical reduction process and (*right*) the physical vacuum process

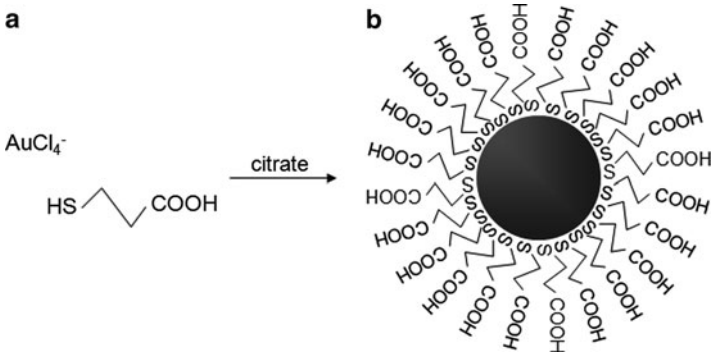

Fig. 6.3 (**a**) Preparation process of 3-mercaptopropionic acid stabilized gold nanoparticles by citrate-reduction. (**b**) The particle sizes depend on the stabilizer/gold ratios [28]

expanded this procedure to a single phase system by using *p*-mercaptophenol as the stabilizer [30]. After these Brust's invention, many publications have appeared, and these particles are called as monolayer-protected (or stabilized) clusters (or particles) (MPCs). The thiol stabilizers give high stability to the nanoparticles but

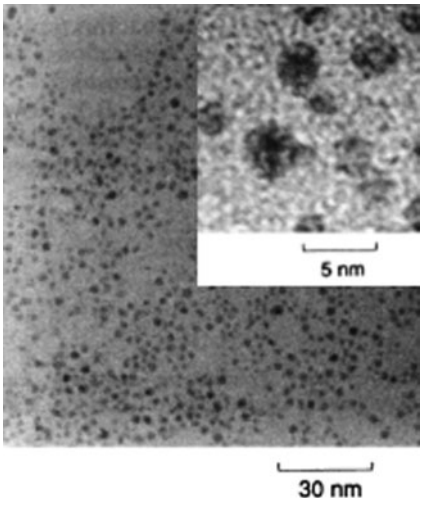

Fig. 6.4 TEM image of alkyl-thiol-stabilized gold nanoparticles by $NaBH_4$-reduction of $AuCl_4$-ions [29]

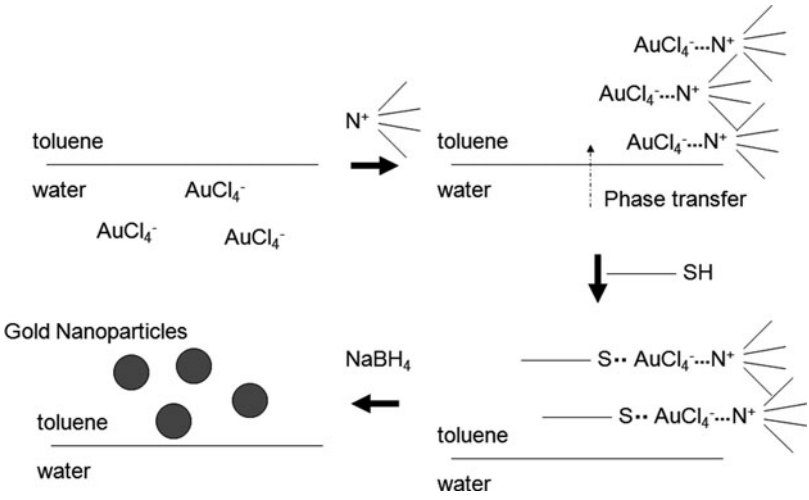

Fig. 6.5 Schematic illustration of alkylthiol-stabilized gold nanoparticles prepared by NaBH4-reduction of $AuCl_4$-ions: Two-phase process [29]

they can be substituted by addition of other free thiol stabilizer molecules into the dispersion.

PVP (poly(*N*-vinyl-2-pyrrolidone))-stabilized metal nanoparticles can be readily produced by alcohol reduction of the corresponding metal ions [5, 32–34]. Alcohol can be a good reducing reagent of precious metal ions and it changes to aldehyde or ketone by oxidation (Fig. 6.6). This alcohol reduction is mild and easy. PVP-stabilized nanoparticles of platinum group metals can work as effective catalysts. Especially, various alloy nanoparticles can be obtained by this process, especially,

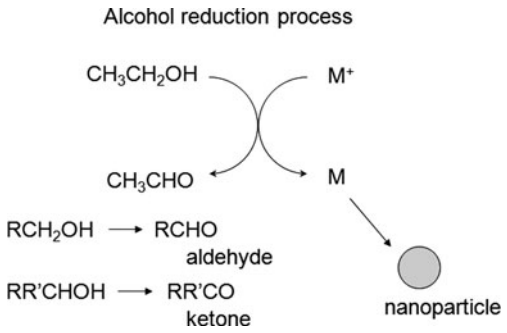

Fig. 6.6 Alcohol-reduction process of PVP-stabilized metal nanoparticles

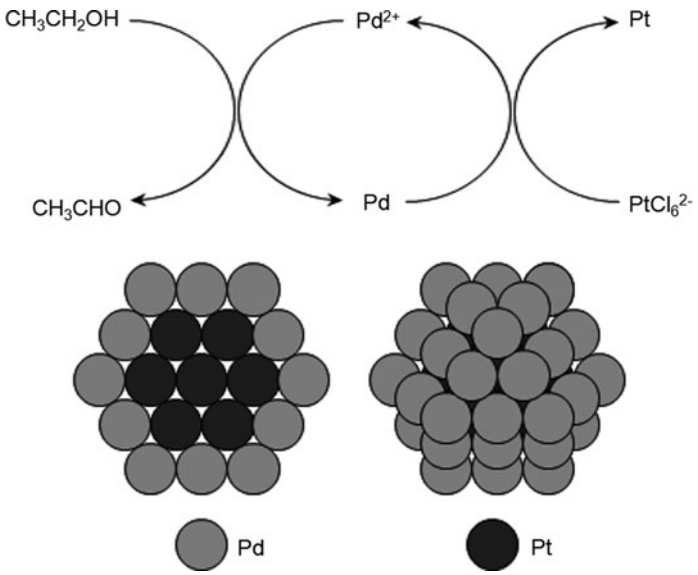

Fig. 6.7 Core-shell Pd/Pt nanoparticles stabilized by PVP prepared by simultaneous reduction process

core-shell type nanoparticles can be prepared by simultaneous reduction of the two corresponding metal ions (Fig. 6.7) [35–37].

6.3 Assembly Formation

Impressive strides have been made in the assembly formation of nanoparticles with various metals, sizes and shapes to obtain their unusual properties not only from the particles themselves but also from their assembled structures. In this section,

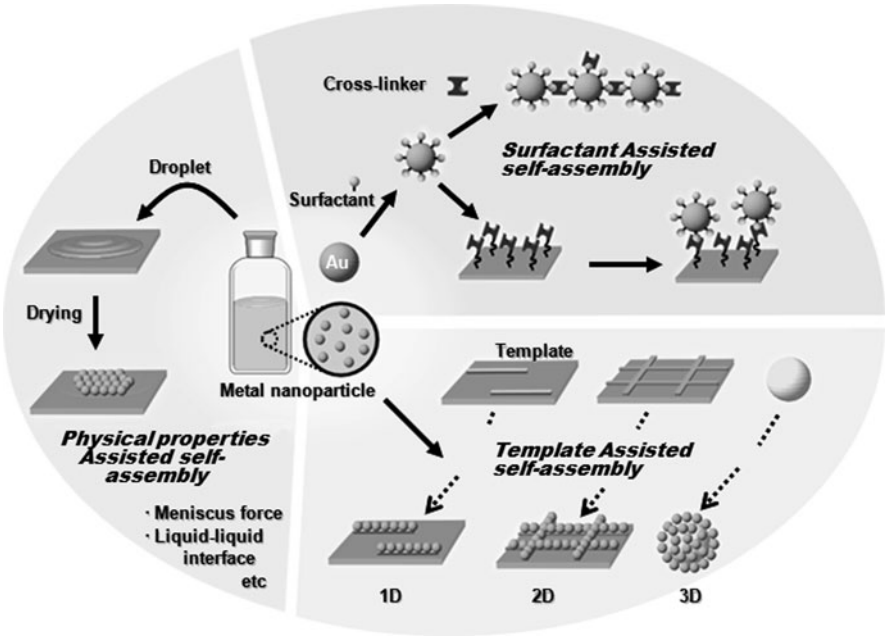

Fig. 6.8 Schematic illustration of controlled low-dimensional assembly formation of metal nanoparticles

we would like to introduce various methods to prepare controlled low-dimensional assemblies of nanoparticles (Fig. 6.8). Immobilization of nanoparticles on solid substrates will also be treated in this section.

6.3.1 Two Dimensional Assembly Formation of Nanoparticles by Simple Evaporation of Dispersions

Drop a dispersion of uniform-sized nanoparticles followed by slow drying often gives ordered two-dimensional arrays of nanoparticles. A feature of gold and silver particles is reported that it is tend to form highly ordered superlattices spontaneously and simply by the combination of drop-out of nanoparticle dispersion and evaporation of the solvent on a suitable substrate [23, 38–42]. Whetten and co-worker demonstrated such self-assembling phenomenon of nanoparticles, three dimensional nanoscale periodicity, for the first time by preparing of the monodispersed nanoparticles and X-ray diffraction techniques [43]. In some cases, crystallites of a size of several tens of micrometers have been observed. On the other hand, Schmid et al. recently reported the formation of three-dimensional crystals of thiol protected Au_{55} clusters and their characterization [44]. In Fig. 6.9a, STM image of a gold

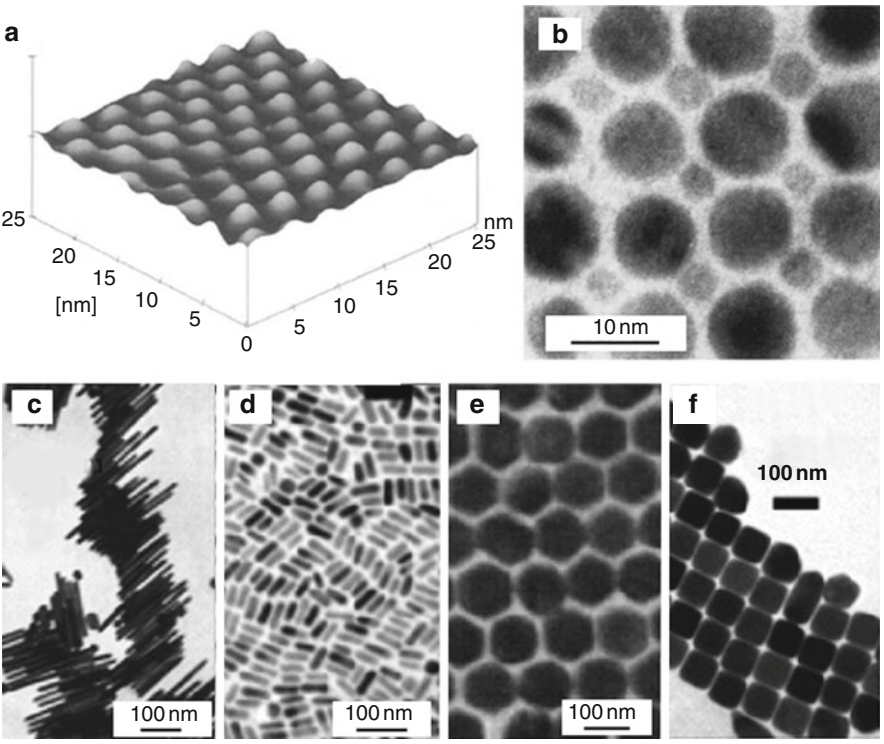

Fig. 6.9 (**a**) STM image of self-assembled superlattice of 3.5 nm gold particles on an HOPG substrate. The particles are stabilized by hexanethiol [43]. (**b**) TEM micrograph of a section of an AB (NaCl-type) superlattice of silver nanoparticles stabilized by decanethiol having a bimodal size distribution [47]. Self-assembly patterns formed by various shapes and sizes of gold nanoparticles, as visualized by TEM. (**c**) Ribbon structure formed from nanorods of high aspect ratios (>5); (**d**) globally isotropic but locally ordered arrangement of nanorods of low aspect ratios; gold nanocrystals with hexagonal profiles (**e**) and cubic profiles (**f**)

nanoparticles (2.4 nm) superlattice on highly ordered pyrolytic graphite (HOPG) deposited by drop casting of a nanoparticle dispersion and evaporation of the solvent (toluene) is shown. They proposed that the hydrocarbon chains of the nanoparticle play an important role in superlattice formation [45]. Such superlattices of particles are not limited to single-sized (monodispersed, highly uniform) sphere nanoparticles. For example, in the case of two monodispersed particles fractions give very interesting ordering phenomena, formation of bimodal structure [46]. Surprisingly various ordered bimodal structures such as AB, AB_3, AB_4, and AB_{13} were possible. AB structure is a two-dimensional analogue of the NaCl crystal structure. Decanethiol-stabilized silver particles of 8 and 3 nm diameter (Fig. 6.9b) gave such AB structure [47].

Highly ordered self-assembly patterns by various shape and size of nanoparticles have also been reported intensively. For example, nanorods with a high (>5,

Fig. 6.9c) and a low (Fig. 6.9d) aspect ratios, gold nanocrystals with hexagonal profiles (Fig. 6.9e) and cubic profiles (Fig. 6.9f), etc. can also provide ordered two-dimensional structures [40]. These results clearly show that the shape and the crystallographic facets of nanocrystals have a strong influence to the nature of the self-assembly patterns [40, 42].

6.3.2 *Two Dimensional Arrays Formation on Liquid–Liquid Interfaces*

The highly ordered and dimensional controlled nanoparticle single two-dimensional layer film can be prepared easily in a liquid–liquid interface and can be transferred on an appropriate substrate surface. For example, two-dimensional assembly of the citrate acid-protected spherical gold nanoparticles was instantly formed by pouring methanol into the two phase mixture of non-polar organic solvent (hexane, etc.) and aqueous colloidal dispersion of citrate-protected gold nanoparticles (Fig. 6.10a) [48, 136, 137]. The colorless interface changed to gold with the view of diagonal direction and from perpendicular direction, the interface area showed

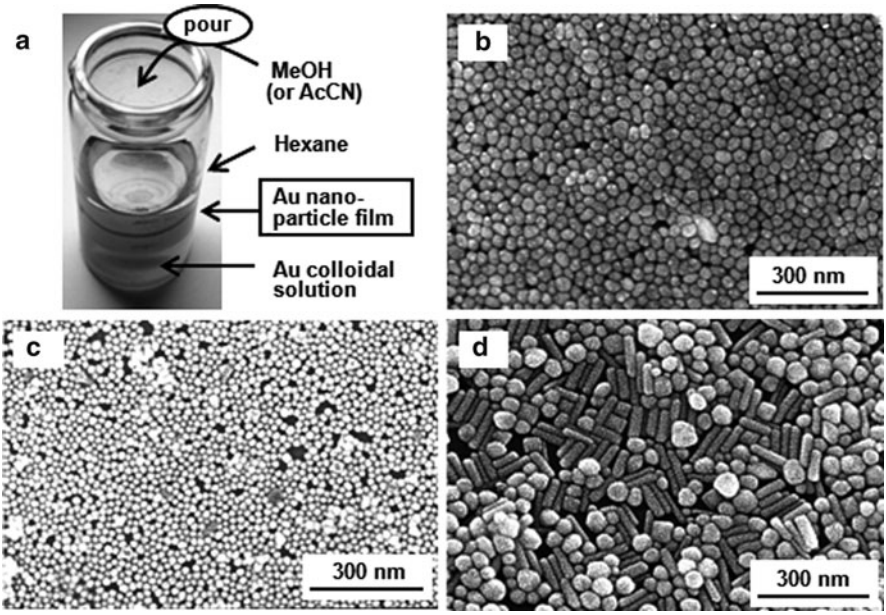

Fig. 6.10 (**a**) Formation process of 2D citrate-stabilized gold nanoparticle layer at the interface between hexane and water by pouring methanol. (**b**) SEM image of close-packed 2D layer of gold nanoparticles with the diameter of 36 nm. (**c**) SEM image of close-packed 2D layer of gold nanoparticles with the diameter of 18 nm. (**d**) SEM image of close-packed 2D layer of gold nanorods

blue color. This clearly implies that the plasmon of the gold nanoparticles at liquid–liquid interface were coupling each other. It means that a highly closely packed two dimensional array of gold nanoparticles was generated at the interface at least in optical order. Sequentially, the assembly could be successfully transferred onto a hydrophilic appropriate substrate, for example a glass plate and a ITO substrate, to form the single-layer nanoparticle film on them. From the SEM images of the obtained nanoparticle film, highly close packed nanoparticles can be seen even with various nanoparticle sizes (36 nm; Fig. 6.10b, 18 nm; Fig. 6.10c). With this process, even non-spherical particle, for example, gold nanorods also form a closely packed layer on the substrate (Fig. 6.10d).

6.3.3 Direct Preparation of Nanostructures on a Substrate

In this section, we will introduce some examples of direct preparation processes of nanoparticles and nanoarchitectures on substrates. The first example is a thermal activation of molecularly linked nanoparticle assembly, which is recently reported by Zhong et al. [49]. The key process of this handling is the thermal treatment of the removal of the shell/linking organic materials, including protective reagents and stabilizers (Fig. 6.11a), and sequentially the treatment to activate the aggregation of neighborhood nanoparticle. The change in size of individual nanoparticles (e.g., DT-capped $Au_{2\,nm}$) cast on mica as a result of the thermal treatment at 225°C can be detected by the change in the height data of in situ AFM images (Fig. 6.11b). The shrinkage is due to the removal of the capping-shell molecules. They also described the effect of shell/linker (11-mercaptoundecanoic acid: MUA, 15-mercaptohexadecanoic Acid: MHA, 1,9-nonanedithiol: NDT) and substrate (mica, HOPG), to obtain molecularly linked nanoparticle assembly (Fig. 6.11c). As the result, the assembly, agglomeration and growth of nanoparticles could be controlled with a smart choice of such conditions.

Second example is “Angle-Resolved nanosphere lithography (NSL)”, that is reported by Duyne et al. [50]. This work presents a direct novel approach for fine-tuning of the size, shape, and interparticle spacing of nanoparticles on substrate (Fig. 6.12c). The most important thing of this process is its high *simplicity*. This is accomplished by controlling the angle, θ, between the surface normal of the sample assembly with nanosphere mask and the propagation vector of the material deposition beam, as shown in Figs. 6.12a, b. In Fig. 6.12c, comparison between the experimental results and the simulated nanoparticle array geometries are collected, and we can clearly understand its excellent qualitative agreement.

6.3.4 Control of Nanoparticle Assembly by Stabilizing Reagents

The stabilizing reagents, protecting molecules, and surfactants of nanoparticles, which are surrounding the particle surface, play a very important roll for the

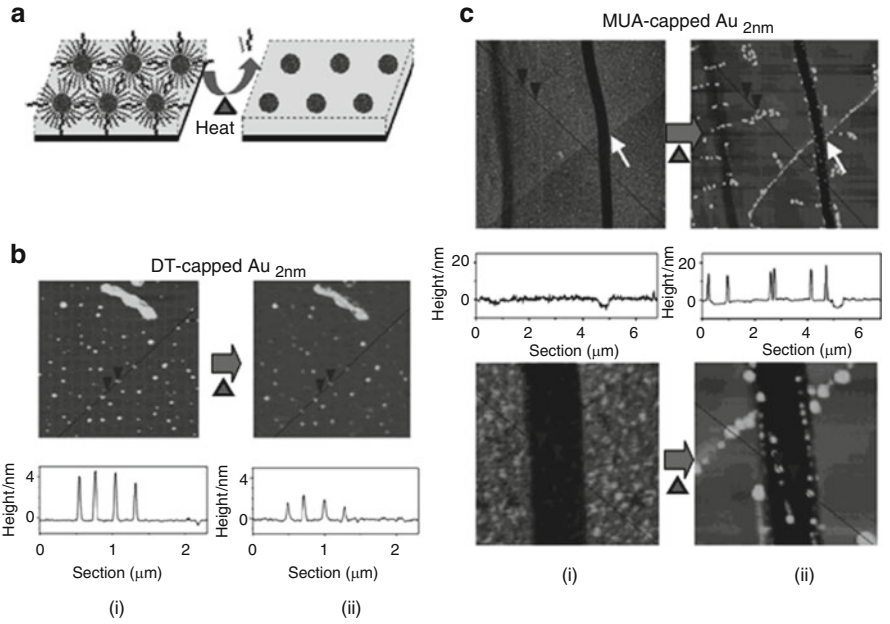

Fig. 6.11 (**a**) Schematic illustration of the thermal activation of a core-shell-type nanoparticle assembly on a planar substrate surface. (**b**) in situ AFM images ($2 \times 2\ \mu\ m^2$) for DT-capped Au_{2mm} on mica before (i) and after (ii) thermal treatment at 225°C for 30 min (image acquired after cooling to r. t.). The *top* bar of the nanoparticles serves as an internal location feature. The cross-section view corresponds to the line drawn in the image. (**c**) in situ AFM images (*top panel*: $5 \times 5\,\mu m^2$; *bottom panel*: $1 \times 1\,\mu m^2$) for MUA-Au_{2nm} on HOPG before (i) and after (ii) thermal treatment (225°C, 5 min). The images in the bottom panel are magnified views of the indicated area. The cross-sectional view corresponds to the line drawn in the image [49]

assembly formation and the immobilization of nanoparticles, and they show a key part to create an interaction between each nanoparticle and the substrate. Therefore, the smart design and choice of such compound is one of the research targets in this field. Indeed, many scientists have made much effort to prepare the assembly of nanoparticles with various surfactants, for example, those with different lengths of alkyl chains for hydrophobic interaction [51–53], those with multifunctional groups for host-guest interaction [54, 55] and/or those with functional groups which can form covalent bonds [56], those with hydrogen bonding groups which can attach to DNA molecules [11, 57–63], bio-recognition surfactant molecules [64, 65], those with charged head groups for electric static interaction with templates [60, 66–68], hydrosilylation between silicon and unsaturated bonds [69–71] and so on. In this section, we introduce the nanoparticle assemblies from the viewpoint of such unique surfactant molecules.

Most nanoparticles with a few nanometers of the diameter were protected by alkyl thiols, recently according to the simplicity of their preparation [29, 30]. Relatively long alkyl chains of thiol compounds work as surfactant. We will introduce

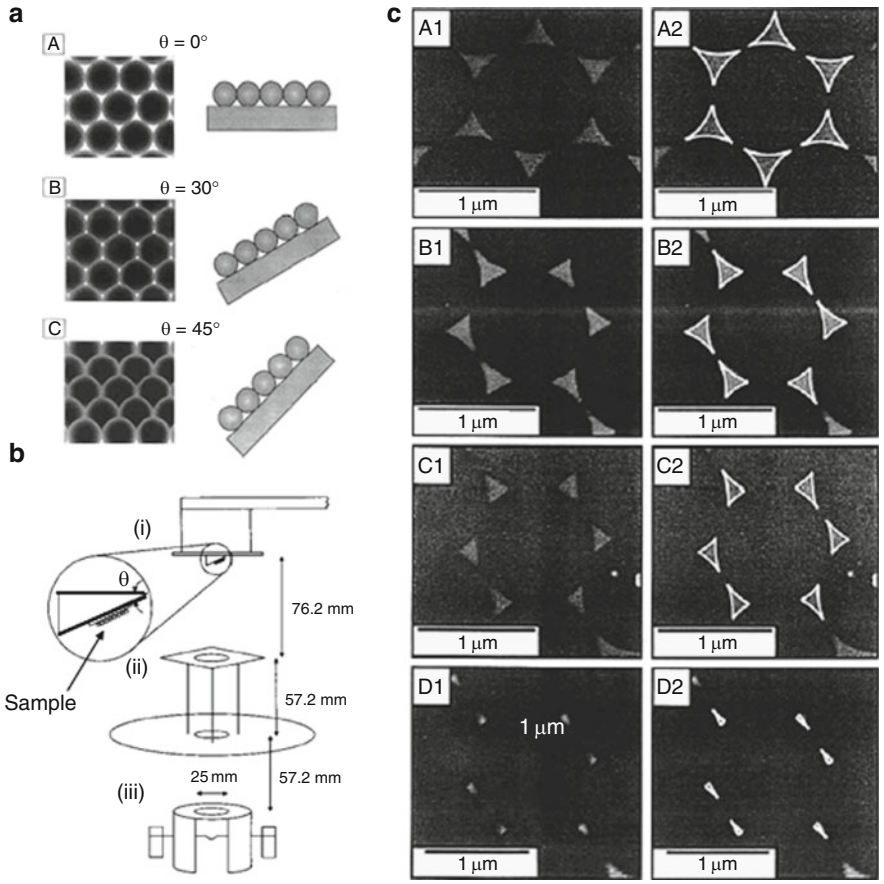

Fig. 6.12 (**a**) Schematic illustration showing top and side views of nanosphere masks used for AR NSL (Angle-Resolved nanosphere lithography) at $\theta = 0°, 30°$ and $45°$ and $\phi = 0°$. (**b**) Schematic diagram of the apparatus used for AR NSL: (i) quartz crystal microbalance and sample assembly, (ii) collimation plates, and (iii) the thermal atomic source. (**c**) FE-SEM images of AR NSL fabricated nanoparticle arrays and images with simulated geometry superimposed, respectively. (A1, A2) $\theta = 10°, \phi = 28°$; (B1, B2) $\theta = 20°, \phi = 2°$; (C1, C2) $\theta = 26°, \phi = 16°$; and (D1, D2) $\theta = 40°, \phi = 2°$. All samples are Cr deposited onto Si(111) substrates. Images were collected at 40 k magnification [50]

here the assembly of gold nanoparticle with an alkyl chain. The most famous assembly style with alkyl thiol protected metal nanoparticle is a nanocrystal superlattice (NCS) by simple casting/evaporation as we introduced in the previous section. Self-assembled NCSs can form two dimensional layer structures as well as three dimensional bulk crystals (Fig. 6.13A) [51]. This phenomenon was simply explained with the role of surface energy in forming self-assembled superlattices and the strong interaction between the alkyl chains with the neighborhood nanoparticles. The most observable shape of Ag nanocrystals is truncated octahedra (Fig. 6.13A), which

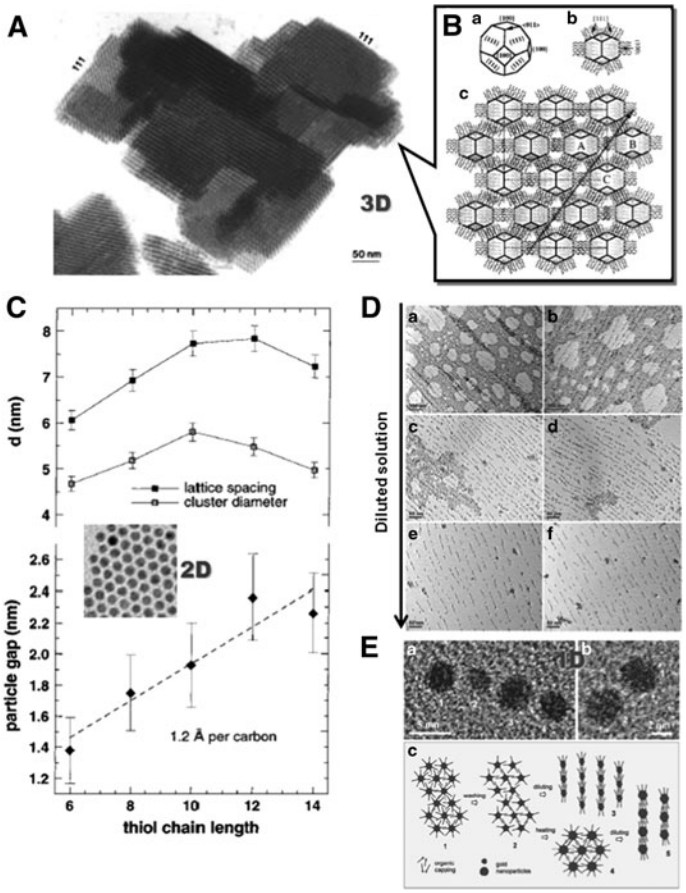

Fig. 6.13 (**A**) 3D-superlattice assembly of Ag nanocrystals [51]. (**B**) Diagram of the truncated octahedron morphology of the Ag nanocrystals, with the 111 and 100 facet structure and ⟨011⟩ direction designated. (b) [100] projection of the TO nanocrsytal with adsorbates. (c) [100]s projection of the NCS model, showing the distribution of passivated molecules between the nanocrystals. The projected unit cell is represented by a *rectangle*. (**C**) Dependence of the average cluster size, lattice spacing, and nanocluster gap on thiol chain length. Inset: TEM image of the 2D lattice [52] (**D**) TEM images of 1D assemblies of Au nanoparticles (ethanol washed and 150°C heat-treated) in toluene solvent: normal suspension (a,b), diluted suspension (c,d), and more dilute suspension (e,f). [53] (**E**) HRTEM images (a,b) of the 150°C heated sample: (a-1) a particle viewed along [111] axis, (a-3 and a-4) lattice fringes of d111 viewed with a tilted angle, (b-1) a fivefold symmetry seen on a decahedral particle, (a-2,b-2) two randomly oriented particles. The process flowchart (c) of this work: (1) as-prepared nanoparticles, (2) partial removal of surface organics, (3) assemblies of the washed sample, (4) the heat-assisted particle growth, and (5) parallel 1D assembly of larger particles. The organic surfactants refer to DT molecules, and TOAB is not shown in this illustration

has six {100} facets and eight {111} facets. The thiolate molecules with an alkyl chain are assumed to be distributed uniformly on the facets of the nanocrystals (Fig. 6.13B). On the basis of the adsorbate structure model shown in Fig. 6.13B, in which the alkyl-thiol ligands from each facet are assumed to be codirected and tightly bunched, the corresponding chain-packing structure in the NCS is given in Fig. 6.13C. Authors explained the assembly structures with the contributions of the projected alkyl-thiol ligands adsorbed on each surface. For example, Ag nanocrystals A and C in Fig. 6.13B are assembled by arranging the {111} facets toward each other. In this case, the nanoparticles were interacted through the alkyl-thiol ligands on only each {111} facets. On the other hand, the nanocrystals A and B are assembled by facing the {100} facets, contributed by the alkyl-thiol ligands on {100} face and additional alkyl-thiol ligands on {111} face at an angle with the projection direction. Therefore, the projected density of the alkyl-thiol ligands between particles A and B is expected to be higher than that between A and C (or B and C). Authors also described that the facet to facet distance between {100} facets of the two neighboring nanocrystals, that is particle gap, is 1.5–2.0 nm, while the length of the alkyl-thiol ligands is 1.8 nm. This clearly indicates that the interdigitation of the alkyl-thiol ligands distributed on the surfaces of two adjacent nanocrystals occurs. Further, Martin and co-workers show that the particle gap and the lattice spacing in the coherent domains of superlattice can be determined as a function of the thiols' alkyl chain lengths (Fig. 6.13C)[52]. On the other hand, the assembling styles have not been limited only two dimensional or three dimensional superlattice. Zheng et al. identified the parameters of key processes to generate parallel unidirectional one-dimensional assemblies of gold nanoparticles with the assistance of organic surfactants [53]. When the concentration of the Au nanoparticles is high, two-dimensional hexagonal arrays are mainly formed. However, parallel-line assemblies of the Au nanoparticles are also aligned across the surfaces (Fig. 6.13D(a, b)). They are smooth and stable, extending several micrometers without breaking their linearity. The two-dimensional arrays was diminished with addition of more toluene in the suspensions, as shown in Fig. 6.13D(c, d). At the lowest concentration region of Au nanoparticles (Fig. 6.13D(e, f)), the 1D assemblies became predominant. Therefore, to control the assembly dimension, especially at the preparation of one-dimensional assembly, the strategy of changing the nanoparticle concentration is useful even in the case of another kind of interaction, such as electro static interaction.

Torigoe, Yonezawa, and co-workers prepared dendron type-thiol-stabilized gold nanoparticles by $NaBH_4$-reduction process [72]. As dendron is bulky structures, it prevents hexagonal close packing of nanoparticles and show quasi 1D structures by just casting on a carbon grid.

In the case of the metal nanoparticle assembly via hydrophobic interaction between alkyl chains, we have to pay much attention to the condition for assembly and the strategy for application. To expand the prospects for application, the various methods and interactions for assemblies have been investigated. For example, a functional groups had been previously immobilized on the surface of a metal nanoparticle as the surfactant, and then a material to be able to interact with the

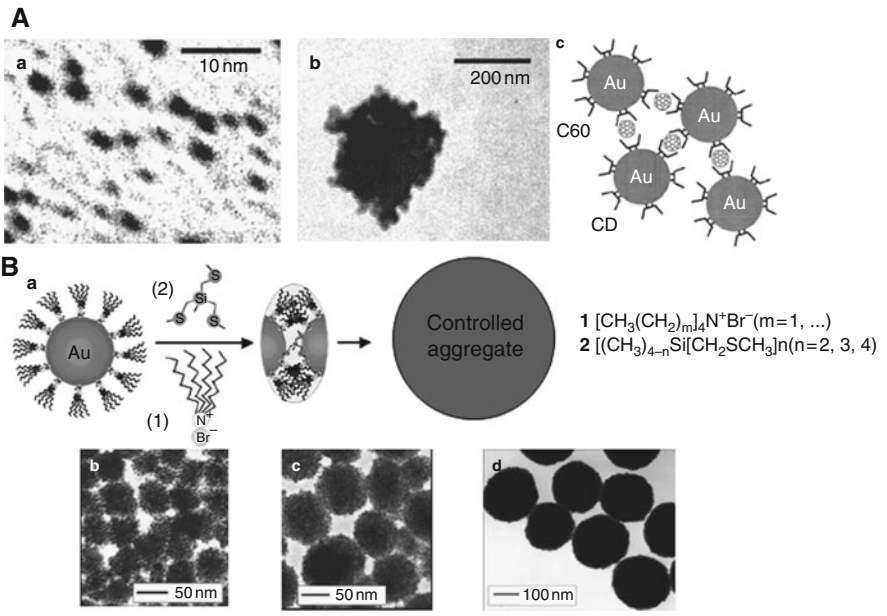

Fig. 6.14 (**A**)[54] TEM images of (a) γ-CD-capped gold nanoparticles and (b) C_{60}-induced aggregation. (c) Schematic illustration of the structure of fullerene-induced network of γ-CD-capped gold nanoparticles in aqueous dispersion. (**B**)[75] (a) Schematic illustration of the mediation-template strategy for quaternary ammonium-stabilized gold nanoparticles and a mediator (2) (b–d) TEM images of the **2**-mediated nanoparticle assemblies prepared by various conditions

functional group on the nanoparticle was added, to obtain the nanoparticle assemblies via non-covalent bonds with the functional groups. As the example of such a host-guest interaction, Kaifer et al. reported the network aggregates formed by C_{60} and gold nanoparticles capped with cyclodextrin (Fig. 6.14A) [54]. In this case, Control of the shape of nanoparticle aggregation have been quite difficult. However, recently, the monodispersed assembly with a clear spherical shape could be prepared with the smart choice of surfactant and mediator by Zhong et al. [73–75] and other researchers [76]. They call the method for the size-controllable assembly of nanoparticles as "mediator-template strategy", as shown in Fig. 6.14B. With this method, the building blocks toward the preparation of size-controllable and monodispersed spherical assemblies (20–300 nm diameters) are multidentate thioether ligands as molecular mediators and tetraalkylammonium-capped gold nanoparticles (5 nm) as templates. They explained about the phenomena that the combination of the mediation force of the multidentate thioether and the hydrophobic force of the tetraalkylammonium template established the interparticle linkage and stability.

In other case of assembly with a linker, the biological recognized molecules, such as biotin-streptavidin [64, 65] or DNA compensatory binding formation [11, 57–59] to bind tightly and selectively, have been often used instead of the artificial host-guest molecules. As an interestingly case with the interaction, Murphy et al.

reported an end-to-end assembly of gold nanorods [65]. The strange assembly of nanorod was explained by using the characteristic of gold nanorod and postulation described below. Most of nanorods are covered with a shape-directing surfactant, cetyltrimethylammonium bromide (CTAB) as at least a bilayer on the nanorod surface. It is postulated that the CTAB preferentially binds to the {100} faces, along the length of the rods, compared to the end {111} Au faces (head and tail). Thus, the molecule such as biotin-disulfide seemed to be unsuccessful at displacing the CTAB bound to the length of the gold nanorods, and bound to the end {111} Au faces of nanorod preferentially, resulting in preferential end-to-end linkages upon the addition of streptavidin.

In the case of the assembly via the covalent bonding formation, Yamada et al. reported the alternative integration with multisulfide porphyrin and gold nanoparticles [56]. The integration was confirmed by monitoring the absorption of porphyrin at around 420 nm and assembled gold nanoparticles at around 550–600 nm (plasmon absorption). The covalent bond is more stable than other kind of interactions, such as hydrophobic interaction, hydrogen bonds, metal coordination, and so on. Thus, the assembly allows choosing many kinds of preparation methods even if they are not mild conditions, and tends to be used to the practical application, for example, photoelectric conversion devices and sensors.

In the previous section, we have introduced the assemblies of alkyl-chain-modified gold nanoparticles, because the alkyl chains for hydrophobic interaction to other nanoparticles have already capped the metal nanoparticles as a protective reagent since their preparation stage. While, much amount of examples on gold nanoparticle capped with charged protective reagents including organic acids have been investigated and reported since 1950s [26, 27]. In these cases, the charge of protective reagents on metal nanoparticles prevents the aggregation of each nanoparticle with the static repulsion. However, thought it was imaginable at once, the charged protective reagent-capped gold nanoparticles are very easy to be assembling by addition of another charged material. So in this section, we introduce two examples about the assembly of the charged surfactant or protective reagent capped metal nanoparticle. The former is the example of assembly with negative charged metal nanoparticles and positive charged molecules [11, 66], and the latter is about assembly with negative charged metal nanoparticles and positive charged metal nanoparticles [67].

The first example was the assembly with citrate acid capped metal nanoparticles and viologen derivatives, reported by Willner et al. The assemblies had been prepared on a electrode with the alternative integration method at first [77–81], and then have been extended to the solution system. They also controlled the dimension of the nanoparticles assembly with the cationic and oligocationic species and concentration. Interestingly, the strategy for the dimensional control of nanoparticle is consistent with the other various cases, and it is independent on the protective reagent [53,66,80]. Aggregation is followed by the appearance of features at around 600–900 nm in the visible absorbance spectrum (Fig. 6.15b, c) and SEM (Fig. 6.15d, e) [82]. Based on these results, they summarized as shown in Fig. 6.15a and below: Multiply charged aggregating reagents can bind nanoparticles together into dense

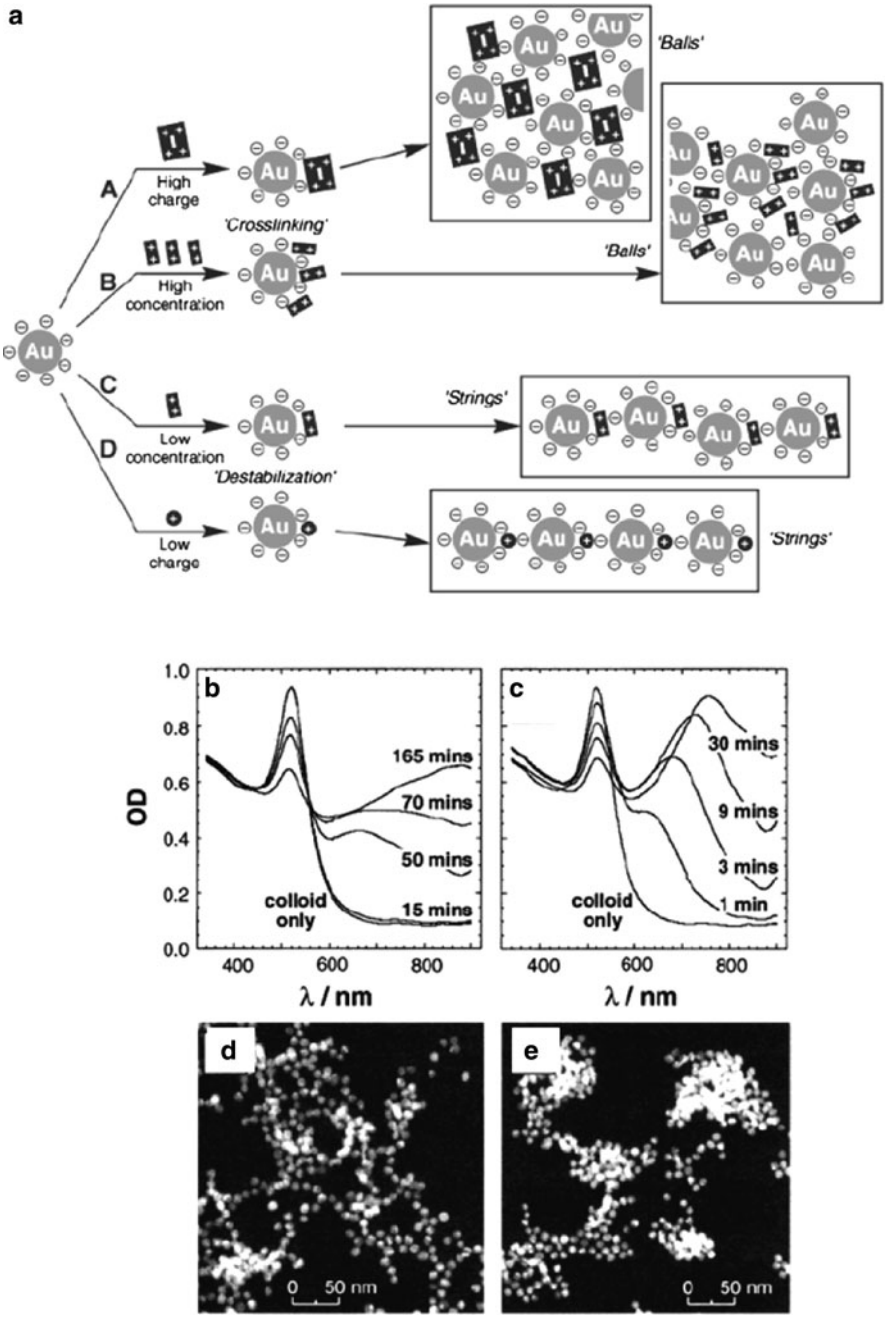

Fig. 6.15 (**a**) Possible mechanisms for the formation of stringlike and ball-like aggregates of Au nanoparticles based on crosslinker charge and concentration. Absorbance spectra of aggregating Au-colloid solutions various times after the addition of methyl viologen dichloride at final concentrations of (**b**) 1×10^{-5} M and (**c**) 1×10^{-4} M. Representative micrographs of nanoparticles aggregated with 2 at concentrations of (**d**) 1×10^{-5} M and (**e**) 1×10^{-4} M [82]

aggregates, displaying an absorbance at around 700 nm, whereas singly charged aggregate reagents cause a slower aggregation into string-like aggregates with a less defined absorbance. Whereas multiply charged aggregate reagents can "cross-link" the layers in a multilayer structure on a surface, singly charged aggregate reagents cannot. In short, the control of the charge concentration, in other words magnitude of interaction in a space, is the most important matter to control the dimension of nanoparticle assembly.

The later example, reported by Grzybowski et al., is a more interesting case from the viewpoint that the things in the nanometer order are identical to the macroscopic character that could confirm with optical microscopy [67]. This is the self-assembly of charged, equally sized metal nanoparticles (gold and silver) leads to the formation of large, sphalerite (diamond-like) crystals, in which each nanoparticle has four oppositely charged neighbors. In the preparation procedure, $HS(CH_2)_{10}COOH$ (MUA: 1.63 nm) and $HS(CH_2)_{11}NMe_3^+Cl^-$ (TMA: 1.9 nm) were used as the surfactant of gold and silver nanoparticle, respectively. From the TEM observation, the core size of Au and Ag nanoparticle were estimated to be 5.1 and 4.8 nm, so the average size of the building blocks, AuMUA (∼8.60 nm) and AgTMA (∼8.36 nm), were very similar. When the AgTMAs and AuMUAs solutions at the same molar ratio were mixed (pH: 9.7), the positively charged AgTMAs interacted with the negatively charged AuMUAs, and the aggregates rapidly precipitated, in which the overall charge of the NPs was neutralized. Based on the XRD measurements, SEM observations, as well as the energy dispersive spectroscopy (EDS) measurements in STEM (Fig. 6.16c) of the aggregates, they concluded that nanoparticles are arranged on a diamond lattice with each nanoparticle surrounded by four oppositely charged neighbors at the vertices of a tetrahedron (Fig. 6.16b), closely related to that of sphalerite ZnS except the sizes of the nanoparticle "ions". We can find the various kinds of the overall crystal morphologies, for example octahedral, truncated tetrahedral, truncated and twinned octahedral, and triangular, identical to those observed for their macroscopic diamond or sphalerite ZnS counterparts.

6.3.5 Nanoparticle Assembly with Templates

We have discussed in the previous sections about the physical properties and surfactant-assisted self-assembly formations of metal nanoparticles. These assembling methods are quite beautiful and intelligent, because they are induced by the spontaneous driving force for assembling by smart choice of the conditions. In the cases of practical use, however, the methods described below are rather tend to be required; (1) the method to make a desirable size, length, shape, architecture and position, etc., (2) a simple and easy method, and (3) highly stable assemblies. From these viewpoints, as a final section for a preparation of nanoparticle assembly, we introduce here the template assisted self-assemblies of nanoparticles. This section is classified to three stories corresponding to the dimension (such as 1D, 2D and 3D) of the template and assembly.

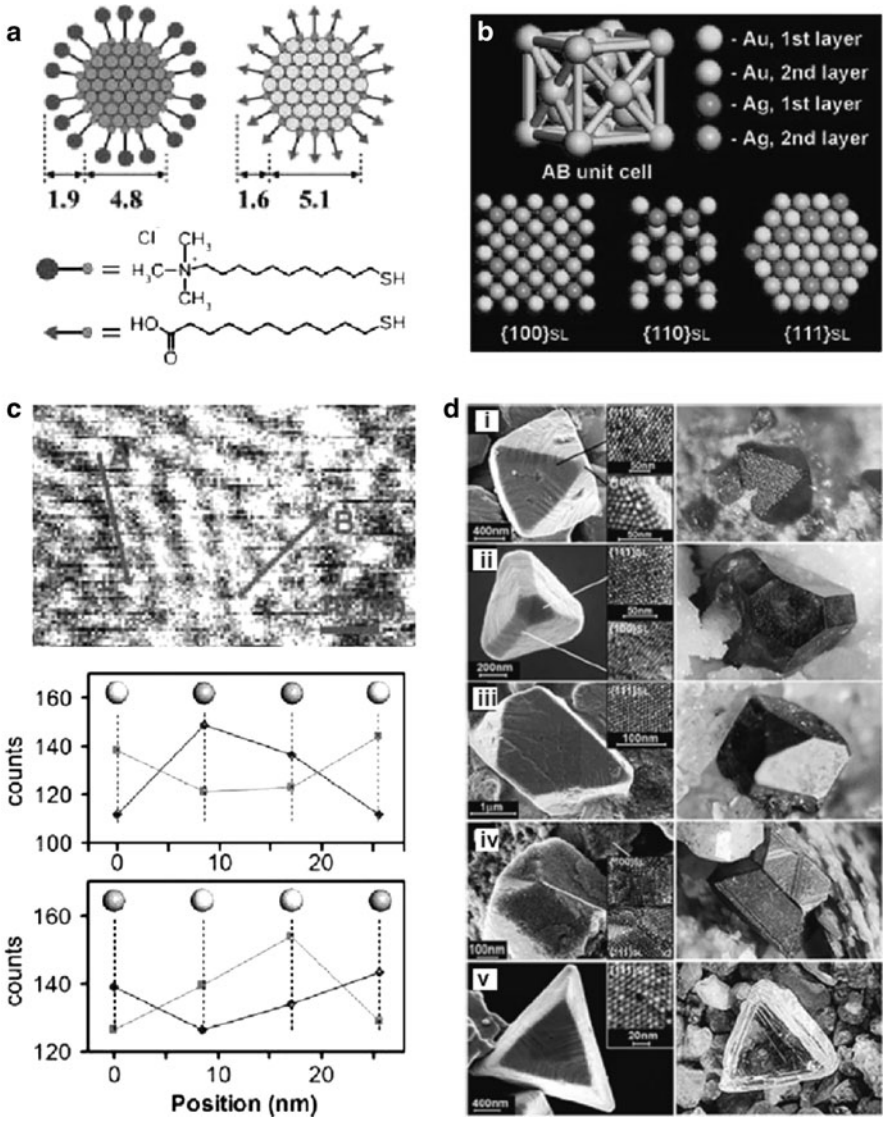

Fig. 6.16 (**a**) Scheme and average dimensions (in nanometer) of AuMUA and AgTMA nanoparticles used as the model system. Particle compositions are $Au_{4100}L_{380}$ (where L is MUA) and $Ag_{3400}L_{340}$ (where L is TMA); (**b**) Scheme of an AB unit cell and the projections of $\{100\}_{SL}$, $\{110\}_{SL}$, $\{111\}_{SL}$ planes. (**c**) Compositional analysis of the NP crystal faces. *Upper*: STEM image of a hexagonal {111} face, *lower*: the EDS analysis in STEM mode. (**d**) Different morphologies of the AuMUA-AgTMA crystals (*left column*) and their macroscopic sphalerite (SL) (i–iv) and diamond (v) counterparts (*right column*). (i) Octahedron; insets show $\{111\}_{SL}$ and $\{100\}_{SL}$ faces. (ii) Cut tetrahedron; insets show $\{111\}_{SL}$ and $\{100\}_{SL}$ faces from cut top and from cut edge, respectively. (iii) Octahedron with two triangular faces cut; inset shows the $\{111\}_{SL}$ face. (iv) Twinned octahedron; insets magnify $\{111\}_{SL}$ faces at the location of twinning and the $\{100\}_{SL}$ face of a broken neighboring crystal. (v) Truncated tetrahedron; inset shows top view of the $\{111\}_{SL}$ face [67]

6.3.5.1 One-Dimensional Nanoparticle Assembly with Templates

The one dimensional alignment of nanoparticles was the basic technique to write and represent a straight line, a bend line, and a complicated design with the nanoparticles freely. The technique reminds us of a nano-wiring, indispensable in the nano- and micro- optoelectronic devices in the next generation. The key process of this technique is just how to constantly align nanoparticles on the substrate, in short, how to prepare the template freely and desirably for the resulting nanoparticles immobilization. So in this section, we introduce here the 1D nanoparticle alignment with the various examples of templates, prepared by an AFM lithograpy [83–86], a straight extended DNA [87, 88], and an electro deposition [89].

The nanoparticle immobilization and the nanowires self-assembled on the patterned monolayer template have been investigated by Sagiv et al. Their approach combines surface self-assembly with nanolithography by a conductive AFM tip [83–86]. The preparation procedure is schematically shown in Fig. 6.17. Firstly, the nano-electrochemical patterning process was carried out by utilizing electrical pulses with an AFM tip to induce the local chemical reactions in nanometer-scale on the top surface of certain highly ordered long-tail organosilane SAM on silicon (Fig. 6.12a). Concretely, the oxidation of surface exposed vinyl ($-CH{=}CH_2$) and methyl ($-CH_3$) groups to hydroxyl-containing functions ($-CO_2H$ etc.) was demonstrated. This first nanolithography step is just the key factor to prepare the template. So after that, the cascades of the selective molecular interaction (Fig. 6.17b), reaction of the end groups (Fig. 6.17c), and immobilization of metal particles (Fig. 6.17d, e) were occurred only on the template of the pattered SAM, to obtain nanowires and patterns (AFM images are shown in Fig. 6.17). With this method, freely designed lines and patterns can be inscribed, on the other hand, the preparation rate and scale are limited by the performance and instinct limitation of the AFM at the electrochemical process with an AFM Tip.

By using well-stretched DNA templates, various processes have been proposed. Yonezawa et al. used quaternary ammonium stabilized gold nanoparticles which were densely attached to the aligned DNA molecule [87]. Although the particles were highly positively charged according to the quaternary ammonium ($-N(CH_3)_3^+ Br^-$) group which is always ionized at any pH conditions. Thanks to the rigidity of helix structures of DNA molecules, gold nanoparticles were tightly affixed onto the DNA template. The inter-particle distance was controlled by the stabilizing reagent lengths. For example, 2.2-nm length quaternary ammonium alkylthiol-stabilized gold nanoparticle shows the 3.8 nm inter-particle distance. It is probably due to the interdagitated structure of the hydrophilic quaternary ammonium groups. They also showed densely packed 1D alignment of thiocholine ($HS-(CH_2)_2^-N(CH_3)_3^+$)-stabilized gold nanoparticles [68]. In this case, gold nanoparticles were fused each other to form larger structures on DNA molecules. This is probably due to the lower melting temperature of nanosized particles according to the size effect. However, they also produced thiocholine-stabilized palladium nanoparticles and also attached densely to DNA molecules (Fig. 6.18) [90]. In that case, no fusion of palladium nanoparticles was observed on DNA molecules, but this nanoparticle 1D assembly

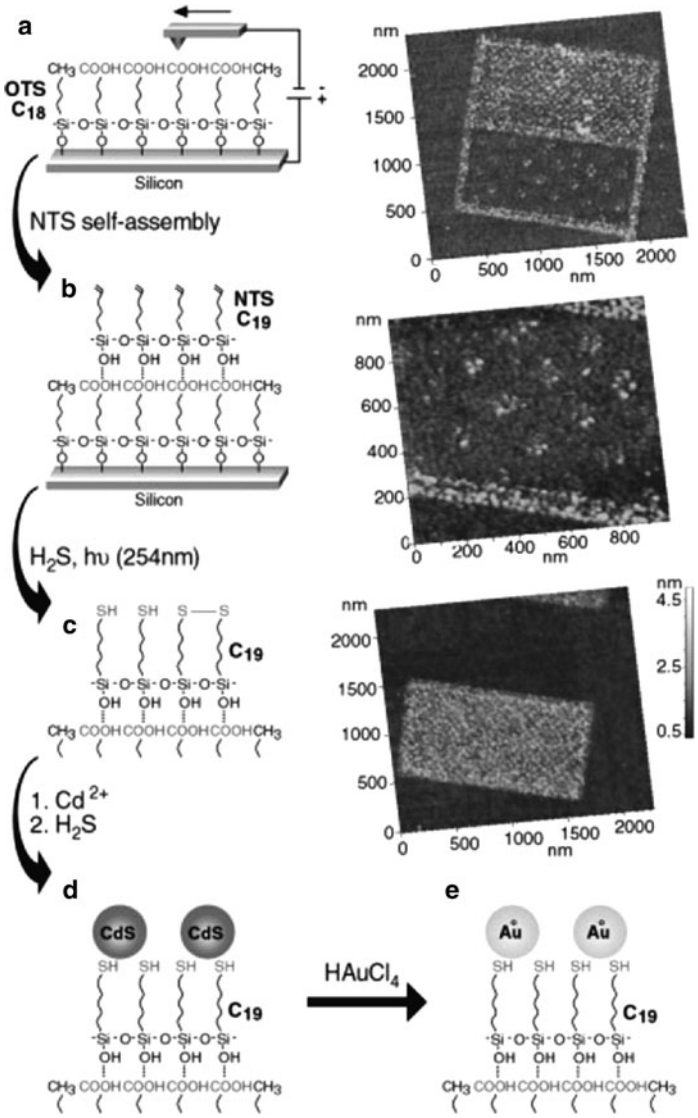

Fig. 6.17 Scheme of the hierarchical self-assembly of gold nanoparticles onto an organic bilayer template pattern on silicon, and example of semicontact topographic AFM images of planned arrays of gold nanoparticles. (**a**) Tip induced non-destructive nanolothographic process to prepare the template, (**b**) NTS self-assembly, (**c**) Formation of functional group (–S–S–, and –SH), (**d**) CdS particle anchoring, (**e**) conversion CdS to metallic fold via redox chemical process [86]

shows ohmic electroconductivity. We have also prepared 1D assembly of ZnO nanoparticles, which was post-cationized by a quaternary ammonium type coupling reagent [91]. This ZnO nanoparticle array showed the possibility of nanophotonic signal transfer (Fig. 6.19).

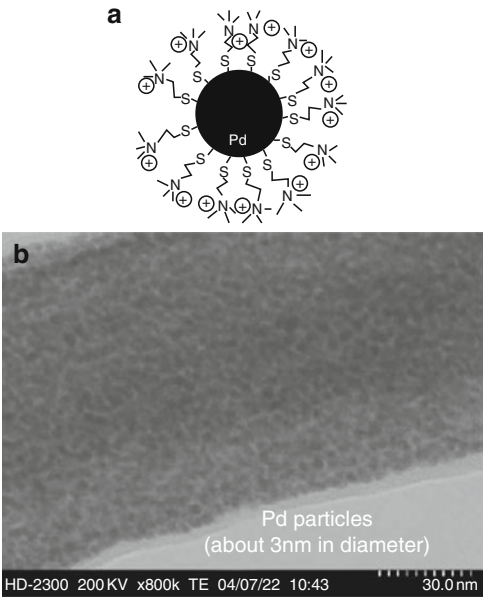

Fig. 6.18 (**a**) Schematic illustration of thiocholine-stabilized palladium nanoparticles. (**b**) STEM image of DNA-Pd wire. Pd particles are about 3 nm in diameter and the surface of the DNA-Pd wire was covered by Pd nanoparticles [90]

Ohtani et al. developed a simple method for highly ordered assemblies of gold nanoparticles along DNA on substrates (Fig. 6.20). The driving force of the strong attachment is the electrostatic interaction between the oxidized and positively charged aniline-capped gold nanoparticles and the negatively charged DNA. They carried out two different assembly methods: Method I, the DNA was starched and fixed on the substrate at first, and then the gold nanoparticles were attached along the DNA, whereas in Method II the treatment orders were reverse order. As the result, the different assembling styles, such as continuous depositions (Fig. 6.20b, c) of method I and necklace-like depositions (Fig. 6.20d) of method II of the gold nanoparticles along DNA molecules were achieved. This method seems to be quite useful because this is a quite simple method for assembling of metal nanoparticles with well-aligned and long-range order, except lack of the perfect control of the shape of template for preparation of desirably wiring. However, the problem has been resolved recently by using various programmed DNAs, mentioned in the next section [88].

The next example of template-assisted self-assembly of metal nanoparticle is a little different from the previous ones. This is a microwires reported by Velev et al., assembled by dielectrophoresis from suspensions of metallic nanoparticles. In this case, they did not use any special template materials, but apply an electric field as a kind of template [89]. The microwires form after introduction of a suspension of gold nanoparticles (diameter: ∼15–30 nm) into a thin chamber electrodes (the gap: varies from 2 mm to more than 1 cm) in an electric field intensity of 250 V cm^{-1}. The wires can grow faster than 50 μm per second to lengths exceeding 5 mm (Fig. 6.21a). Then finally, when the wire was completely assembled, there

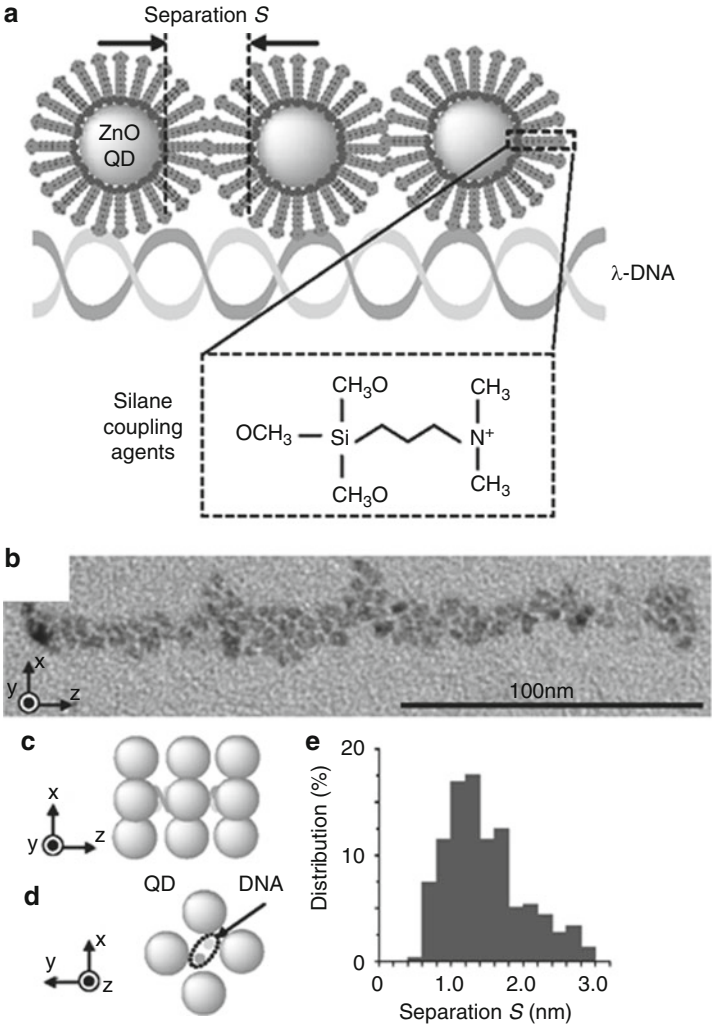

Fig. 6.19 (**a**) Schematic illustration of cationic ZnO quantum dots (QDs) alignment along the λ DNA. *S*: separation between QDs. (**b**) TEM image of aligned ZnO QDs on DNA. (**c**) and (**d**) Schematic illustrations of the QD alignment along the DNA. (**e**) Distribution of the separation lengths between QDs (*S*) [91]

was a clear and sharp jump in the electrical current through the cell. This indicates that the microwires consisting of gold nanoparticles have a good ohmic conductance. Interestingly, they demonstrated that the growth process of microwires can be controlled in a variety of ways on the basis of these principles. The dielectrophoresis is concerned with the polarisability of the particles and the solvent, and a gradient of the electric field. Thus, the wire growth direction is controlled by disturbing the homogeneity of the electric field. In deed, they demonstrated the easiest

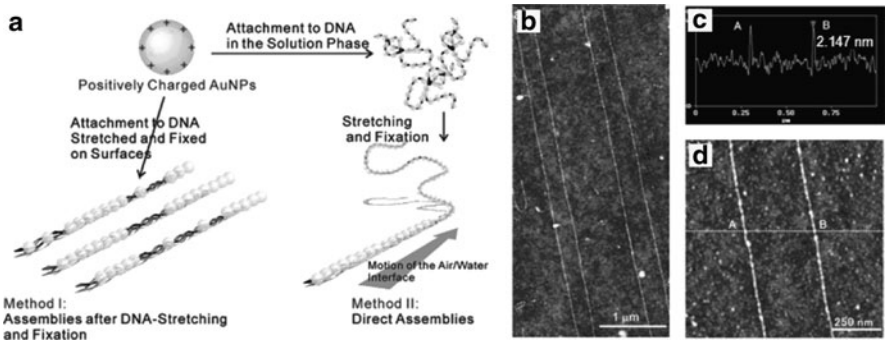

Fig. 6.20 (**a**) Procedure of assemblies of gold nanoparticles onto DNA. AFM images of highly ordered assemblies of Au NPs onto DNA molecules using method I. (**b**) Image in a large scan range. (**c**) Scan profile along the *white line* of the image (**b**). The height scale is 5 nm in both images. (**d**) Image in a smaller scan range [88]

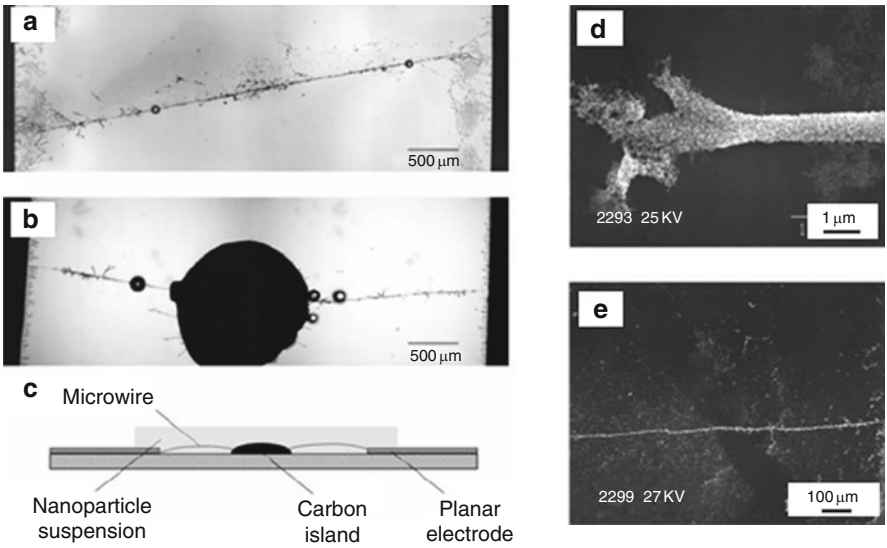

Fig. 6.21 (**a**) A composite optical micrograph of a gold microwire spanning a 5-mm gap between planar gold electrodes. (**b**) Two wires that have connected to opposite sides of a conductive carbon island deposited in the middle of the gap, and (**c**) schematics of the above configuration. (**d**) SEM image of the end of a growing microwire showing the structure in the growth area and uniform cylindrical porous body. (**e**) SEM image of a long and thin microwire [89]

example, introduction of a conductive carbon paint as an island in the gap between the electrodes. Such objects create the gradient in the electric field and cause the microwire to grow toward them, and spontaneously to connect these islands to the both electrodes (Fig. 6.21b, c). From SEM images (Fig. 6.21d, e), the effective diameter of the microwires can be estimated to be ∼1 m. They tabled the specific

resistance of the microwire, and it depends on the conditions of assembly and ranges from 3×10^{-6} to 20×10^{-6} ohm · m. This resistivity is about three orders of magnitude higher than that of bulk solid gold, and is comparable to that of a number of metallic alloys. They explained the result that the microwires are assembled from aggregated nanoparticles and their specific conductance will be much lower than that of bulk gold because of their porosity and small inter-particle contact areas. Anyway, this method is a quite simple assembly process, and seems to become a candidate of the process for wet electronic and bioelectronic circuits.

6.3.5.2 Two-Dimensional Assembly with Templates

Two-dimensional (2D) alignment of nanoparticles was appropriate for the technique to draw a design and/or a pattern of nanoparticles to add the noble optical and electrical properties. The key process of this technique is also how to prepare the desired 2D template pattern freely for the resulting nanoparticle immobilization, and the advanced and intelligent techniques are requisite. In this section, we introduce the 2D nanoparticle patterning with the various 2D templates, prepared by using assembling of and/or caged protein complexes [92–101], ring shape proteins [102, 103], programmable assemblies of DNA [104, 105].

The strategy for preparing the 2D metal nanoparticle arrays by using the assembly of caged protein was reported by Yamashita [92], which has been followed by many scientists since then. In those days, it was reported by Douglas et al. that a nanometer sized material could be prepared in the cage of protein and virus by a bio-mineralization [96]. In addition, the methods to obtain arrays of, the major cellular iron-strage protein (Fig. 6.22a), have been intensely studied and it has become possible to make large 2D crystals or arrays of at an air–water interface [106–108]. Based on these previous results, he transferred a two-dimensional array of iron-oxide loaded molecules formed by self-assembly at an air-water interface onto a hydrophobic silicon (Si) surface and eliminated the protein shell of the molecule, apoferritin, with 1 h heat-treatment at 500°C under nitrogen atmosphere (Fig. 6.22b). Scanning electron microscopy (SEM) observations show a well-ordered array of nanometer sized dots on the Si surface before and after the heat treatment at 500°C. The elimination of organic protein shell and leaving only the iron cores by this treatment were confirmed by AFM observation with the contact mode, Fourier transform IR (FT-IR) spectrophotometer analysis, and the measurement of the weight loss. He prospected that this method would be utilized to the quantum electronic devices, because various kinds of metals and metal complexes could be encapsulate in the caged molecules, and the 2D nano-dot arrays of these metals and compounds can be readily produced by this method. And after this paper, he and his co-worker in deed introduce this method to the application, floating gate metal-oxide-semiconductor [93].

The preparation of desired 2D assembly of nanoparticles is the second step of free and complicated patterning in the nanometer order, of course, the first step is the 1D assembles. For the purpose, the unique 2D shape and designed molecules

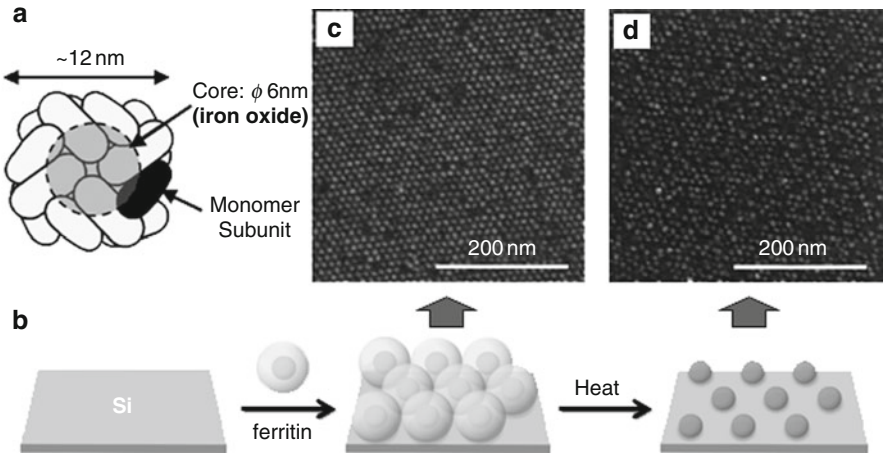

Fig. 6.22 (**a**) Schematic drawing of the molecule viewed down a fourfold axis and (**b**) the preparation procedure of 2D array of on Si substrate. HR-SEM images of the silicon substrate with the 2D array; (**c**) before and (**d**) after heat-treatment under nitrogen at 500°C for 1 h [92]

were employed as a template for assembling of nanoparticles [102, 103]. One of the simplest examples of rapid synthesis is the assembly of nanoparticle ring structures based on protein templates, demonstrated by Behrens et al. [102]. They used tublin, about 8 nm in length with diameters ranging from 4 to 5 nm, as a template, and the AFM images and the line profile of tublin ring structure on Si are shown in Fig. 6.23a. The metallization of the ring-like tubulin assemblies involves two steps: (1) Ca^{2+} ions direct the assembly of tubulin into spiral-shaped protein structures, and (2) enlargement of the nanoparticles, in short the deposition of Ag nanoparticles into spiral-shaped arrays along the backbone of the spiral-shaped biostructure (Fig. 6.23b). The mean distance of 7.31 ± 0.99 nm between Ag particles is almost identical to the theoretical center-to-center distance of 7.9 nm between two neighboring tubulin dimers. So, they suggested that one Ag particle is preferably nucleated by the α, β-tubulin heterodimer. This method is a quite simple and easy way to prepare, but it was unfortunately limited a constant shape of circle. On the contrary, if the template shape was freely designed and controlled, the application field will be extremely extended. For example, Belcher et al. reported the assembly of various nanoachitectures, straight bounded lines and Y-shaped structure, including nanoparticle arrays, heteronanoparticle architectures, and nanowires utilizing highly engineered M13 bacteriophage as templates [104]. In other case, Yan and co-workers reported the 2D assembly of gold nanoparticles functionalized with a single DNA strand (1:1 conjugate of a Au NP with the 109-base-DNA strand; Fig. 6.24a) on three different 2D patterned structural templates which are constructed from self-assembled DNA tiles [105]. For the purpose of preparation of the lattice structures, they used two building blocks, that is, the annealed DNA tile (blue) carrying one gold nanoparticle to introduce the nanoparticle in the 2D assembly, and three different lattice structures of DNA tiles (brown) to change and

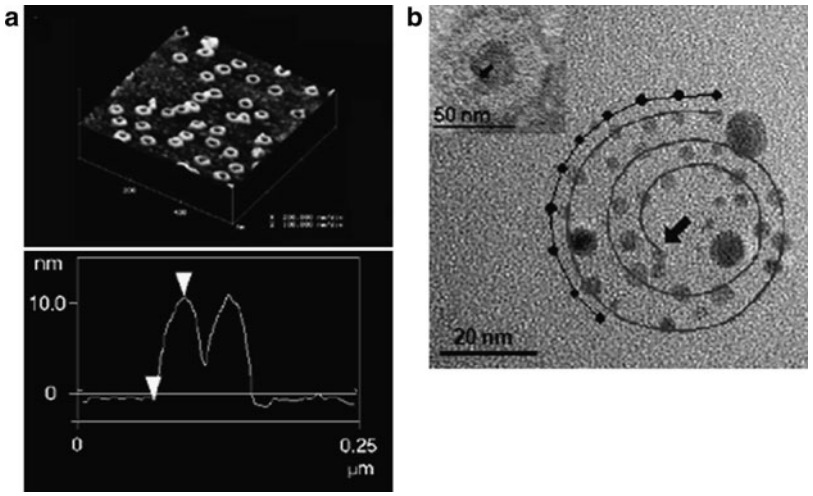

Fig. 6.23 (**a**) AFM image (tapping mode) of tubulin ring structures on a thermally oxidized silicon wafer. The heights of the ring structures (fixed by 1% GA) predominantly range from 8 to 15 nm. The profile shows a height of 10.6 nm. (**b**) TEM image of Ag nanoparticles immobilized on the tubulin assembly, reflecting the spiral-shaped order of the tubulin subunits (inset image: tubulin spiral negatively stained with uranyl acetate). The center-to-center distance measured between the particles (marked by *black points*) is 7.31–0.99 nm [102]

control the shape and size of 2D patterned lattice structure (Fig. 6.24b–d). From the AFM images of three 2D assemblies, we can recognize that the periodicity and the interparticle spacings of the nanoparticle arrays can be precisely controlled through variation of the DNA-tile dimensions.

Electrostatic interaction is a good candidate also for two-dimensional assembly. nanoparticle should gather each other on a substrate with an oppositely charged surface. However, some papers have mentioned that the electrostatic repulsion between the particle themselves prevents the densely packed structure on the substrate surface. To overcome such problems, Yonezawa et al. proposed highly positively charged surfaces to immobilize anionic nanoparticles densely on the substrate. A bilayer membrane with quaternary ammonium head groups was applied for this purpose. Onto such highly positively charged surface, anionic nanoparticle were densely attached [109].

6.3.5.3 Three-Dimensional Assembly with Templates

As the final section of the template assisted metal nanoparticle assembly, we introduce the tree dimensional (3D) nanoparticle assembling. The procedure of 3D assembly is rather easier than the ones for 1D and 2D assemblies, because the metal nanoparticles are just covered on the surface of template materials. However, such 3D assemblies are highly useful to prepare the dense system of metal nanoparticles, where the properties of nanoparticle tend to be enhanced. So, we just

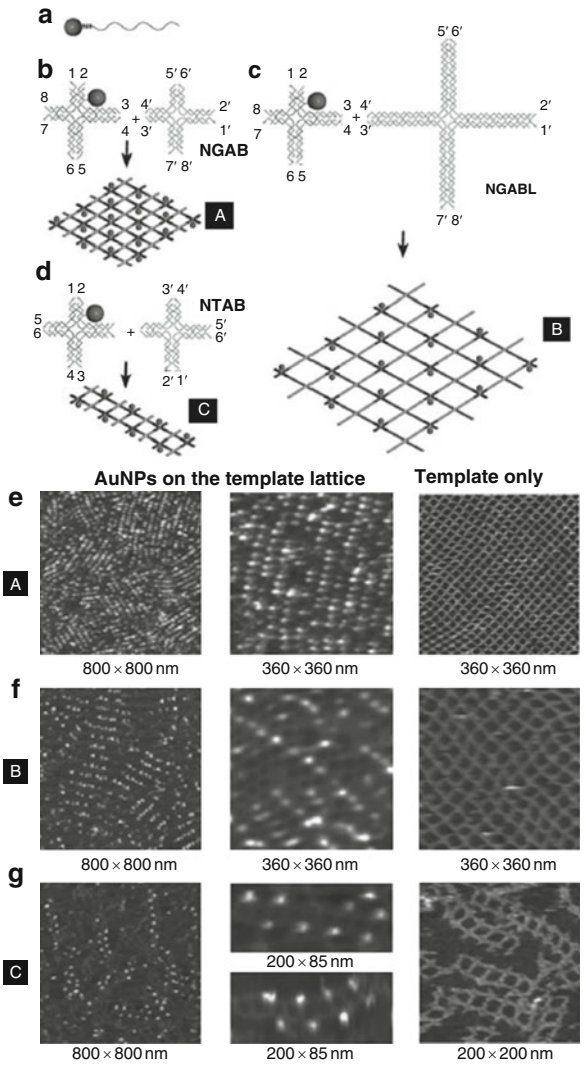

Fig. 6.24 Schematic representations of the DNA-templated assembly of periodical AuNP nanoarrays. (a) 1:1 conjugate of a Au NP (*ball*) with a thiolated DNA strand (*curved line*). (b) AuNP on an NGAB lattice (**A**). The DNA strands self-assemble into the cross-shaped A (*blue*) and B (*orange*) tiles with sticky ends so that 1 is complemented with 1', 2 with 2', and so forth. The central strand on A tile carries the AuNP into the self-assembled 2D nanogrid. (c) A AuNP on an NGABL lattice (**B**). The A tile remains the same as in (b), and the four arms of the B tiles are each elongated by four DNA helical turns, thus the 2D arrays assembled have a larger cavity. (d) A AuNP on an NTAB lattice (**C**). They self-assemble into 1D nanotrack by modifying the sticky ends of the A and B tiles. Note: all the A tiles share the same central strand that carries the AuNP. AFM images show the patterning of AuNPs on the self-assembled DNA nanostructures. (e) AuNPs on NGAB lattices (**A**). (f) AuNPs on NGABL lattices (**B**). (g) AnNPs on NTAB lattices (**C**) [103, 105]

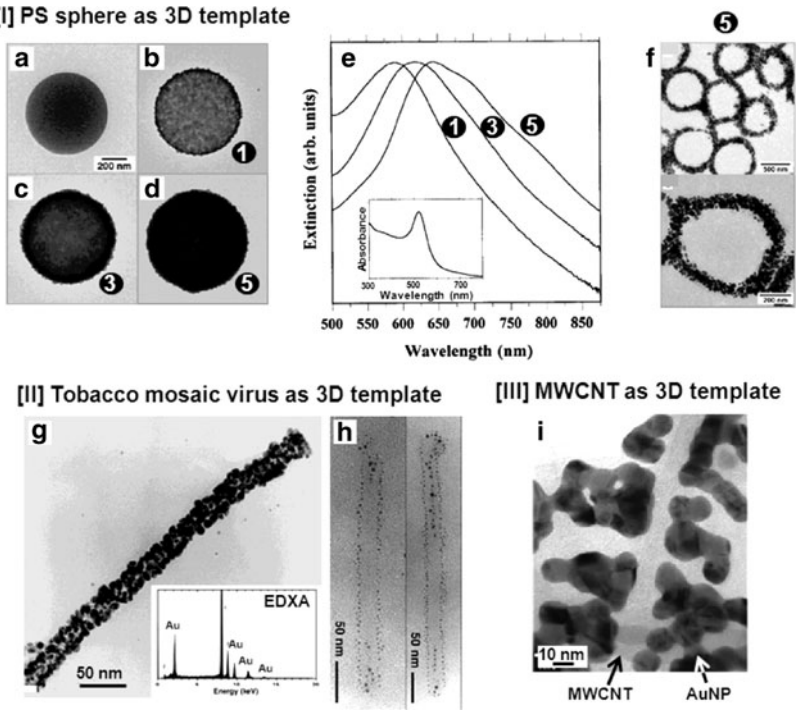

Fig. 6.25 [I] TEM micrographs of (**a**) a polyelectrolyte (PE3)-coated PS sphere and PE3-modified PS spheres coated with (**b**) one (**1**), (**c**) three (**3**), and (**d**) five (**5**) $Au@SiO_2$ nanoparticle/PDADMAC multilayers. (**e**) Normalized extinction spectra of $Au@SiO_2$ nanoparticle/PDADMAC multilayer-coated PS spheres with different multilayer shell thicknesses dispersed in aqueous solution. The shell thicknesses are 21 nm (**1**), 52 nm (**3**), and 82 nm (**5**). The inset shows the absorption spectrum of the $Au@SiO_2$ nanoparticles in aqueous solution. (**f**) TEM micrographs of single TMV rod with dense coating of discrete gold nanoparticles. Inset image: corresponding EDX spectrum [122]. (**g**) TEM images of mutant E95Q/D109N showing rows of 3 (2 nm silver particles on the outer surface and in the inner channel.) [115] [III] (**i**) TEM image of MWCNT-AuNP films [117]

list here the examples of 3D assemblies, prepared using polystyrene (PS) [110–114], tobacco mosaic virus [115, 116], carbon nanotubes [117], and dendrimers [118–121] as template materials. One of the most convenient and well-used 3D templates for nanoparticle assemblies is polystyrene (PS) beads, because of their real spherical shape, well-controlled various sizes commercially available, hydrophobic surfaces and functional groups to immobilize nanoparticles, etc. On the surface of PS beads, the immobilization and integration techniques of the particles on the planar substrate, such as layer-by-layer method, etc., can be applied to prepare the assembly (Fig. 6.25a–f) [122]. When we use a cylindrical template, for example TMV [115, 116] and carbon nanotube [117], the cylindrical assemblies can be obtained (Fig. 6.25g–i). In addition, TMV is a 300-nm long hollow cylindrical protein complex with an outer diameter of 18 nm and a 4 nm-wide inner

cavity [123], and interestingly the preparation of 1D metal nanoparticle arrays were demonstrated. From the viewpoint of the particle assembly not only on the outer side but also in the inner space of the template, dendrimers seem to be an attractive template because the environment and chemical structure of the inner space and outer surface can be desirably controlled by a well-designed chemical synthetic approach. Crooks and co-workers utilized the nanoparticle encapsulated in the dendrimer as catalysts, and the dendrimers themselves as a reactor [124]. In other case, Yamamoto et al. prepared the metal ion-coordinated dendrimers [118], it is not the assembly of metal nanoparticles, but applied to the various field, such as a hole transport material [119], electroluminescence [120] and dye-sensitized solar cell [121], etc. The coordinated metal ions could be readily reduced to form metal nanoparticles which became a good catalyst [125].

6.3.5.4 Reversible Assembly

One of the quite recent trends of the researches on nanoparticle assembly is addition of reversibility to assembly formation. This ability is indispensable and/or makes high value to the application use of nanoparticle assembling phenomena as a sensor from the viewpoint of multi-usage. In the concrete, temperature-controlled or pH-controlled reversible assembly with a specific surfactant, such as DNA [11, 57], carboxyl group functionalized molecules/proteins [126], and polymers [127], etc., are reported. Here, we introduce an example of reversible assembly of DNA molecules capped gold nanoparticle, reported by Mirkin et al. They designed two non-complementary oligonucleotide sequences with mercapto groups and bind on the surfaces of two sets of gold nanoparticles as the surfactant. The gold nanoparticles do not recognize each other and behave a dispersed set of particles, therefore, the color of mixed solution was kept red due to their plasmon absorption (Fig. 6.26a). Once they added a linker duplex DNA which can perfectly recognize the sequences immobilized on the two different batches of gold nanoparticles, the particles begin to come together and the color was changed from red to blue. The pictures and typical light absorption spectra are shown in Fig. 6.26b, c. The key of reversibility is the cross-link system by using the complementary hybridization of linker DNA and surfactant DNA, because the hybridization process of DNA molecules is reversible. The DNA interconnects made by hydrogen bonding can be broken by heating. This reversibility cannot be achieved with normal salt-flocculated gold particles. Once such nanoparticles are aggregated, larger clusters are generated, eventually resulting in the precipitation of bulk gold. On the other hand, they demonstrated the aggregation and association can be drive repeatedly with a thermal control, and this change could be monitored by the absorbance change of the solution at 260 and 700 nm (Fig. 6.26d).

6.3.5.5 Systematic Immobilization of Nanoparticles onto Substrates

Nanoparticles have a huge ability originated from their large specific surface, electronic properties, optical properties, and so on. The nanoparticle assembles induce

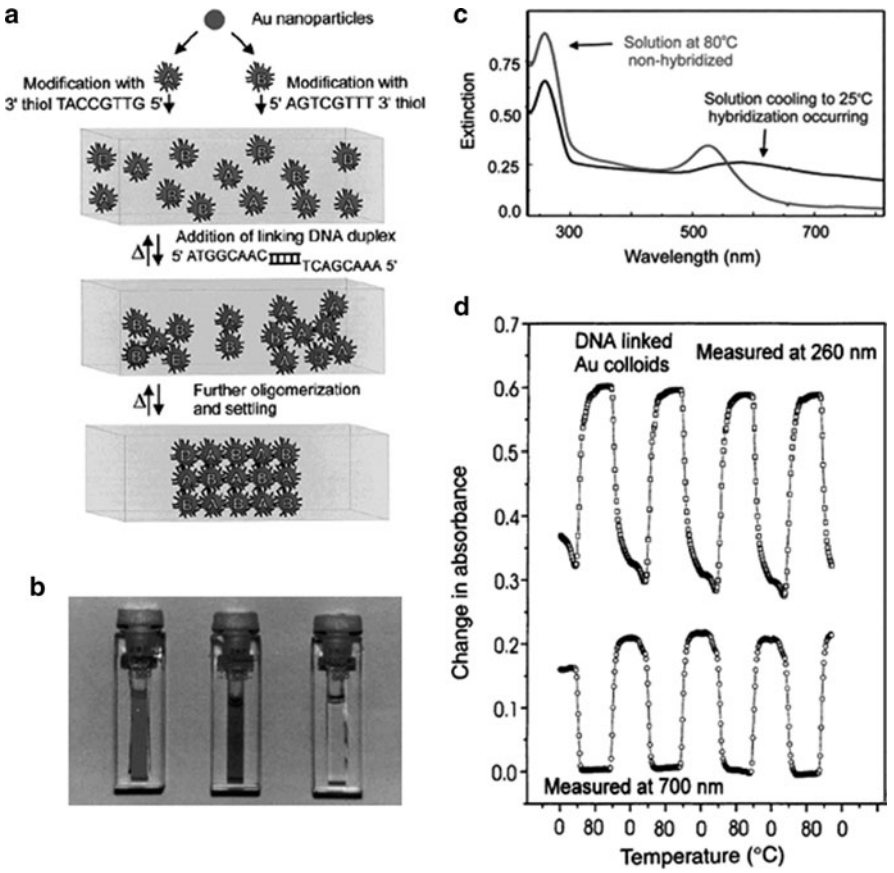

Fig. 6.26 (**a**) Schematic illustration showing the DNA-based nanoparticle assembly strategy. Mixing two non-complementary oligonucleotide-attached gold nanoparticles give no assembly formation and they independently disperse. Into this mixed dispersion, a linking oligonucleotide strand including a 12-base-pair overlap in the middle is added, then assembly of the nanoparticles is observed. Heating of the assembly above the dissociation temperature of the duplex gives independent dispersion again. (**b**) Solutions of 13-nm diameter Au nanoparticles before (*left cuvette*) and after (*center cuvette*) DNA-induced assembly. After extended periods of time a polymetric precipitate forms and settles to the bottom of the cuvette (*right cuvette*). (**c**) The UV–vis spectrum of oligonulecotide-modified 13 nm particles before (*red line*) and after (*blue line*) DNA-induced assembly. (**d**) Absorbance vs. temperature/time profile for DNA/colloid hybridized materials. At low temperatures, the Au colloids aggregate owing to the hybridization of "linking" DNA. At high temperature (80°C), the nanoparticles dehybridize and form a dark red dispersion. The temperature vs. time profile shows that this is a reversible process [57]

a unique and noble properties which beyond the original properties of nanoparticle. In this section, we would like to focus on the systematic immobilization of nanoparticles, especially from the three viewpoints of application: an increase in number, an enhancement of the nanoparticle effect, and an addition of a function.

Increase in Number

The most famous example to use the large specific surface of nanoparticles is the dye sensitized solar cell with TiO_2 semiconductor nanoparticle, reported by Gratzel et al. [128]. The assembly of TiO_2 nanoparticles on an ITO electrode made the roughness factor of the electrode 1,000-folds compared to a planar electrode, and as a result, the photocurrent of the photovoltaic cells using this modified electrode remarkably increased. By Willner's group, the increase strategy with nanoparticles was introduced to the various applications, e.g., an electrochemical sensor (Fig. 6.27b), a photo-electric conversion (Fig. 6.27c), and a DNA sensor based on QCM (Fig. 6.27d) and so on. They produced multi-structure assemblies on an electrode consisting of gold nanoparticles capped with negative charged citrate acid ($\sim$15 nm) and cationic molecules via electrostatic interactions, as shown in Fig. 6.27a [81, 129]. As an example, we describe here the multi-structure assemblies consisting gold nanoparticles and a porphyrin derivative by alternately repeating the electrostatic adsorption procedures (layer-by-layer assembling). The build-up of multi-structure assemblies were pursued by an absorption spectroscopic observation and a cyclic voltammetry measurement [129]. The photocurrent action spectrum also grew up with increasing the cycle of alternate assembling, as shown in Fig. 6.27c. In the case of the DNA diagnostic sensor, they used compensate DNA hydrogen interactions for the preparation of nanoparticle assembly instead of the electrostatic interaction, and distinguished a mismatch of DNA by monitoring the degree of nanoparticle assembly with QCM (Fig. 6.27d).

These are smart examples of application. However, in the case of the alternate self-assembling system, the assembling processes are considerably time-consuming. On the other hand, Yamada et al. reported another approach, that is, electrolyte-induced precipitation. That is one of a salting-out system and has used as the more convenient fabrication of multi-structure assemblies (Fig. 6.28A) [130, 131]. First, the electrode is placed at the bottom of a glass vessel containing the colloidal solution of nanoparticles. Then, an aqueous solution of $NaClO_4$ is added, resulting precipitation (salting-out) of nanoparticles on the electrode. Finally, the thiol derivative molecules (in this case, the molecule was ruthenium-viologen linked compound) were self-assembled on the surfaces of metal nanoparticle, giving three-dimensional multi-structures. This is only a two-step process. With this approach, the number of immobilized molecules as well as the photocurrent intensity of this structure are more than 15-fold larger than those obtained with a planar monolayer electrode, as can be verified from the comparison of the redox waves of the V^{2+} moiety at CV measurements and the photocurrent action spectra (Fig. 6.28C). Typical SEM images of the above described multi-structure of gold nanoparticles are shown in Fig. 6.28B. From these images, we can find the thickness and the surface area depend on the volume of the dispersion of the gold nanoparticles which we used at the salting-out procedure, and whereas the degree of agglomerates of the gold nanoparticles on each electrodes are almost similar and independent on the volume of the dispersion.

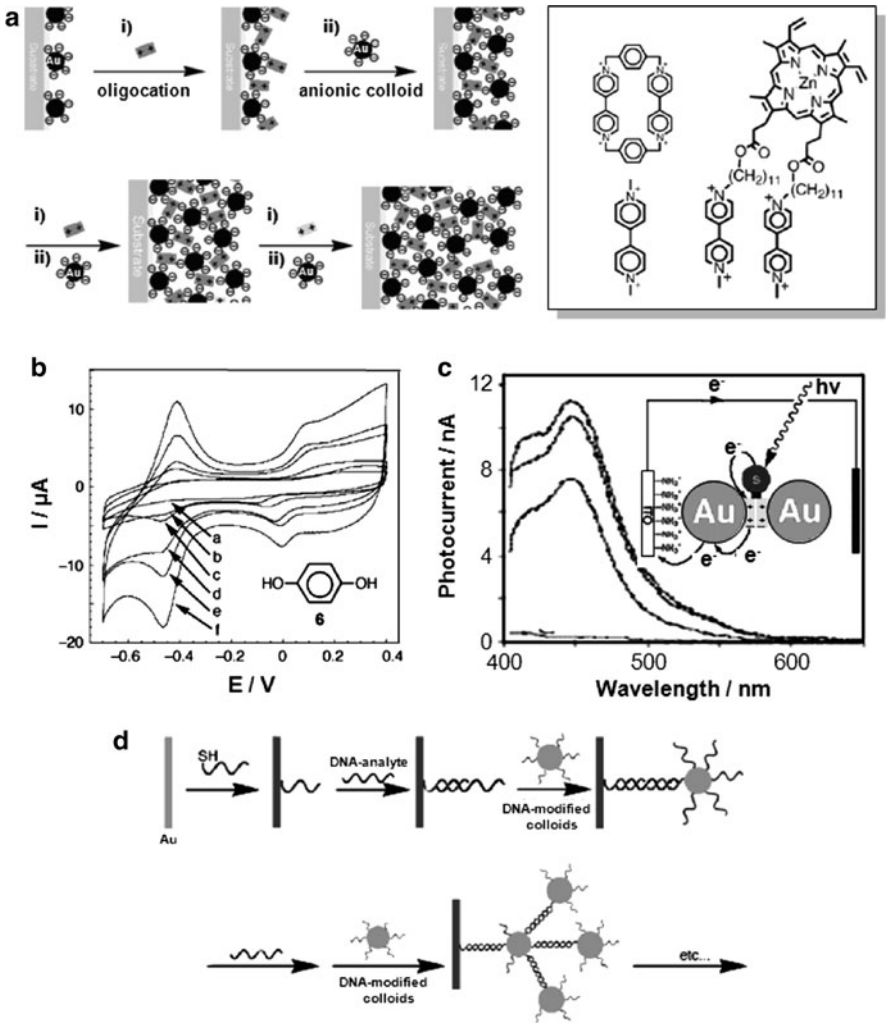

Fig. 6.27 (**a**) Method for the construction of oligocation-crosslinked Au-nanoparticle multilayers by electrostatic interactions. The first particle layer is formed by the interaction of a nanoparticle solution with an amine-functionalized surface. Inset molecules are viologen-based cationic functional crosslinkers. (**b**) Cyclic voltammograms of hydroquinone ($1'10^{-5}$M) in 1–5 layer gold nanoparticle/cyclobis(paraquat-p-phenylene) arrays. (**c**) Photocurrent action spectra obtained from 0-, 1-, 3-, and 4-layer of Ru sensitizer-bipylidinium dyad type catenane-crosslinked Au nanoparticle arrays. Inset image: Mechanism for the generation of a photocurrent from a photosensitizer-bipyridinium dyad crosslinked Au nanoparticle superstructure. (**d**) Method for the construction of DNA-crosslinked nanoparticle arrays for the sensing of a DNA analytes [81, 129]

The salting-out method as a nanoparticle immobilization on a solid substrate has been applied to the photo-electrochemical study of bio-material, which has a bigger body than organic artificial compound and an essential defect for signal-to-noise ratio. Terasaki et al. used these methods to increase the photo-induced

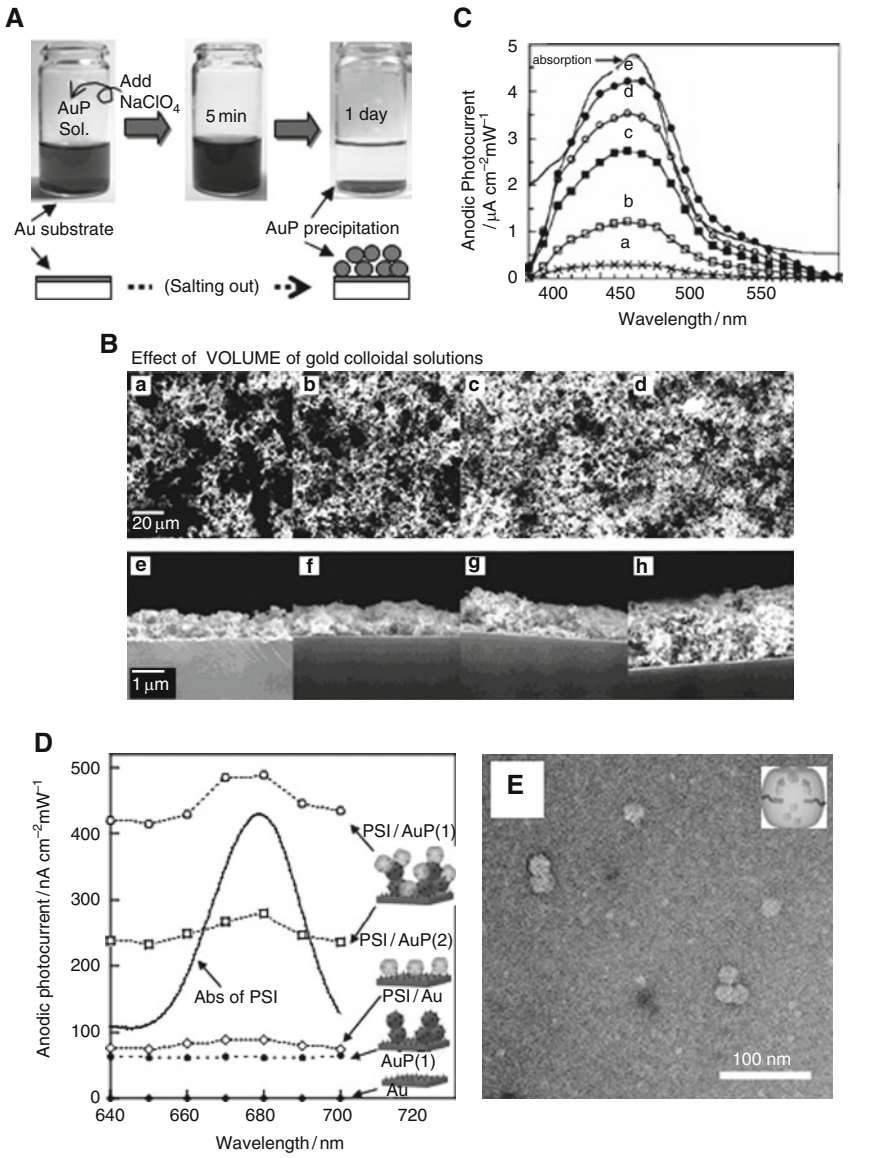

Fig. 6.28 (**A**) Method for the construction of gold particle assembly by a salting out process. (**B**) SEM images of the tris(2,2'-bipyridine)ruthenium(II)-viologen linked thiol (RuVS)-AuP/Au electrodes. RuVS-AuP/Au electrodes are prepared by precipitation of gold particles from the colloidal dispersion by the salting out process. (**C**) Photocurrent action spectra of (a) the RuVS/Au and (b–e) RuVS-AuP/Au electrodes. The RuVS-AuP/Au electrodes are prepared by the salting out process from the colloidal dispersions: (b) 10, (c) 20, (d) 30, and (e) 50 cm^3. (**D**) Photocurrent action spectra from PSI-gold nanoparticle hybrid electrode, (*square*) PSI/AuP(1) assembly, (*circle*) PSI/AuP(2) assembly, (*diamond*) PSI on Au plate, (*filled circle*) AuP(2) on Au plate, and (*filled diamond*) Au plate. AuP(1) and AuP(2) structures were prepared by using Au nanoparticle dispersion with different quantities. (**E**) TEM image of PSI (photosystem I) [130–133]

electron signal from the photosynthetic protein complexes, such as photosystem I (PSI) [132] and photosystem II (PSII) [133]. We here show the example of gold nanoparticle-PSI hybrid electrodes. In this case, 15 nm gold nanoparticles that were comparable to the size of PSI (Fig. 6.28E), were used and the AuP-PSI multi-structure was prepared in a similar manner as described above. The orientation of PSI was controlled by use of the anionic mercaptopropanesurfonate (MPS) SAM as an interlayer. Since PSI has absorption bands in the longer wavelength region (>650 nm), the molecular excitation by the enhanced localized field on the gold nanoparticle surface, if any, must be well overlapped with each other in terms of wavelength. In fact, they obtained larger photocurrent responses with increasing the number of gold nanoparticles (Fig. 6.28C).

Enhancement of Effects

One of the most attention properties of metal nanoparticles, such as silver and gold, are strong enhancement of the electric field of localized surface plasmon (LP), where the surface plasmon resonance (SPR) is observed in the visible- to- near infrared region. As a typical example, the field enhancement for the incident light wave at 521 nm is estimated to be as high as 21 times for a gold nanoparticle of 50 nm diameter, and 256 times at 365 nm light for a silver nanoparticle (Okamoto and Fukui, Unpublished results). In addition, the electric field is remarkably enhanced at the nanospace between two closely located metal nanoparticles, and at the point of metal nanorods and nanoprisms of triangular shape, etc. [134,135]. The enhanced electromagnetic field is also expected to couple with the electronic excitation of the molecules located near the particle surface. Because the electromagnetic filed of surface plasmon has similar properties with the light field, and it strongly localizes on the surface. Excitation of immobilized molecules at the metal surface is expected with this system, and has been verified by strong Raman and fluorescence enhancement. From these viewpoints, control and optimization of the shape and the alignment of metal nanoparticles, and the nanostructures constituted with metal nanoparticles must be requisite for the practical use. Yamada et al. had investigated the effects of these factors with gold spherical and rod like nanoparticle [136,137]. To be concrete, they have demonstrated three comparisons by monitoring the Raman signals of rordamin 6G as a probe: (1) comparison of nanostructures consisted by salting-out process of gold nanoparticle (35 nm) with various salts, such as NaOH and $NaClO_4$ (NS-35($NaClO_4$) and NS-35(NaOH) in Fig. 6.29a), (2) comparison of the size of spherical gold nanoparticles (15 and 35 nm) using salting-out process (NS-35($NaClO_4$) and NS-35($NaClO_4$) in Fig. 6.29a), (3) comparison of the shape of nanoparticles (rods with two aspect ratios and sphere in Fig. 6.29b). As the result, the higher intensities of raman signals were obtained in the case of the more effectively agglomerated nanostructure and the lager nanoparticles (Fig. 6.29a). Interestingly, the raman signals could be observed in the 2D assemblies of gold nanorods in spite of no sensitivity in the 2D assemblies of spherical gold nanoparticles. This result indicates that the gold nanorods have a high potential as a plasmonics material.

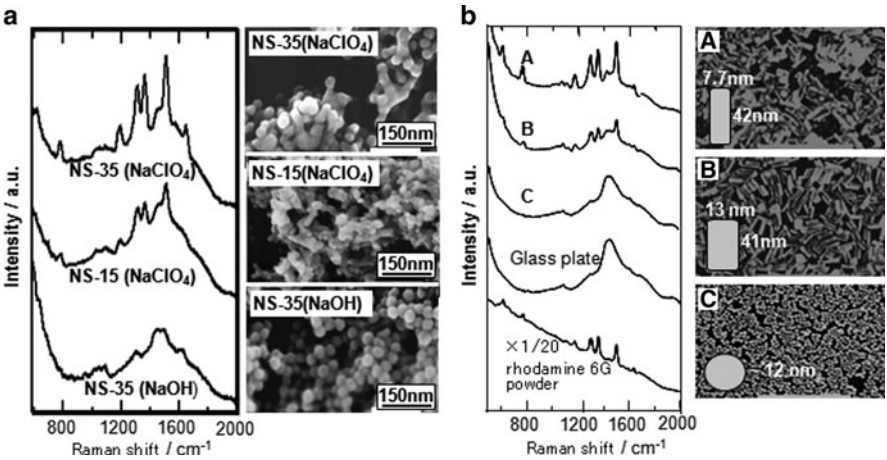

Fig. 6.29 (**a**) (*left*) Nonresonance Raman scattering spectra of rhodamine 6G (R6G) on the gold nanoparticle sample plates and (*right*) the SEM images of the surface of the corresponding sample plates. NS-35($NaClO_4$): Plate prepared with 35-nm sized gold nanoparticles deposited by addition of an aqueous $NaClO_4$ (3M) solution. NS-15($NaClO_4$): Plate prepared with 15-nm sized gold nanoparticles deposited by addition of an aqueous $NaClO_4$ (3M) solution. NS-35(NaCl): Plate prepared with 35-nm sized gold nanoparticles deposited by addition of an aqueous NaCl (3M) solution. (**b**) (*left*) Nonresonance Raman scattering spectra of R6G on the gold nanoparticle or nanorod sample plates and (*right*) the SEM images of the surface of the corresponding sample plates. (A) Plate prepared with gold nanorods with the diameter of 7.7 nm and the length of 42 nm. (B) Plate prepared with gold nanorods with the diameter of 13 nm and the length of 41 nm. (C) Plate prepared with gold nanoparticles with the diameter of 12 nm [136, 137]

Moreover, the signal enhancement with localized plasmon resonance (LPR) has been extended to the other applications, such as a photoelectric conversion device. In the previous work, SPR (Fig. 6.30a) has been successfully applied to the enhancement in photocurrent, due to enhanced excitation of SAMs of porphyrin at the surface of gold film that was coupled with a prism. On the other hand, Terasaki and Yamada et al. firstly show the photocurrent enhancement by using the LPR of metal nanoparticles. The comparison of plasmon resonance profiles between metal film (SPR) and nanoparticles (LPR) is illustrated in Fig. 6.30a [138]. They prepared a self-assembled monolayer of N3 dye (inset picture of Fig. 6.30b) on the surfaces of nano-structured gold electrode prepared by salting-out procedure (see Fig. 6.28A). And they compared the photocurrent action spectra between the nano-structured gold electrodes and the planar ones, under the comparable surface coverage condition. Figure 6.30b shows the ratio of photocurrents as the function of wavelength. If the ratio depends only on the ratio of molecular coverage, it should be constant and be independent in the whole wavelength region studied. However, the ratio certainly tends to increase in the longer wavelength region, and the profile well corresponds to the absorption spectrum of the nano-structured electrode. Thus, the effect of LPR on the photocurrent enhancement is strongly indicated. Further, they proved such photocurrent enhancement was originated from the fluorescence enhancement of dye molecules on the gold nanoparticles.

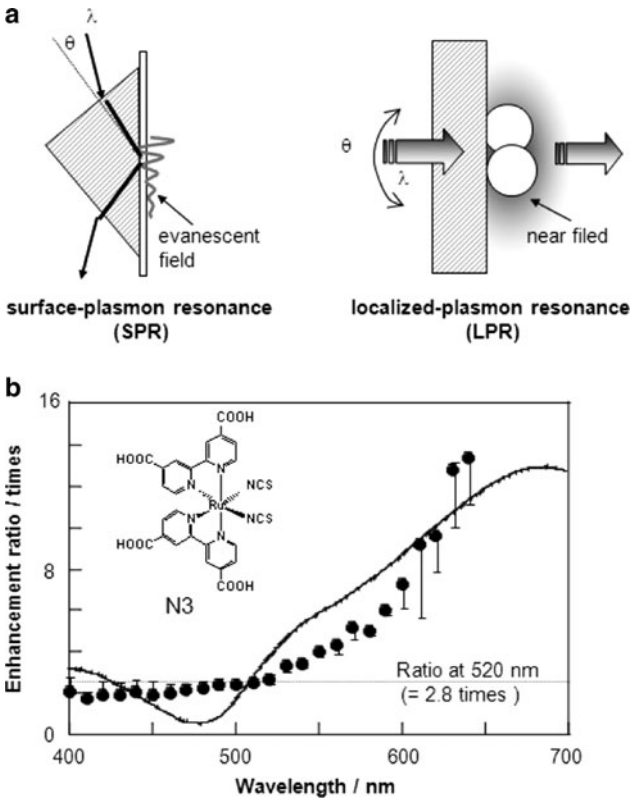

Fig. 6.30 (**a**) Schematic illustration of processes of surface-plasmon resonance (SPR) and localized-plasmon resonance (LPR). (**b**) Photocurrent ratio of a ruthenium dye (N3)-modified nanostructured electrode (SPR) to planar electrodes (LPR) (*filled circle*), and the transmission absorption spectrum (*solid line*) of the nanostructured electrode [138]

Addition of Novel Functions

Originally, the formation of 1D array with metal nanoparticles have been much expected to achieve a nano-wiring of the opto-electronic device in the next generation. In the preparation process, metal nanoparticles would be immobilized on the substrate and necked to the neighbor metal nanoparticles. Whereas, the recent techniques about control the gap and space of the neighbor metal nanoparticles has introduced a novel function to the metal nanoparticle array, such as a plasmon waveguide [139, 140] and a single electron transistor (SET) with coulomb blocked phenomenon [141, 142].

The plasmon waveguide consisting of closely spaced (50 nm) 1D alignment of silver nanorods (30–90 nm) was firstly demonstrated by Maier et al. [139]. For the purpose to prove energy transportation along the waveguide, the waveguides are excited by the tip of a near-field scanning optical microscope. Based on the result of

this experiment, they firstly proved electromagnetic energy transport from a localized subwavelength source, the nanorod excited by the SNOM tip, to a localized detector over distances of about 500 nm in plasmon waveguides. In other case, Ohtsu et al. have proposed and fabricated an optical far/near-field conversion device that consisted of a nanodot coupler and an SPP condenser with gold nano architectures [140]. Yatsui et al. used cationic ZnO nanodots immobilized on DNA molecules as a 1D nanophotonic signal transfer system [91].

One of the attractive gold of application with assembling nanoparticle should be SET, because the ability is originated from the unique phenomenon which occurs only in nanometer order, coulomb blocked phenomenon [141, 142]. At a process of building up a SET device with metal nanoparticles, the important key is how to selectively assemble and place these nanoparticles into the desired positions. Yoo, Cheon and co-workers reported a SET using a DNA-assisted assembly of nanoparticles [143]. In this paper, the DNA molecules acted not only as the assembler, but also as the modulator for the electron tunneling behaviors of SETs. From the plots of I_{SD} as a function of the back-gate voltage (V_G) at several temperatures ($V_{SD} = 0.2$ V), we can recognize coulomb oscillations clearly up to 100 K with the period of $\Delta V_G \sim 10$ V.

Originally, the coulomb blocked phenomenon appears on the one by one metal nanoparticle. Thus, if we can prepare the ultrahigh photoelectron conversion system on the metal nanoparticle, we will obtain a single photon electron transistor device (SPED). In other word, the key process of the SPED is how to prepare the ultrahigh photo-electron conversion system. Terasaki, Yonezawa and their co-workers suggested employing a bio-component as a part of artificial device [144, 145], because bio-components have achieved ultrahigh performance compared to the artificial ones. Bio-components from living bodies are very attractive nano-materials, because they have already achieved ultra-high and ultimate performance as the result of many cycles of mutation and natural selection. It is well known that during photosynthesis, the quantum yield of the electron transfer is almost unity. Therefore, the photosynthetic protein complex, photosystem I (PSI) is highly appropriate for the SPED, and in deed we use PSI as the photo-electric conversion material, combined on the metal nanoparticle. The scheme of this research is given in Fig. 6.31a. At first, VK_1 was extracted from the isolated intact PSI, to obtain PSI(-VK_1) with a pocket at the place where VK_1 was originally located in the PS, and other similar shape molecule can be inserted (reconstituted) in the pocket. Secondly, the designed molecular wire, naphthoquinone-sulfur linked molecular wire with a gold nanoparticle ($NQC_{15}S$-AuNP, particle size: ca 1.6 nm) was reconstituted with PSI. The molecular wire for signal transduction from PSI to artificial device was designed from the viewpoints of the shape to be inserted the pocket where VK_1 is extracted, the redox potential to relay the electron from PSI, and the molecular length of the wire to output electrons from a pocket without VK1 to outside of PSI. At the treatment of PSI, the extraction and reconstitution, the PSI bioactivity was always checked by monitoring the absorbance of P700. This result indicates that the naphthoquinone unit was inserted in the pocket of VK_1, and efficient multi-step electron transfer was recovered. These treatments was confirmed not only by the

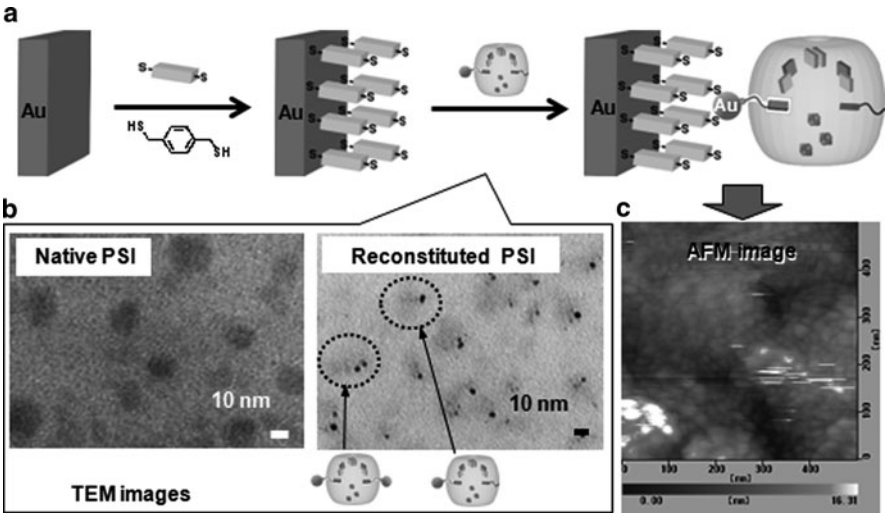

Fig. 6.31 (**a**) Methods for immobilization of gold nanoparticle-reconstituted PSI onto a gold electrode surface. (**b**) TEM images of (*left*) native PSI molecules and (*right*) nanoparticle-reconstituted PSI molecules. (**c**) AFM images of gold nanoparticle-reconstituted PSI modified gold surface [144]

spectrum method, but also by TEM images directly, in other word they succeeded in the visualization of the reconstitution of the designed molecular wire with gold nanoparticle to the PSI($-VK_1$). From the TEM images in Fig. 6.31b, both a large gray circle ($\sim$10 nm) and a clear small black dot ($\sim$2 nm) were observed. The gray circle corresponds to an intact PSI (the gray color corresponds to the Mg ions in PSI) and the black dot corresponds to a gold nanoparticle.

To prove the signal transduction of photo-electrons from PSI via a molecular wire, they immobilized the reconstituted PSI on the gold electrode, and measured a photocurrent measurement upon the gold electrode was performed. The immobilization procedure of reconstituted PSI on a gold electrode and the AFM image are shown in Fig. 6.31a, c. The reconstituted PSI immobilized gold electrode was prepared by a direct connection between the gold nanoparticle in the molecular wire and a gold electrode by using bi-thiol compound as the interlayer. When monochromatic light was irradiated, the photocurrent responses to the anodic direction were observed. The action spectrum, shown in Fig. 6.32b, shows a clear peak around 680 nm, which is consistent with the absorption spectrum of PSI (dashed line). This result clearly indicates that these photocurrent responses are due to the photo-excitation of PSI. A practical application as an electronic device, such as an imaging device, was examined by adapting the reconstructed PSI on a gate of an FET (Fig. 6.32a. PSI@NQC_{15}S-AuNP was immobilized on an Si_3N_4 thin layer on the gate of FET by a silane coupler which has a mercapto group. Light irradiation at 670 nm caused a drastic change in the voltage between the gate and the source (V_{GS}). Light intensity affected to the magnitude of VGS, and indeed the biosensor system

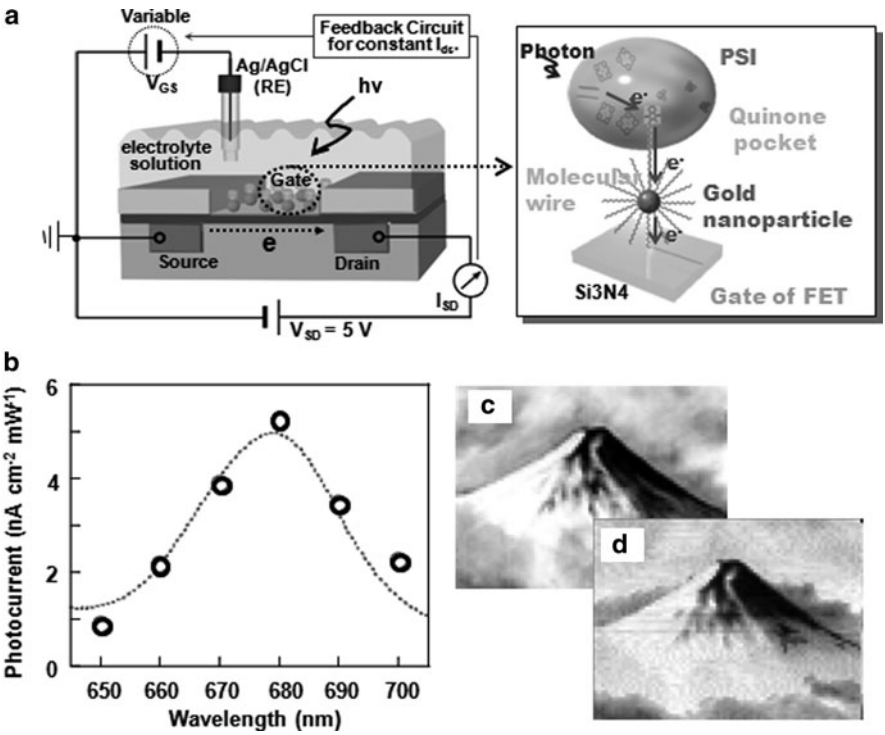

Fig. 6.32 (**a**) Schematic illustration of the FET module with the gate modified with nanoparticle-reconstituted PSI molecules (*left*). The concept of photosensor composed of nanoparticle-reconstituted PSI (*right*). A photon is converted to an electron and transferred to a gold nanoparticle. (**b**) A photocurrent action spectrum upon nanoparticle-reconstituted PSI molecules immobilized gold electrode (○). *Dotted line* is an absorption spectrum of PSI molecules. (**c**) An input image and (**d**) the out put image obtained with the FET system (**a**) [144, 145]

interpreted a grey-scale image of Mt. Fuji (Fig. 6.32d). Surprisingly, the lifetime of this FET system was more than 1 year.

6.4 Conclusions

In this section, we have introduced the various preparative processes and applications of nanoparticle assemblies. Nanoparticles show specific properties which depend strongly on their sizes. Various self-assemble techniques and molecular interactions are used for nanoparticle assembly. Not only the inorganic core of the particles but also organic shells are highly important for assembly formation. The assembly formation enhances such unique properties, and it makes them "real" materials.

Acknowledgements The part of our nanoparticle studies were supported by Grant-in-Aids from MEXT or JSPS, Japan.

References

1. G. Schmid (ed.), *Clusters and Colloids* (Wiley, Weinheim, 1994)
2. G. Schmid (ed.), *Nanoparticles* (Wiley, Weinheim, 2004)
3. F. Caruso (ed.), *Colloids and Colloid Assemblies* (Wiley, Weinheim, 2004)
4. M. Haruta, N. Yamada, T. Kobayashi, S. Iijima, J. Catal. **115**, 301 (1989)
5. N. Toshima, T. Yonezawa, New J. Chem. **22**, 1179 (1998)
6. D.L. Feldheim, C.D. Keating, Chem. Soc. Rev. **27**, 1 (1998)
7. S. Chen, R.S. Ingram, M.J. Hostetler, J.J. Pietron, R.W. Murray, T.G. Schaaff, J.T. Khoury, M.M. Alvarez, R.L. Whetten, Science **280**, 2098 (1998)
8. J.M. Perez, F.J. Simeone, Y. Saeki, L. Josephson, R. Weissleder, J. Am. Chem. Soc. **125**, 10192 (2003)
9. A.Y. Soohyoun, T.R. Decory, A.J. Baeumner, R.A. Durst, Anal. Chem. **75**, 2256 (2003)
10. H.J. Richter, J. Phys. D **32**, R147 (1999)
11. C.A. Mirkin, R.L. Letsinger, R.C. Mucic, J.J. Storhoff, Nature **382**, 607 (1996)
12. D.J. Maxwell, J.R. Taylor, S. Nie, J. Am. Chem. Soc. **124**, 9606 (2002)
13. F. Patolsky, K.T. Raniit, A. Lichtenstein, I. Willner, Chem. Commun. **12**, 1025 (2000)
14. S.F. Cheng, L.K. Chau, Anal. Chem. **75**, 16 (2003)
15. S. Abalde-Cela, P. Aldeanueva-Potel, C. Mateo-Mateo, L. Rodriguez-Lorenzo, R.A. Alvarez-Puebla, L.M. Liz-Marzan, J. Roy. Soc. Interface **7**, S435 (2010)
16. T. Yonezawa, H. Kawasaki, A. Tarui, T. Watanabe, R. Arakawa, T. Shimada, F. Mafune, Anal. Sci. **25**, 339 (2009)
17. H. Kawasaki, T. Yonezawa, T. Watanabe, R. Arakawa, J. Phys. Chem. C **111**, 16278 (2007)
18. C.T. Chen, Y.C. Chen, Anal. Chem. **77**, 5912 (2005)
19. Web site of The British Museum : The Lycurgus Cup; http://www.britishmuseum.org/explore/highlights/highlight_objects/pe_mla/t/the_lycurgus_cup.aspx
20. M. Faraday, Philos. Trans. R. Soc. Lond. **147**, 145 (1857)
21. M. Kerker, J. Colloid Interface Sci. **112**, 302 (1986)
22. T. Yonezawa, N. Toshima, in *Advanced Functional Molecules and Polymers*, ed. by H.S. Nalwa. Processing and Spectroscopy, vol. 2, chap. 3 (Overseas Publishers Association, 2001), pp. 65–86
23. M.C. Daniel, D. Astruc, Chem. Rev. **104**, 293 (2004)
24. M.A. Hayat, *Colloidal Gold* (Academic, New York, 1989)
25. M.P. Pileni, J. Phys. Chem. B **105**, 3358 (2001)
26. J. Turkevich, P.C. Stevenson, J. Hiller, Discuss Faraday Soc. **11**, 55 (1951)
27. G. Frens, Nat. Phys. Sci. **241**, 20 (1973)
28. T. Yonezawa, T. Kunitake, Colloids Surf. A **149**, 193 (1999)
29. M. Brust, M. Walker, D. Bethell, D.J. Schiffrin, J. Chem. Soc. Chem. Commun. **7**, 801 (1994)
30. M. Brust, J. Fink, D. Bethell, D.J. Schiffrin, C.J. Kiely, J. Chem. Soc. Chem. Commun. **16**, 1655 (1995)
31. A.C. Templeton, W.P. Wuelfing, R.W. Murray, Acc. Chem. Res. **33**, 27 (2000)
32. H. Hirai, Y. Nakao, N. Toshima, J. Macromol. Sci.-Chem. **A13**, 727 (1979)
33. H. Hirai, N. Toshima, in *Tailored Metal Catalysts*, ed. by Y. Iwasawa (D. Reidel Publishers, Dordrecht, 1986), pp. 121–140
34. T. Teranishi, M. Miyake, Chem. Mater. **10**, 594 (1998)
35. T. Yonezawa, N. Toshima, J. Chem. Soc. Faraday Trans. **91**, 4111 (1995)
36. N. Toshima, M. Harada, T. Yonezawa, K. Kushihashi, K. Asakura, J. Phys. Chem. **95**, 7448 (1991)

37. M. Harada, K. Asakura, N. Toshima, J. Phys. Chem. **98**, 2653 (1994)
38. M. Brust, C.J. Kiely, Colloids Surf. A **202**, 175 (2002)
39. J.R. Heath, C.M. Knobler, D.V. Leff, J. Phys. Chem. B **101**, 189 (1997)
40. T.K. Sau, C.J. Murphy, Langmuir **21**, 2923 (2005)
41. N.R. Jana, Angew. Chem. Int. Ed. **43**, 1536 (2004)
42. B. Nikoobakht, Z.L. Wang, M.A. El-Sayed, J. Phys. Chem. B **104**, 8635 (2000)
43. R.L. Whetten, J.T. Khoury, M. Alvarez, S. Murthy, I. Vezmar, Z.L. Wang, P.W. Stephens, C.L. Cleveland, W.D. Luedtke, U. Landman, Adv. Mater. **8**, 428 (1996)
44. G. Schmid, W. Meyer-Zaika, R. Pugin, T. Sawitowski, J.P. Majoral, A.M. Caminade, C.O. Turrin, Chem. Eur. J. **6**, 193 (2000)
45. W.D. Luedtke, U. Landman, J. Phys. Chem. **100**, 13323 (1996)
46. C.J. Kiely, J. Fink, M. Brust, D. Bethell, D.J. Schiffrin, Nature **396**, 444 (1998)
47. C.J. Kiely, J. Fink, J.G. Zheng, M. Brust, D. Bethell, D.J. Schiffrin, Adv. Mater. **12**, 640 (2000)
48. N. Terasaki, unpublished data
49. J. Luo, V.W. Jones, L. Han, M.M. Maye, N.N. Kariuki, C.J. Zhong, J. Phys. Chem. B **108**, 9669 (2004)
50. C.L. Haynes, A.D. McFarland, M.T. Smith, J.C. Hulteen, R.P. van Duyne, J. Phys. Chem. B **106**, 1898 (2002)
51. Z.L. Wang, S.A. Harfenist, R.L. Whetten, J. Bentley, N.D. Evans, J. Phys. Chem. B **102**, 3068 (1998)
52. J.E. Martin, J.P. Wilcoxon, J. Odinek, P. Provencio, J. Phys. Chem. B **104**, 9475 (2000)
53. Y.X. Zhang, H.C. Heng, J. Phys. Chem. B **110**, 16812 (2006)
54. J. Liu, J. Alvarez, W. Ong, A.E. Kaifer, Nano Lett. **1**, 57 (2001)
55. P.K. Sudeep, B.I. Ipe, K.G. Thomas, M.V. George, S. Barazzouk, S. Hotchandani, P.V. Kamat, Nano Lett. **2**, 29 (2002)
56. S. Yamada, T. Tasaki, T. Akiyama, N. Terasaki, S. Nitahara, Thin Solid Films **438–439**, 70 (2003)
57. C.A. Mirkin, Inorg. Chem. **39**, 2258 (2000)
58. L.M. Dillenback, G.P. Goodrich, C.D. Keating, Nano Lett. **6**, 16 (2006)
59. J.H. Lee, J. Cheon, S.B. Lee, Y.W. Chang, S.I. Kim, Y.H. Yoo, J. Appl. Phys. **98**, 084315 (2005)
60. J. Liu, Y. Lu, J. Am. Chem. Soc. **127**, 12677 (2005)
61. B. Zou, B. Ceyhan, U. Simon, C.M. Niemeyer, Adv. Mater. **17**, 1643 (2005)
62. A. Ongaro, F. Griffin, L. Nagle, D. Iacopino, R. Eritja, D. Fitzmaurice, Adv. Mater. **16**, 1799 (2004)
63. C. Sonnichsen, B.M. Reihard, J. Liphardt, A.P. Alivisatos, Nat. Biotechnol. **23**, 741 (2005)
64. S. Mann, W. Shenton, M. Li, S. Connolly, D. Fitzmaurice, Adv. Mater. **12**, 147 (2000)
65. K.K. Caswell, J.N. Wilson, U.H.F. Bunz, C.J. Murphy, J. Am. Chem. Soc. **125**, 13914 (2003)
66. Y. Yang, S. Matsubara, M. Nogami, J.L. Shi, W.M. Huang, Nanotechnology **17**, 2821 (2006)
67. A.M. Kalsin, M. Fialkowski, M. Paszewski, S.K. Smoukov, K.J.M. Bishop, B.A. Grzybowski, Science **312**, 420 (2006)
68. T. Yonezawa, S. Onoue, N. Kimizuka, Chem. Lett. **31**, 1172 (2002)
69. T. Yonezawa, K. Uchida, Y. Yamanoi, S. Horinouchi, N. Terasaki, H. Nishihara, Phys. Chem. Chem. Phys. **10**, 6925 (2008)
70. Y. Yamanoi, N. Shirahata, T. Yonezawa, N. Terasaki, N. Yamamoto, Y. Matsui, K. Nishio, H. Masuda, Y. Ikuhara, H. Nishihara, Chem. Eur. J. **12**, 314 (2006)
71. T. Yonezawa, Y. Yamanoi, H. Nishihara, J. Nanosci. Nanotechnol. **8**, 1518 (2008)
72. S. Nakao, K. Torigoe, K. Kon-no, T. Yonezawa, J. Phys. Chem. B **106**, 12097 (2002)
73. M.M. Maye, S.C. Chun, L. Han, D. Rabinovich, C.J. Zhong, J. Am. Chem. Soc. **124**, 4958 (2002)
74. M.M. Maye, J. Luo, I.S. Lim, L. Han, N.N. Kariuki, D. Rabinovich, T. Liu, C.J. Zhong, J. Am. Chem. Soc. **125**, 9906 (2003)
75. M.M. Maye, I.S. Lim, J. Luo, Z. Rab, D. Rabinovich, T. Liu, C.J. Zhong, J. Am. Chem. Soc. **127**, 1518 (2005)

76. I. Hussain, Z. Wang, A.I. Cooper, M. Brust, Langmuir **22**, 2938 (2006)
77. R. Blonder, L. Sheeney, I. Willner, Chem. Commun. **13**, 1393 (1998)
78. M. Lahav, A.N. Shipway, I. Willner, M. Nielsen, J.F. Stoddart, J. Electroanal. Chem. **482**, 217 (2000)
79. A.N. Shipway, M. Lahav, R. Blonder, I. Willner, Chem. Mater. **11**, 13 (1999)
80. M. Lahav, T. Gabriel, A.N. Shipway, I. Willner, J. Am. Chem. Soc. **121**, 258 (1999)
81. A.N. Shipway, I. Willner, Chem. Commun. **20**, 2035 (2001)
82. A.N. Shipway, M. Lahav, R. Gabai, I. Willner, Langmuir **16**, 8789 (2000)
83. S. Hoeppener, R. Maoz, S.R. Cohen, L.F. Chi, H. Fuchs, J. Sagiv, Adv. Mater. **14**, 1036 (2002)
84. R. Maoz, E. Frydman, S.R. Cohen, J. Sagiv, Adv. Mater. **12**, 725 (2000)
85. R. Maoz, E. Frydman, S.R. Cohen, J. Sagiv, Adv. Mater. **12**, 424 (2000)
86. R. Maoz, S.R. Cohen, J. Sagiv, Adv. Mater. **11**, 55 (1999)
87. T. Yonezawa, S. Onoue, T. Kunitake, Kobunshi Ronbunshu **56**, 855 (1999)
88. H. Nakao, H. Shiigi, Y. Yamamoto, S. Tokonami, T. Nagaoka, S. Sugiyama, T. Ohtani, Nano Lett. **3**, 1391 (2003)
89. K.D. Hermanson, S.O. Lumsdon, J.P. Williams, E.W. Kaler, O.D. Velev, Science **294**, 1082 (2001)
90. M. Hosogi, G. Hashiguchi, M. Haga, T. Yonezawa, K. Kakushima, H. Fujita, Jpn. J. Appl. Phys. **44**, L955 (2005)
91. T. Yatsui, Y. Ryu, T. Morishima, W. Nomura, T. Kawazoe, T. Yonezawa, M. Washizu, H. Fujita, M. Ohtsu, Appl. Phys. Lett. **96**, 133106 (2010)
92. I. Yamashita, Thin Solid Films **393**, 12 (2001)
93. K. Yamada, S. Yoshii, S. Kumagai, A. Miura, Y. Uraoka, T. Fuyuki, I. Yamashita, Jpn. J. Appl. Phys. **45**, 8946 (2006)
94. T. Douglas, D.P.E. Dickson, S. Betteridge, J. Charnock, C.D. Garner, S. Mann, Science **269**, 54 (1995)
95. T. Douglas, E. Strable, D. Willits, A. Aitouchen, M. Libera, M. Young, Adv. Mater. **14**, 415 (2002)
96. T. Douglas, M. Young, Nature **393**, 152 (1998)
97. M.T. Klem, D. Willits, M. Young, T. Douglas, J. Am. Chem. Soc. **125**, 10806 (2003)
98. R.A. McMillan, J. Howard, N.J. Zaluzec, H.K. Kagawa, R. Mogul, Y.F. Li, C.D. Paavola, J.D. Trent, J. Am. Chem. Soc. **127**, 2800 (2005)
99. T. Ueno, M. Suzuki, T. Goto, T. Matsumoto, K. Nagayama, Y. Watanabe, Angew. Chem. Int. Ed. **43**, 2527 (2004)
100. S.S. Mark, M. Bergkvist, X. Yang, E.R. Angert, C.A. Batt, Biomacromolecules **7**, 1884 (2006)
101. C. Chen, M.C. Daniel, Z.T. Quinkert, M. De, B. Stein, V.D. Bowman, P.R. Chipman, V.M. Rotello, C.C. Kao, B. Dragnea, Nano Lett. **6**, 611 (2006)
102. S. Beherns, W. Habicht, K. Wagner, E. Unger, Adv. Mater. **18**, 284 (2006)
103. C. Lin, Y. Liu, S. Rinker, H. Yan, Chem. Phys. Chem. **7**, 1641 (2006)
104. (a) Y. Huang, C.Y. Chiang, S.K. Lee, Y. Gao, E.L. Hu, J. de Yoreo, A.M. Belcher, Nano Lett. **5**, 1429 (2005) (b) K.T. Nam, B.R. Peelle, S.W. Lee, A.M. Belcher, Nano Lett. **4**, 23 (2004)
105. J. Sharma, R. Chhabra, Y. Liu, Y.G. Ke, H. Yan, Angew. Chem. Int. Ed. **45**, 730 (2006)
106. T. Furuno, H. Sasabe, K.M. Ulmer, Thin Solid Films **180**, 23 (1989)
107. H. Yoshimura, T. Scheybani, W. Baumeister, K. Nagayama, Langmuir **10**, 3290 (1994)
108. T. Scheybani, H. Yoshimura, W. Baumeister, K. Nagayama, Langmuir **12**, 431 (1996)
109. T. Yonezawa, S. Onoue, T. Kunitake, Adv. Mater. **10**, 414 (1998)
110. D.I. Gittins, A.S. Susha, B. Schoeler, F. Caruso, Adv. Mater. **14**, 508 (2002)
111. Z.J. Liang, A. Susha, F. Caruso, Chem. Mater. **15**, 3176 (2003)
112. G. Kaltenpoth, M. Himmelhaus, L. Slansky, F. Caruso, M. Grunze, Adv. Mater. **15**, 1113 (2003)
113. F. Caruso, R.A. Caruso, H. Mohwald, Science **282**, 1111 (1998)
114. F. Caruso, Adv. Mater. **13**, 11 (2001)
115. E. Dujardin, C. Peet, G. Stubbs, J.N. Culver, S. Mann, Nano Lett. **3**, 413 (2003)
116. T. Yonezawa, S. Onoue, N. Kimizuka, Chem. Lett. **34**, 1498 (2005)
117. K.Y. Lee, M.J. Kim, J. Hahn, J.S. Suh, I.Y. Lee, K. Kim, S.W. Han, Langmuir **22**, 1817 (2006)

118. T. Imaoka, H. Horiguchi, K. Yamamoto, J. Am. Chem. Soc. **125**, 340 (2003)
119. N. Satoh, J.-S. Cho, M. Higuchi, K. Yamamoto, J. Am. Chem. Soc. **125**, 8104 (2003)
120. N. Satoh, T. Nakashima, K. Yamamoto, J. Am. Chem. Soc. **127**, 13030 (2005)
121. A. Kimoto, K. Masachika, J.-S. Cho, M. Higuchi, K. Yamamoto, Chem. Mater. **16**, 5706 (2004)
122. F. Caruso, M. Spasova, V. Saigueirino-Maceira, L.M. Liz-Marzan, Adv. Mater. **13**, 1090 (2001)
123. S. Lobert, G. Stubbs, Acta Cryst. **A46**, 993 (1990)
124. R.M. Crooks, M.Q. Zhao, L. Sun, V. Chechik, L.K Yeung, Acc. Chem. Res. **34**, 181 (2001)
125. I. Nakamula, Y. Yamanoi, T. Yonezawa, T. Imaoka, K. Yamamoto, H. Nishihara, Chem. Commun. **44**, 5716 (2008)
126. S. Si, T.K. Mandal, Langmuir **23**, 190 (2007)
127. T. Kang, S. Hong, I. Choi, J.J. Sung, Y. Kim, J.S. Hahn, J. Yi, J. Am. Chem. Soc. **128**, 12870 (2006)
128. M. Grätzel, Acc. Chem. Res. **42**, 1788 (2009)
129. A.N. Shipway, E. Katz, I. Willner, ChemPhysChem **1**, 18 (2000)
130. Y. Kuwahara, T. Akiyama, S. Yamada, Langmuir **17**, 5714 (2001)
131. T. Akiyama, K. Inoue, Y. Kuwahara, N. Terasaki, Y. Niidome, S. Yamada, J. Electroanal. Chem. **550–551**, 303 (2003)
132. N. Terasaki, N. Yamamoto, M. Hattori, N. Tanigaki, T. Hiraga, K. Ito, M. Konno, M. Iwai, Y. Inoue, S. Uno, K. Nakazato, Langmuir **25**, 11969 (2009)
133. N. Terasaki, N. Yamamoto, T. Hiraga, I. Sato, Y. Inoue, S. Yamada, Thin Solid Films **499**, 153 (2006)
134. Y. Chen, C. Wang, Z. Ma, Z. Su, Nanotechnology **18**, 325602 (2007)
135. L.J. Sherry, R. Jin, C.A. Mirkin, G.C. Schatz, R.P. van Duyne, Nano Lett. **6**, 2060 (2006)
136. M. Suzuki, Y. Niidome, Y. Kuwahara, N. Terasaki, K. Inoue, S. Yamada, J. Phys. Chem. B **108**, 11660 (2004)
137. M. Suzuki, Y. Niidome, N. Terasaki, K. Inoue, Y. Kuwahara, S. Yamada, Jpn. J. Appl. Phys. **43**, L554 (2004)
138. N. Terasaki, S. Nitahara, T. Akiyama, S. Yamada, Jpn. J. Phys. Chem. **44**, 2795 (2005)
139. S.A. Maier, P.G. Kik, H.A. Atwater, S. Meltzer, E. Harel, B.E. Koel, A.A.G. Requicha, Nat. Mater. **2**, 229 (2003)
140. W. Nomura, M. Ohtsu, T. Yatsui, Appl. Phys. Lett. **86**, 181108 (2005)
141. H. Birk, M.J.M. DeJong, C. Chonenberger, Phys. Rev. Lett. **75**, 1610 (1995)
142. A. Zabet-Khosousi, A.A. Dhirani, Chem. Rev. **108**, 4072 (2008)
143. J.H. Lee, J. Cheon, S.B. Lee, Y.-W. Chang, S.-I. Kim, K.-H. Yoo, J. Appl. Phys. **98**, 084315 (2005)
144. N. Terasaki, N. Yamamoto, K. Tamada, M. Hattori, T. Hiraga, A. Tohri, I. Sato, M. Iwai, M. Iwai, S. Taguchi, I. Enami, Y. Inoue, Y. Yamanoi, T. Yonezawa, K. Mizuno, M. Murata, H. Nishihara, S. Yoneyama, M. Minakata, T. Ohmori, M. Sakai, M. Fujii, Biochim. Biophys. Acta **1767**, 653 (2007)
145. N. Terasaki, N. Yamamoto, T. Hiraga, Y. Yamanoi, T. Yonezawa, H. Nishihara, T. Ohmori, M. Sakai, M. Fujii, A. Tohri, M. Iwai, Y. Inoue, S. Yoneyama, M. Minakata, I. Enami, Angew. Chem. Int. Ed. **48**, 1585 (2009)

Index

Adiabatic, 25, 29, 33, 35, 46
Alcohol reduction, 190, 193
Alternating electric field, 165, 166
Alumina, 38
AN-AuNP, 170–172, 183
AND gate, 10, 14
Angular spectrum representation, 54
Anisotropy, 181
Annihilation, 4, 6
Anti-bunching, 22
Anti-counterfeiting, 77, 78, 89, 92
Aperture, 19, 28–30
Argon plasma, 49
Assembly, 162–166, 176, 177, 182, 183, 189–191, 193–211, 213–223, 225–229, 231
Atom photonics, 54
Atomic force microscopy (AFM), 95–100, 104, 105, 111, 112, 115, 118–120, 122, 123, 167, 169–176, 179, 180, 183, 198, 199, 208, 212–216, 227
AuNP, 164, 166, 170, 173–175, 177–179, 181
AuNRs, 162, 163
Autonomy and robustness, 61

Borohydride reduction, 191
Broadcast, 23

Carniglia-Mandel model, 54
Carrier-carrier scattering, 14
Carrier lifetime, 11, 14
CdSe, 16
Cetyltrimethyl ammonium bromide, 163
Chevron pattern, 97, 115, 117
Citrate reduction, 190, 191
Coalescence, 109, 110, 112, 123
Coherent phonon, 5, 6, 24, 26, 40, 46, 49, 55
Content addressable memory, 23
Conversion efficiency, 66, 69–71
Creation operator, 4, 5
Critical thickness, 95, 96, 98
Crystal lattice, 5, 6, 23, 32
CTAB, 163
CTR, 110
CuCl, 11, 13, 14, 19, 21, 23
Cyano-bridged metal complex, 73

1D, 161–167, 170, 175, 176, 179, 180
Dark-field optical microscopy, 177–181
Degenerate, 47
Dendrimer, 218
Dendron, 202
Density-of-states (DOS), 143
Desk-top machine, 35
3D island, 94, 95, 97, 113, 114, 118
Dielectrophoresis, 166
Diffraction, 2, 9, 20, 30, 31
  grating, 32, 35
  limit, 161, 162, 179
Dimer plasmon, 153
Dip-pen nanolithography, 164, 165, 185
Dislocation, 94, 102, 119
Dislocation , 109
Dispersion relation, 143, 144
Displacement operator, 5
Dissociation energy, 24
DNA, 7, 16, 162, 166–184, 199, 203, 208, 210–216, 218–221, 226
DNA stretching, 168, 170, 182, 183
Dressed photon, 1, 3–5, 9, 14, 18, 54

Electric dipole-allowed, 10, 20, 25, 48, 51
Electric dipole-forbidden, 10, 20, 25, 28, 48, 51, 55

M. Ohtsu (ed.), *Progress in Nanophotonics 1,* Nano-Optics and Nanophotonics,
DOI 10.1007/978-3-642-17481-0,

Electric-field, 167
Electromagnetic wave, 161, 179
Electron beam lithography, 31, 34, 68
Electron-electron (e-e) scattering, 145
Electron-hole pair, 4, 48, 50
Electron-phonon (e-ph) scattering, 145
Electrostatic interaction, 210, 215, 220
Elementary excitation, 5, 55
Epitaxial growth, 94
Evaporation, 195, 196, 200
Excited state, 105–107
Exciton, 10, 13, 22
Experimental visibility, 88, 89
Exposure time, 29
Extinction spectrum, 131, 132

Facet, 97, 98, 115, 117, 118
Fall time, 11, 23
Fan-out, 14
Faraday, 190, 229
Far-mode observation, 80
Ferritin, 213, 214
Feynman diagram, 3, 5
Fiber probe, 6, 25, 35
Finite-difference time-domain (FDTD), 66
Fluorescence, 34, 44
Frank-van der Merwe (FM) mode, 94
Free photon, 3, 4, 17, 44, 48
Frens, 191, 229
Frequency up-converter, 15
Fresnel zone plate, 32

GaAs, 94–96, 98, 100–107, 109–113, 116–124
GaAsSb, 110, 120–123
GaN, 52
Global sum, 23
Gold, 189–193, 195–198, 200, 202–204, 206, 208, 210–214, 217–220, 222–224, 226–229
Gold nanoparticle, 129, 131, 140, 141, 145, 149, 153–155
Gold nanorod, 162–164
Green dyadic, 131, 138, 139
Grid structure, 82, 83, 85, 89
Ground state, 101, 105, 107

Hanbury Brown and Twiss method, 22
Hard template, 166
Head-to-tail, 163, 164
Heisenberg uncertainty relation, 2
Hierarchical hologram, 77–80, 89
High-temperature (HT) phase, 73
Host-guest, 199, 203
Hot spot, 179
Hydrodynamic flow, 167
Hydrophilic, 169, 182
Hydrophobic, 162, 165, 168–170, 182

π-core, 170
Immobilization, 189, 191, 193, 195, 197, 199, 201, 203, 205, 207–209, 211, 213, 215, 217–219, 221, 223, 225, 227, 229, 231
InAs, 12, 14, 19, 32, 94–124
Incident light, 181
Infrared photon, 52
InGaAs, 101–103, 111, 118–121, 123
Input terminal, 10, 17
π–π interaction, 170, 172, 183
Interdiffusion, 106, 109
Intermittent growth, 94, 109, 113–116, 123
π-stacking, 170, 183

Langmuir-Blodgett, 165
Lattice mismatch, 94
Light emitting diode, 35
Lightning rod effect, 151, 156
Local density-of-states (LDOS), 134, 138
Localization, 2, 5
Localized plasmon resonance (LPR), 161, 224, 225
Localized surface plasmon (LP), 223
Long-wavellength approximation, 5, 10
Longitudinal mode, 132, 142
Low-temperature (LT) phase, 73
Lycurgus cup, 190

Macro-scale observation, 63
Magnetic storage system, 7
Magnetic tweezer, 167
Magnified-transcription, 63
Mass-production, 2, 34
MBE, 93–95, 98, 106, 123
Mediator-template, 203
Meniscus forces, 167
Metallic nanoarray, 180–182
Metal nanoparticles, 161
Metal-semiconductor-metal photodetector, 52
Mie theory, 129, 131, 140
Misfit dislocation, 119, 120
MNPs, 161–166, 170, 172, 176–181, 183, 184
Molecular beam epitaxy, 93, 124

Molecular bridge, 54
Molecular vibrational energy, 25
Mole-fraction ratio, 41
Monte-Carlo method, 100
Morphology, 48, 52
Multiple exposures, 30

Nano-beak, 8
Nanohole, 94, 103–105, 121, 123
Nano-patterned media, 7
Nanoparticle, 190, 195–200, 202–204, 206, 208–210, 213–215, 217–229
Nanophotonic code, 78, 81–90
Nanophotonic matching, 63, 65
Nanoplate, 151, 152
Nanorod, 132, 133, 141–151, 156
Nanosphere lithography, 198, 200
Nanostructure, 127, 145, 149, 151, 155, 156
Near-field interaction, 152, 154–156
Near-field optical microscope (NOM), 60, 128, 134–136, 138, 157
Near-field scattering, 140
Near-mode observation, 80, 85, 89
Nonadiabatic, 26
Non-invasive attack, 23
Non-linear process, 137, 148
NOT gate, 12
Numerical visibility, 84

One-dimensional (1D), 161–167, 170, 175, 176, 179, 180
One-dimensional (1D) scanning, 60
Optical computing, 61
Optical field, 127, 128, 133, 135, 149–157
Optically inactive, 30
Optical nano-fountain, 18, 24, 53
Optical near-field, 2, 11, 17, 36, 49, 136, 137
Optical switch, 10
Optical trapping, 167
Output terminal, 19

Parallel processing, 60–62, 73, 90, 92
Particle in a box, 133, 156
PDMS, 177–182
Phase-relaxation, 13
Phenaz-TMA, 173
Phenaz-TMA/AuNP, 173–177, 180, 183, 184
Phonon-assisted, 26, 35, 40
Phonon-assisted desorption, 38
Phonon-assisted photochemical etching, 37
Phonon-photon, 5
Photo-absorption energy, 24
Photochemical reduction, 173, 175, 183
Photochemical vapor deposition, 24
Photocurrent, 48
Photoinduced phase transition, 73–75
Photolithography, 2, 14, 28, 35
Photoluminescence (PL), 12, 19, 23, 42, 43, 96–109, 113, 115, 116, 120, 121, 149
Photomask, 28
Photoresist, 28, 34
Photosystem I (PSI), 222, 223, 226–228
Photovoltaic device, 48, 52
Planck's constant, 2
Plasmon, 127–129, 131–135, 140, 141, 143–145, 148, 150–153, 155–157
  absorption, 189, 190, 204, 218
  mode, 132–134, 142, 150, 151, 156
  waveguides, 162, 179
Pn-junction, 49
Polarization, 162, 180–182, 184
  conversion, 66, 69
  dependency, 83–85, 87–89
Poly-L-lysine, 167
Poly(2-polyvinyl pyridine), 166
Polymerase chain reaction (PCR), 176
Porphyrin, 204, 220, 224
Post-growth annealing, 94, 109, 123
PPhenaz, 169, 170, 172
PPhenaz-TMA, 172, 173
PPhenaz-TMA/DNA, 172–174
Probe-free nanophotonics, 60, 63, 90
Probe-scanning, 90
PVB, 168, 170
PVCz, 168–170

QCM, 220
QD, 93, 95–98, 100, 101, 103–106, 109, 112–123
Qualitative innovations, 1, 20, 54
Quantitative innovations, 2, 9, 20, 53
Quantum dot, 9, 54, 93, 94, 96, 100, 103, 109, 113, 116, 118, 123, 124
Quantum efficiency, 51
Quasi-particle, 3

Real photon, 3
RF-sputtering, 48, 49
Rise time, 11
Rolling circle amplification (RCA), 176
Routing table, 23

Sb, 110–112, 120
Sb-mediated growth, 94, 109, 110, 123
Scanning electron microscopy (SEM), 69
Schwobel barrier, 38
Selective chemical etching, 6
Self-assembled, 93
Self-assembled monolayer (SAM), 208, 223, 224
Self-assembled QD, 93, 95, 96
Self-assembly, 162, 164, 166
Self-formation, 93, 94, 104, 116, 118–120, 124
Self-organized processe, 36
Self size-limiting, 96, 98, 103, 105
Shape-engineered nanostructure, 65, 66
Side-to-side, 163, 164
Silanization, 167
Silver, 189, 195, 196, 206, 217, 223, 225
Single electron transistor (SET), 225, 226
Single photon, 22
Size- and conformation-controlling technology, 52
SNOM, 172, 174
Soft template, 166
Soft X-ray, 32
Solar cell battery, 52
Solvent evaporation, 177
Spherical nanoparticle, 128, 129, 131, 133, 140, 156
Spheroid, 130
Sputtering, 38
Stacking growth, 117, 118
Stark effect, 51
STEM, 101, 104, 105, 107, 108, 117, 118, 206, 207, 210
Step, 95, 104, 111, 115, 120–123
Strain, 94–97, 100–104, 109, 111, 113, 116–118, 120, 121, 123
Stranski-Krastanov (SK) growth mode, 93
Surface enhanced Raman scattering (SERS), 128, 162, 176, 179, 184
Surface migration, 96, 104, 109
Surface plasmon resonance (SPR), 189, 223–225
Surface segregation, 100, 101, 111
Surfactant, 111

Thermal equilibrium state, 46
Thiocholine, 208, 210
Thiol, 190–193, 195, 199–202, 220, 222, 227
Threshold, 29
Throughput, 34
Tobacco mosaic virus (TMV), 217
TP, 162, 181–184
Transfer-printing, 162
Transient transmission, 146–148, 156
Transition dipole, 4
Transmission electron microscopy (TEM), 119, 170, 174, 175, 193, 196, 201, 203, 206, 211, 215, 217, 222, 227
Transverse mode, 142
Triplet state, 25
Tublin, 214
Turkevich, 191, 229
Two-photon excitation, 145, 150–153, 155

Uniaxial, 181
Up-converted photon, 45

Vibration mode, 5, 26
Viologen, 204, 205, 220–222
Virtual photon, 2, 55
Volmer-Weber (VM) mode, 94

Wavefunction, 127, 133–135, 142, 143, 145, 148, 150, 152, 156, 157
Wavelength-selectivity, 50
Wetting layer, 98, 107, 108, 111, 113

Xe lamp, 30
X-ray crystal truncation rod (CTR) scattering, 110
XRD, 96

Yukawa function, 5, 11

ZnO nanorod, 12, 16